# Microstructure and Mechanical Properties of Ductile Die-cast Al-Mg-Si-Mn Alloys

A thesis submitted for the degree of
Doctor of Philosophy

By

**Douglas Watson**

Department of Mechanical, Aerospace and Civil Engineering
College of Engineering, Design and Physical Sciences
Brunel University London, Uxbridge, Middlesex UB8 3PH
United Kingdom

October 2015

Supervision: Dr. Shouxun Ji

Prof. Zhongyun Fan

# Abstract

Aluminium alloys have been seen a dramatic increase in transport manufacturing in past two decades. This is primarily driven by the achievement of effective weight-savings, increased vehicle fuel efficiency and reduced $CO_2$ emissions in transport. One of the significant progresses in most recent years has been in the application of aluminium-intensive car body structure, in which the manufacturing of thin wall castings with improved ductility is one of the critical issues. High pressure die casting (HPDC) is a fast and economical near-net shape manufacturing method to produce thin wall components. Therefore the application of HPDC process to make thin wall structural components for aluminium-intensive car body structure is one of the most challenges in recent development. However, the currently available die cast aluminium alloys are unable to fulfil this requirement because of the insufficient ductility, which is essential for joining castings with sheets and extruded parts. This has become critical in further development and extensive acceptance in car manufacturing industry.

Generally, the mechanical properties of die castings are determined by alloy composition, defect levels and microstructure in the castings. In the present study, the significant achievement is the development of Al-Mg-Si-Mn alloy for HPDC process to provide improved ductility in die castings in order to satisfy the requirement of mechanical properties, in particular ductility for the application in automotive body structure. Starting from the thermodynamic analysis and CALPHAD (Computer Coupling of Phase Diagrams and Thermochemistry) modelling of Al-Mg-Si system for solidification and phase formation, the alloy composition was optimised using international standard tensile samples to review the effect of various alloying elements on the mechanical properties.

Another achievement is the understanding of the solidification and microstructural evolution, the relationship between the microstructure and mechanical properties, and the strengthening mechanisms in the developed alloy. The solidification behaviour in the shot sleeve and in the die cavity was examined for the formation of the primary α-Al phase, eutectic Al-$Mg_2Si$ phases in the alloy. The morphology, size and size distribution of the primary α-Al phase were characterised under different solidification conditions. The growth morphology of the primary α-Al phase formed in the shot sleeve and in the die cavity was analysed using the Mullins-

Sekerka instability theory and the growth rate of eutectic Al-$Mg_2Si$ phases during solidification was calculated using Jackson-Hunt theory.

Still another achievement is the study of the effect of Mn and Fe on the morphology, size and distribution of various Fe-rich compounds in the Al-Mg-Si alloy produced by HPDC process. The assessment was associated with the mechanical properties of yield strength, ultimate tensile strength and elongation with different Fe and Mn contents. CALPHAD modelling of multi-component Al-Mg-Si-Mn-Fe and Al-Mg-Si-Fe systems was studied to find out the effect of Fe impurity in the Al-Mg-Si alloy. The precise accumulation of iron during HPDC using fully recycled materials was examined to predict the maximum cycles to produce castings with required mechanical properties. The strengthening mechanism and the relationship between the microstructure and mechanical properties are explored in the alloy made by secondary materials. Furthermore, the effect of nickel on the microstructure and mechanical properties of the die-cast Al-Mg-Si-Mn alloy was also studied in association with the formation of Ni-rich intermetallics during solidification in the die-cast Al-Mg-Si-Mn alloy containing different Ni contents.

The final achievement is the understanding of the repeatability of die castings made by the new alloy with industrial scale components. The tensile properties of standard samples that were obtained directly from HPDC process and made by the machined die castings at different locations were further assessed for the reproducibility of casting components made by the Al-Mg-Si-Mn alloy. The distributions of yield strength, ultimate tensile strength and elongation of the tensile samples were analysed by the average values with standard deviations and by the Weibull statistical model with three parameters. The correlations between the mechanical properties and the microstructural features, porosity levels and fracture morphology were investigated for the different types of samples. It was found that three-parameter Weibull analysis was capable of analysing the reproducibility of die cast components and the scattering of tensile properties was mainly due to the presence of porosity and non-uniform microstructure in the die-castings.

# Acknowledgement

I would like to thanks Dr. Shouxun Ji at Brunel University London for his unlimited support and guidance from experimental design and microstructure characterisation and scientific understanding of this topic, Professor Zhongyun Fan at Brunel University London for his encouragement during my undergraduate studies, Dr. Mark White at Jaguar Land Rover for giving opportunities to fulfil my goals.

This research is supported by EPSRC under LiME research centre and TSB, UK.

I also thank my colleagues at BCAST, Dr. Hailin Yang, Dr. Wenchao Yang, Dr. Feng Yan, Dr. Yun Wang for helps in the HPDC experiments and materials characterisation, Dr. Feng Gao for help in CALPHAD calculation, Mr. Camello Nunez, Mr. Peter Lloyd and Mr. Stephen Cook for help in running and maintaining the machines, Mr. Matthew Ralph for the help in administration.

Finally, my gratitude to my family for their support and understanding through the period of study.

# Table of Contents

# Chapter 1
# Introduction

## 1.1 Background and Challenges

Aluminium alloys have been seen a dramatic increase in manufacturing in past two decades [1]. This is primarily driven by the achievement of effective weight-savings, increased vehicle fuel efficiency and reduced $CO_2$ emissions in transport [2]. It has been generally believed that weight reduction through the use of lightweight materials remains a very successful and simple means of improving fuel economy and reducing harmful emissions in the manufacture of transport [3]. Increases in aluminium alloys for automotive applications provide significant opportunities for weight reduction and therefore real scope to achieve the environmental goals [4,5]. The automotive industry has used a range of aluminium components in power trains and chassis including transmission housings, cylinder heads, inlet manifolds, engine sumps, wheels, as well as for decorative trim items [6]. An increasing trend in replacing steel parts with lighter aluminium ones has seen aluminium alloys being used extensively in other automotive areas. One of the significant progresses in most recent years has been in the application of aluminium-intensive car body structure [7,8].

In the automotive body structure, both wrought and cast aluminium alloys are essential in frame-space design and monocoque design of aluminium-intensive passenger cars [7,9]. The currently available wrought alloys are listed in Table 1.1 [2, 10]. The mechanical properties of alloys are 124 to 240 MPa of yield strength, 220 to 317 MPa of ultimate tensile strength, and 10 - 30% of elongation. Some alloys that are usually used for external surfacing exhibit excellent paint baking hardenability. The yield strength increases by up to 60% after paint baking. In order to maximize the benefits of aluminium-intensive car body structure, the die castings need to have comparable mechanical properties with the components made with aluminium sheet. However, the mechanical properties of currently available die-cast alloys, as

listed in Table 1.2 [11,12], are not competitive and cannot satisfy the industrial requirement. In particular, the ductility is not sufficient in manufacturing and in application. To increase the strength of castings, the wall thickness needs to be increased for the available alloys. However, several extra manufacturing steps and extra tools have to be added in production to make quality products. These still cannot avoid the insufficiency of ductility and also are not preferred in industry due to the increase of casting weight and processing costs. Therefore, the cast alloy needs to be specially developed for car body structure and similar applications.

Table 1.1 The mechanical properties of aluminium wrought alloys used for automotive body structure [10,11].

| | As-received | | | | After Paint Baking |
|---|---|---|---|---|---|
| Alloy-Temper | Yield Strength (MPa) | Ultimate Strength (MPa) | Total Elongation (%) | Uniform Elongation (%) | Yield Strength (MPa) |
| 5030-T4 | 138 | 276 | 30.0 | - | 172 |
| 5754-H22 | 185 | 245 | 15 | - | - |
| 5754-H26 | 245 | 290 | 10 | - | - |
| 6009-T4 | 124 | 221 | 25.0 | 21.0 | 234 |
| 6010-T4 | 172 | 290 | 24.0 | 21.0 | 255 |
| 6013-T4 | 186 | 317 | 25.0 | 23.3 | 324 |
| 6016-T4 | 139 | 248 | 29.0 | 21.5 | 221 |
| 6063-T6 | 214 | 241 | 18.0 | - | - |
| 6082-T6 | 250 | 290 | 10.0 | - | - |
| 6111-T4 | 159 | 290 | 27.5 | 22.0 | 261 |

On the other hand, compared to other high volume materials, aluminium production has one of the largest energy differences between primary and secondary production: 186 MJ/kg for primary compared to 10-20 MJ/kg for secondary, which means that only 5% of the energy is needed for recycling of aluminium alloys [13 ]. Therefore, recycling is a major sustainable approach to continue the use of aluminium because of the huge benefits in energy resilience manufacturing and the cost saving of products [14,15]. As a result, the application of secondary materials is increasingly attractive for manufacturing such as transport because light-weighting is an important consideration. Currently, more than a third of all the aluminium produced globally originates from traded materials and scraped materials [16]. In addition to the obvious

economic dimension, growing environmental concerns and heightened social responsibility over the last ten years have served to boost recycling activity of aluminium alloys in order to conserve resources and to avoid littering. However, although the recycled aluminium can be utilised for almost all aluminium applications, the accumulation of impurities in the recycled materials provides a significant and long-term compositional barrier to maintain the aluminium alloys within required range [17 ], which result in the down grade of recycled materials. The problematic impurities are different for various aluminium alloys, but it is always associated with iron because of the easy picking up during manufacturing. Therefore, it is necessary to have an assessment for the effect of impurity elements on the microstructure characterization and mechanical properties. This will provide the fundamentals to identify the effective strategies throughout the production process to mitigate the elemental accumulation within contaminated secondary materials.

Table 1.2. Typical mechanical properties of aluminium die-cast alloys commonly available in industry.

| | | Ultimate Tensile Strength (MPa) | | Yield Strength 0.2% offset (MPa) | | Elongation in 50mm (%) | |
|---|---|---|---|---|---|---|---|
| Alloy | Main alloying elements | Ref. [12] | Ref. [13] | Ref. [12] | Ref. [13] | Ref. [12] | Ref. [13] |
| 360 | Al-Si | 300 | 324 | 170 | 172 | 2·5 | 3 |
| A360.0 | Al-Si | 320 | 317 | 170 | 165 | 3.5 | 5 |
| 364 | Al-Si | - | 296 | - | 159 | - | 7.5 |
| 380 | Al-Si-Cu | 320 | 331 | 160 | 165 | 2.5 | 3 |
| A380.0 | Al-Si-Cu | 320 | 324 | 160 | 159 | 3·5 | 4 |
| 383 | Al-Si-Cu | 310 | - | 150 | - | 3.5 | - |
| 384 | Al-Si-Cu | 330 | 324 | 170 | 172 | 2.5 | 1 |
| 390 | Al-Si-Cu-Mg | 280 | 279 | 240 | 241 | <1 | 1 |
| 8390 | Al-Si-Cu-Mg | 320 | - | 250 | - | <1 | - |
| 392 | Al-Si-Mg-Cu | 290 | 290 | 270 | 262 | <1 | <0.5 |
| 413 | Al-Si | 300 | 296 | 140 | 145 | 2.5 | 2.5 |
| A413.0 | Al-Si | 290 | 241 | 130 | 110 | 3.5 | 3.5 |
| 443 | Al-Si-Cu | - | 228 | - | 110 | - | 9 |
| 513 | Al-Mg-Zn | - | 276 | - | 152 | - | 10 |
| 516 | Al-Mg-Si | - | 283 | - | - | - | 10 |
| 518 | Al-Mg | 310 | 310 | 190 | 186 | 5 | 8 |

Furthermore, although high pressure die casting (HPDC) has been widely used to make aluminium castings for automotive body structure and is still attracting in producing thin wall and high dimensional accuracy components, HPDC usually fill the die cavity with turbulence flow [18], which results in the high possibility of forming defects in castings, in which the gas-entrapped porosity and shrinkage porosity are two main categories of defects [19]. Moreover, the defect distribution in HPDC castings is very random and irregular, which exhibits a large uncertainty of mechanical properties in different castings [20]. As a result, the inconsistency of mechanical properties in die castings is a general phenomenon in HPDC process. Generally, in order to compensate the detrimental effect of the internal defects, a relatively large design margin has to be given for the castings. With a great safety coefficient the extra materials are required and the actual distribution of internal defects in the castings is relatively unimportant. However, in the specific structural applications in automobile, the material weight is one of the major concerns, and therefore the reproducibility of castings becomes great important. Consequently, it is also an important matter to assess the consistence and reliability of die castings using statistical approaches, and to understand the variability in the mechanical properties of castings, in particular, for the mechanical properties affected by the various parameters and casting processes.

## 1.2 Research Objectives

The main objectives of the present study are:

- To study the effect of alloying elements on the microstructure and mechanical properties of Al-Mg-Si-Mn alloy.
- To optimise the composition of Al-Mg-Si-Mn alloy that is capable of providing good strength and ductility.
- To understand the relationship between solidification, microstructure and the resultant mechanical properties of aluminium alloys in HPDC process.
- To study the effect of impurity elements, Fe in particular, on the microstructure and mechanical properties.
- To study the effect Ni on the microstructure and mechanical properties.

- To assess the reproductivity via Weibull analysis for different types of tensile samples made directly by high pressure die casting and machined from trials castings with Al-Mg-Si-Mn alloy.

## 1.3 Outline of Thesis

Following the introduction in Chapter 1, the literatures review will be given in Chapter 2, in which an introduction of HPDC process and solidification theories for metal casting are introduced including the classification of HPDC, high integrity HPDC, classical theories of heterogeneous nucleation and constitutional undercooling during nucleation and growth, casting defects in HPDC and the currently available commercial die cast alloys. Also in Chapter 2, the existing studies on aluminium alloys, in particular Al-Mg-Si system and the methods for statistical models are reviewed.

Chapter 3 describes the experimental procedures, the examination equipment and techniques.

Chapter 4 presents the development of a die-cast aluminium alloy that can satisfy the requirement of mechanical properties, in particular ductility for application in automotive body structure. The investigation of the effect of various alloying elements on the mechanical properties will be introduced and the optimised alloy composition will be provided.

Chapter 5 investigates the solidification process and microstructural evolution of the ductile alloy. The solidification behaviour in the shot sleeve and in the die cavity will be examined for the formation of the primary α-Al phase, eutectic Al-$Mg_2Si$ phases in the alloy. The morphology, size and size distribution of the primary α-Al phase will be characterised under different solidification conditions. The phases formed in the different stages of solidification will be identified and quantified. In the discussion, the growth morphology of the primary α-Al phase formed in the shot sleeve and in the die cavity will be analysed using the Mullins-Sekerka instability theory. Jackson-Hunt theory will be used to calculate the growth rate of eutectic Al-$Mg_2Si$ phases during solidification.

Chapter 6 focuses on the effect of Mn and Fe on the morphology, size and distribution of various Fe-rich compounds in the Al-Mg-Si alloy produced by HPDC process. The mechanical properties of yield strength, ultimate tensile strength and elongation will be assessed with

different Fe and Mn contents. The role of alloy chemistry on the effect of Fe and Mn will be investigated by CALPHAD modelling of multi-component Al-Mg-Si-Mn-Fe and Al-Mg-Si-Fe systems. The thermodynamic modelling and the experimental findings of the Fe-rich intermetallic compounds will be studied with respect to the role of Mn on combating the detrimental effect of Fe in the Al-Mg-Si alloy. The discussions are focused on the phase formation of different Fe-rich intermetallic phases and the relationship between Fe-rich compounds and mechanical properties of the die-cast Al-Mg-Si alloys.

Chapter 7 focuses on the effect of nickel on the microstructure and mechanical properties of the die-cast Al-Mg-Si-Mn alloy. The formation of Ni-rich intermetallics during solidification in the die-cast Al-Mg-Si-Mn alloy containing different Ni contents will be investigated. The CALPHAD modelling of multi-component Al-Mg-Si-Mn-Ni will be studied to help the understanding of microstructural formation.

Chapter 8 describes the repeatability of the castings. The tensile properties of standard samples that were obtained directly from high pressure die-castings and made by the machined high pressure die-castings at different locations will be assessed for the reproducibility of casting components made by the Al-Mg-Si-Mn alloy. The distributions of yield strength, ultimate tensile strength and elongation of the samples will be analysed by the average value with standard deviations and by the Weibull statistical model with three parameters. The correlations between the mechanical properties and the microstructural features, porosity levels and fracture morphology will be investigated for the different types of samples.

Chapter 9 presents the main conclusions of this study. The suggestions for the future work of the developed alloy are given in Chapter 10.

# Chapter 2

# Literature Review

## 2.1 High Pressure Die Casting (HPDC)

The HPDC process is characterized by low cost, high efficiency, near-net shape manufacturing, in which the molten metal is injected into a metallic die cavity under high speed and high intensification [21,22]. There are two kinds of HPDC processes used in industry: the hot chamber process and the cold chamber process. The main difference between them is the method of holding and delivering the molten metal into the metallic die cavity [23,24].

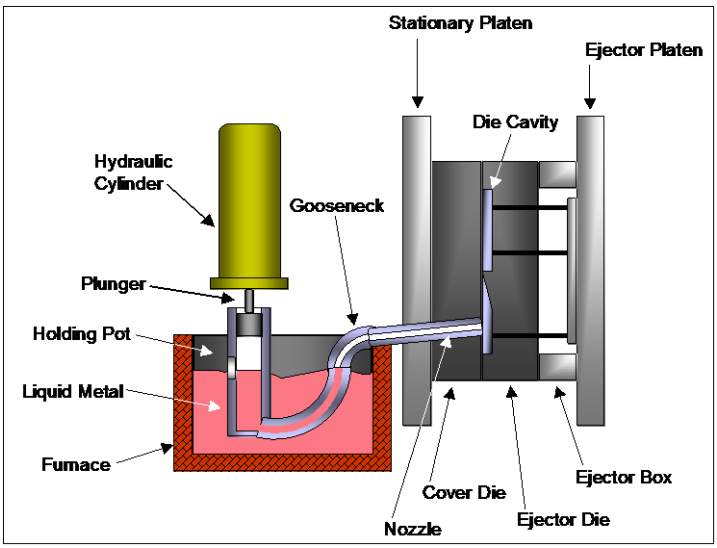


Fig. 2.1 Graphical illustration of hot chamber die casting [26].

In the hot chamber HPDC process [25], molten metal is drawn from the reservoir into the gooseneck and is injected into the die cavity by lowering the plunger position, as shown in Fig. 2.1 [26]. At the beginning of the cycle the piston of the machine is retracted, which allows the molten metal to fill the "gooseneck". The pneumatic or hydraulic powered piston then forces this metal out of the gooseneck into the die [27]. The advantages of this system include fast

cycle times (approximately 15 cycles a minute) and the convenience of melting the metal in the casting machine [21]. The disadvantages of this system are that it is limited to use with low-melting point metals and that aluminium cannot be used because the metal injection system can be rapidly degraded and some of the iron ion are picked up while in the molten pool [26,28]. Therefore, hot-chamber machines are primarily used with zinc, tin, and lead based alloys [26,29].

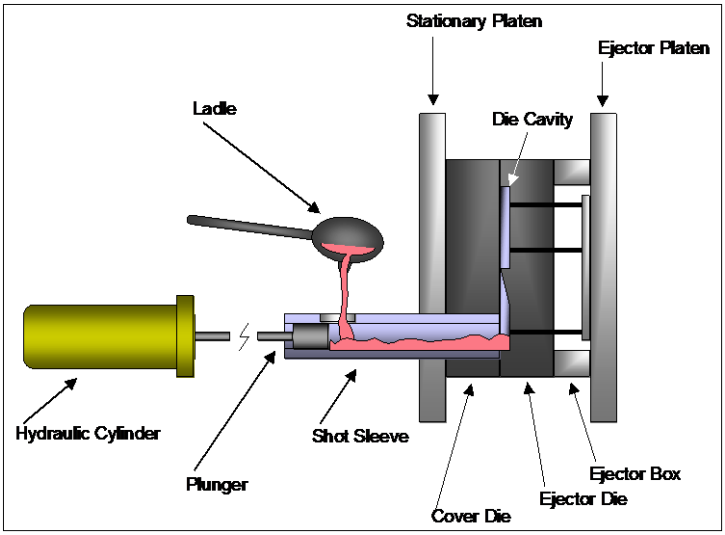


Fig. 2.2 Graphical illustration of cold chamber die casting [32].

In the cold chamber HPDC process, as shown in Fig. 2.2 [32], alloy is melted and held in a separate holding furnace. Then a precise amount of molten metal is transported to the cold-chamber machine where it is fed into an unheated shot chamber (or injection cylinder). This shot is then driven into the die by a hydraulic or mechanical piston. This biggest disadvantage of this system is the slower cycle time due to the need to transfer the molten metal from the furnace to the cold-chamber machine [30]. However, the shot sleeve is the only part in contact with the melt for a short period of time in each casting cycle. It is therefore capable of being used for aluminium, magnesium and copper alloys, which have higher melting temperatures. The cold chamber HPDC has been used to produce a variety of aluminium components to fulfil different requirements. Compared to other casting methods, cold chamber HPDC has a much higher production rate. It is able to cast components with a close dimensional tolerance, which can minimise the cost of further machining. Components with thinner wall thickness and complex shapes can be produced by HPDC, which can reduce the overall casting weight and number of parts in an assembly. Meanwhile, secondary alloys can also be used in the HPDC, which can further reduce the cost [31].

There are four steps in traditional high-pressure die casting: die preparation, filling, ejection, and shakeout. The dies are prepared by spraying the mould cavity with lubricant. The lubricant both helps control the temperature of the die and it also assists in the removal of the casting. The dies are then closed and molten metal is injected into the dies under high pressure; between 10 and 175 MPa. Once the mould cavity is filled, the pressure is maintained until the casting solidifies. The dies are then opened and the shot (shots are different from castings because there can be multiple cavities in a die, yielding multiple castings per shot) is ejected by the ejector pins. Finally, the shakeout involves separating the scrap, which includes the gate, runners, spurs and flash, from the shot. This is often done using a special trim die in a power press or hydraulic press. Other methods of shaking out include sawing and grinding. A less labour-intensive method is to tumble shots if gates are thin and easily broken; separation of gates from finished parts must follow. This scrap can be recycled by remelting it onsite or sending to professional alloy fabricators [32].

The high-pressure injection leads to a quick fill of the die, which is required so the entire cavity fills before any part of the casting solidifies [26,32]. In this way, discontinuities are avoided, even if the shape requires difficult-to-fill thin sections. This creates the problem of air entrapment, because when the mould is filled quickly there is little time for the air to escape [26]. This problem is minimized by including vents along the parting lines, however, even in a highly refined process there will still be some porosity in the centre of the casting.

Advantages of high pressure die casting include [26,32]:

- Excellent dimensional accuracy (dependent on casting material, but typically 0.1 mm for the first 2.5 cm and 0.02 mm for each additional centimetre.
- Smooth cast surfaces (Ra 1–2.5 micrometres).
- Thin walls can be cast as compared to permanent mould casting (about 0.75 mm).
- Inserts can be cast-in (such as threaded inserts, heating elements, and high strength bearing surfaces).
- Reduces or eliminates secondary machining operations.
- Rapid production rates.
- Casting tensile strength as high as 415 MPa.
- Casting of low fluidity metals.

The main disadvantage to die casting is the very high capital cost [26,32]. Both the casting equipment required and the dies and related components are very costly, as compared to most other casting processes [27,32]. Therefore to make die casting an economic process a large production volume is needed. Other disadvantages are that the process is limited to high-fluidity metals, and casting weights must be between 30 grams and 10 kg. In the standard die casting process the final casting will have a small amount of porosity. Therefore, the conventional de castings is not heat treatable or weldable, because the heat causes the gas in the pores to expand, which causes micro-cracks inside the part and exfoliation of the surface.

## 2.2 Improvement in HPDC

Due to the turbulence flow in die filling and the high cooling rate during solidification, the existence of internal defects in the die cast components is a common disadvantage. In order to improve the HPDC process, development has been focused on new techniques to produce high integrity castings, in which entrapped air can be minimised and further heat treatment can be used to enhance the mechanical properties. The main techniques include vacuum assisted HPDC [32,33], semi-solid metal process [33], Acurad and heated-manifold direct-injection die casting.

The vacuum assisted high pressure die-casting uses a vacuum pump to evacuate the air from the shot sleeve and the die cavity to eliminate the entrapped air during casting [34]. The vacuum is maintained until the injection cycle is completed. Almost all of the air is positively evacuated from the mould. The vacuum atmosphere not only can reduce the porosity level in final casting but it can also assist the die filling of melt during the casting. A good vacuum in the mould cavity enables the alloy to flow into blind recesses in complex shapes. It also allows the fronts of the molten metal to merge freely without forming shuts. Whatever vacuum method is employed, if it works well, improved quality and reduced scrap can he guaranteed. Benefits of vacuum assisted die casting [35]:

- Rejections due to porosity are virtually eliminated.
- Rejections after secondary processing are virtually eliminated.
- Excellent surface quality is ensured.
- Product density and strength are increased.

- Larger, thinner, and more complex, castings are made possible.
- Less casting pressure is required.
- Tool life and mould life are extended.
- The die closes better.
- Flash is reduced or eliminated.

Semi-solid metal casting (SSM) is a near net shape variant of high pressure die casting [33]. SSM is working at a temperature that puts the metal between its liquidus and solidus temperature. Ideally, the metal should be 30 to 65% solid, which provides thixotropy and pseudo-plastic property and thus less turbulence flow during the die filling. The temperature range mainly depends on the material, which is 5-10°C and for aluminium alloys [36]. The SSM slurry contain globular primary phase surrounded by the liquid phase before filling die cavity. The process combines the advantages of casting and forging. The potential for this type of process was first recognized in the early 1970s [37]. There are four different processes: thixocasting, rheocasting, thixoforging. Semi-solid casting is typically used for high-end castings. The castings produced by semisolid process contain relatively low porosity levels. Consequently, they can be further heat treated to obtain improved mechanical properties. According to different mechanism, SSM process mainly includes Thixocasting, Rheocasting and Thixoforging. Thixocasting utilizes a pre-cast billet with a non-dendritic microstructure. Induction heating is normally used to re-heat the billets to the semi-solid temperature range, and die casting machines are used to inject the semi-solid material into hardened steels dies. Thixocasting is being performed commercially over the world and has the ability to produce extremely high quality components due to the product consistency. The main disadvantage is that it is expensive due to the special billets that must be used [33,38]. Other disadvantages include a limited number of alloys, and scrap cannot be directly reused. Unlike thixocasting, rheocasting develops the semi-solid slurry from the molten metal produced in a typical die casting furnace/machine [33,38]. This is a big advantage over thixocasting because it results in less expensive feedstock, in the form of typical die casting alloys, and allows for direct recycling. Thixoforging is similar with Thixocasting, which uses a partially solidified billet but use an open die in a forging press to achieve production of sound heat-treatable components that are free of entrapped oxides and which have excellent static and dynamic properties. Thixoforging is mainly for wrought alloys [33,38].

Acurad was a die casting process developed by General Motors in the late 1950s and 1960s [38,39]. The name is an acronym for accurate, reliable, and dense. It was developed to combine a stable fill and directional solidification with the fast cycle times of the traditional die casting process. The process pioneered four breakthrough technologies for die casting: thermal analysis, flow and fill modelling, heat treatable and high integrity die castings, and indirect squeeze casting [40]. The Acurad system employs a bottom fill system that requires a stable flow-front. The Acurad system was the first die casting process that could successfully cast low-iron aluminium alloys, such as A356 and A357. In a traditional die casting process these alloys would solder to the die. Similarly, Acurad castings could be heat treated and meet the U.S. military specification MIL-A-21180. Acurad system employs patented double shot piston design. The idea is to use a second piston (located within the primary piston) to apply pressure after the shot have partially solidified around the perimeter of the casting cavity and shot sleeve. While the system is not very effective, it leads the manufacturer of the Acurad machines to discover that it is just as effective to apply sufficient pressure at the right time later in the cycle with the primary piston; this is indirect squeeze casting [41].

Another development is the Oxygen-rich die casting [42]. It is identical to the standard process except oxygen is injected into the die before each shot to purge any air from the mould cavity. This causes small dispersed oxides to form when the molten metal fills the die, which virtually eliminates gas porosity. An added advantage to this is greater strength. Unlike standard die castings, these castings can be heat treated and welded. This process can be performed on aluminium, zinc, and lead alloys.

Heated-manifold direct-injection die casting, also known as direct-injection die casting or runner-less die casting, is a zinc die casting process where molten zinc is forced through a heated manifold and then through heated mini-nozzles, which lead into the moulding cavity. This process has the advantages of lower cost per part, through the reduction of scrap (by the elimination of spurs, gates and runners) and energy conservation, and better surface quality through slower cooling cycles [43, 44].

These developments can be basically described as the control of the solidification process and to reduce the defects in the castings. These are the two aspects in the HPDC process. Therefore the following parts review the solidification and defects formation in HPDC castings.

## 2.3 Solidification in Cold Chamber HPDC

In casting of metals, the nucleation events occur by heterogeneous nucleation on substrates that provide an appropriate interface. The classical theory on heterogeneous nucleation is given in textbooks on solidification [45, 46], and is commonly assessed in grain refinement theory [47]. In the forthcoming section, the physical fundamentals for nucleation are outlined.

At a specific temperature, the thermodynamically stable state has the lowest free energy ($G$). For a given undercooling, $\Delta T$, there is a driving force for solidification $\Delta G = G_s - G_l$. The undercooling has to be sufficiently large to provide the energy required for forming new interfaces. For a sphere with radius $r$, $\Delta G$ consists of two competing terms; the interfacial energy, (proportional to $r^2$), and the free energy per volume, (proportional to $r^3$):

$$\Delta G = \left( 4\pi \cdot r^2 \gamma_{sl} + \frac{4}{3}\pi \cdot r^3 \Delta G_v \right)\left( \frac{2 - 3\cos\theta + \cos^3\theta}{4} \right) \tag{2.1}$$

The last term in equation 2.1 is the shape factor function, $f(\theta)$, where $\theta$ is the wetting angle between the nucleus and the substrate. Good wetting occurs when $\theta$ is small, and $f(\theta)$ becomes 0 when $\theta = 0$. Thus, when the wetting between the crystal and substrate improves, the nucleation barrier decreases. This is taken advantage of in the casting process, where inoculants are added to the melt. It is required that they are thermodynamically stable over a sufficient time period, possess low lattice disregistry, good wetting, are sufficiently large to overcome the surface energy barrier, possess suitable density, are adequately small and evenly distributed to be accepted in the casting [48].

Solidification in the HPDC process is essentially the same as that in a conventional casting process, which can be described in two stages, i.e. nucleation and growth. The solidification of alloys begins when crystals are nucleated on suitable substrates at a sufficient undercooling of the melt. In the dynamic nature of the casting process, the nucleation events can occur by several mechanisms in the absence of chemical additions of inoculants. Filling the shot sleeve in HPDC is similar to pouring of melt into a permanent mould. The liquid in contact with the cold mould wall is rapidly cooled below the liquidus temperature, $T_{liq}$. The classical theories then predict three different scenarios [21,22]:

(1) The melt becomes thermally undercooled adjacent to the mould wall. The thermal undercooling can be sufficient to overcome the required nucleation undercooling, which depends on the substrates that are present. Furthermore, the thermal gradient, which depends on the melt superheat and the mould wall temperature, can alter the amount of thermal undercooling. The heat loss by means of radiation at the melt surface generates a thermal undercooling which is sufficiently large for nucleation of crystals.

(2) During growth, the solubility variations result in solute rejections at the growing interface creating a solute enriched zone in the liquid. This is shown in Figure 2.3 for a planar growth front. From the interface, the solute concentration $C_L$ decreases with distance to diffuse extra solutes into liquid, while the local temperature ahead the growth interface varies by the curve $T_{liq}$. The actual temperature in the liquid, imposed by the simultaneous solute diffusion and extraction of latent heat of fusion, is $T_m$. A constitutionally undercooled zone is therefore present, in which suitable substrates can become more crystals. Meanwhile, during growth, the latent heat is conducted into the surrounding melt which generates the thermal gradient required for constitutional undercooling. For an equiaxed dendrite the principal difference between alloy systems is the growth restriction factor (*GRF*): $GRF=mLC_o(k-1)$ [49 ]. Furthermore, the solute undercooling is typically larger than the thermal undercooling by a factor of 100-1000 [50,51].

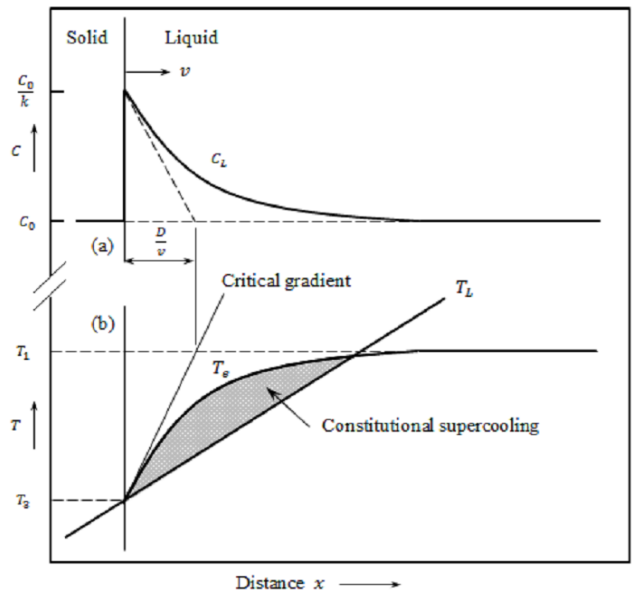


Fig. 2.3 Illustration of principles for constitutional undercooling in constrained grown[50]. Solute rejection at the crystal interface and simultaneous release of latent heat of fusion generates a constitutionally zone.

(3) Furthermore, dendrite fragmentation processes involves the complexity of: micro-segregation, thermal and solutal convection, solid/liquid diffusion and ripening. Nevertheless, it is important to be aware that the fragmentation of dendrites in general represents a significant source of equiaxed dendrites in the casting process.

When the melt cools, crystals survive and solidification eventually proceeds. Further growth involves solute segregation which can generally be described by the Gulliver-Scheil equation. In the case of no solid diffusion and complete mixing in the liquid, the expression takes the form [ref. porter]

$$c_l = c_0\left(1 - f_s\right)^{(k-1)} \qquad (2.2)$$

This equation overestimates the amount of eutectic but is relatively representative at low solid fractions, and has been suitable in most applications in the doctorate work. Crystals that grow evolve into dendrites and develop different order branches which depend on the dendrite tip radius ($r$), the local thermal gradient ($G$), solute diffusion ($D$) and the constitutional conditions that are present. When the diffusion fields encapsulating the crystals impinge on each other, peripheral growth is substituted by coarsening [46]. Eventually, the crystals are no longer free to move. The consequence of this on the solidifying structure is explained dendrite coherency.

During the casting of alloys, a common mode of solidification is the nucleation and growth of numerous equiaxed crystals. If no other phases form first, free crystals impinge on one another during growth, creating a crystal network. This point during solidification is commonly termed “dendrite coherency” [51] and [52], although the term “coherency” is also used to describe other transitions in the mushy zone. Dendrite coherency is often thought of as the transition from mass to interdendritic feeding and to be the solid fraction at which difficulties in feeding solidification shrinkage begin. Beyond coherency, the restrictions imposed on the liquid flow, and the development of contraction stresses in the continuous solid network, can result in common casting defects such as macrosegregation, hot tearing, shrinkage and gas porosity. The rigidity of the developing dendritic network may also have a significant impact on the formation of defects.

## 2.4 Defects Formed in HPDC

In HPDC process, there are basically two types of casting defects. One is related with process operation and the other is related with metallurgy. Therefore, the review will be summarised in process-related defects and metallurgical-related defects, although there is often an interrelationship between the process parameter and metal defects [21, 23].

The defects related to process include cold laps, cold shuts, laminations, flow marks, knit lines, scratches, sinks, die soldering, hot tearing, shrinkage porosity, misruns and lubricant stain. Cold laps, cold shuts, laminations and flow mark defects are all surface defects. They are seen visually on the casting or with the aid of a low power magnification and/or zyglo penetrant techniques. Such defects relate to problems with metal temperature being too low, inadequate gating, incorrect die injection parameters, or combinations of all these factors. Divergent metal streams converge, do not mix properly, and solidify prematurely, which results in such surface discontinuities. The severity of such defects and their effect on casting properties and performance can vary. Because of these defects, there is cause for a careful review of the operating parameters [24,26].

Sinks on the casting surface general shrinkage due to inadequate feeding and/or excessive metal temperature. Shrinkage porosity occurs due to inadequate gating, feeding or excessive temperature. Misruns occur when there is inadequate feed metal or lack of venting. This results in the casting detail not filling out, and not completing the desired design features.

Die soldering is an obvious visual surface defect, which is also related to metal composition (iron content), die and die coating condition [53,54]. Aluminium has a low solubility for iron, but normally 0.80% or more is required to mitigate die soldering tendencies [55]. Heat checking of the die metal and stickers exacerbate die soldering. Too much or too little die spray and die temperature variation also increase the tendency for die soldering [56,57].

Lubricant stains on the surface often relate to the excessive use of lubricant or breakdown in lubricant delivery systems. Poor die surface can also result in casting surface defects. Hot cracking or hot tearing can result from constraints in the casting design during solidification; mishandling during ejection or trimming operations; or alloy inhomogeneity, resulting in weak sections [58].

Metallurgical related defects include gas porosity (also includes air entrapment which is process-related), inclusions, (oxides, corundum refractory, flux), blisters, leakers. Metallurgically related defects often arise from failure to adequately address the natural phenomena, which occurs in aluminium alloy melting process—control of hydrogen and oxidation products (i.e. inclusions). The latter originate with refractory erosion; inherent oxides retained from the melt stock and returns; and inability to completely separate oxide skim and dross from the melt prior to transfer to the casting furnace, which directly feeds the die casting press. Corundum is an extremely hard form of aluminium oxide, which can form at high temperatures over a long time in the melting furnace. Furnace cleaning often loosens corundum, which can become entrained in the melt during transfers; eventually ending up in the die casting holding furnace; and subsequently into the die-casting itself as the ladle delivers.

Porosity is one of the most common forms of defect in die castings. It limits the use of die castings if heat treatment is required because of blistering [23-26]. In structural applications, porosity can act as a stress concentrator creating initiation sites for cracks. Therefore, the existence of porosity is detrimental for the mechanical properties such as tensile strength, elongation, and fatigue strength and fracture toughness [59]. In the HPDC process, the porosity can be divided into two types, according to the mechanisms of formation: shrinkage related pores and gas related pores.

Shrinkage porosity is mainly caused by the solidification behaviour of specific alloy compositions preventing melt feeding [21-26]. During solidification, the chemical composition changes in the remaining melt over temperature for aluminium alloys. This is the main reason to form constitutional undercooling and the formation of dendritic morphology of the primary phase. With the increase of the volume fraction of dendrites, a skeleton can be formed and the liquid is unable to fulfil the skeleton due to the blockage of the pass way [60]. The shrinkage porosity is thus formed. The shrinkage porosity is mainly due to a poor casting structure design, inadequate temperature control of the die block, inadequate inject pressure, and low melt temperature. For the aluminium alloys with high iron content, the Fe-rich phases formed at the early stage of the solidification prevent the melt flow through the feeding channels and therefore promote the formation of shrinkage porosity [24].

Gas porosity is predominately caused by hydrogen in the melt, trapped air, steam and by-products from organic lubricants used in the HPDC process. Hydrogen is the only gas soluble in aluminium [21-25]. It is over 10 times more soluble in liquid Al than in solid Al, and hence

is rejected from the solid phase into the inter-dendrite/granular liquid during solidification. Gas pores form when sufficient super saturation of hydrogen in the liquid occurs. The percentage and size of porosity increases by increasing the initial hydrogen content [61]. The alloy composition can alter the initial hydrogen level in the melt [62]. In liquid aluminium, silicon, copper, zinc and iron decrease hydrogen solubility, whereas lithium, magnesium and titanium increase this. On top of the alloy composition, the hydrogen solubility increases when the melt temperature is increased.

Hot cracking/ hot tearing normally occurs during the last part of solidification in the casting where there is a big change with the configurations and re-entrant angles in the die [63]. Since those parts are thicker than other sections, it takes longer for the melt to solidify due to the heat being difficult to release. Besides the die shape, the alloy composition could also have an effect on the hot cracking formation [64]. The freezing range and fraction of eutectic Al-$Mg_2Si$ phase, which are governed by the alloy composition, can strongly affect the hot cracking formation. A longer freezing range can result in the pre-solidified dendrites interlocking the melt flow path, which in turn leads to the last part of solidifying without melt filling and thus forming cracks [65]. Elements like Zn, which have a low melting temperature, can lead to a larger solidification range and increase the risk of hot tearing. For alloys close to eutectic composition, the majority of the liquid solidifies isothermally at a small temperature range. If the contraction of stresses occurs, the developed cracks can be healed by backfilling the remaining melt [64].

## 2.5 Aluminium Alloys Available in HPDC Process

The HPDC process requires alloys with superior castability, die soldering resistance and good resistance to cracking during solidification. A number of cast aluminium alloys can be used for the HPDC process, which includes aluminium-silicon alloys, aluminium-silicon-copper alloys, aluminium-silicon-magnesium alloys, aluminium-magnesium alloys. The registered composition are summarised in Table 2.1. The detail physical properties are summarised in Table 2.2 to 2.4 for Al-Si alloys, Al-Si-Mg/Cu alloys and Al-Mg alloys. In this section, the review will focus on the die cast alloys.

Table 2.2 Aluminium silicon alloys [66]

| Alloy | Casting temperature (°C)[67] | Solidification range (°C) | Density at 20°C (g/cm$^3$) | Coefficient of linear thermal expansion 20-100°C (µm/mK) | Coefficient of linear thermal expansion 20-200°C (µm/mK) | Coefficient of linear thermal expansion 20-300°C (µm/mK |
|---|---|---|---|---|---|---|
| AlSi12(Fe) | 635-705 | 577-590 | | 20 | | |
| AlSi9 | 635-705 | 577-605 | | 21 | | |
| 413.0 | 635-705 | 577-585 | 2.657 | 20.4 | 21.4 | 22.4 |
| A413.0 | 635-705 | 577-585 | 2.657 | 20.4 | 21.4 | 22.4 |
| C443.0 | 635-705 | 577-630 | 2.69 | 20.4 | 23 | 24 |

Table 2.3 Aluminium silicon alloys [68]

| Alloy | Casting temperature (°C) | Solidus (°C) | Liquidus (°C) | Density at 20°C (g/cm$^3$) | Coefficient of linear thermal expansion 20-100°C (µm/m.K) | Coefficient of linear thermal expansion 20-300°C (µm/m.K |
|---|---|---|---|---|---|---|
| AlSi10Mg(Fe) | | | 580-600 | | 21 | |
| AlSi11Cu2(Fe) | | | 560-590 | | 20 | |
| AlSi12Cu1(Fe) | | | 575-590 | | 20 | |
| AlSi8Cu3 | | | 580-605 | | 21 | |
| AlSi9Cu3(Fe) | | | 565-600 | | 21 | |
| AlSi9Cu3(Fe)Zn | | | 565-600 | | 21 | |
| 360.0 | 635-705 | 555 | 580-600 | 2.63 | 21 | 23 |
| 380.0 | 635-705 | 540 | 570-605 | 2.71 | 22 | |
| 383.0 | 615-700 | 515 | 565-590 | 2.74 | 21.1 | |
| 384.0 | 615-700 | 515 | 555-585 | 2.823 | 20.8 | |
| 390.0 | | 505 | 650 | 2.73 | 18 | |
| 392.0 | | | | | | |
| A360.0 | 635-705 | 555 | 580-600 | 2.63 | 21 | 23 |
| A380.0 | 635-705 | 540 | 570-605 | 2.71 | 21.8 | |
| B390.0 | | 505 | 650 | 2.73 | 18 | |

Table 2.1 Compositions of registered aluminium alloys for the HPDC process [30,69].

| Alloy | Si | Fe | Cu | Mn | Mg | Cr | Ni | Zn | Sn | Ti | other Each | Total | Al |
|---|---|---|---|---|---|---|---|---|---|---|---|---|---|
| 343 | 6.7-7.7 | 1.2 | 0.5-0.9 | 0.5 | 0.1 | 0.1 | | 1.2-2.0 | 0.5 | | 0.1 | 0.35 | Bal. |
| 360 | 9.0-10.0 | 2 | 0.6 | 0.35 | 0.4-0.6 | | 0.5 | 0.5 | 0.15 | | | 0.25 | Bal. |
| A360.0 | 9.0-10.0 | 1.3 | 0.6 | 0.35 | 0.4-0.6 | | 0.5 | 0.5 | 0.15 | | | 0.25 | Bal. |
| 361 | 9.5-10.5 | 1.1 | 0.5 | 0.25 | 0.4-0.6 | 0.2-0.3 | 0.2-0.3 | 0.5 | 0.1 | 0.2 | 0.05 | 0.15 | Bal. |
| 364 | 7.5-9.5 | 1.5 | 0.2 | 0.1 | 0.2-0.4 | 0.25-0.5 | 0.15 | 0.15 | 0.15 | | 0.05 | 0.15 | Bal. |
| 369 | 11.0-12.0 | 1.3 | 0.5 | 0.35 | 0.25-0.45 | 0.3-0.4 | 0.05 | 1 | 0.1 | | 0.05 | 0.15 | Bal. |
| 380 | 7.5-9.5 | 2 | 3.0-4.0 | 0.5 | 0.1 | | 0.5 | 3 | 0.35 | | | 0.5 | Bal. |
| A380.0 | 7.5-9.5 | 1.3 | 3.0-4.0 | 0.5 | 0.1 | | 0.5 | 3 | 0.35 | | | 0.5 | Bal. |
| B380 | 7.5-9.5 | 1.3 | 3.0-4.0 | 0.5 | 0.1 | | 0.5 | 1 | 0.35 | | | 0.5 | Bal. |
| 383 | 9.5-11.5 | 1.3 | 2.0-3.0 | 0.5 | 0.1 | | 0.3 | 3 | 0.15 | | | 0.5 | Bal. |
| 384 | 10.5-12.0 | 1.3 | 3.0-4.5 | 0.5 | 0.1 | | 0.5 | 3 | 0.35 | | | 0.5 | Bal. |
| A384.0 | 10.5-12.0 | 1.3 | 3.0-4.5 | 0.5 | 0.1 | | 0.5 | 1 | 0.35 | | | 0.5 | Bal. |
| 385 | 11.0-13.0 | 2 | 2.0-4.0 | 0.5 | 0.3 | | 0.5 | 3 | 0.3 | | | 0.5 | Bal. |
| 390 | 16.0-18.0 | 1.3 | 4.0-5.0 | 0.1 | 0.45-0.65 | | | 0.1 | | 0.2 | 0.1 | 0.2 | Bal. |
| B390 | 16.0-18.0 | 1.3 | 4.0-5.0 | 0.5 | 0.45-0.65 | | 0.1 | 1.5 | | 0.2 | 0.1 | 0.2 | Bal. |
| 392 | 18.0-20.0 | 1.5 | 0.4-0.8 | 0.2-0.6 | 0.8-1.2 | | 0.5 | 0.5 | 0.3 | 0.2 | 0.15 | 0.5 | Bal. |
| 393 | 21.0-23.0 | 1.3 | 0.7-1.1 | 0.1 | 0.7-1.3 | | 2.0-2.5 | 0.1 | | 0.1-0.2 | 0.05 | 0.15 | Bal. |
| 413 | 11.0-13.0 | 2 | 1 | 0.35 | 0.1 | | 0.5 | 0.5 | 0.15 | | | 0.25 | Bal. |
| A413.0 | 11.0-13.0 | 1.3 | 1 | 0.35 | 0.1 | | 0.5 | 0.5 | 0.15 | | | 0.25 | Bal. |
| C443.0 | 4.5-6.0 | 2 | 0.6 | 0.35 | 0.1 | | 0.5 | 0.5 | 0.15 | | | 0.25 | Bal. |
| 515 | 0.5-1.0 | 1.3 | 0.2 | 0.4-0.6 | 2.5-4.0 | | | 0.1 | | | 0.05 | 0.15 | Bal. |
| 516 | 0.3-1.5 | 0.35-1.0 | 0.3 | 0.15-0.4 | 2.5-4.5 | | 0.25-0.4 | 0.2 | 0.1 | 0.1-0.2 | 0.05 | | Bal. |
| 518 | 0.35 | 1.8 | 0.25 | 0.35 | 7.5-8.5 | | 0.15 | 0.15 | 0.15 | | | 0.25 | Bal. |

Table 2.4 Aluminium magnesium alloys [70]

| Alloy | Casting temperature (°C) | Solidus (°C) | Liquidus (°C) | Density at 20°C ($g/cm^3$) | Coefficient of linear thermal expansion 20-100°C (μm/m.K) |
|---|---|---|---|---|---|
| AlMg9 | | | | | 24 |
| 518.0 | | 535 | 620 | 2.57 | 24.1 |

## 2.6 Al-Si Alloys

Si is very cheap as a raw material and the most popular element used in cast aluminium alloys. Silicon has a high latent heat, which is 4.5 times higher than aluminium [71], which result in good castability and weldability. Silicon also has a low density (2.34 $g/cm^3$), which is an advantage in reducing the overall weight of the cast component. Silicon has a very low solubility in aluminium; it therefore precipitates as virtually pure silicon, which is hard and hence improves the abrasion resistance. The copper-free alloys are used for low- to medium-strength castings with good corrosion resistance; the copper-bearing for medium- to high-strength castings, where corrosion resistance is not critical. Because of their excellent castability, it is possible to produce reliable castings, even in complex shapes, in which the minimum mechanical properties obtained in poorly fed sections are higher than in castings made from higher-strength but lower-castability alloys.

The addition of Si to aluminium forms a binary eutectic alloy with a eutectic point at 12.6wt.%Si and the eutectic temperature being 577°C. Generally Al-Si alloys with 7-18wt.% Si have excellent fluidity due to the narrow freezing range and low viscosity. Unlike aluminium that shrinks, Si expands during solidification. This contributes to a lower shrinkage rate of the Al-Si alloys and a linear decrease of shrinkage with the increase of Si. The total shrinkage reaches zero when Si addition is at 25wt.%. Even though Si has a lower electrolytic potential than aluminium, Al-Si alloys still have a good corrosion resistance like pure aluminium because Si is inert to most of the corrosive environments [72]. Therefore, the low thermal expansion coefficient, high hardness and wear resistance can be achieved by increasing silicon content in aluminium alloys.

The mechanical properties of Al-Si alloys mainly depend on the morphology and distribution of the primary and eutectic Al-Si phases. Al-Si alloys can provide better performance when mixed with fine and well distributed primary phases [73]. The faceted and acicular shaped Si phase contributes to a higher hardness and strength but lower elongation. Fig. 2.6 shows the properties of Al-Si alloys as a function of Si concentration. The Si contributes to significant enhancement on the yield strength but with a dramatic decrease of the ductility. The popular Al-Si based alloys are 413.0, C443.0 alloys. The 413.0 alloy is a eutectic Al-Si alloy and has the best fluidity amongst cast alloys. Therefore it can be used to cast large and complex shape castings with thin wall thickness. The hypo-eutectic C443 alloy has 4.5-6 wt.% Si content, with a fair good castability. Therefore, it can only be used to make components requiring higher ductility and better corrosion resistance.

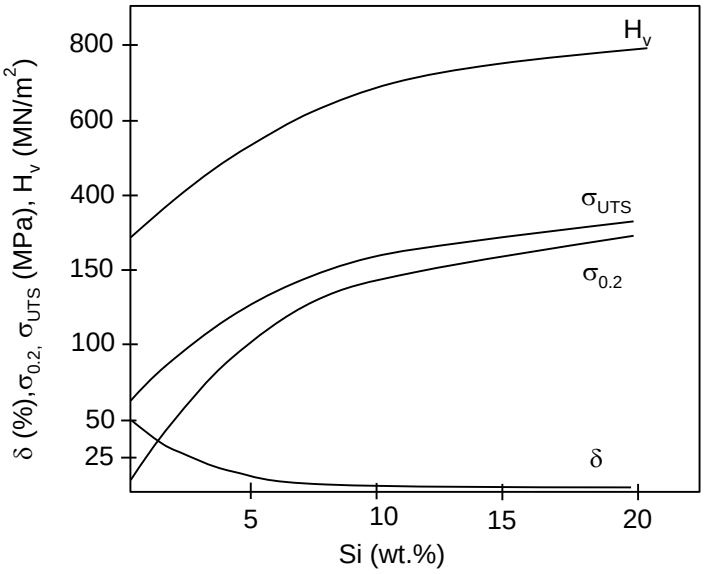


Fig. 2.6 Mechanical properties of Al-Si alloy as a function of Si content in the alloy [75].

## 2.7 Al-Si-Cu Alloys

In order to increase the strength of Al-Si based die cast alloys, 3- 5 wt.% copper is introduced to the Al-Si alloys. Copper forms an intermetallic phase with Al that precipitates during solidification either as blocky $CuAl_2$ or as alternating lamellae of α-Al + $CuAl_2$ [71]. During solidification, in the presence of iron, other copper containing phases form, such as $Cu_2FeAl_7$ or Q-$Al_5Cu_2Mg_8Si_6$ [71]. The $CuAl_2$ phase can be blocky shape or finely dispersed α-Al and $CuAl_2$ particles within the interdendritic regions, as shown in Figure 2.7. The presence of

nucleation sites, such as $FeSiAl_5$ platelets or high cooling rates during solidification can result in fine $CuAl_2$ particles [71]. The blocky $CuAl_2$ phase particles are difficult to dissolve during solid solution heat treatment, unlike the fine $CuAl_2$ phase particles that can dissolve within 2 hrs solid solution heat treatment [74]. Magnesium is present as $Mg_2Si$ in Al-Si-Mg alloys if Mg is not in solution. Mg can also form a true quaternary compound $Cu_2Mg_8Si_6Al_5$ with other alloy elements in Al-319 alloy. In the absence of Cu, high Fe and Mg result in the appearance of π-$FeMg_3Si_6Al_8$. The π phase is difficult to dissolve during solid solution heat treatment [75].

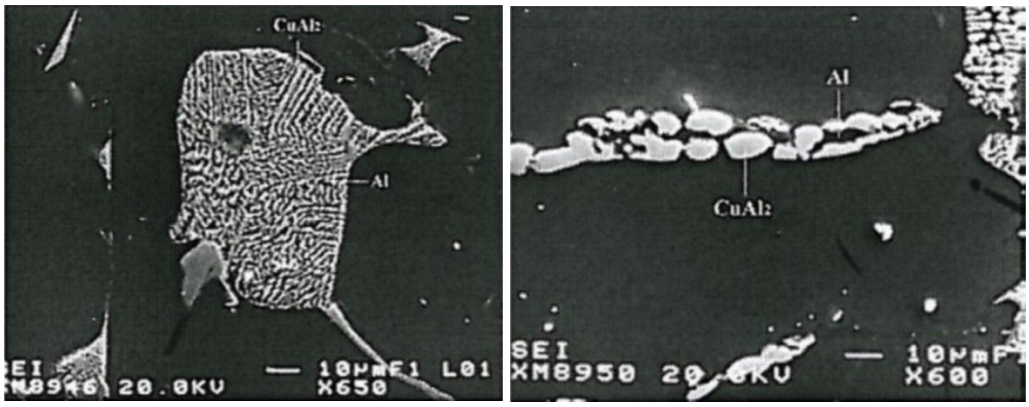


Figure 2.7. Cu-rich phases in as-cast 319 alloy: (a) Eutectic $Al_2Cu$ and (b) blocky $Al_2Cu$ [76].

With the increase of the Cu content, hardness increases, but the strength and ductility exhibit different behaviours [71]. When Cu is present in solid solutions as evenly distributed spheroidal particles, maximal strengthening can be achieved. Whilst the Cu phase is present as a continuous network at grain boundaries, it has little enhancement on strength but a significant decrease on ductility. As the solidus temperature of the alloy is significantly decreased by the Cu addition, the solidification range of the alloy is increased. This increases the risk of forming hot tearing. The Cu-containing aluminium alloys normally have a low corrosion resistance because Cu can disperse in the aluminium oxide film and prevent complete passivation [24-31]. 380.0 alloys is a typical Al-Si-Cu based alloy for HPDC, which shows good castability, high mechanical properties (yield strength 160MPa, UTS 315MPa and elongation 3%) and large tolerance of impurities.

With a desired high strength, zinc can be added into Al-Si-Cu. Zinc has high solubility in aluminium in a solid state, but no visible and detectable second phase can be formed up to 1wt.% Zn [30]. When Zn combines with Mg it forms $MgZn_2$, which can significantly increase the strength of aluminium alloys. B390 alloy is an Al-Si-Cu based alloy with a 1.5 wt.% Zn, and

0.45-0.65 wt.% Mg. It shows a relatively high yield strength of 250 MPa and low ductility of <1%. Due to the high content of Cu and Zn in the alloy, more attention is required to prevent the formation of hot tearing in castings.

## 2.8 Al-Si-Mg Alloys

Magnesium is the basis for strength and hardness development in heat treated aluminium-silicon alloys [30]. With a small amount of Mg addition into Al-Si alloys, Mg combines with Si and forms $Mg_2Si$ phase, to strengthen the alloy. With a T6 heat treatment, $Mg_2Si$ precipitates from the matrix and contributes to a superior strengthening effect. As there is limited solubility of $Mg_2Si$ in α-Al, the useful solubility of $Mg_2Si$ limit corresponds to approximately 0.70% Mg, beyond which either no further strengthening occurs or matrix softening takes place. The Al-Si-Mg series alloys (i.e. 360.0) are also considered as a general purpose alloy with good castability and good strength (yield strength 170 MPa, UTS 305MPa and elongation 3%). When the Mg addition ranges from 0.4 wt.% -0.6 wt.%, the $Mg_2Si$ phase increases the strength and hardness at the expense of ductility and impact strength. Since the lower electrolytic potential of magnesium, the Al-Si-Mg alloys have a higher corrosion resistance.

Hekmat-Ardakan and Ajersch [77] reported that various amounts of additional Mg in an A390 (Al-17 %Si-4.5%Cu-0.5Mg) results in the formation of the $Mg_2Si$ phase in the microstructure. There are three Mg addition levels at which $Mg_2Si$ intermetallics form at different reactions, as shown in Fig. 2.8. When the Mg content is below 4.2 wt.%, the $Mg_2Si$ intermetallic phase only appears in the ternary eutecitc zone. When the Mg content is between 4.2 wt.% and 7.2 wt.%, $Mg_2Si$ phase can be formed in both ternary eutectic zone and ternary eutectic reaction. Primary $Mg_2Si$ phase forms when the Mg content is above 7.2 wt.%. Lin et al. [78] also found that 4 wt.% Mg in Al-19Si alloy results in the formation of the primary $Mg_2Si$ phase. The yield strength can be slightly increased and the ductility further decreases by the addition of Mg in the hyper-eutectic Al-Si alloys.

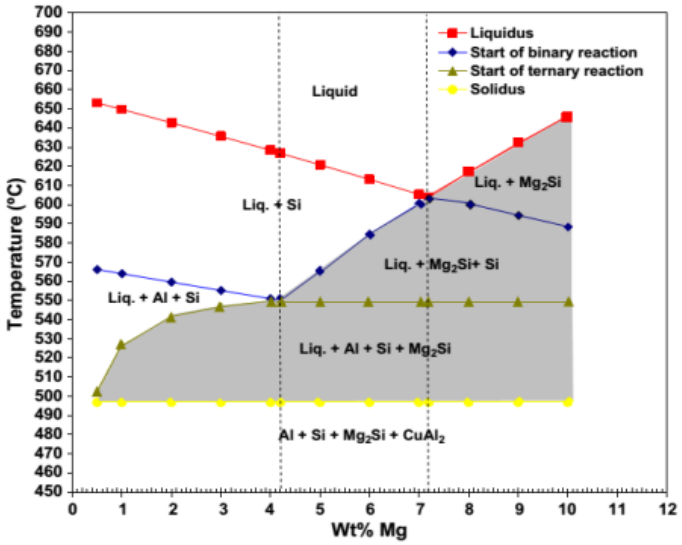


Fig. 2.8 The effect of Mg on the transition reactions and corresponding temperatures of A390 alloys [77]. Critical points are at 4.2% and 7.2% Mg. The shaded zone shows the solidification interval of $Mg_2Si$ intermetallic phase for different Mg.

## 2.9 Al-Mg Alloys

In comparison with Al-Si based die cast alloys, the Al-Mg based die cast alloys require more care in gating, with the position and size being of increased importance. There needs also a better control of the temperature gradients due to the greater risk of hot tearing and oxidising tendencies [45-47] .Thus, a limited number of Al-Mg alloys are currently used in the HPDC process. Al-Mg alloys have high strength and good ductility, good machinability, weldability and an attractive appearance whether as-cast, machined, polished or anodised [45-47]. With the increase of the Mg content in Al-Mg alloys, both yield strength and UTS can significantly increase but with a reduction of ductility. The Al-Mg alloys (i.e. 518) have a high corrosion resistance, high strength (yield strength 193MPa, UTS 310MPa) and high ductility (elongation 5%), thus can be used for simple shaped components where good corrosion resistance is needed due to its poor castability.

## 2.10 Fe in Aluminium Alloys

A variety of Fe-rich intermetallic phases have been observed in aluminium alloys. In Al-Si-Fe system there are five main Fe-rich phases: $Al_3Fe$ (or $Al_{13}Fe_4$), α-$Al_8Fe_2Si$ (possibly α-$Al_{12}Fe_3Si_2$), β-$Al_5FeSi$, δ-$Al_4FeSi_2$ and γ-$Al_3FeSi$ [73]. Among them, β-$Al_5FeSi$ usually appears as highly faceted platelets up to several millimetres and it therefore causes the most serious loss of strength and ductility in the castings [79, 80]. However, the α-$Al_8Fe_2Si$ phase has been reported as the compounds with many different types of morphology [ 81 , 82 ]. The morphological changes from plate to Chinese script or compact shapes were reported to enhance mechanical properties [83, 84]. On the other hand, manganese has been widely used to suppress the development of long needle-shaped Fe-rich phases and to promote the formation of compact Fe-rich phases in aluminium alloys [85]. In hypoeutectic Al-Si alloys containing Fe, Mn and Mg, three Fe-rich phases of α-$Al_{15}(FeMn)_3Si_2$, β-$Al_5FeSi$ and π-$Al_8FeMg_3Si_6$ compounds have been identified[8,86]. In the commonly used Al-Si-Mg cast alloys, with a Mn/Fe ratio of 0.5, the structure of Fe-rich intermetallics is body centred cubic α-$Al_{15}(FeMn)_3Si_2$ [87,88], which may appear as hexagonal, star-like, or dendritic crystals at different Mn/Fe ratios [89]. However, in the various results from previous studies, the effect of Fe on the microstructure is in good agreement in the most popular Al-Si cast alloys, but it is inconsistencies for the influence of Fe on the mechanical properties of castings. Meanwhile, the amount of Mn needed to neutralize Fe has not been well established [90,91]. Although Mn/Fe ratio of 0.5 is desirable for the transformation of β-$Al_5FeSi$ to α-$Al_{15}(FeMn)_3Si_2$ [29,30].

The formation of Fe-rich intermetallics is greatly affected by solidification conditions during casting [92,93]. The superheat and cooling rate have been reported to affect the nucleation and growth of the Fe-rich phases and thus to be able to modify the morphology and size of the intermetallics in aluminium alloys [94,95]. At high cooling rates as in the case of HPDC, the occurrence of primary β-AlFeSi needles is shifted towards higher iron levels at Fe>1% [96,96]. These observations are important in understanding the microstructure features of Al-Si and Al-Si-Cu cast alloys. However, insight in solidification of other alloys is still limited in terms of the Fe-rich intermetallic phases at different contents of Fe and Mn, especially under high cooling rate with HPDC process. Meanwhile, the thermodynamic modelling by CALPHAD is becoming an important tool in alloy development, which can determine the phase formation under the equilibrium condition. The thermodynamic modelling of Al-Fe-Mn-Si system has

been carried out by Balitchev et al. [97]. They achieved reasonably good results by treating the α-AlFeMnSi phase as a stoichiometric compound. The similar approaches were also used by Fang et al. [98] for the formation of Fe-rich intermetallics in semisolid processed A380 and A356 alloys. These results provided a guideline for understanding the solidification and phase formation process.

## 2.11 Ni in Aluminium Alloys

Nickel is defined as impurity in many commercial aluminium alloys with a limitation of 0.2wt.%, although it was used as alloying element up to a level of 2.5 wt.% in some commercial aluminium alloys, which can be found in both wrought and casting alloys [99,100]. Nickel has been recognised as a strongly partitioning and slow-diffusing element [101]. Nickel is almost insoluble in aluminium; with solubility being about 0.05 wt.% at 640 $^{o}$C and less than 0.005 wt. % at 450 $^{o}$C. In the Al-Ni binary alloy, the addition of nickel up to 2 wt.% give an increase in the strength of aluminium, but decreases in ductility [100]. Similar results were found in multicomponent aluminium systems and the aluminium matrix is unlikely to contain Ni levels above the equilibrium solubility. It was reported that Ni was mainly associated with iron to form AlFeSi intermetallics at low levels and to form $Al_3Ni$ intermetallics at higher concentration, such as in an Al-Mg-Si wrought alloy containing 1.4wt.% Ni [102]. A recent investigation [102] has also shown that Ni additions up to 0.05 wt.% did not have an obvious influence on the phase constituents of AA6063 alloy, but this level was only at 0.015wt.%Ni for AA3102 alloy. A significant influence on the microstructure were observed in the as-cast condition of AA3102 alloy when Ni content was 0.05wt.%. For A356 alloy, Ni additions up to 0.02 wt.% did not have significant influences on the as-cast microstructure, but a new phase was formed when the Ni addition was increased to 0.05wt.%. A variety of intermetallics have been found to be AlFeMgSi and AlFeSi phases in the as-cast and heat-treated A356 alloy [102, 103].

## 2.12 Repeatability and Weibull Analysis

In HPDC, the melt usually fill the die cavity with turbulence flow. These result in the high possibility of forming varied defects in individual casting. More importantly, the defect

distribution is very random and irregular, exhibiting a large uncertainty in different castings. Consequently, the inconsistency of mechanical properties in die castings is a general phenomenon in production. Gokhale et al. [104,105] examined the effect of porosity on the tensile strength of cast alloys and confirmed that the tensile properties is decisively dependent on the distribution and size of microporosity. Surappa et al. [106] pointed out that the tensile properties of Al-7%Si-0.4%Mg alloy are affected by the cracking initialled from eutectic Si-particle and micro-voids. Lee and Shin [107] found that the tensile strength and elongation of as-cast alloy have a strong inverse parabolic dependence on microporosity variation. The variability in the mechanical properties of castings made in the same conditions has been an important matter in engineering application. The quantification of load carrying capacity is critical to describe the material property to the external load. In practice, a relatively large design margin has to be given in order to eliminate the effect of internal defects.

Statistical evaluations are effective approaches to analyse the reliability and repeatability of castings because of brittle fracture in structure and especially wide scatter of measuring data [108]. In the often used average value or the minimum value of measurement, when assessing the mechanical properties of the castings, the testing data from different locations are usually overlapped, although the average value can be different. This phenomenon actually exists in many cases when assessing a new casting process or new materials. Therefore, the widely used average value with standard deviation seems insufficient to differentiate their characteristics. As such, the statistical properties provide more information [109].

Weibull statistics has been extensively used characterize the failure of brittle materials. Numerous studies in the engineering literature have reported the Weibull parameters where the strengths are related to fractographically determined defect types and sizes in a wide range of materials [110,111]. Weibull analysis are becoming more common in relate to examine the defects to strengths of brittle materials, especially for the castings [112,113]. In comparison with other statistical methods, Weibull statistical analysis has more reliable values in property evaluation from the point of variables in life and strength parameters [114,115]. In the early studies, the two-parameter Weibull modulus appeared to be a useful measure of the reliability of the casting process [116, 117]. Therefore, the two-parameter Weibull modulus has been extensively used to characterize the tensile properties [118]. Recently, the use of three-parameter Weibull statistics has been explored to illustrate its superior analytical potential over the traditional two-parameter approach [119]. The three-parameter Weibull analysis provides

new information including the minimum values of strength below which the material is extremely unlike to fail. As such, the three-parameter Weibull statistical analysis is expected to be more useful to assess the properties of castings [111,112].

## 2.13 Scope of the Current Research

In the HPDC process, the unique characteristics in quality and cost efficiency are attractive in automotive applications, in particular in body structure, where castings are characterised by thin wall, large project area and complicated shape. In the meantime, the castings need to assemble with sheet and/or extruded components made by wrought alloys. Therefore, the alloys are required to have improved ductility.

The present study aims to develop a die castable ductile aluminium alloy based on the Al-Mg-Si system. In order to make the die castable Al-Mg-Si based alloys, the effect of alloying elements on the microstructure and mechanical properties will be investigated. These elements are expected to modify the alloy microstructure and improve the mechanical properties of the die cast alloy. The effect of alloying elements on the solidification and microstructural evolution, and the mechanical properties of Al-Mg-Si alloys, will be investigated by the combination of the thermodynamic calculation and experimental validation. The CALPHAD calculation will be applied to understand the effect of the solute elements on the liquidus temperature, phase formation, microstructural evolution and solidification process. The calculation results will be used to guide experimental work and validate alloy composition. The microstructure and mechanical properties of the alloy will be examined to understand the effect of the selected elements. The relationship between the microstructure and mechanical properties will be further investigated to identify the strengthening mechanism in the alloys.

Fe and Ni tolerance in the Al-Mg-Si-Mn alloy will be investigated as it is important for recycling. The precise accumulation of iron during HPDC using fully recycled materials will be examined to predict the maximum cycles to produce castings with required mechanical properties. The strengthening mechanism and the relationship between the microstructure and mechanical properties are discussed introduce the alloy made by secondary materials. Meanwhile, the statistics analysis of the castings will be made as an important step for the developed alloy in application. Weibull statistical analysis of the mechanical properties

including the yield strength, the ultimate strength and the elongation of the alloy prepared by HPDC will be carried out to compare the reproductivity of the casting. The measured mechanical properties of castings will also be assessed by the conventional average value with standard deviation approach. The microstructure, defects levels and fractural graphical behaviour will be analysed in relation to the Weibull parameters.

# Chapter 3
# Experimental Details

## 3.1 Melt Preparation

In the present study, alloys were manufactured from commercial purity materials. The specific compositions of raw materials are shown in Table 3.1. Commercial pure (CP) Al ingots and CP-Mg were supplied by Norton Aluminium and Magnesium Elektron, respectively. The size of each ingot was 25 Kg for the CP-Al metal and 7 Kg for the CP-Mg metal. The master alloy Al-50wt.%Si and Al-20wt.%Mn were supplied by Avon Metals Ltd and around 5kg of each ingot. The Al-46wt.%Fe was supplied by KBM Affilips and received as small slices with sizes ranging from 0.5 to 2 cm. It was smashed into small granules (1mm in diameter) before being used. The Al-5wt.%Be, CP-Cu and CP-Zn were supplied by William Rowland Limited. The Al-5wt.%Be and CP-Cu were received as extruded billets (1cm in diameter and 5 to 7cm in length) with about 10g/billet for Al-5wt.%Be and about 40g/billet for the CP-Cu. Zn was received as semi-spherical small ingots with 4cm in diameter and about a 200g/ingot. In each experiment, about 6-10 kg of melt was prepared in an A25 clay-graphite crucible with a dimension of 210×280×155mm, and an electric resistance furnace was used to heat up the crucible and metals during melting, as shown in Figure 3.1. The clay graphite crucible was coated with brine-nitride to prevent contamination during the melting.

**(a) Preparing of Al-Mg-Si-Mn Melts**

During the experiments, each element was weighed to a specific ratio with 5wt. % extra amounts for burning loss compensation during melting. In each experiment, about 6-10 kg of melt was prepared in a clay-graphite crucible. An electric resistance furnace was used to heat up the crucible and metals during melting. All elements, except Mg, were added into the crucible and heated up to 750°C. After all the initial elements were melted, the melt was held at 750 °C for 3hrs for homogenisation and the Mg ingots were preheated at 200°C. Then the

Al-Be master alloy was added at a level of 15ppm of Be, followed by the Mg ingots. After that, the melt was held at 750°C for 30mins for homogenisation, before degassing.

Figure 3.1 The photo of the electric resistance furnace and the clay-graphite crucible used in the current study.

Table 3.1 Composition of raw materials used in this study (wt. %)

| | Si | Mg | Mn | Fe | Ti | Zn | Cu | others | Al |
|---|---|---|---|---|---|---|---|---|---|
| CP*-Al | 0.03 | <0.001 | 0.001 | 0.08 | 0.006 | 0.003 | 0.001 | | 99.86 |
| CP-Mg | 0.012 | 99.9 | 0.016 | 0.003 | 0.00 | 0.00 | 0.0007 | <0.001 | 0.019 |
| Al-50Si | 49.07 | 0.01 | 0.02 | 0.36 | 0.02 | 0.01 | 0.00 | 0.00 | Bal |
| Al-20Mn | 0.1 | 0.08 | 19.0 | 0.4 | 0.02 | 0.02 | 0.04 | | Bal |
| Al-46Fe | 0.06 | | 0.18 | 46.45 | | | | | Bal |
| Al-5Be | 0.019 | 0.016 | <0.01 | 0.029 | <0.01 | <0.01 | <0.01 | Be 5.48 | Bal |
| CP-Cu | | | | | | | 99.99 | | |
| CP-Zn | | | | | | | 99.99 | | |

(*CP stands for commercial purity)

For all the experiments, the melt was subjected to fluxing and degassing using commercial fluxes and rotary degassers with $N_2$.The degassing process lasted around 3.0 minutes, with a rotating speed of 500rpm/min and a gas flow of 10 L/min. The structure of the degassing mechanism is shown in Figure 3.2.

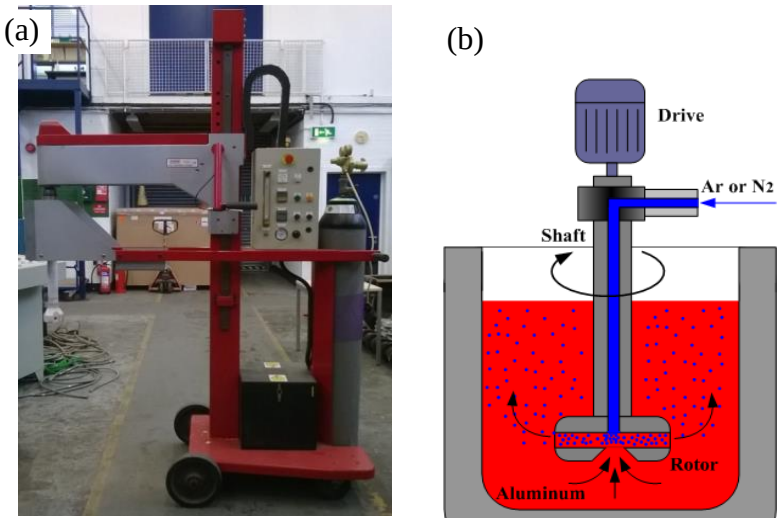


Figure 3.2 (a) Photo of the degassing machine used in experiments and (b) schematic diagram of the rotary degassing process.

In the rotary degassing method, the rotor was immerged in the crucible under the melt surface and chemically inactive gas, $N_2$, was purged through the rotating shaft and rotor. The rotating of shaft produced a large number of fine bubbles, which had a very high surface area-to volume ratio. Large surface areas promoted fast and effective diffusion of hydrogen into the gas bubbles, due to the difference of the [H] partial pressure between liquid and $N_2$ gas bubbles. Then the hydrogen was taken out of the melt through the bubbles. After rotary degassing, a granular flux was applied on the top surface of the melt to protect the melt.

The sample for composition analysis was taken from the melt after degassing. A mushroom sample was made by casting the melt directly into a steel mould for the composition analysis. The mushroom sample was ground down to 800 grid abrasive grinding paper by removing a depth of 2-5mm. The composition of each alloy was obtained from an optical mass spectroscopy, as shown in Figure 3.3, which was calibrated before each session and the machine was switch on at least 30 minutes before starting testing. One proxy sample was measured before testing the useful sample as a warming up of the machine. During measurement, at least five spark analyses were performed and the average value taken as the chemical composition of the alloy.

**(b) Addition of Mn**

The Mn additions were weighted at the required content with 5wt. % extra amounts for burning loss compensation during melting. An Al-20wt.%Mn master alloy was added into the crucible

with the CP-Al and Al-50wt.%Si ingots at beginning of melting. Due to the high melt temperature of the Al-20wt.%Mn master alloy, the melt was held at 750 °C for 3hrs, with occasional stirring to homogenise the composition.


Figure 3.3 The optical mass spectroscopy for alloy composition analysis.

**(c) Addition of Fe**

Fe was added only when it was required. It was added into clay-graphite crucible together with the CP-Al, Al-50wt.%Si and Al-20wt.%Mn alloys. In order to guarantee composition uniformity, the melt was held about 2 hours, with occasional stirring, to accelerate the dissolving process. Spark analysis was performed during the melt holding to confirm whether the Fe was fully dissolved. Since Fe significantly increases the liquidus of the alloy, the holding temperature for the melt with Fe addition was 100°C above its liquidus, which was calculated using CALPHAD.

**(d) Addition of Cu**

Cu was added only needed when essential; it was added into the clay-graphite crucible with the CP-Al, Al-50 wt.%Si and Al-20 wt.%Mn. The burning loss of Cu is very low; therefore no burning loss was applied during melting. Due to the high melt temperature of the pure Cu, the melt was held at 750°C about 2 hours, with occasional stirring to homogenise the composition.

## 3.2 High Pressure Die Casting

A standard cold chamber HPDC machine, DAK450-54, made by Frech Ltd. was used for producing tensile samples. The over view of the machine is shown in Figure 3.4, and the main technical parameters are shown in Table 3.2. The plunger diameter was 70mm, and the effective shot sleeve length was 50cm. A set of die was used to make standard tensile test samples. The size of the samples were designed according to ASTM B557-06 [120]. The detailed structure of the diecasting, with biscuit and over flow, is shown in Figure 3.5. Six tensile test samples were made in each shot. In the die block, a number of channels were made for heating and cooling the die to maintain it at a required temperature. During casting, the die block was heated by circulation of mineral oil at 250 °C.

Table 3.2 Main parameters of DAK450-54 HPDC machine used for the present study.

| | | | |
|---|---|---|---|
| Locking force | 5000 kN | Max. injection force | 548 kN |
| Locking stroke | 675 mm | Injection stroke | 500 mm |
| Ejector force | 241 kN | Plunger diameter | 60 – 100 mm (70 mm used) |
| Ejector stroke | 150 mm | Casting volume | 942 – 2617 $cm^3$ |
| Operation pressure | 160bar | Special casting pressure | 1936 – 2697 $daN/cm^2$ |

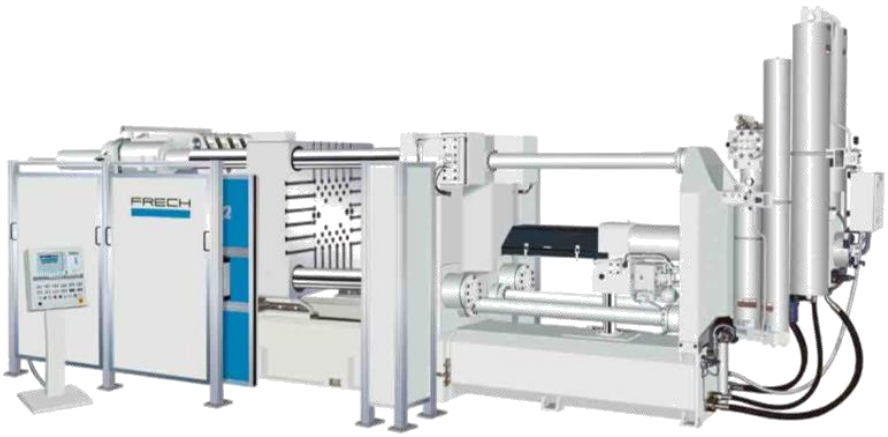


Figure 3.4 The Frech DAK450-54 cold chamber HPDC machine used in experiments

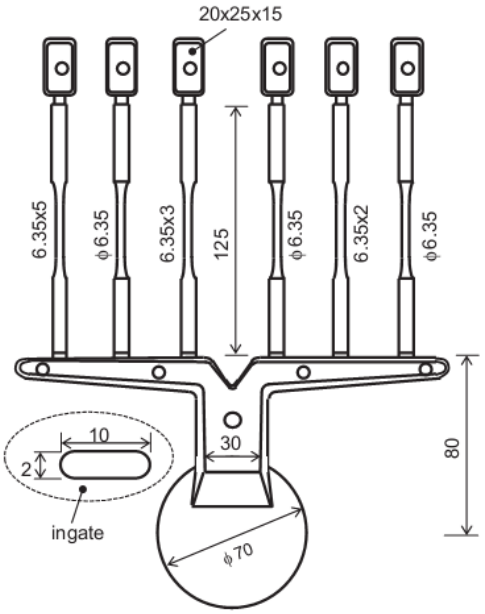


Figure 3.5 Diagram of diecastings for the standard tensile testing samples of cast aluminium alloys according to the specification defined in the ASTM B557-06. The overflow and biscuit are designed in association with the cold chamber diecasting machine and the dimensions are in mm.

The steps for the HPDC process include: (a) carefully clean the die surfaces of any material left from previous castings and coat with a graphite oil based lubricant to aid ejection of cast samples; (b) transport the melt from the crucible by using a born nitride coated steel ladle and wait until the melt temperature reaches a pre-set temperature (60 °C above the alloy liquidus), then pour the melt into the shot sleeve of the HPDC machine; (c) activate the HPDC machine to apply the shot according to the set profile of the plunger speed, position and pressure. The machine automatically runs through the cycle of injection, intensification, dwelling (while the casting fully solidifies) and finally ejection of the cast component.

During casting, the weight of each shot was bout 800g. The injection profile for the speed and pressure are shown in Figure 3.6. According to Figure 3.5, the total ingate area is 1.2cm$^2$, and the total area for the plunger is 38cm$^2$. With the speed of the plunger shown in Figure 3.7, the ingate speed is calculated as 32m/s. By comparing the calculated speed with the commonly used injection speed for aluminium alloys, which is 3-80 m/s and typically between 20 and 35m/s [121], the casting parameters selected for the present study are appropriate.

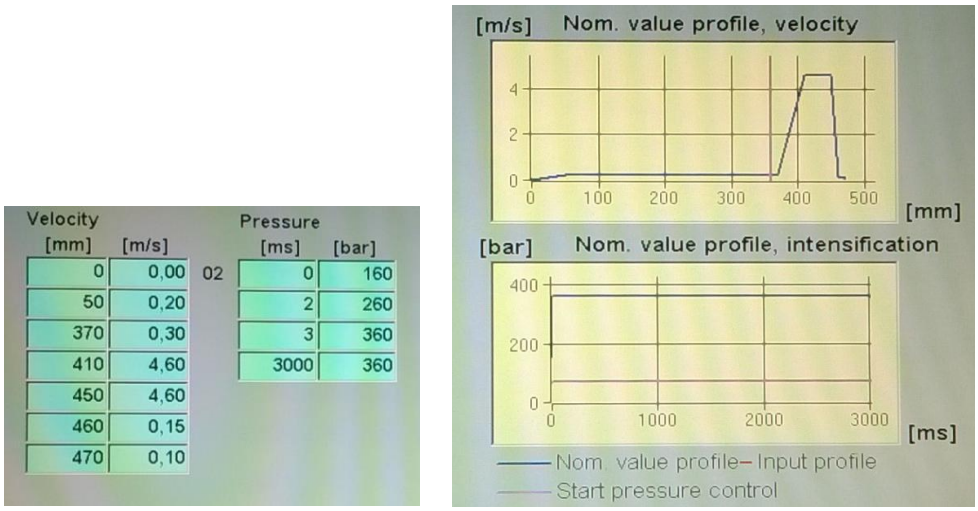


Figure 3.6 The programed injection velocity and pressure profiles for the Frech DAK450-54 450 tone cold chamber HPDC machine

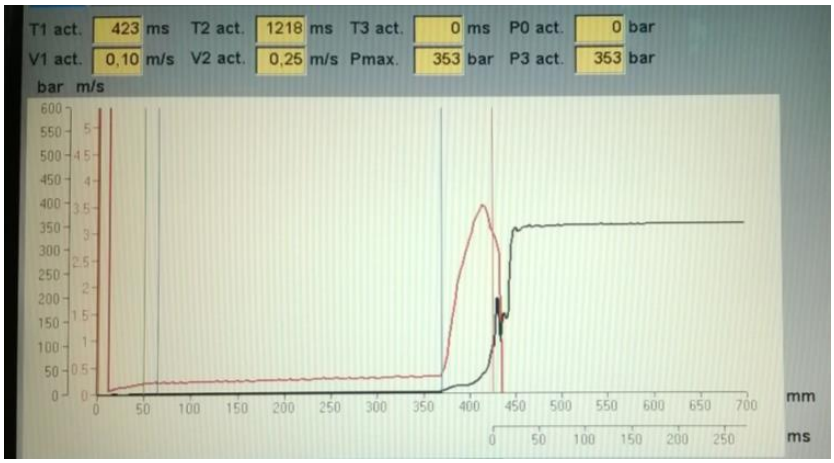


Figure 3.7 The actual injection profiles of the piston forwarding along the shot sleeve and the pressure with the time after trigged at 430mm during HPDC process.

## 3.3 Microstructure Observation and Analysis

### 3.3.1 Sample Preparation for Microstructure Analysis

Specimens for microstructural examination were cut from the middle of the round tensile samples and mounted in Bakelite by Buehler SimpliMet® 1000. The Bakelite mounted specimens were grinded and polished by using a Buehler Automet® 250 machine. Varied grits of SiC abrasive papers (120#, 600#, 800#, 1200#, 2400#, and 4000#) were used to grind the mounted samples. The grinding times for each paper bellow 2500 grid were about 1.0min, and

30s for 2500# and 4000# papers. Silica suspension (OPS) was used to polish the samples for 3-10min with a load of 5N. After polishing, specimens were cleaned in an ultrasonic bath (Engisonic B220) for 10 minutes to remove dirt from the surface. There was no etching on all samples were carried out using 10vol.%NaOH water solution. The etching time varied from 30s to 1 min according to the condition of each sample.

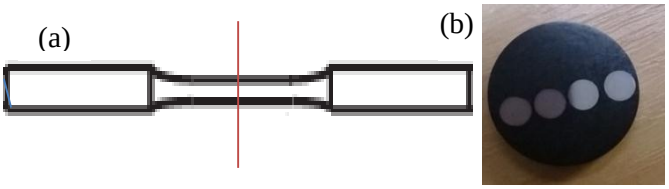


Figure 3.8 (a) Graphical illustration of the cutting position for the microstructure observation, and (b) the photo of Bakelite mounted specimens.

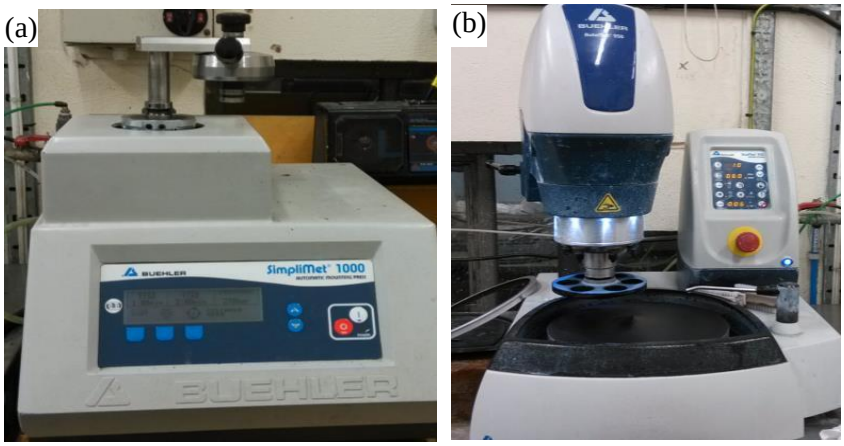


Figure 3.9 (a) The photo of the Buehler SimpliMet 1000 machine for sample Bakelite mounting, and (b) the photo of the Buehler Automat 250 machine.

### 3.3.2 Optical Microscope

A Zeiss Optical Microscopy (OM) equipped with an AxioCam MRC digital camera and computer was used to observe microstructures from non-etched surfaces, as shown in Figure 3.10. "Axioshop 2MaT0" software was used to acquire pictures from digital camera and analyse the images. The microstructures of the alloy were taken at 1-2mm from the edge of specimens in order to get a representative structure. The grain size, shape factor, and volume fraction, porosity fraction were measured by using the automatic measurement program in the

"Axioshop 2MaT0" software, as shown in Figure 3.11. Manual adjustments for contrast, phase selection, and phase segregation were required during the automatic measurement. Five to ten different fields on the cross section of the sample were analysed from each specimen, and the average was taken as the actual measurement value. Equivalent diameter is the diameter of a circle having the same area as that of the particle/or phase [122]. It can be calculated as:

$$\text{Equivalent diameter} = (4\text{Area}/\pi)^{0.5} \qquad (3.1)$$

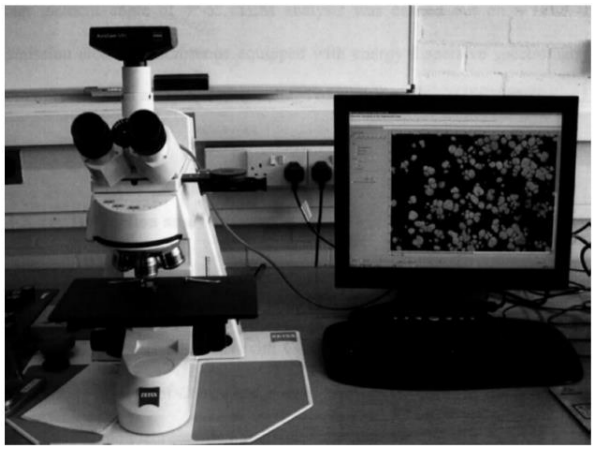

Figure 3.10 The photo of Zeiss Optical Microscope (OM) with an AxioCam MRC digital camera.

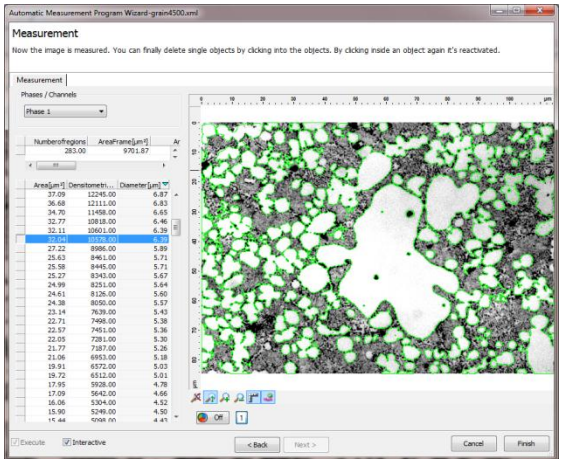


Figure 3.11 The interactive interface of the automatic measurement program in the"Axioshop 2MaT0" software.

### 3.3.3Scanning Electron Microscope (SEM)

The advantage of SEM over optical microscopy is the large depth of field and higher resolution, thus producing high resolution images at high magnification. A typical SEM instrument, showing the electron column, sample chamber, EDS detector, electronics console, and visual display monitors. The scanning electron microscope (SEM) uses a focused beam of high-energy electrons to generate a variety of signals at the surface of solid specimens. The signals that derive from electron-sample interactions reveal information about the sample including external morphology (texture), chemical composition, and crystalline structure and orientation of materials making up the sample. In most applications, data are collected over a selected area of the surface of the sample, and a 2-dimensional image is generated that displays spatial variations in these properties. Areas ranging from approximately 1 cm to 5 microns in width can be imaged in a scanning mode using conventional SEM techniques (magnification ranging from 20X to approximately 30,000X, spatial resolution of 50 to 100 nm). The SEM is also capable of performing analyses of selected point locations on the sample; this approach is especially useful in qualitatively or semi-quantitatively determining chemical compositions (using EDS), crystalline structure, and crystal orientations (using EBSD). The design and function of the SEM is very similar to the EPMA and considerable overlap in capabilities exists between the two instruments.

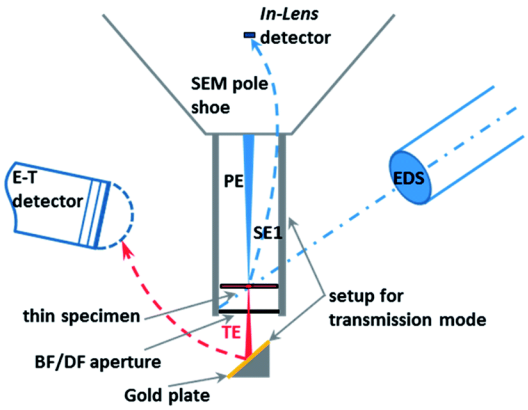


Figure 3.12 Diagram of SEM system.

Accelerated electrons in an SEM carry significant amounts of kinetic energy, and this energy is dissipated as a variety of signals produced by electron-sample interactions when the incident

electrons are decelerated in the solid sample. These signals include secondary electrons (that produce SEM images), backscattered electrons (BSE), diffracted backscattered electrons (EBSD that are used to determine crystal structures and orientations of minerals), photons (characteristic X-rays that are used for elemental analysis and continuum X-rays), visible light (cathodoluminescence–CL), and heat. Secondary electrons and backscattered electrons are commonly used for imaging samples: secondary electrons are most valuable for showing morphology and topography on samples and backscattered electrons are most valuable for illustrating contrasts in composition in multiphase samples (i.e. for rapid phase discrimination). X-ray generation is produced by inelastic collisions of the incident electrons with electrons in discrete orbitals (shells) of atoms in the sample. As the excited electrons return to lower energy states, they yield X-rays that are of a fixed wavelength (that is related to the difference in energy levels of electrons in different shells for a given element). Thus, characteristic X-rays are produced for each element in a mineral that is "excited" by the electron beam. SEM analysis is considered to be "non-destructive"; that is, x-rays generated by electron interactions do not lead to volume loss of the sample, so it is possible to analyse the same materials repeatedly.


Figure 3.13 The photo of Zeiss Supera 35 FEG scanning electron microscope (SEM) equipped with an energy dispersive X-ray spectrometer (EDX) facility.

The SEM system at Brunel University is a Zeiss Supra 35VP FEG scanning electron microscope, as shown in Figure 3.12. For chemical composition analysis, the SEM was equipped with an energy dispersive X-ray spectrometer (EDX) and Oxford Instruments Inca. The data was then ZAF corrected. During experiments, a working voltage of 3-20KV and a working distance of

8-10 mm were selected to take images. When the quantitative analysis was selected, a 20KV accelerating voltage was used and the system was calibrated with Cu before each session. The accuracy of the quantitative EDX was within 0.1%. To minimise the influence of the interactive volume, at least five analyses on selected grains were conducted for each phase and the average was taken as the measurement.

## 3.4 Mechanical Property Measurement

The strength of a material is its ability to withstand an applied load without failure. The field of strength of materials deals with forces and deformations that result from their acting on a material. The methods employed to predict the response of a structure under loading and its susceptibility to various failure modes takes into account the properties of the materials such as its yield strength, ultimate strength, Young's modulus; in addition the mechanical element's macroscopic properties (geometric properties), such as it length, width, thickness, boundary constraints and abrupt changes in geometry such as holes are considered. The stresses and strains that develop within a mechanical member must be calculated in order to assess the load capacity of that member. This requires a complete description of the geometry of the member, its constraints, and the loads applied to the member and the properties of the material of which the member is composed. With a complete description of the loading and the geometry of the member, the state of stress and of state of strain at any point within the member can be calculated. Once the state of stress and strain within the member is known, the strength (load carrying capacity) of that member, its deformations (stiffness qualities), and its stability (ability to maintain its original configuration) can be calculated. The calculated stresses may then be compared to some measure of the strength of the member such as its material yield or ultimate strength. The calculated deflection of the member may be compared to deflection criteria that are based on the member's use. The calculated buckling load of the member may be compared to the applied load. The calculated stiffness and mass distribution of the member may be used to calculate the member's dynamic response and then compared to the acoustic environment in which it will be used.

Material strength refers to the point on the engineering stress-strain curve (yield stress) beyond which the material experiences deformations that will not be completely reversed upon removal of the loading and as a result the member will have a permanent deflection. The ultimate

strength refers to the point on the engineering stress-strain curve corresponding to the stress that produces fracture, as shown in Figure 3.14.

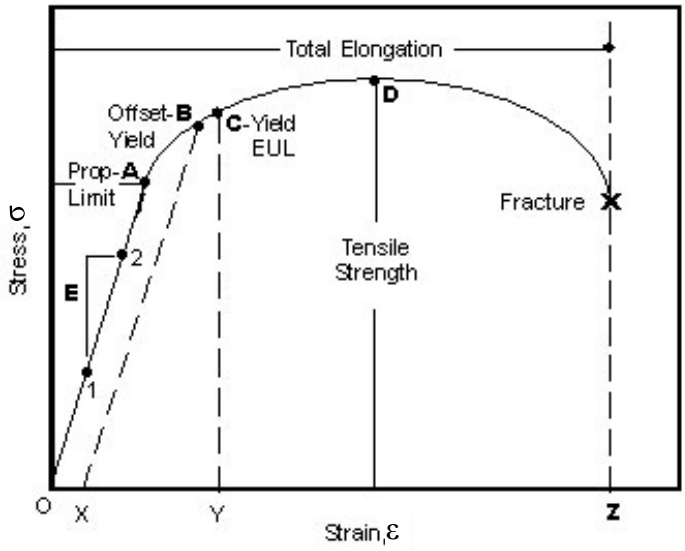


Figure 3.14 Diagram of tensile property testing

A universal materials testing machine, Instron® 5569, equipped with Bluehill software and a ± 50KN load cell was used for the tensile tests, as shown in Figure 3.15. The tensile test results including yield stress, ultimate tensile strength and Young's modulus were recorded by the Bluehill software during automatic testing. The stress (σ) (calculated from the load) and strain (ε) (calculated from the extension) was either plotted as nominal stress against nominal strain, or as true stress against true strain. The yield strength was measured as 0.2% proof stress on the stress-strain curve, the elongation was measured at the fracture strain and the UTS was measured as the fracture stress. All the round samples were tested at room temperature (25°C) with a 25mm gauge length extensometer and an extension ramp rate of 2mm/min, strain rate: $1.33\times10^{-3}s^{-1}$. The data was then collected from the average value of 10 to 15 samples without showing obvious casting defects on the fracture surfaces.

Figure 3.15 The photo of Instron® 5569 universal materials testing machine.

## 3.5 CALPHAD Calculation

The CompuThermal PandaT 8.2 software (Figure 3.16) is a powerful software program for calculating thermodynamic properties and phase diagrams in multi-component systems [123]. The calculations are based on models for the Gibbs free energy of each phase in a particular system [124]. The thermodynamic parameters required for calculations are optimised and achieved by data collected from published journals and other commercial thermodynamic databases, therefore the model fits the available experimental data for a given phase [125]. The temperature-composition is used as a calculation space and one or more points in the temperature-composition space can be defined in each calculation.

In the present study, the Al8 database was used to calculate phase formation, solid fraction, solidification range and non-equilibrium solidification curve in the Al-$Mg_2Si$ alloys with excess Mg and other solute elements. The Al8 database was loaded with 22 common elements and 182 phases. Both the Equilibrium model and Scheil model were used during calculation. This enables a preview of the selected alloy in the liquidus, microstructural evolution and phase formation, solidification process, the effect of different solute contents on the phase formation and guidance in the experimental validation of the alloy in selected composition, melting preparation and casting processes.

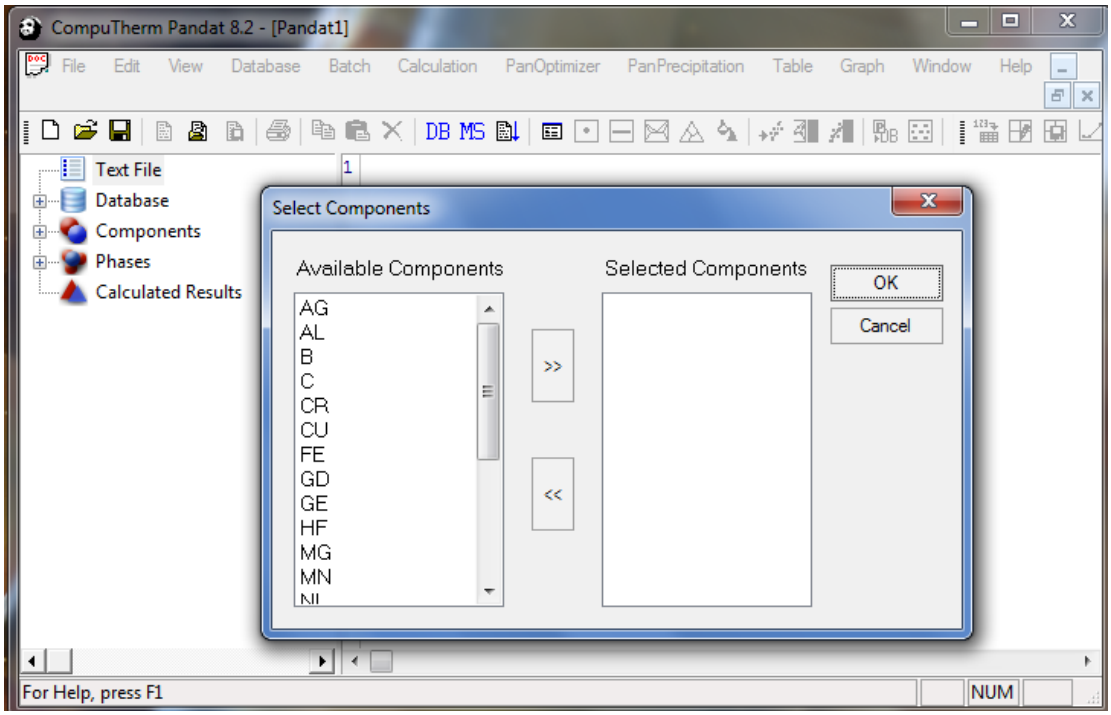


Figure 3.16 The interactive interface in the CumpuThermal Pandat 8.2 software.

The section calculation was used to acquire the two-dimensional (2D) section of the Al-$Mg_2Si$ alloys with varied solute elements. Three non-collinear points in the calculation space were used to define a 2D section, as shown in Figure 3.17. The calculation parameters are listed in Table 3.2. In the results shown in following Chapters, the isopleth sections of the alloys were calculated. The Y-axis to the origin point was set with the temperature descending from 1000°C to 0°C. The X-axis was set with an ascending of calculated elements. The isopleth sections of the alloy with varied solute elements were set with the origin composition. The solidification ranges for the alloy with varied solute elements were acquired from the isopleth sections of each alloy system by calculating the temperature range between the solidus and the liquidus. The non-equilibrium calculations were based on the Scheil model under 1 atmosphere pressure. The maximum temperature step was set at 4°C, and the calculation was stopped when the solid fraction was less than 0. The weight fraction of each phase and the concentration variation of different elements were acquired from the non-equilibrium results.

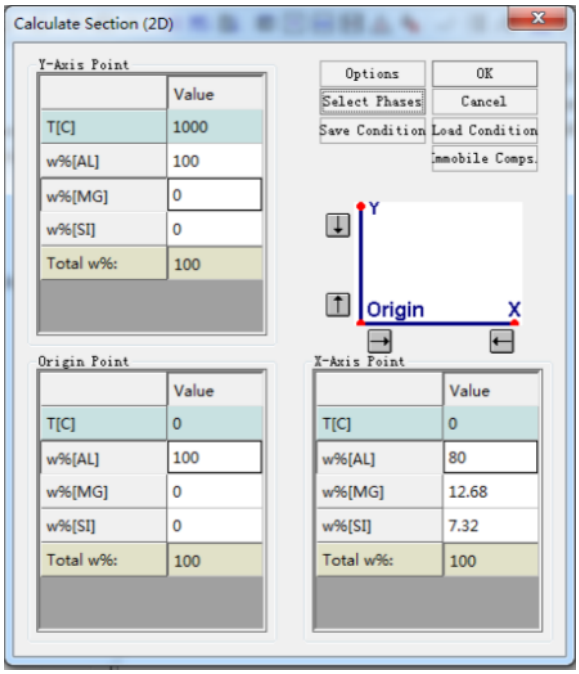


Figure 3.17 The interactive interface in the CumpuThermal Pandat 8.2 software for the 2D section calculation.

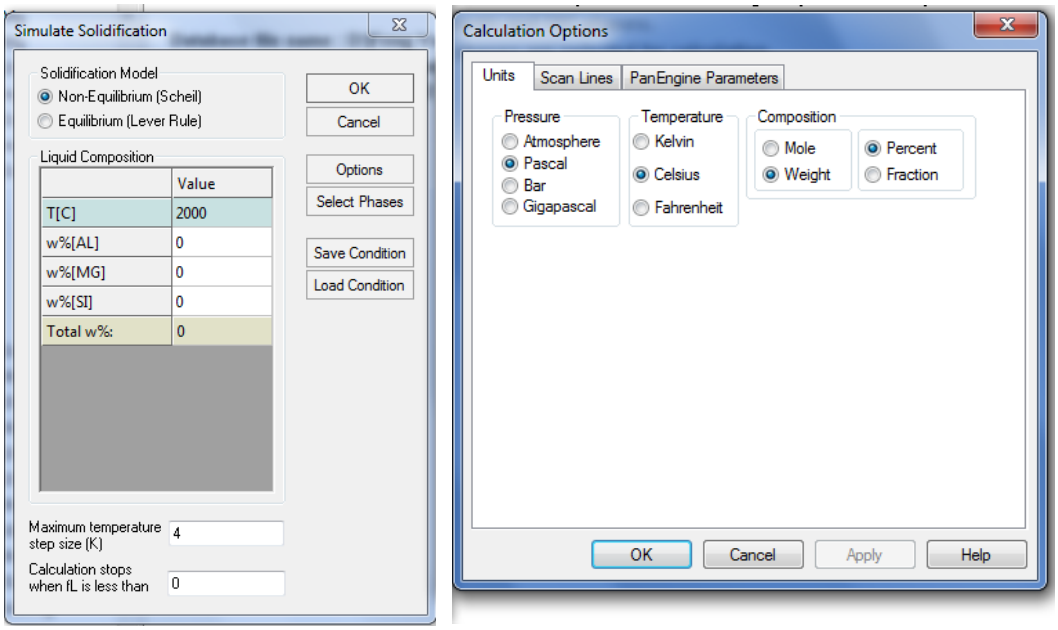


Figure 3.18 The interactive interface in the CumpuThermal Pandat 8.2 software for the solidification calculation and the calculation options.

# Chapter 4
# Composition Optimisation of Al-Si-Mg-Mn Alloy

## 4.1 Introduction

Currently, there is still a lack of clear requirement for the cast alloys used in automotive body structure, partially because of the insufficient experience in the application of aluminium automotive body. However, we can obtain indications from the extensively used wrought alloys in the body structure. The basic requirements for the cast alloys suitable for automotive body structure are summarized as follows:

(1) Die-castable at typical wall thickness of 2 to 4mm with low level of porosity,
(2) Excellent ductility with breaking elongation at least 15% under as-cast condition,
(3) A level of 150MPa of yield strength and 300MPa of ultimate tensile strength of die casting under as-cast condition,
(4) Appropriate corrosion resistant,
(5) Potential of paint baking hardening at 180$^{o}$C for 30 minutes that is commonly used in industry,
(6) Compatible with wrought aluminium alloys used as sheet/extruded parts in automotive body structure. This is particularly important for the possible closed loop recycling of materials in the future.

Of these requirements, the properties and cost are two major concerns. The requirements of the properties include the mechanical performance and the corrosion resistance. The cost control includes the use of die castings that can easily achieve massive production and hence lowering the component cost. Meanwhile the compatibility with wrought alloys can reduce the recycle cost at the end life of vehicles.

The properties of a die-cast alloy depend firstly on its composition, although the effect of the processing during its production is also very important. Each alloying element affects the alloy

properties both independently and interactively [126]. Currently, the die-cast aluminium alloys include Al-Si-Cu, Al-Si and Al-Mg-Si and Al-Mg alloys, as shown in Table 2.2, 2.3 and 2.4. Al-Si-Cu and Al-Si alloys are the most popular die-cast alloys that offer a good combination of strength, castability and processability, but less ductility. Al-Mg-Si alloy can provide a better ductility, but still is not sufficient for car body structure. The specification of available Al-Mg-Si die-cast alloys varies in different countries. Some of them are listed in Table 4.1 with the grade designation and composition [127,128]. The alloys provide mechanical properties at 90-120MPa of yield strength, 170-280MPa of ultimate tensile strength and 3-5% of elongation. To meet the requirement mentioned above for the automotive body structure, the ductility needs to be improved significantly, while both the yield strength and the ultimate tensile strength should be further improved. On the other aspects, high level of magnesium in aluminium alloys can easily cause oxidization during processing and extra care needs to be taken for Mg content in the alloy, although it can be minimized by adding a small amount of beryllium.

In consideration of the wrought aluminium alloys that have been extensively used in automotive body structure; the main alloying elements are Mg, Si and Cu, as seen in Table 2.1. Therefore it is advantage to use Al-Mg-Si alloy for automotive body structure if its ductility can be improved under as-cast condition. This can offer a possibility to achieve closed loop recycling at the end life of body structure, which is beneficial for the environment and cost-saving. In recent years, trials have been made to add rare earth elements or scandium to Al-Mg-Si alloys in order to improve the mechanical properties [129, 130]. However, the utilization of costly elements is not preferred in industry. Therefore, the development of new Al-Mg-Si die-cast alloy should firstly focus on the composition optimization with less level of the costly elements.

Table 4.1 The composition of die-cast Al-Mg-Si alloy designed in different countries.

| Country | Alloy | Si | Mg | Fe | Cu | Mn | Zn | Ti | Others | Al |
|---|---|---|---|---|---|---|---|---|---|---|
| UK (BS1490) | LM5 | 0.3 | 3.0-6.0 | 0.8 | 0.1 | 0.3-0.7 | 0.1 | 0.05 | Ni0.3, Pb0.1 | Bal. |
| China (GB/15115) | YL302 | 0.8-1.3 | 4.5-5.5 | ≤1.2 | ≤0.1 | 0.1-0.4 | ≤0.2 | ≤0.2 | - | Bal. |
| Germany (DIN) | GK-AlMg5Si | 0.9-1.5 | 4.8-5.5 | 0.4 | 0.03 | ≤0.4 | 0.1 | 0.001 | - | Bal. |
| France (NFA57-105) | AG66 | 0.4 | 5.0-7.0 | 0.5 | 0.1 | 0.5 | 0.2 | 0.2 | Ni0.05,Pb0.05, Sn0.05 | Bal. |
| Russia (ГОGT 2685) | AMr4K1 | 1.3-1.7 | 4.5-5.2 | 0.4 | 0.7-1 | 0.6-0.9 | - | 0.1-0.25 | Be 0.003 | Bal. |
| Japan (JIS H2212) | ADC6 | ≤1.0 | 2.6-4.0 | ≤0.6 | ≤0.1 | 0.4-0.6 | ≤0.4 | | Ni≤0.1,Sn≤0.1 | Bal. |
| USA (ASTM B179) | 516.0 | 0.3-1.5 | 2.5-4.5 | 0.35-1.0 | 0.3 | 0.15-0.4 | 0.2 | 0.1-0.2 | Ni0.25-0.4 | Bal. |
| Sweden | 4163 | 0.5-1.5 | 4.0-6.0 | 0.5 | 0.1 | 0.5 | 0.2 | 0.2 | Ni0.05,Pb0.05, Sn0.05 | Bal. |

This Chapter describes the development of a die-cast aluminium alloy that can satisfy the requirement of mechanical properties, in particular ductility for application in automotive body structure. The CALPHAD (calculation of phase diagrams) method [ 131 ] was used to systematically analyse the Al-Mg-Si-Mn based alloys in thermodynamics such as the freezing ranges, phase formation and transformation temperatures, and the fractions of each phase during solidification. The experimental investigation for the effect of various alloying elements on the mechanical properties was carried out and the optimised alloy composition was finalised. Because the paint baking hardening has been widely used in automobile industry for property enhancement of aluminium alloys, an investigation of the effect of a simulated ageing process at 180$^{o}$C on the mechanical properties of casting was also carried out.

## 4.2 Thermodynamic Assessment of Al-Mg-Si-Mn Alloy

### 4.2.1 Basic consideration during CALPHAD calculation

In order to understand the solidification behaviour and compound formation at different element combinations in the Al-Mg-Si-Mn based alloys, the thermodynamics evaluation was carried out using the PanAl database in Pandat software [128]. During calculation, several factors are considered in order to improve the ductility:

(1) Primary intermetallics phase. As the primary intermetallics decrease the ductility of castings, the primary intermetallics phase in the cast alloys should be strictly controlled in order to improve the ductility. This means that the alloy composition should be controlled within or very close to the range where α-Al primary phase can be formed as prior phase during solidification.

(2) Primary α-Al phase. In the cast aluminium alloys, the primary fcc α-Al phase improves the ductility and enhances the solution strengthening. Therefore, it is desirable that the alloy has a high volume fraction of the primary α-Al phase in the as-cast microstructure. However, the increase of primary α-Al phase needs to reduce the solute content, which will reduce the actability. Therefore, the balance is critical.

(3) $Mg_2Si$ phase. $Mg_2Si$ is a strengthening phase but harmful to ductility of the cast alloys. Therefore, the amount of the $Mg_2Si$ phase should be controlled at a reasonable level to maintain the optimised combination of the strength and ductility.

(4) Freezing range. Freezing range plays a very important role in determining the solidification microstructure of the alloy. A wide freezing range will promote the formation of hot tearing and porosity in castings, resulting in the reduction of the mechanical properties including ductility. Therefore, it is preferred to have a relatively narrow freezing range in cast alloys.

(5) Impurity elements. The introduced elements as impurity promote the formation of intermetallics in the alloy. In order to minimise their detrimental effect, it is necessary to control the content of the impurities by forming solid solution rather than intermetallics during solidification.

### 4.2.2 Calculation of the effects of Mg and Si

Figure 4.1 shows the freezing ranges of the Al-Mg-Si alloys. As seen the solidification range changed rapidly with various the Mg and Si contents. All the results showed reductions of solidification range with increasing Mg content first and then increases with further increase of the Mg contents. The minimum solidification ranges corresponded to the different Mg and Si contents, but the low Si was usually associated with low Mg at the minimum solidification ranges. When Si was from 2wt.% to 5wt.%, the minimum freezing range was small with the corresponding Mg content from 5wt.% to 9wt.%. Figures 4.2 and 4.3 show the sectional liquidus of Al-Mg-Si alloy affected by Mg and Si contents. It is seen that the Mg content was associated with Si. If Mg was at 4wt.%, Si content should be controlled below 2.2wt.% in order to obtain primary α-Al as prior solidification phase. If Mg was at 6wt.%, Si content could be at a level of less than 1wt.%. This means that a higher Mg content is usually associated with low Si content in the alloy.

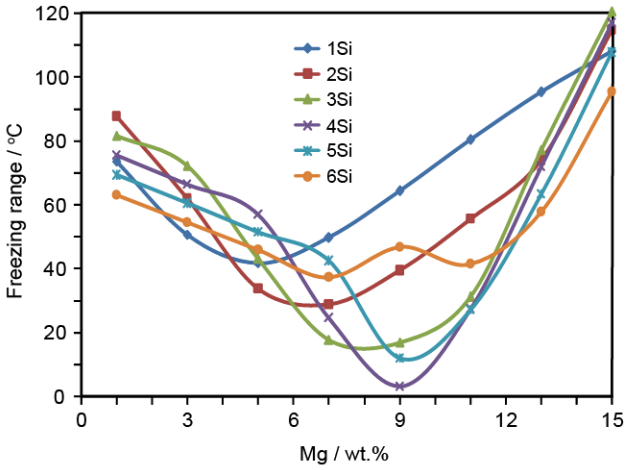


Figure 4.1 The freezing ranges of Al-Mg-Si alloys.

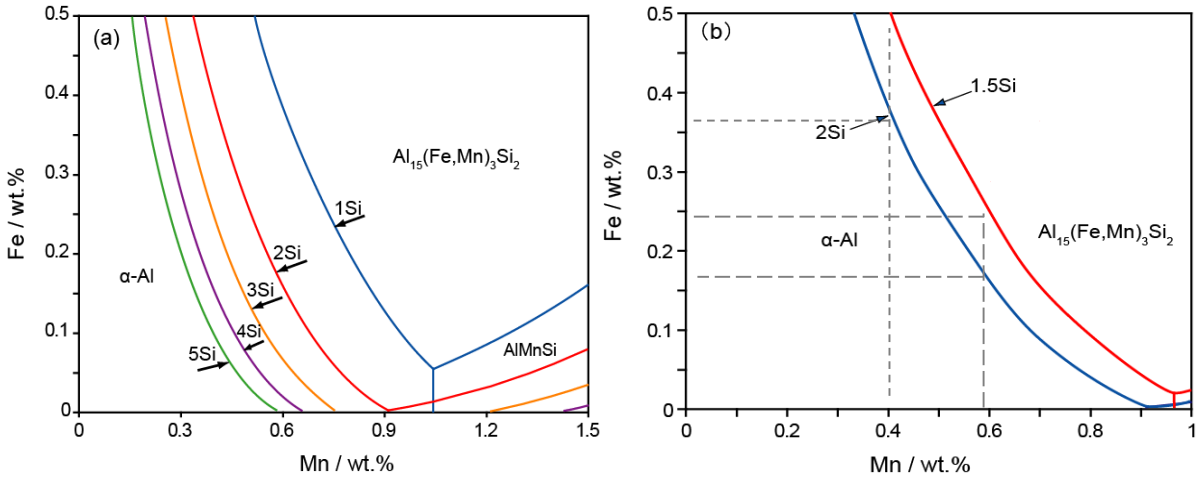


Figure 4.2 Sectional liquidus of (a) Al-5Mg-(1, 2, 3, 4, 5) Si-Mn-Fe and (b) Al-5Mg-(1.5, 2) Si-Mn-Fe.

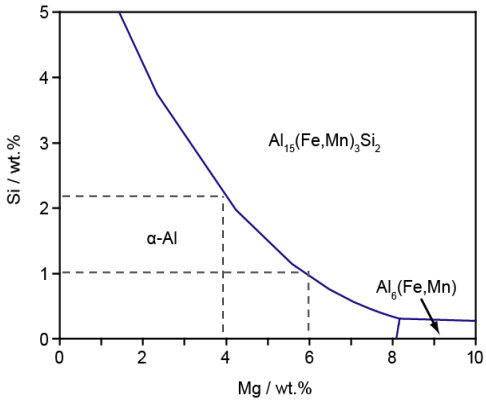


Figure 4.3 Sectional liquidus of Al-Mg-Si alloys with different Mg and Si (note: calculation with 0.6Mn-0.25Fe in the alloys).

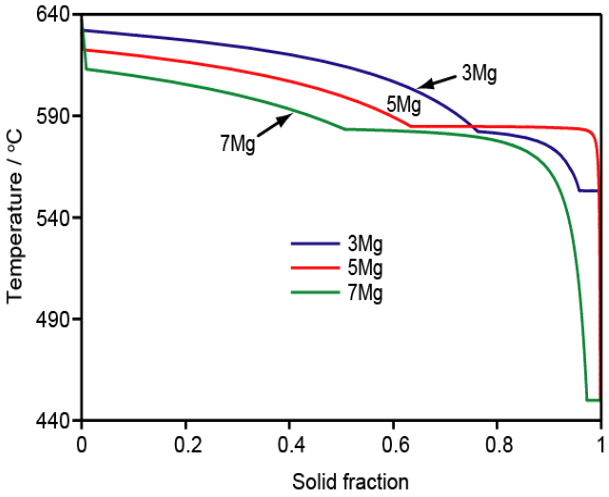

Figure 4.4 The solidification simulations of Al-(3,5,7)Mg-2Si alloys using Scheil model (note: calculation with 0.6Mn-0.25Fe in the alloys).

Table 4.2 The phase fraction of each phase of Al-(3, 5, 7)Mg-2Si-0.6Mn-0.25Fe alloys calculated using Scheil model.

| Phase | Al-3Mg-2Si-0.6Mn-0.25Fe | Al-5Mg-2Si-0.6Mn-0.25Fe | Al-7Mg-2Si-0.6Mn-0.25Fe |
|---|---|---|---|
| α-Al | 0.9491 | 0.9340 | 0.9083 |
| $Al_{15}(Fe,Mn)_3Si_2$ | 0.0168 | 0.0178 | 0.0185 |
| $Mg_2Si$ | 0.0282 | 0.0463 | 0.0487 |
| $Al_8FeMg_3Si_6$ | 0.0014 | 0 | 0 |
| β-AlFeSi | 0.0005 | 0 | 0 |
| Si | 0.0040 | 0 | 0 |
| α-AlFeSi | 0 | 0.0003 | 0 |
| $Al_{13}Fe_4$ | 0 | 0.0003 | 0.0006 |
| β-AlMg | 0 | 0.0013 | 0.0239 |

Figure 4.4 shows the solidification simulation of Al-(3, 5, 7) Mg-2Si alloys using Scheil model in the CALPHAD method. From calculation, about 99% liquid was solidified at 589 $^oC$ in Al-5Mg-2Si alloy, it, therefore, representing the finish of solidification. The volume fractions of each phase in Al-(3, 5, 7)Mg-2Si alloys are shown in Table 4.2. From Table 4.2 and Figure 4.4, it is seen the Al-5Mg-2Si was capable of producing a good combination of the volume fraction of each phase and the good solidification ranges. Therefore, it could be the good selection for the alloy composition.

### 4.2.3 Calculation of the effect of Fe and Mn

The effect of Mn on the liquidus projection of Al-Mg-Si system is calculated and shown in Figure 4.5 for the sectional liquidus of the alloys with 0.3, 0.6 and 0.9wt.% Mn. The results show that the range of the primary α-Al phase became smaller with the increase of Mn content. The primary $Al_{15}(Fe,Mn)_3Si_2$ phase emerged between the α-Al and the $Mg_2Si$ phases when Mn content was increased to a level of 0.6wt.%. Meanwhile, it is seen that the area of forming primary AlMnSi phase became larger with the increase of Mn content. Furthermore, when Mn content was increased to 0.9wt.%, the $Al_{15}(Fe,Mn)_3Si_2$, AlMnSi and AlFeMn phases solidify

as prior primary phase before the formation of primary α-Al phase in the alloy. As mentioned above, the formation of the primary intermetallic phases are undesirable. Therefore, the Mn content needs to be controlled at low level in the Al-Mg-Si alloys.

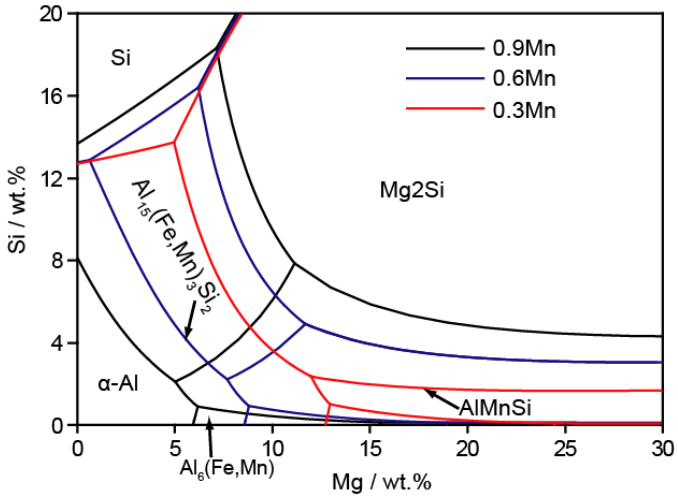


Figure 4.5 The effect of Mn on the liquidus projection of Al-Mg-Si system.

The vertical sections of 0.3 and 0.6wt.% Mn in the Al-Mg-2Si-Mn quaternary system are presented in Figure 4.6, from which it can be seen that, in the Al-rich side, $Al_{15}(Fe,Mn)_3Si_2$ phase solidified after the solidification of primary α-Al phase with 0.3 and 0.6wt.% Mn. In the phase diagram, the freezing range of the alloy with 0.3wt.% Mn essentially equalled to that with 0.6wt.% Mn. However, the formation range of $Al_{15}(Fe,Mn)_3Si_2$ phase in the alloy with 0.3wt.% Mn was much smaller than that with 0.6wt.% Mn. The Mn content in the alloy could be further optimised through examining the vertical sections of the equilibrium phase diagram in the alloys with varied Mg and Si. It is seen that 0.6±0.1wt.% Mn addition could suppress the formation of the primary intermetallic phases during solidification.

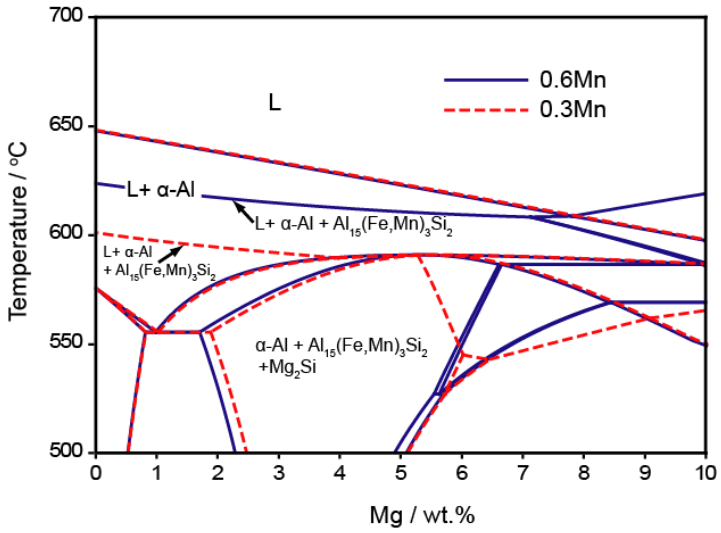


Figure 4.6 The vertical sections of 0.3 and 0.6wt.% Mn in the Al-Mg-2Si-Mn quaternary system.

The effect of Fe and Mn in the alloy can be analysed with various Mg and Si contents. This can be seen from the sectional liquidus of Al-5Mg-(1, 2, 3, 4, 5) Si-Mn-Fe alloys, as shown in Figure 4.8, which revealed that the Mn/Fe ratio was important for the formation of intermetallics in the alloys. In order to eliminate the formation of primary $Al_{15}(Fe,Mn)_3Si_2$ phase the Fe concentration should be limited to a low level of 0.05wt.% in the alloy when Si content was 1wt.% and Mg content was up to 8wt.%. This is obviously difficult to achieve in production. However, by comparing the results in Figure 4.5 and 4.7, the limitation of Fe content could be increased if Si was at a higher level and the Mg content also could be lowered to a level of 5wt.%. When Si was increased in the alloy, the liquidus lines move from higher Mn and Fe contents to lower Mn and Fe contents. In other words, when Mn was fixed, the increased Si was associated with a higher Fe content at the liquidus temperature. When Fe content was fixed, the increased Si in the alloy was associated with a lower Mn content at the liquidus temperature. Figure 4.7b shows the sectional liquidus temperature of the alloy with 5wt.%Mg and varied Si contents. It is seen the Mn/Fe ratios was different in order to obtain primary α-Al phase in the alloys during solidification. When Mn was at 0.4wt.%, Fe concentration could be 0.37wt% at 2wt.%Si , but Fe concentration could be up to 0.5wt.% at 1.5wt.%Si. However, when Mn was increased to 0.6wt.%, Fe concentration could be only 0.16wt% at 2wt.%Si and could be 0.25wt.% at 1.5wt.%Si. Therefore, the selection of Mn

content could be altered with the variation of Fe and Si content. It is desirable that the Mn content should be controlled at a lower level in order to have higher Fe content in the alloy. However, Mn was an important element to prevent the die soldering in aluminium alloys. As a result, the content of Mn is suggested to be 0.6wt.% with a comprehensive consideration, and thereby, Fe concentration is suggested to be less than 0.25wt.%.

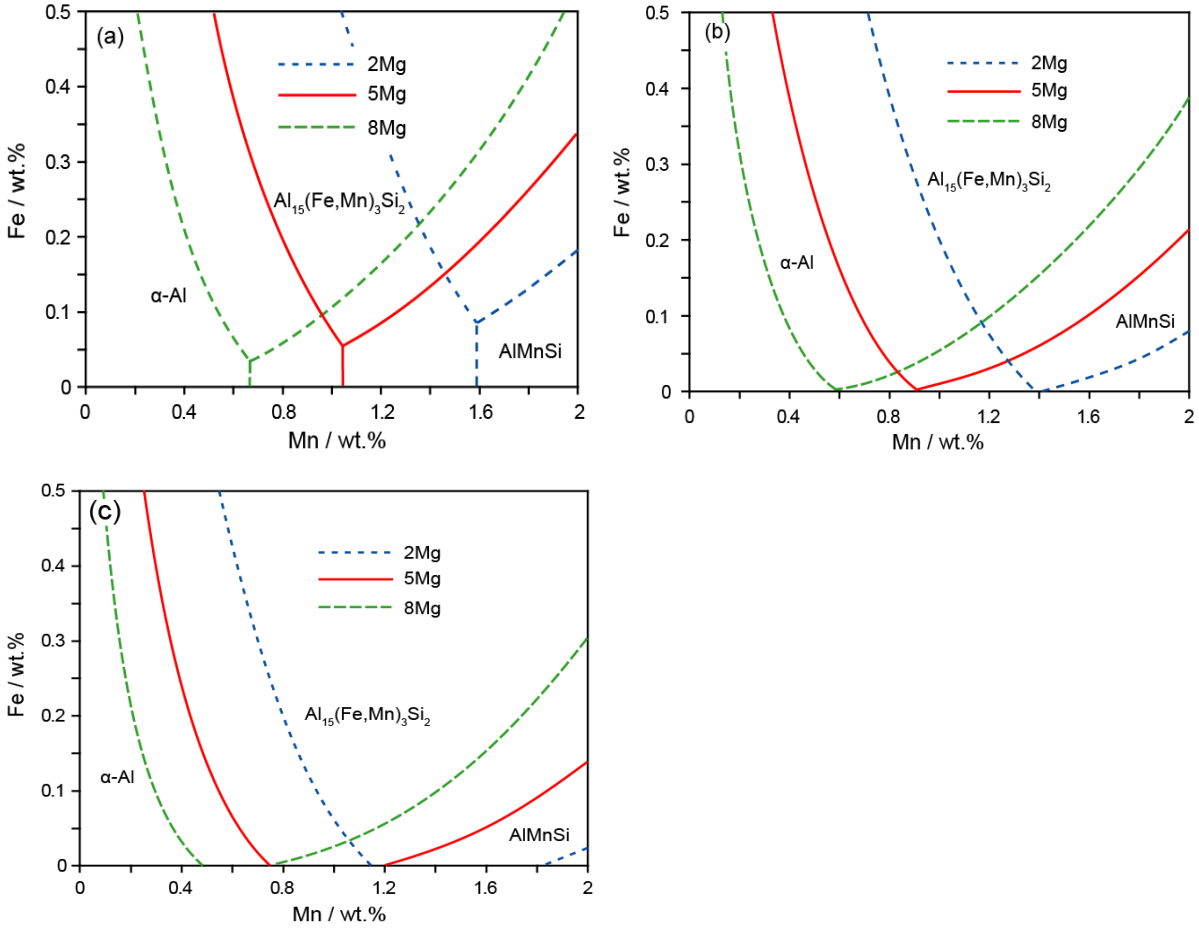


Figure 4.7 Sectional liquidus of (a) Al-(2,5,8)Mg-1Si-Mn-Fe, (b) Al-(2,5,8)Mg-2Si-Mn-Fe, and (c) Al-(2,5,8)Mg-3Si-Mn-Fe.

### 4.2.4 Solidification and phase formation

The calculated vertical section of Al-5Mg-Si-0.6Mn-0.25Fe alloy is shown in Figure. 4.8. The binary eutectic reaction point of L→ α-Al + $Al_{15}(Fe,Mn)_3Si_2$ was 1.45wt.% Si at 625°C. Thus the Al-5Mg-2Si-0.6Mn-0.25Fe alloy was very close to eutectic composition. In equilibrium state, very little $Al_{15}(Fe,Mn)_3Si_2$ could solidify as prior phase at 631°C, then the α-Al phases

solidify in association with the $Al_{15}(Fe,Mn)_3Si_2$ phase, from L→ α-Al + $Al_{15}(Fe,Mn)_3Si_2$ at 623°C, which was a deviatory binary eutectic reaction. With the decrease of temperature, the liquid undertakes a eutectic reaction of L→ α-Al + $Al_{15}(Fe,Mn)_3Si_2$ + $Mg_2Si$ at 584°C. As the solidification of melt usually does not follow equilibrium reaction, especially for casting process, the Scheil module is used to simulate the solidification process.

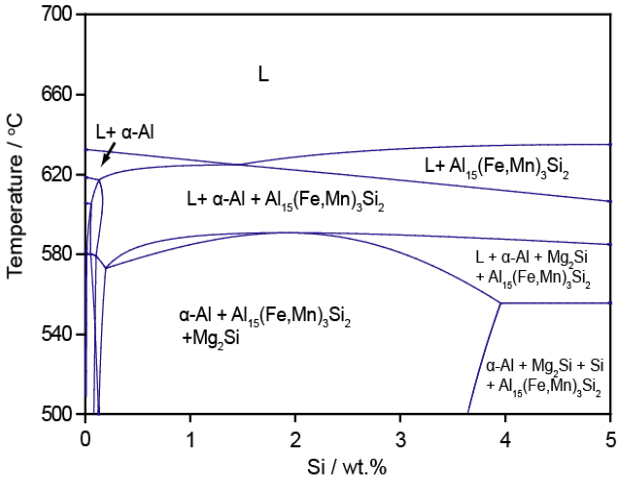


Figure 4.8 The calculated vertical section of Al-5Mg-Si-0.6Mn-0.25Fe alloys.

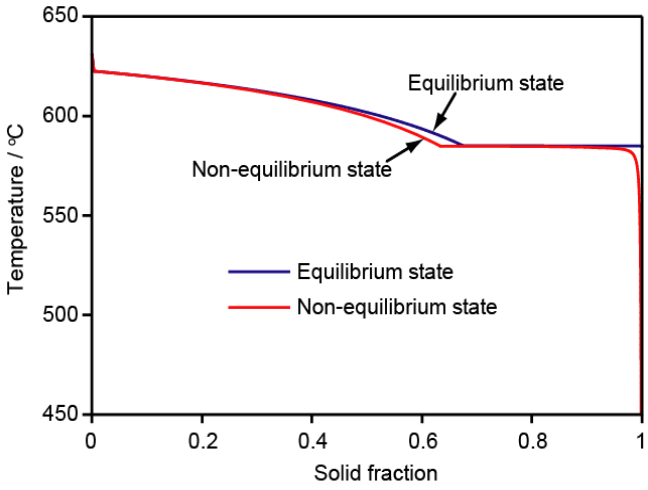


Figure 4.9 Solidification processes at equilibrium and non-equilibrium states.

For comparison purpose, it was calculated the solidification process using the CALPHAD method in equilibrium state and non-equilibrium state, in which the level rule and Scheil model are used respectively. Figure 4.9 shows the calculated results in the equilibrium and non-equilibrium states for the Al-5Mg-2Si-0.6Mn-0.25Fe alloy. It is seen that the solid fraction in non-equilibrium state was less than that in equilibrium state before the occurrence of eutectic

reaction L→ α-Al + $Al_{15}(Fe,Mn)_3Si_2$ + $Mg_2Si$. This means that less $Al_{15}(Fe,Mn)_3Si_2$ phase was solidified in the binary reaction and more eutectic microstructure was formed in non-equilibrium state. The solidification processes of the Al-5Mg-2Si-0.6Mn-0.25Fe alloy in the equilibrium and non-equilibrium states are listed in Table 4.3. It can be seen that the primary α-Al phase amount solidified at first stage (L→ α-Al + $Al_{15}(Fe,Mn)_3Si_2$) in equilibrium state is 6.4 percent more than that in non-equilibrium state. However, the total amount of α-Al phase solidified in equilibrium state equalled to that in non-equilibrium state. Several reactions including L→ α-Al + $Al_{15}(Fe,Mn)_3Si_2$ + $Mg_2Si$ + α-AlFeSi, L→ α-Al + $Mg_2Si$ + $Al_{13}Fe_4$, and L→ α-Al + $Mg_2Si$ + β-AlMg could occur during the subsequent solidification according to the calculation using Scheil model. It is seen that the remnant liquid prior to these reactions was at a level of no more than 0.08,Therefore, these reactions might not take place simultaneously and completely in the following stage of non-equilibrium solidification, in particular, under high cooling rate such as high pressure die casting. Moreover, the solid fraction of the coarse primary α-Al phase solidified was at a level of 0.616 calculated by Scheil model, which was close but less than the critical amount of forming solid skeleton. By calculating the solid fraction of varied phases in the Al-8Mg-2Si-0.6Mn-0.25Fe alloy in the equilibrium and non-equilibrium states, the results are shown in Table 4.4. The results in Tables 4.3 and 4.4 revealed that the phase fraction of $Al_{15}(Fe,Mn)_3Si_2$ solidified at the first stage increased from 0.017 to 0.018 when Mg was increased from 5wt.% to 8wt.%. The phase fraction of primary α-Al phase decreased from 0.616 to 0.425 for the same level of increase of Mg content in the alloy. The reduction of the amount of the primary α-Al phase was significant at a level of 0.191. The increased solid fraction of the primary α-Al phase was beneficial for the improvement of ductility of the alloy. On the other hand, the calculation confirmed that the amount of $Mg_2Si$ phase solidified at the last stage increased with Mg. As the $Mg_2Si$ phase and β-AlMg phase was detrimental to the elongation of the alloy. The amount of these intermetallic compounds should be tightly controlled. The amount of α-AlFeSi phase and $Al_{13}Fe_4$ phase were negligible.

Table 4.3 The solidification processes of the Al-5Mg-2Si-0.6Mn-0.25Fe alloy at the equilibrium and non-equilibrium states.

| Equilibrium state | | Non-equilibrium state | |
|---|---|---|---|
| Reaction | Phase fraction | Reaction | Phase fraction |

| | | | |
|---|---|---|---|
| $L \rightarrow Al_{15}(Fe,Mn)_3Si_2$ | $f(Al_{15}(Fe,Mn)_3Si_2)=0.0035$<br>$f(liquid)=0.9965$ | $L \rightarrow Al_{15}(Fe,Mn)_3Si_2$ | $f(Al_{15}(Fe,Mn)_3Si_2)=0.0035$<br>$f(liquid)=0.9965$ |
| $L \rightarrow \alpha\text{-}Al + Al_{15}(Fe,Mn)_3Si_2$ | $f(Al_{15}(Fe,Mn)_3Si_2)=0.0193$<br>$f(\alpha\text{-}Al)=0.6558$<br>$f(liquid)=0.3249$ | $L \rightarrow \alpha\text{-}Al + Al_{15}(Fe,Mn)_3Si_2$ | $f(Al_{15}(Fe,Mn)_3Si_2)=0.0169$<br>$f(\alpha\text{-}Al)=0.6161$<br>$f(liquid)=0.3670$ |
| $L \rightarrow \alpha\text{-}Al + Al_{15}(Fe,Mn)_3Si_2 + Mg_2Si$ | $f(Al_{15}(Fe,Mn)_3Si_2)=0.0202$<br>$f(\alpha\text{-}Al)= 0.9373$<br>$f(Mg_2Si)= 0.0425$ | $L \rightarrow \alpha\text{-}Al + Al_{15}(Fe,Mn)_3Si_2 + Mg_2Si$ | $f(Al_{15}(Fe,Mn)_3Si_2)=0.0178$<br>$f(\alpha\text{-}Al)=0.8617$<br>$f(Mg_2Si)= 0.0365$<br>$f(liquid)=0.0840$ |
| | | $L \rightarrow \alpha\text{-}Al + Al_{15}(Fe,Mn)_3Si_2 + Mg_2Si + \alpha\text{-}AlFeSi$ | $f(Al_{15}(Fe,Mn)_3Si_2)=0.0178$<br>$f(\alpha\text{-}Al)=0.8951$<br>$f(Mg_2Si)= 0.0414$<br>$f(\alpha\text{-}AlFeSi)=0.0003$<br>$f(liquid)=0.0454$ |
| | | $L \rightarrow \alpha\text{-}Al + Mg_2Si + Al_{13}Fe_4$<br>and<br>$L \rightarrow \alpha\text{-}Al + Mg_2Si + Al_{13}Fe_4 + \beta\text{-}AlMg$ | $f(Al_{15}(Fe,Mn)_3Si_2)= 0.0178$<br>$f(\alpha\text{-}Al)= 0.9340$<br>$f(Mg_2Si)= 0.0463$<br>$f(\alpha\text{-}AlFeSi)= 0.0003$<br>$f(Al_{13}Fe_4)= 0.0003$<br>$f(\beta\text{-}AlMg)= 0.0013$ |

Table 4.4 The solidification processes of the Al-8Mg-2Si-0.6Mn-0.25Fe alloy at the equilibrium and non-equilibrium states.

| Equilibrium state | | Non-equilibrium state | |
|---|---|---|---|
| Reaction | Phase fraction | Reaction | Phase fraction |
| $L \rightarrow Al_{15}(Fe,Mn)_3Si_2$ | $f(Al_{15}(Fe,Mn)_3Si_2)=0.0112$<br>$f(liquid)=0.9888$ | $L \rightarrow Al_{15}(Fe,Mn)_3Si_2$ | $f(Al_{15}(Fe,Mn)_3Si_2)=0.0112$<br>$f(liquid)=0.9888$ |
| $L \rightarrow \alpha\text{-Al} + Al_{15}(Fe,Mn)_3Si_2$ | $f(Al_{15}(Fe,Mn)_3Si_2)=0.0189$<br>$f(\alpha\text{-Al})=0.4458$<br>$f(liquid)=0.5353$<br>$f(Al_{15}(Fe,Mn)_3Si_2)=0.019192$ | $L \rightarrow \alpha\text{-Al} + Al_{15}(Fe,Mn)_3Si_2$ | $f(Al_{15}(Fe,Mn)_3Si_2)=0.0180$<br>$f(\alpha\text{-Al})=0.4247$<br>$f(liquid)=0.5573$<br>$f(Al_{15}(Fe,Mn)_3Si_2)=0.018826$ |
| $L \rightarrow \alpha\text{-Al} + Al_{15}(Fe,Mn)_3Si_2 + Mg_2Si$ | $f(\alpha\text{-Al})=0.929137$<br>$f(Mg_2Si)=0.051671$ | $L \rightarrow \alpha\text{-Al} + Al_{15}(Fe,Mn)_3Si_2 + Mg_2Si$ | $f(\alpha\text{-Al})=0.727301$<br>$f(Mg_2Si)=0.038551$<br>$f(liquid)=0.215321$<br>$f(Al_{15}(Fe,Mn)_3Si_2)=0.0189$ |
| | | $L \rightarrow \alpha\text{-Al} + Mg_2Si + Al_{13}Fe_4$ | $f(\alpha\text{-Al})=0.8875$<br>$f(Mg_2Si)=0.0493$<br>$f(Al_{13}Fe_4)=0.0006$<br>$f(liquid)=0.0437$<br>$f(Al_{15}(Fe,Mn)_3Si_2)=0.0189$ |
| | | $L \rightarrow \alpha\text{-Al} + Mg_2Si + Al_{13}Fe_4 + \beta\text{-AlMg}$ | $f(\alpha\text{-Al})=0.8927$<br>$f(Mg_2Si)=0.0494$<br>$f(Al_{13}Fe_4)=0.0006$<br>$f(\beta\text{-AlMg})=0.0384$ |

Table 4.5 The phase fraction of each phase of Al-5Mg-1.5Si-0.6Mn and Al-5Mg-2Si-0.6Mn alloys with 0.25, 0.5 and 1wt.% Fe addition calculated using Scheil model.

| Phase | Al-5Mg-1.5Si-0.6Mn | | | Al-5Mg-2Si-0.6Mn | | |
|---|---|---|---|---|---|---|
| | 0.25wt.%Fe | 0.5wt.% Fe | 1wt.% Fe | 0.25wt.% Fe | 0.5wt.% Fe | 1wt.% Fe |
| α-Al | 0.9373 | 0.9291 | 0.9163 | 0.9340 | 0.9258 | 0.9127 |
| $Al_{15}(Fe,Mn)_3Si_2$ | 0.0165 | 0.0225 | 0.0271 | 0.0178 | 0.0236 | 0.0296 |
| $Mg_2Si$ | 0.0346 | 0.0338 | 0.0335 | 0.0463 | 0.0451 | 0.0442 |
| β-AlMg | 0.0108 | 0.0117 | 0.0121 | 0.0013 | 0.0023 | 0.0032 |
| $Al_{13}Fe_4$ | 0.0008 | 0.0029 | 0.0110 | 0.0003 | 0.0005 | 0.0062 |
| α-AlFeSi | 0 | 0 | 0 | 0.0003 | 0.0027 | 0.0041 |

The phase fractions of each phase in Al-5Mg-1.5Si-0.6Mn-0.25Fe alloy and Al-5Mg-1.5Si-0.6Mn-0.25Fe are shown in Table 4. Compared to Al-5Mg-2Si-0.6Mn-0.25Fe alloy, the amount of $Mg_2Si$ phase became less but the amount of β-AlMg and $Al_{13}Fe_4$ phases solidified at the last stage became more in the Al-5Mg-1.5Si-0.6Mn-0.25Fe alloy. As a result, the total amount of brittle intermetallic $Mg_2Si$, β-AlMg and $Al_{13}Fe_4$ phases were almost the same in these two alloys.

## 4.3 Experimental Study of Alloying Elements on Mechanical Properties

### 4.3.1 Effect of Mg and Si

According to thermodynamics assessment, although Mg content can be varied in a relatively large range, it is preferred in a range of 5-8wt.% in Al-Mg-Si based alloy to have a relatively narrow solidification range that is essential for die-cast alloy.

Figure 4.10 shows the experimental results of the effect of Mg and Si on the yield strength, the tensile strength and the elongation of the die-cast alloys, in which other elements were fixed at 0.6wt.%Mn, 0.2wt.%Ti and 0.25wt.%Fe. It is seen that both Mg and Si resulted in a significant increase of the yield strength and the ultimate tensile strength, but a significant decrease of the elongation. When Mg content increased from 4.5wt.% to 8wt.%, the yield strength increased from a level of 140MPa to 170MPa, and the ultimate tensile strength increased from a level of 260MPa to 340MPa, but the elongation decreased significantly from a level of 18% to 10%. When the Mg was at a level of 5-6wt.% and Si content increased from 1wt.% to 2.5wt.%, the

yield strength increased from a level of 125MPa to 160MPa, and the ultimate tensile strength increased from a level of 270MPa to 310MPa, but the elongation decreased from a level of 18% to 14%. The results indicated that Mg can enhance the mechanical properties of the die-cast alloys more significantly than Si can in as-cast state. The results also implied that a higher level of Mg in the alloy can provide more strengthening in solid solution. It was observed that Si could significantly improve the castability and reduce hot tearing defects in the alloy. The addition of Si over 1.5% is essential to produce castings with reduced hot tearing defects.

### 4.3.2 Effect of Ti

Titanium is a popular element used in wrought aluminium alloys as grain refiner in both as-cast state and heat-treated state. The experimental results shown in Figure 4.11 confirm that Ti could significantly increase the elongation of the die-cast Al-Mg-Si alloy at a very low level. The elongation was at a level of 11% at 0.015wt.%Ti and it increased to 18% at 0.15wt.%Ti. It is more significant because Ti could also increase the yield strength and the ultimate tensile strength. The increase of strength was up to 10% when Ti was at a level of 0.2wt.%. Therefore, Ti is an essential element for super ductile die-cast aluminium alloys and the level can be controlled at a level of 0.15wt.%.

### 4.3.3 Effect of Cu

Copper is usually used to enhance paint baking hardenability in wrought alloys. Figure 4.12 shows the relationship between Cu content and the strength and elongation of the die castings. It is seen that Cu slightly increased the yield strength, but significantly decreased the elongation and the ultimate tensile strength of die-cast Al-Mg-Si alloy in as-cast state. The main reasons might be that Cu increases the tendency of hot tearing in the die-cast alloys, which not only reduces the strength and the elongation, but also varies the process conditions. Therefore, the Cu level should be controlled at low as possible to avoid the loss of ductility in the alloy, which is desirable for this development.

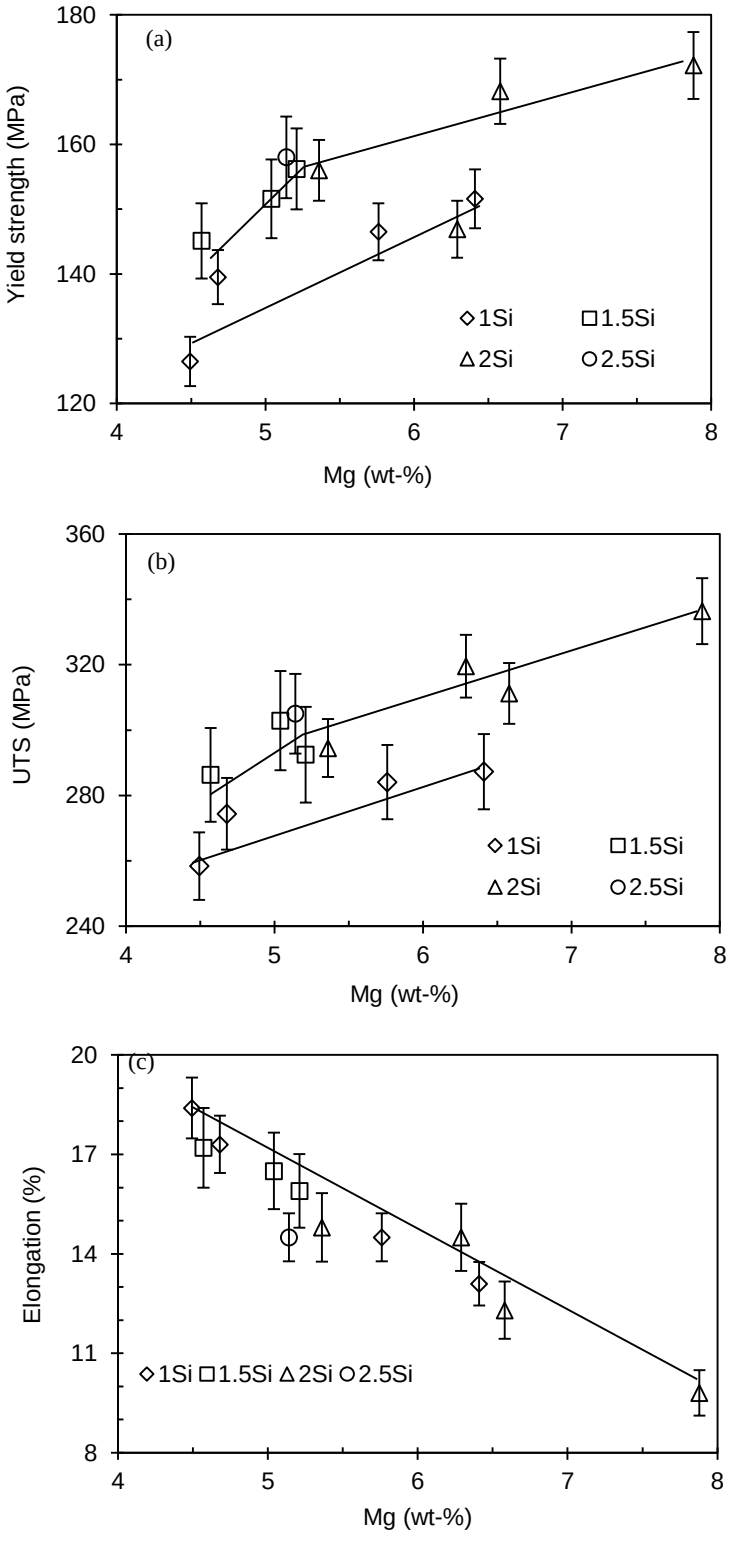


Figure 4.10 Effect of Mg and Si on (a) the yield strength, (b) the ultimate tensile strength (UTS) and (c) the elongation of the Al-Mg-Si die-cast alloy in as-cast state. The other elements in the alloys include 0.6wt.%Mn, 0.2wt.%Ti and 0.25wt.%Fe.

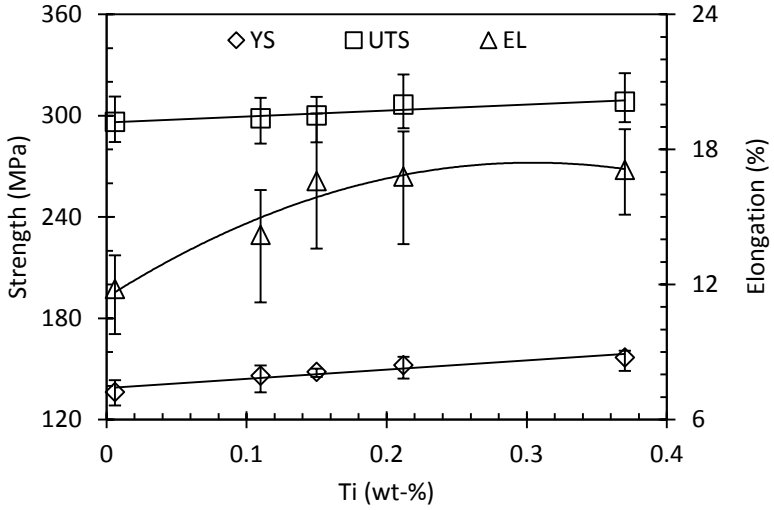


Figure 11.12 Effect of Ti on the yield strength (YS), the ultimate tensile strength (UTS) and the elongation (EL) of the Al-Mg-Si die-cast alloy in as-cast state. The other elements in the alloys include 5wt.%Mg, 1.5wt.%Si, 0.6wt.%Mn and 0.25wt.%Fe.

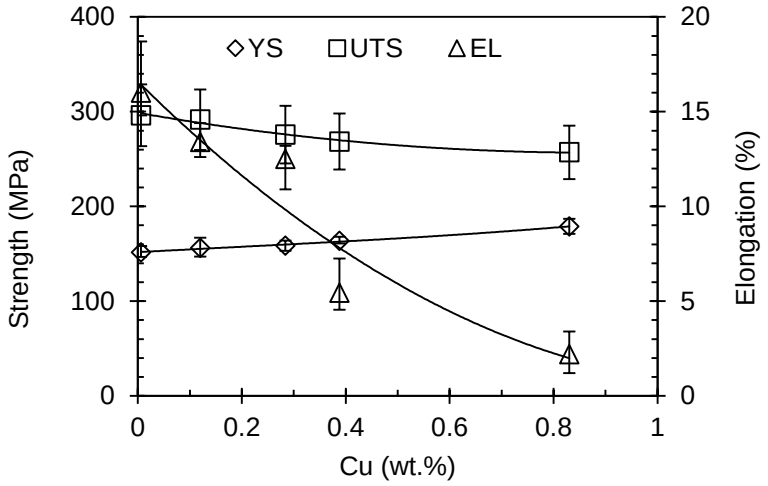


Figure 4.13 Effect of Cu on the yield strength (YS), the ultimate tensile strength (UTS) and the elongation (EL) of the Al-Mg-Si die-cast alloy in as-cast state. The other elements in the alloys include 5wt.%Mg, 1.5wt.%Si, 0.6wt.%Mn, 0.2wt.%Ti and 0.25wt.%Fe.

Based on the experimental results, the optimized composition of the super ductile Al-Mg-Si alloy has been selected at a level of 5-5.5wt.%Mg, 1.5-2.0wt.%Si, 0.5-0.7wt.%Mn and 0.15 - 0.2wt.%Ti. The other elements are impurities and are limited at low level. In particular, Fe should be less than 0.25wt.%. The mechanical properties of the alloy at the optimized composition confirmed that the yield strength of 150MPa, the ultimate tensile strength of 300MPa, and the elongation of 15% were achievable in the designed castings. The value of the

mechanical properties can satisfy the requirements for automotive body structure according to the standard described above.

## 4.4 The Effect of Ageing

Paint baking hardening is one of significant benefits for wrought alloys. Although the paint baking cycle in industry varies from each other in factories, the paint is usually baked at a temperature around 180$^{o}$C. In this work, ageing has been carried out at a fixed temperature of 180$^{o}$C to examine the properties at different times. Figure 4.13 shows the effect of ageing time on the mechanical properties of castings. While the ultimate tensile strength showed no significant variation, the yield strength slightly increased and the elongation decreased with the prolonged ageing time at 180$^{o}$C. With regards to the response at 30 minutes, which is often used in paint baking process, the increase of the yield strength and the decrease of the elongation were less than 10%, respectively. This indicates that the paint baking hardening of die-cast Al-Mg-Si alloy is insignificant under as-cast condition.

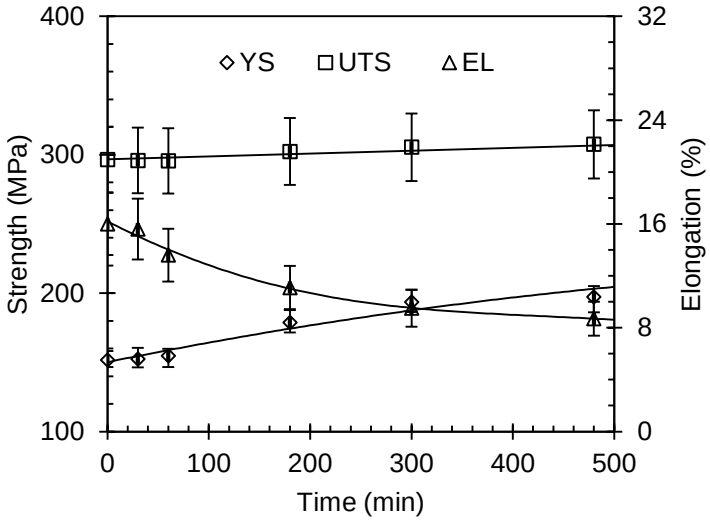


Figure 4.14 Effect of ageing time at 180$^{o}$C on the yield strength (YS), the ultimate tensile strength (UTS) and the elongation (EL) of the Al-Mg-Si die-cast alloy. The other elements in the alloys include 5wt.%Mg, 1.5wt.%Si, 0.6wt.%Mn, 0.2wt.%Ti and 0.25wt.%Fe.

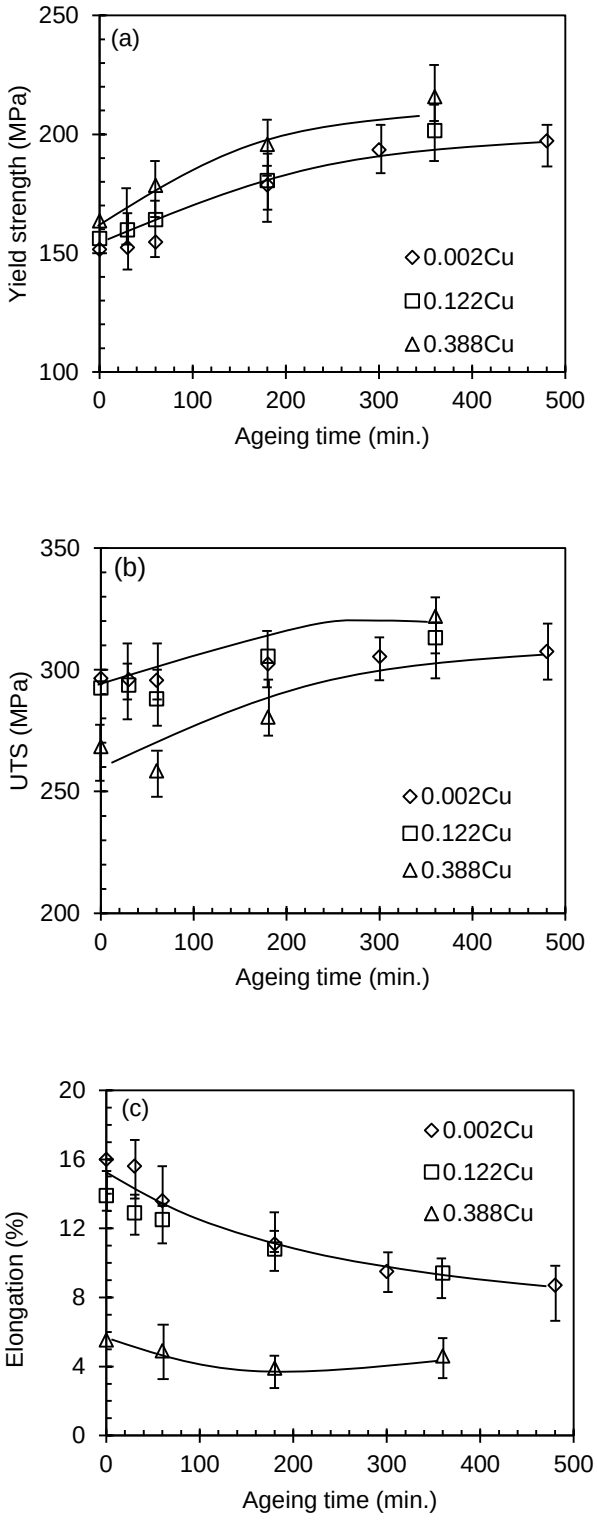


Figure 4.15 Effect of Cu content on the yield strength (YS), the ultimate tensile strength (UTS) and the elongation (EL) of the Al-Mg-Si die-cast alloy aged at 180$^{o}$C. The other elements in the alloys include 5wt.%Mg, 1.5wt.%Si, 0.6wt.%Mn, 0.2wt.%Ti and 0.25wt.%Fe.

In order to enhance the response of paint baking, a further experiment was carried out to study the effect of Cu on the mechanical properties after ageing. The results are shown in Figure 4.14, in which the yield strength and the ultimate tensile strength increased noticeably with the increase of ageing time, but the elongation decreased significantly with the increase of ageing time. In particular, when Cu was at 0.39wt.%, the elongation was so low under both as-cast and aged conditions that the ductility was as low as 6% or lower, which could not satisfy the product requirement. In comparing the results in Figures 4.14 and 4.15; alloys with Cu provide a higher strength, but a lower elongation during the same ageing time.

## 4.5 Effect of Alloying Elements on the Microstructural Formation in HPDC

The typical microstructure of the as-cast Al-Mg-Si-Mn alloy with 5wt.%Mg, 2wt.%Si, 0.6wt.%Mn, 0.2wt.%Ti and 0.25wt.%Fe is shown in Figure 4.15. The microstructure consists of dendrites or fragmented dendrites of primary α-Al phase, globular primary α-Al phase and eutectics phase of α-Al and $Mg_2Si$.

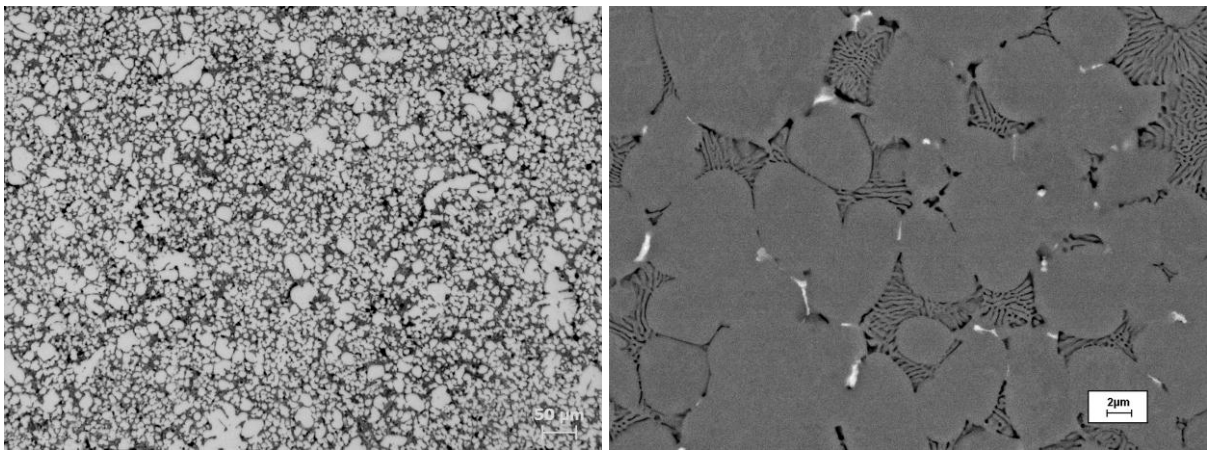


Figure 4.16 (a) Optical micrograph showing the overall distribution of primary α-Al phase with dendrites or fragmented dendrites morphology, (b) image showing the primary α-Al phase with globular morphology and the intermetallics.

In the experimental alloys, the different elements were used to provide strengthening through the formation of different phases during HPDC. Because the alloying elements can alter the solidification process and dominate phase formation, it is necessary to understand the relationship between the alloying elements and the microstructural formation during the solidification in HPDC.

In the Al-Mg-Si system, the primary α-Al phase is prior phase due to the hypoeutectic composition. As the maximum solid solubility of Mg in Al is 17.4wt.% and $Mg_2Si$ in Al is 1.85wt.% under equilibrium condition, the solution strengthening can make a major contribution to mechanical properties. Meanwhile, the $Mg_2Si$ content is at the maximum solubility, which leads to the formation of eutectic Al-$Mg_2Si$ phases between the primary α-Al phase. The $Mg_2Si$ phase can pin the grain boundary sliding under stress. Therefore, the combination between $Mg_2Si$ and extra Mg content can increase strength with appropriate ductility in aluminium alloys. The variations of cooling rate in HPDC result in the formation of different sizes of α-Al phase. The high cooling rate in the die cavity promotes the formation of fine eutectic cells that are distributed randomly in the matrix. In contrast, the lower cooling rate in the shot sleeve (about 10 times lower than that in the die cavity) results in the formation of coarser eutectic Al-Mg2Si phases. The shear and hydrodynamic forces during die filling can divorce the eutectics during passing through the ingate. Therefore, the refined microstructure in die-cast alloys can afford increasing loads, although the non-uniform microstructure may cause un-even distribution of stress.

Mn is largely consumed by the formation of the Fe-rich intermetallics. Therefore, an adequate level of Mn is necessary in order to maintain high Mn/Fe ratio for the formation of the cubic α-AlFeMnSi phase. In the observed α-AlFeMnSi intermetallics, the typical composition is α-Al12(Fe,Mn)3Si, which is made of less Si than that in the common α-$Al_{15}(FeMn)_3Si_2$ compounds. The main reason can be attributed to the low Si concentration in the alloy and the short of Si supply during solidification. In the experimental results, it is also confirmed that Mn/Fe=0.5 is necessary to suppress the formation of the β-AlFe compounds in the as-cast microstructure. β-AlFe intermetallics is immediately observed in the alloys when Mn/Fe<0.5, which is in good agreement with the observation in other alloys including Al-Si, Al-Si-Cu and Al-Si-Mg alloys [6-13]. However, α-AlFeMnSi phase can still be observed at low Mn/Fe ratio. Therefore, the Mn/Fe ratio can be used as an indicator for the formation of β-AlFe compounds, but not for determining the formation of α-AlFeMnSi phase.

Copper increases the strength of Al alloys because of the capability of providing solution strengthening and precipitation strengthening. Copper provides strengthening by forming intermetallics and solutions. The solid solubility of Cu in solid Al is 2.4 at.% Cu and the solid solubility of Al in solid Cu is less than. 0.2 at.% Al at 821 K [132]. Therefore The addition of Cu to Al-Mg alloy system promotes the formation of AlCu intermetallic phase during solidification. The AlCu intermetallics are distributed along the grain boundaries with irregular shapes. Meanwhile, the increasing Cu content increases the amount of intermetallics in the microstructure and can be presented as a continuous network at grain boundaries. Therefore, the strength enhancement from the intermetallics is a balance of the scarification of ductility.

In order to verify the presence of the elements in the identified phase in the experimental alloy, series of intensity maps were performed for the elements Al, Mg, Si, Fe, Mn and Ti at 20 kV, 185nA, 5nm step size and a counting time of 15 ms per step. The results are shown in Figure4.16 with one backscattered SEM micrograph for the analysed area. The presence of Al was evidently highest in the primary α-Al phase. The presence of Mg and Si were at their maximum levels on the eutectic cells. The presence of Fe was at its maximum level in intermetallics. The presence of Mn and Ti were hardly identified in the measurement results. By examining the concentration of Mg on the field of intermetallics presence, there were some overlaps and it was therefore hard to identify whether the intermetallics contained magnesium.

The phase formation and microstructural evolution are critical for high pressure die casting and are closely associated with the solidification process. Therefore, the unique solidification process will be studied and described in next Chapter.

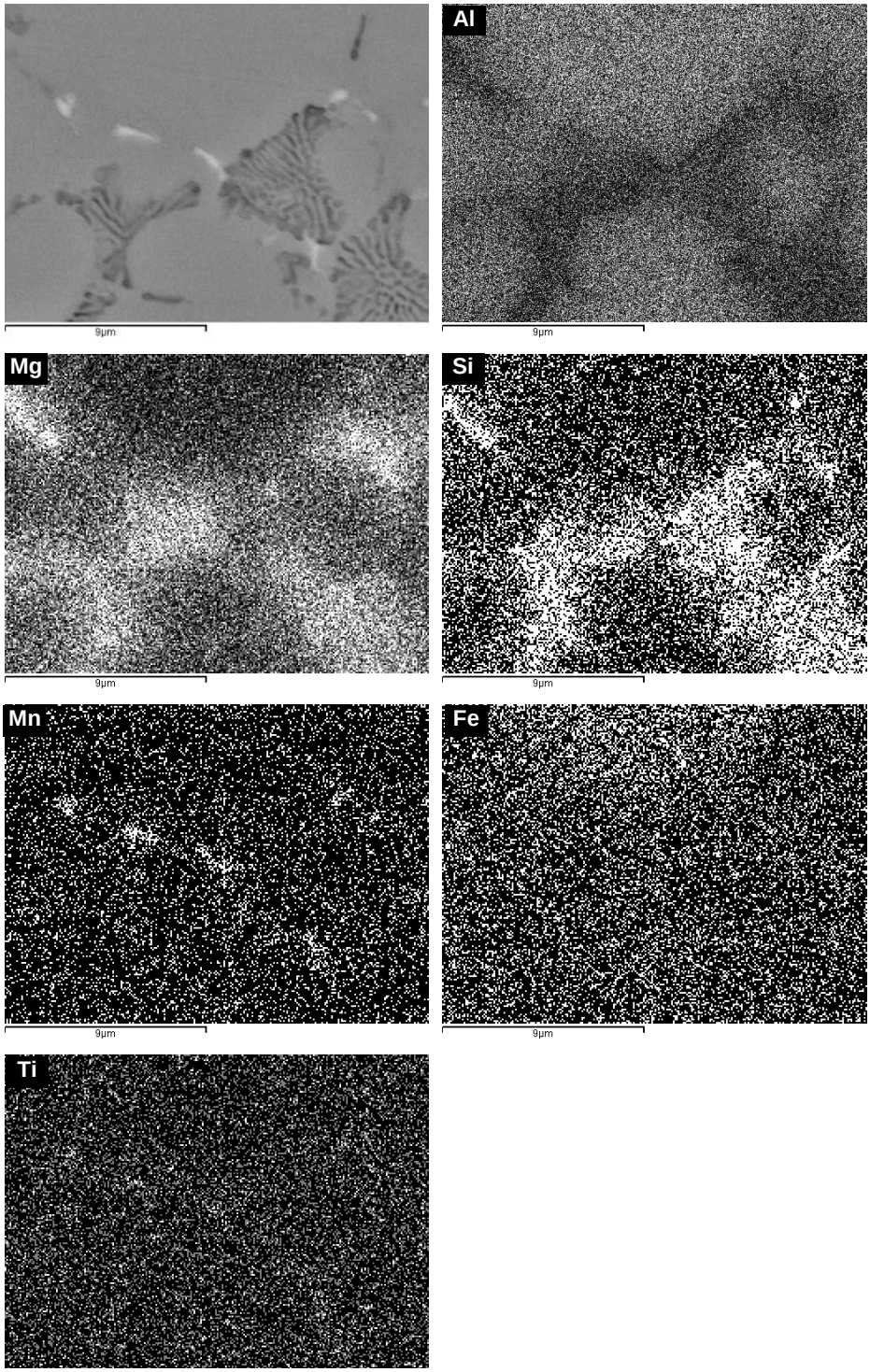


Figure 4.17. Backscattered SEM micrograph and the series of elemental maps showing the distribution of key elements in Al-Mg-Si die-cast alloy. Map conditions: 20 kV, 185nA, 5 nm step size and a counting time of 15 ms per step.

## 4.6 Summary

(1) The super ductile die-cast aluminium alloys for automotive body structure have been developed. The optimized composition comprises of 5-5.5wt.%Mg, 1.5-2.0wt.Si%, 0.5-0.7wt.%Mn, 0.15-0.2wt.%Ti. The other impurity elements should be limited in the alloy; especially Fe should be controlled less than 0.25wt.%. The typical mechanical properties of the die-cast alloy at optimized composition are 150MPa of yield strength, 300MPa of ultimate tensile strength, and 15% of elongation under as-cast condition.

(2) The paint baking hardenability of the alloy is insignificant. The increase of the yield strength of the die-cast alloy is less than 10% after a simulated ageing under 180$^{o}$C for 30min.

(3) Cu can slightly increase the yield strength under as-cast condition or under heat treated condition with significant scarifying the ductility. Therefore, Cu should be limited in the super ductile aluminium alloy.

(4) The microstructure of die-cast aluminium alloys at an optimized composition consists of the primary α-Al phase, the α-AlFeMnSi phase and the eutectics. There are two types of α-Al phase; dendrites or fragmented dendrites solidified in the shot sleeve and globular particles solidified in the die cavity. The α-AlFeMnSi phase is in the form of compact morphology and smaller than 3μm in size. The eutectic cells are about 10μm in size with a lamellar morphology of α-Al phase and $Mg_2Si$ phase.

# Chapter 5
# Solidification of Al-Mg-Si-Mn Alloy during HPDC

## 5.1 Introduction

In Chapter 4, it has been described that Al-Mg-Si based alloys are capable of providing high ductility and an excellent combination of mechanical properties for die castings in the as-cast state. To achieve the required elongation, several critical aspects need to be precisely controlled during manufacturing which include an optimized alloy composition, low level of gas and impurities in melt prior to solidification, minimized defect levels and an optimised microstructure in the castings. These are associated partially or completely with the solidification of the castings. However, the die-cast Al-Mg-Si based alloys are known to have high solidification shrinkage which, therefore, increases the difficulty of producing castings with high integrity [133,134]. As such, the microstructural evolution and the related control during solidification are becoming very important for achieving enhanced mechanical properties of the Al-Mg-Si alloy.

The solidification of Al-Mg-Si based alloys has been the subject of many studies, but most of them fall into the category of wrought alloys [135,136] or high silicon (>5wt.%Si) and low magnesium (<1wt.%) cast alloys (for example, A356) [137,138] produced by sand casting or gravity die casting process. Previous studies were rather limited in describing the solidification and microstructural evolution of high magnesium (>4wt.%) and silicon (>1.5wt.%) cast alloys in HPDC process. Otarawanna *et al.* [139] studied the microstructure formation of AlSi4MgMn and AlMg5Si2Mn castings and found that the salient as-cast microstructural features were similar for both alloys in terms of the externally solidified crystals, defect bands, surface layer, grain size and distribution, porosity and hot tears. Jie *et al.* [140] investigated the microstructure of Al-21.6wt.%Mg alloy solidified under high pressure inside a cylindrical container at a pressure up to 2GPa. They found that the amount of β-$Al_3Mg_2$ phase decreased with increasing pressure and a supersaturated Al(Mg) solid solution was formed at 2GPa. Kimura *et al.* [141]

studied the effect of grain refiner and grain size on the cracking susceptibility of Al-4.5wt.%Mg die-cast alloy. They found that the addition of 0.08wt.%Ti and 0.016wt.%B could achieve significant grain refinement and, therefore, it suppressed cracking formation in Al-Mg die castings. In HPDC process, the melt is injected into the die cavity under high speed (30-50m/s ingate velocity for aluminium alloys) and solidified under high pressure (up to 200MPa in the die cavity) and high cooling rate (up to $10^3$K/s). This results in unique solidification behaviour and offers a fundamental difference to other casting processes. Therefore, theoretical understanding of the solidification process and microstructural evolution in HPDC is important for improving the process itself, microstructural control and the mechanical properties. Moreover, defect formation is closely related to the solidification and microstructure of the castings. This is particularly important in determining the mechanical properties of ductile die-cast aluminium alloys.

In this Chapter, investigation of the solidification process and microstructural evolution of ductile aluminium alloy was carried out using HPDC process. The solidification behaviour in the shot sleeve and in the die cavity was examined for the formation of the primary α-Al phase, eutectic Al-$Mg_2Si$ phases and Fe-rich intermetallics in Al-5wt.%Mg-2wt.%Si-0.6wt.%Mn-0.2wt.%Ti (abbreviated as Al-Mg-Si-Mn hereafter) alloy. The morphology, size and size distribution of the primary α-Al phase are characterised under different solidification conditions. The phases formed in the different stages of solidification are identified and quantified. In the discussion, the growth morphology of the primary α-Al phase formed in the shot sleeve and in the die cavity is analysed using the Mullins-Sekerka instability theory. Jackson-Hunt theory is also used to calculate the growth rate of eutectic Al-$Mg_2Si$ phases during solidification.

## 5.2 As-cast Microstructure of the Die Castings

Figure 5.1 shows the microstructures of the cross-section of a tensile specimen in the die-cast Al-Mg-Si-Mn alloy. It shows a solute enriched circular band that is parallel to the surface of the casting. The similar phenomenon of band formation has been observed by Dahle et al. for different alloys [61]. The band separates the outer skin and the central region of the casting. Two types of primary α-Al phases are seen in the microstructure shown in Figure 5.1. The primary α-Al phase that solidifies in the shot sleeve exhibits a relatively large size with

dendritic or fragmented dendritic morphology. The primary α-Al phase that solidifies in the die cavity shows a relatively smaller size with a globular morphology. A higher volume fraction of the primary α-Al phase that solidifies in the shot sleeve is observed in the central region compared to that in the outer skin region of the casting, as shown in Figure 1b,c&d. The outer skin thickness was measured at 1.0mm for the Al-Mg-Si-Mn alloy in this study, which is smaller than the thickness of 1.5mm measured in Al-Si-Cu alloys [142]. In the transition band zone, the volume fraction of eutectic Al-$Mg_2Si$ phases is higher compared to that in both the skin and the central region.

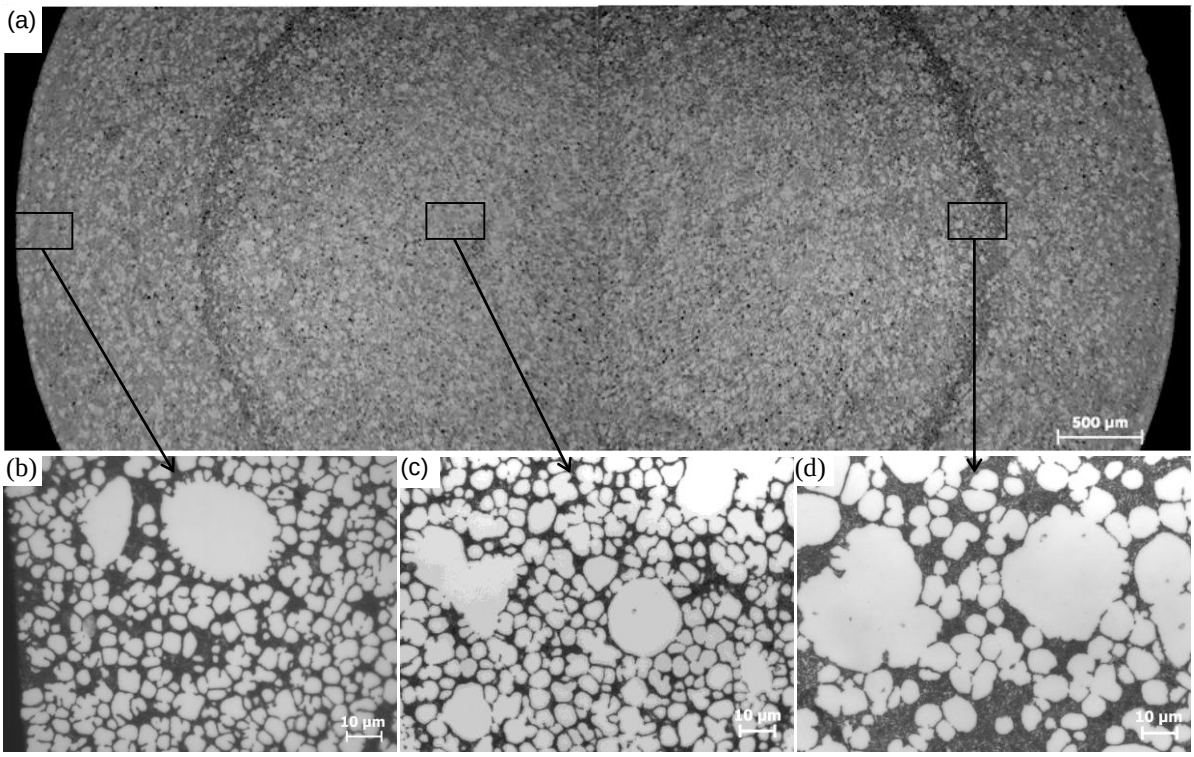


Figure 5.18 Optical micrographs showing the microstructure of the die-cast Al-Mg-Si-Mn alloy, (a) on a cross section of ϕ6.4mm tensile test specimen, (b) in the outer skin region, (c) in the central region, (d) in the band zone. The circular segregation band is 1mm from the surface of casting and has a width from 100 to 150μm.

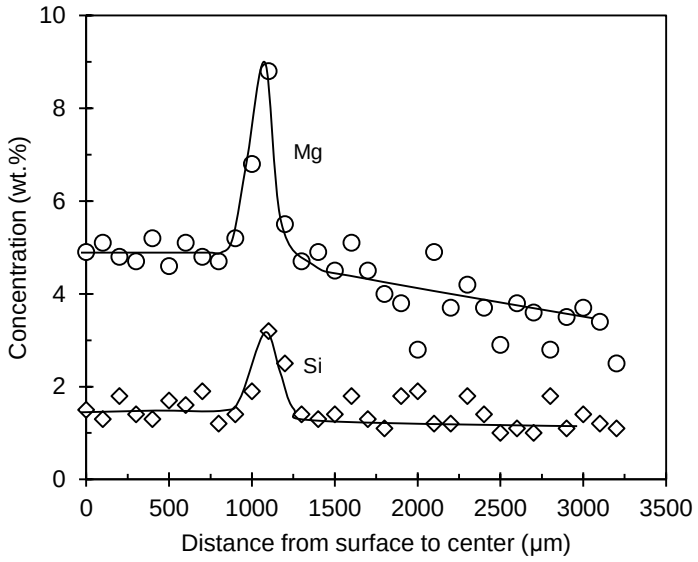


Figure 5.19 SEM/EDS analysis showing the concentration profile of Mg and Si on a section of die-cast ϕ6.4mm tensile specimen of the Al-5wt.%Mg-1.5wt.%Si-0.6wt.%Mn-0.2wt.%Ti alloy.

The composition profile shown in Figure 5.2 is an example of the variation in magnesium and silicon concentration from the surface to the centre of the Al-Mg-Si-Mn casting. The concentrations are consistent in the skin region with a general drop toward to the centre inside the band. For instance, the Mg concentration is close to the nominal composition of 5wt% in the skin region and gradually decreases to 3.8wt.% at the centre of the casting, whilst the Si concentration is also close to its nominal composition at 1.5wt.% in the skin region but slightly lower in the central region. The band zone is found to be enriched in Mg and Si to 8.8wt.% and 2.9wt.%, respectively. The peak of the solute enrichment in the band zone is much higher than the nominal composition in the alloy. The results confirm the segregation of the solute distribution on the cross section of the die castings. The drop in the solute content of Mg and Si from the surface to the centre as well as the peak in the band zone is unusual for conventional solidification. According to the phase diagram and Scheil equation, the composition profile would predict the solute content to increase from the surface to the centre of the casting if the solidification front progresses from the surface to the centre. The formation of central core is related to the solidification conditions and, consequently, has a very different history. However, the relative movement of melt at different parts is one of the most important reasons to form band zone during solidification [11, 61]. One can speculate that the outer region is a chill zone and the central is "backfill" from the runner during solidification to vary the microstructure.

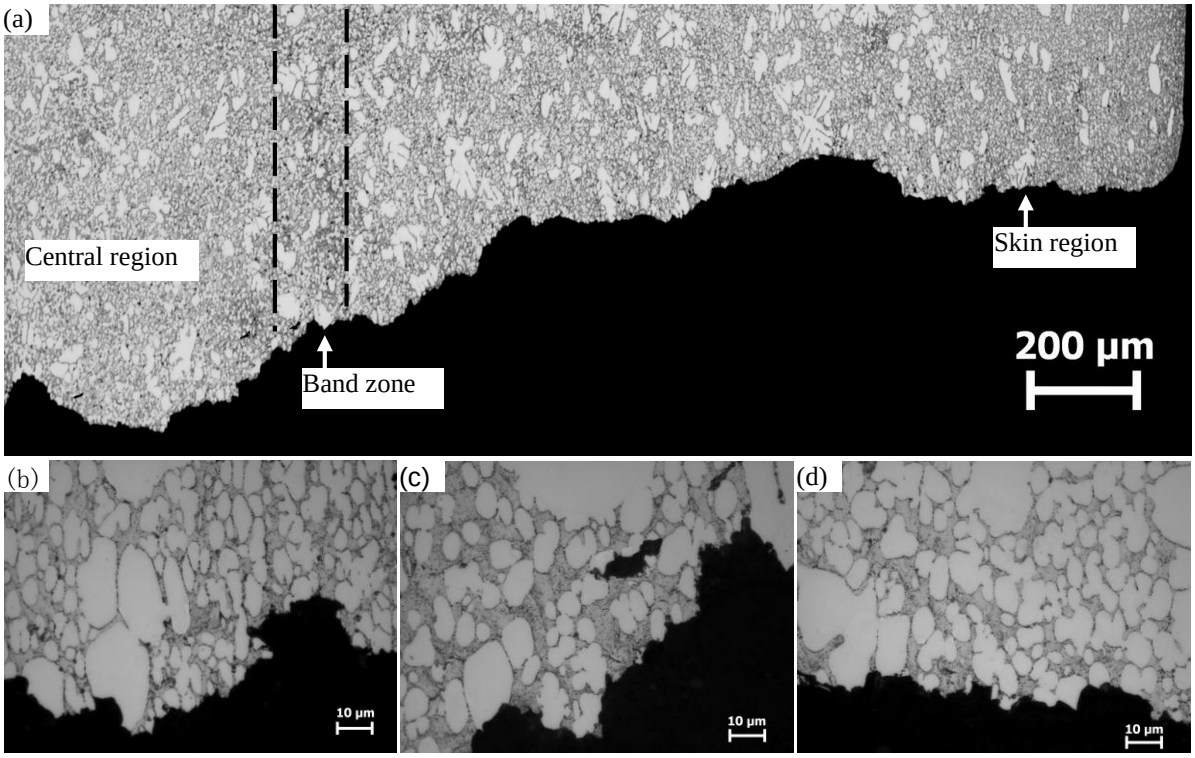


Figure 5.20 Optical micrographs showing the microstructure on a section perpendicular to the fractured surface of the Al-Mg-Si-Mn alloy, (a) over all microstructure, (b) the skin region, (c) the band zone, and (d) the central region.

In order to assess the effect of the non-uniform solute distribution on the mechanical properties of the die castings, a sample was sectioned perpendicularly to its fracture surface. Figure 5.3 shows the microstructure along the fractured surface in the skin region, band zone and central region. It is seen that the sample is uniformly elongated and no apparent neck is observed around the fractured surface. The primary α-Al grains are stretched towards the fractured surface. The micrographs in Figure 5.3 confirm that the fracture occurs mainly along the α-Al grain boundaries, and the fracture across the primary α-Al grains is also found in the skin region, band zone and central region. Meanwhile, a few subsurface pores in irregular shapes are observed close to the fractured surface in the band zone and the central region. This suggests that the cracking as the fracture source is likely initiated in the band zone and the central region under stress. The across sectional micrographs in Figure 5.3 also show that the fracture is a combination of grain-boundary separation and the cleavage fracture across primary α-Al grains.

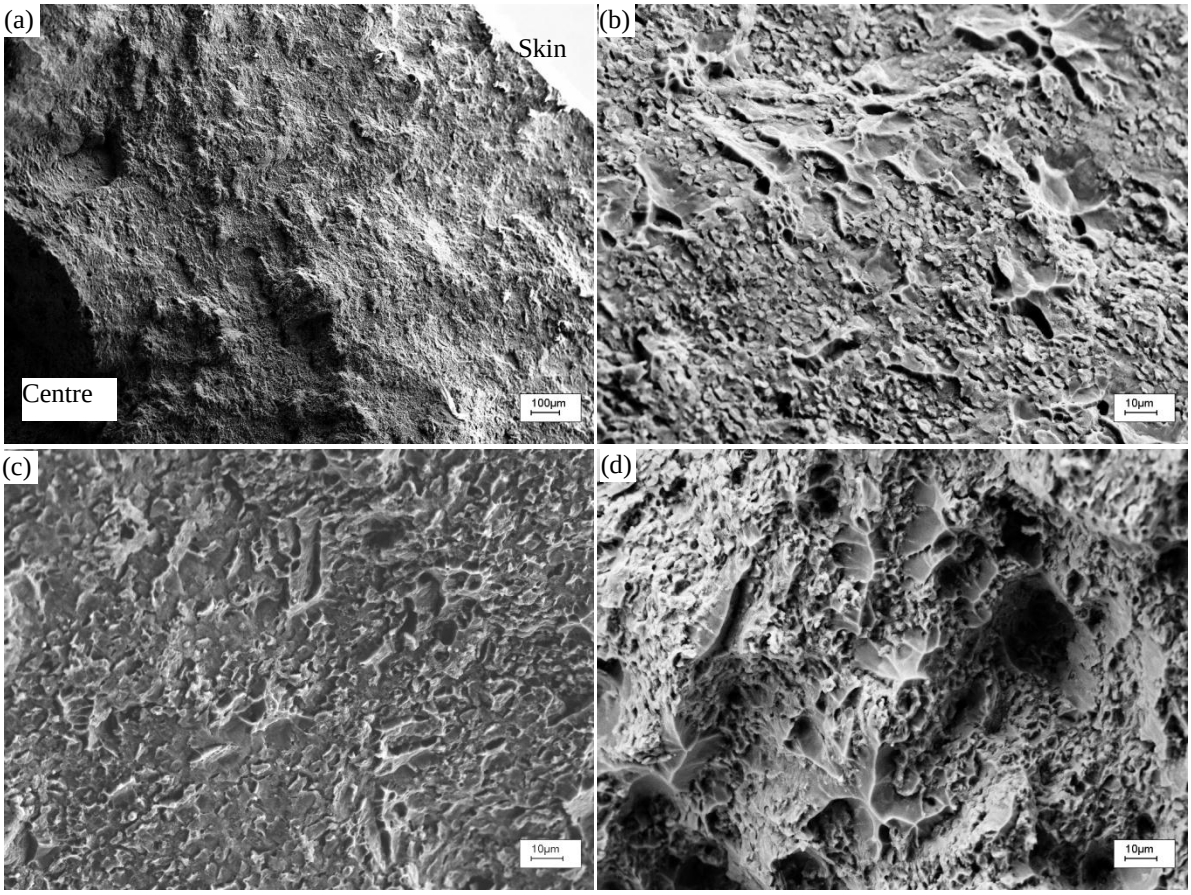


Figure 5.21 SEM images of the fractured surface of the Al-Mg-Si-Mn alloy, (a) overall fractograph from the skin to the centre of the tensile test bar, (b) the fractograph of the skin region, (c) the fractograph of the band zone, (d) the fractograph of the central region.

To confirm the detail, SEM fractographs of a sample fractured at an elongation of 18.4% with ultimate tensile strength of 302.5MPa are shown in Figure 5.4. In the fractographs, porosities are seen as the main defects in the die castings. The fractograph in Figure 5a shows that the fracture is relatively flat in the skin region, but coarse and uneven in the central region. The transition occurs in the band zone. However, there is no significant difference on the fracture morphology in the three regions. A large proportion of intergranular fracture around the fine primary α-Al grains, the cleavage fracture in the relatively large primary α-Al grains, and the decohesion between the $Mg_2Si$ phase and Al phase in the eutectic are observed as the main fracture mechanism in the three regions. The difference in the central region is that small dimpled rupture is also observed in the region. Therefore, the die casting of ductile Al-Mg-Si-Mn alloy exhibits a combination of brittle and ductile fracture. Although the solute-rich segregation in the band zone could initiate the cracking for fracture, the similar cracking is also

found in the central region. Therefore, the band zone is not significantly detrimental in terms of the fracture mechanism in the die-cast Al-Mg-Si-Mn alloy.

## 5.3 The Primary Phase Formed in the Shot Sleeve and in the Die Cavity

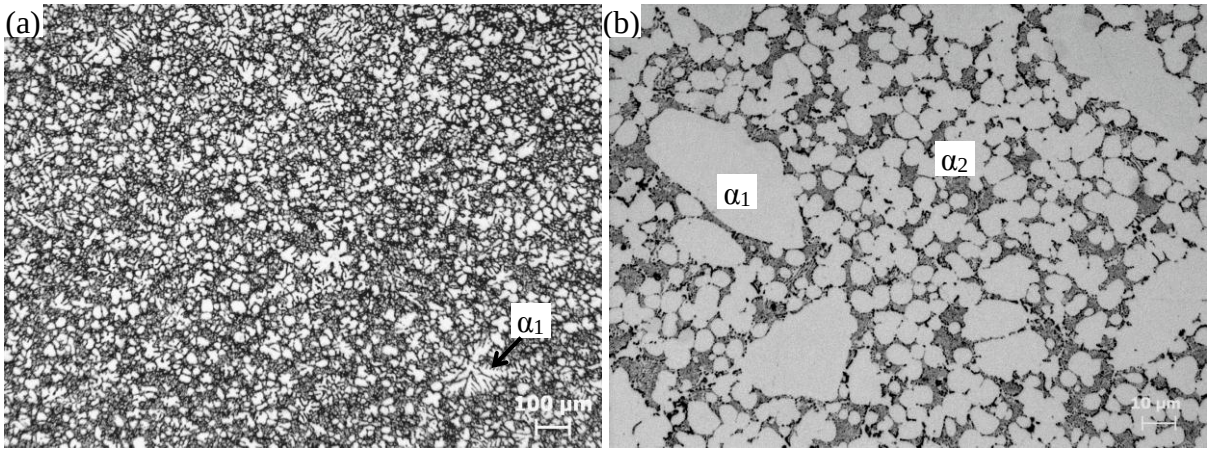


Figure 22.5 Microstructures of die-cast Al-5wt.%Mg-1.5wt.%Si-0.6wt.%Mn-0.2wt.%Ti alloy with a primary $\alpha_1$-Al phase of fs=19%, (a) low magnification image showing the distribution of the primary $\alpha_1$-Al phase, (b) high magnification image showing details of the morphology of the primary $\alpha_2$-Al phase solidified within the die cavity.

Figures 5.5 and 5.6 show the microstructures of the die-cast Al-Mg-Si-Mn alloy with different amounts and morphology of the primary α-Al phase. Two types of primary α-Al phase are seen in the matrix. One shows the morphology of dendrites or fragmented dendrites with a larger size (denoted as $\alpha_1$) and the other is fine globules (denoted as $\alpha_2$). During die casting, the solidification commences when the melt is poured into the shot sleeve. Because the cooling rate inside the shot sleeve is similar to that in gravity die casting, a cooling rate in the range of 20-80 K/s could be achieved [142], the solidification initiates from the nucleation of the α-Al crystals that subsequently grow dendritically in the shot sleeve. The primary α-Al dendrites are fragmented when the melt is injected into the die cavity through the ingate at a high speed, resulting in the formation of fragmented dendrites in the microstructure. Figures 5 and 6 also show the different amounts of the primary α-Al crystals solidified in the shot sleeve, which is determined by the pouring temperature, the rest time, and the temperature of the shot sleeve. Figure 5.7 shows the size distribution of the primary α-Al phase solidified in the shot sleeve, in which the grain size is between 15 and 100μm with a mean of 43μm. The distribution of the

primary α-Al phase shows a very close match to a Gaussian distribution, suggesting that the solidification in the die casting process is relatively consistent for the different amounts of primary α-Al phase.

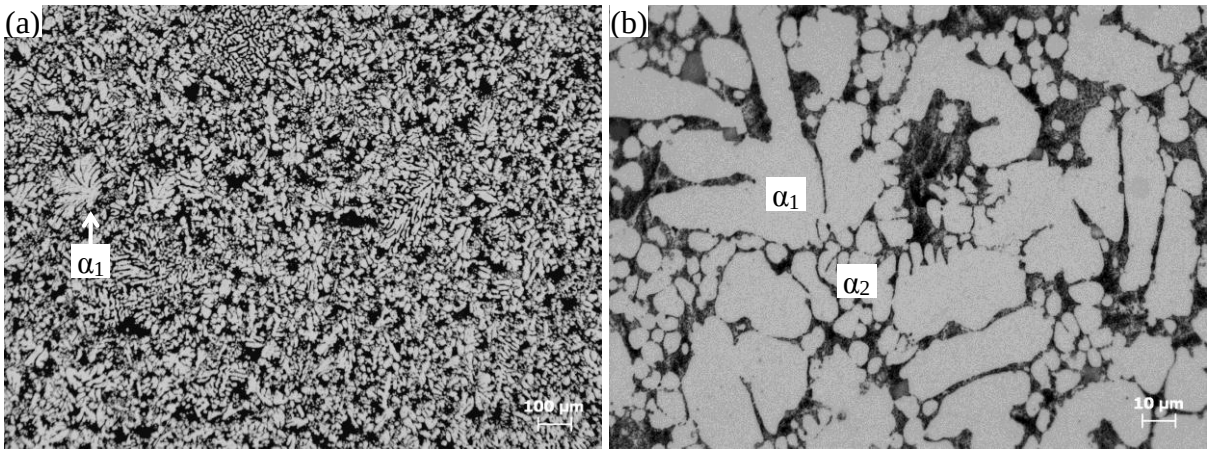


Figure 5.23 Microstructures of die-cast Al-5wt.%Mg-1.5wt.%Si-0.6wt.%Mn-0.2wt.%Ti alloy with a primary $\alpha_1$-Al phase of fs=32%, (a) low magnification image showing the distribution of the primary $\alpha_1$-Al phase, (b) high magnification image showing details of the morphology of the primary $\alpha_2$-Al phase solidified within the die cavity.

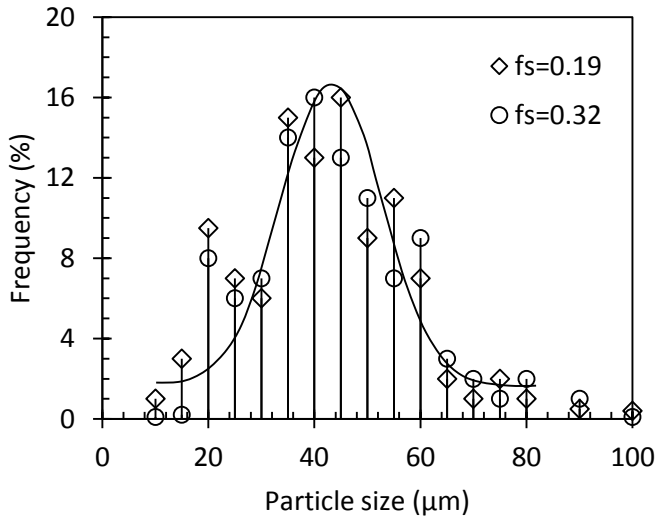


Figure 5.24 The distribution of the solid $\alpha_1$-Al phase solidified in the shot sleeve with a Gaussian distribution with a mean of 43.

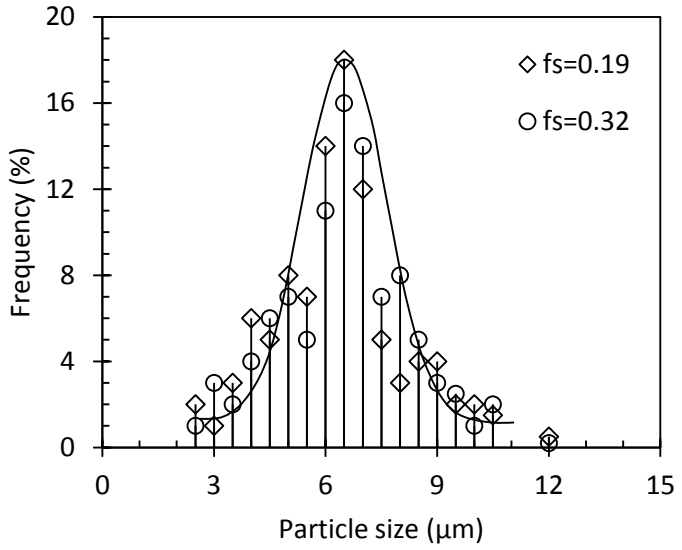


Figure 5.25. The distribution of the solid $\alpha_2$-Al phase solidified in the die cavity with a Gaussian distribution with a mean of 7.5.

When the melt is injected into the die cavity, the remnant liquid in the mixture that contain $\alpha_1$ phase starts to solidify immediately. As shown in Figures 5.5b and 5.6b, $\alpha_2$ phase shows a similar globular morphology, although the amount is at different levels. This suggests that spherical or globular growth occurs during the solidification inside the die cavity. The size distribution of $\alpha_2$ is shown in Figure 5.8, in which the grain size is between 3 and 12 μm and the average is 7.5μm. The distribution curve also matches a Gaussian distribution with a mean of 7.5. As the solidification inside the die cavity occurs under a high cooling rate, which is typically in the range of 400-500 K/s, the high cooling rate increases the nucleation rate and thus stable globular growth could occur for $\alpha_2$ (to be analysed in more details in the next section).

Figure 5.9 shows the relationship between the solid fractions of $\alpha_1$ and $\alpha_2$. For the given alloy, the amount of the primary α-Al phase is mainly determined by the composition. This means that the amount of $\alpha_1+\alpha_2$ is the same for a given composition, although the solidification could be divided into several stages. Therefore, as shown in Figure 5.9, the increase in the amount of $\alpha_1$ results in a decrease in the amount of $\alpha_2$. Figure 5.10 shows the mean grain size and the shape factor for the primary $\alpha_1$ and $\alpha_2$ aluminium phase. For $\alpha_1$, the mean grain size slightly increases and the shape factor slightly decreases with the increase of the volume fraction of $\alpha_1$.

This indicates that the dendritic growth is enhanced at the higher volume fraction of $\alpha_1$ in the shot sleeve. Therefore, the control of the solidification in the shot sleeve is critical to optimise the microstructure. On the other hand, the mean grain size and the shape factor of $\alpha_2$ are essentially the same regardless of the volume fraction. The mean grain size is at a level of 7.5μm and the shape factor is 0.75.

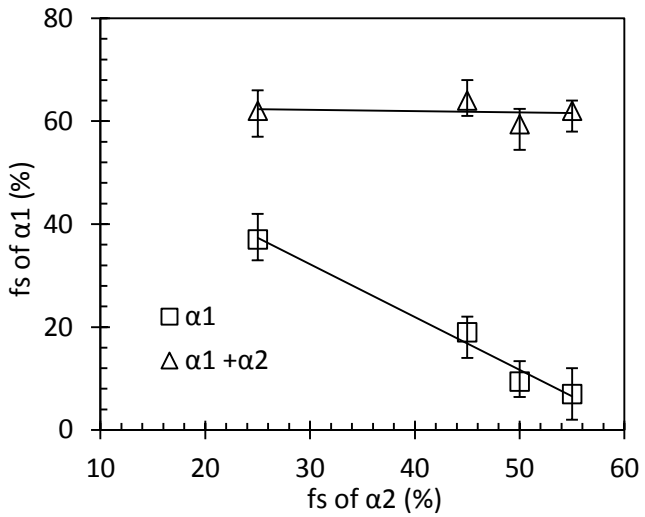


Figure 5.26 The relationship between the solid fraction of the α-Al phase solidified in the shot sleeve ($\alpha_1$) and that solidified in the die cavity ($\alpha_2$).

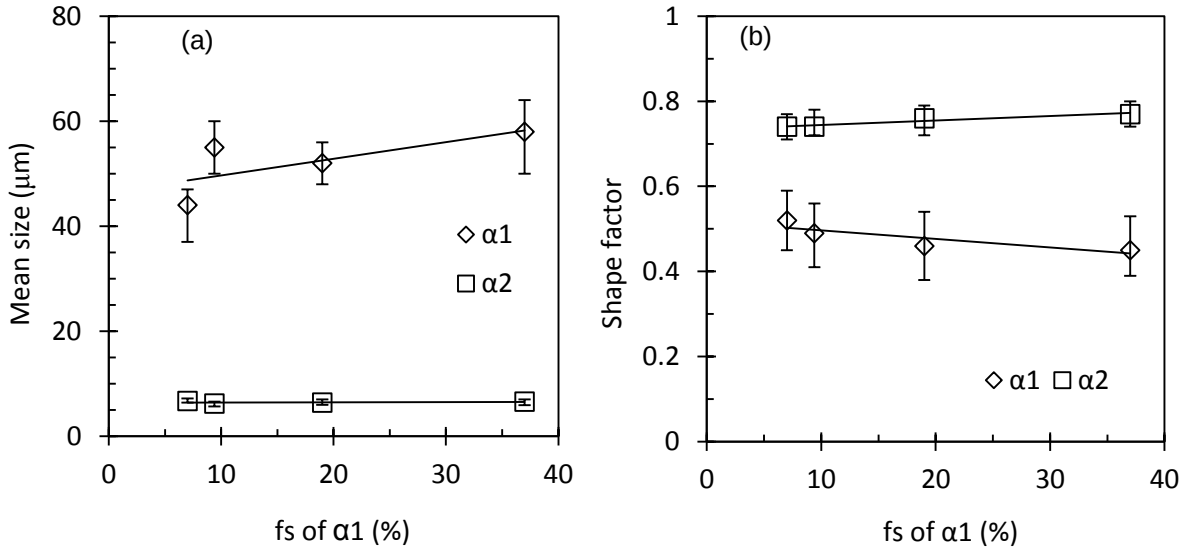


Figure 5.27 The mean size (a) and the shape factor (b) of the primary α-Al phase solidified in the shot sleeve ($\alpha_1$) and in the die cavity ($\alpha_2$) as a function of the solid fraction of $\alpha_1$.

SEM observation of an etched sample was carried out in order to assess the morphology of the primary α-Al phase solidified inside the die cavity. As shown in Figure 11, the boundaries of the fine primary α-Al phase are clear. This implies that many of the globular α-Al phase formed in the die cavity are likely to be individual ones. The solidification of each globule could be initiated from an individual nuclei and grow independently. To further confirm the solidification behaviour, quantitive EDS analysis was performed on the different samples. Figure 5.12 gives the SEM/EDS results of the solid solubility of Mg and Si in both $\alpha_1$ and $\alpha_2$ primary phase as a function of the distance from the grain edge. The average Mg concentrations are 4.5±0.45 and 4.5±0.24wt.% for $\alpha_1$ and $\alpha_2$, respectively. Although it is statistically overlapped, the slightly higher average of Mg concentration in the fine $\alpha_2$ grains reflects the enrichment of the solute element in the remnant liquid inside the die cavity. In addition, according to the equilibrium Al-Mg-Si phase diagram [ 143 ], the lower solidification temperature for the remnant liquid would result in a higher Mg content in the $\alpha_2$ solid solution phase. Meanwhile, the concentration of Si (0.5±0.12 wt. %) in $\alpha_1$ and $\alpha_2$ aluminium phase does not show much variation. One important feature in the EDS analysis shown in Figure 5.13 is that there is hardly any Mg and Si content gradient across $\alpha_1$ and $\alpha_2$ aluminium phase. It is worth emphasising that the concentration variation across the tensile sample, as shown in Figure 5.2, is a phenomenon of macrosegregation that is related to the mould filling process, but the concentration profile in Figure 5.12 is for individual primary α-Al grain regardless of the position in the sample.

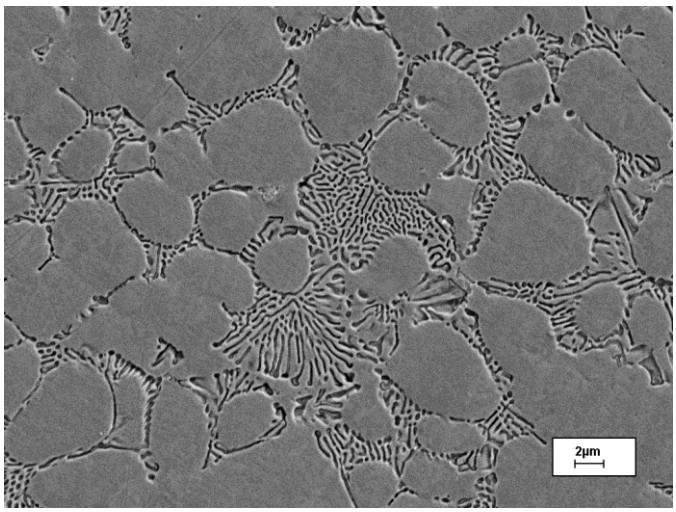


Figure 5.28 The structure of fine $\alpha_2$-Al phase solidified inside the die cavity. The boundaries of the $\alpha_2$-Al phase are well defined by the grain boundaries and the eutectic Al-$Mg_2Si$ phases.

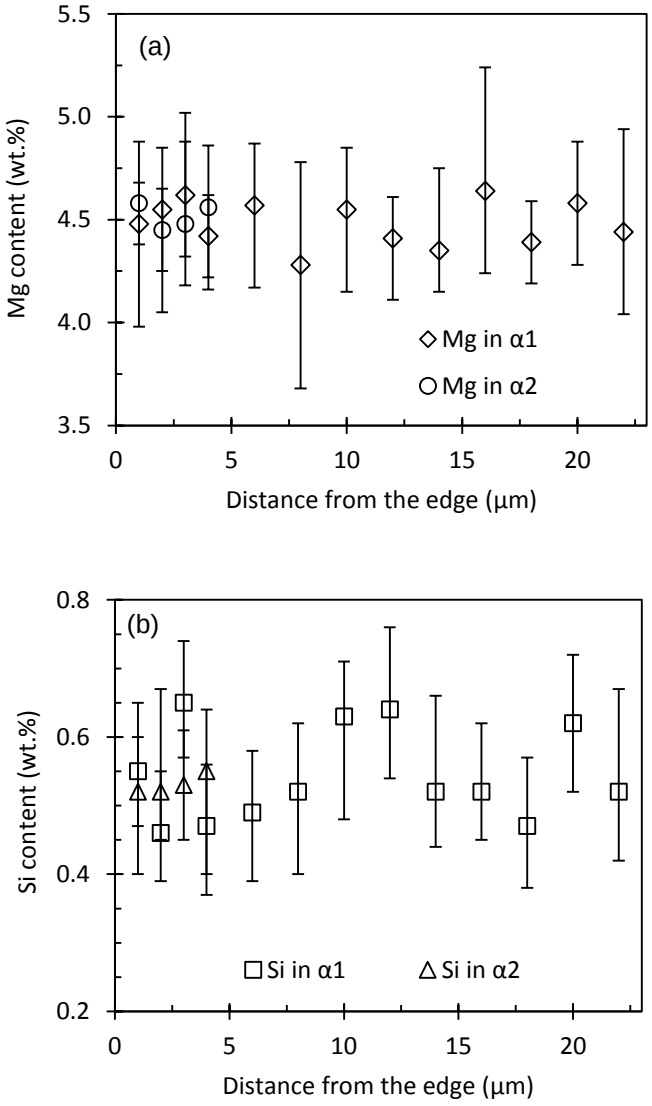


Figure 5.29 SEM/EDS results showing (a) the solid solubility of Mg and (b) the solid solubility of Si in the primary α-Al phase solidified in the die cavity ($\alpha_2$) and in the shot sleeve ($\alpha_1$).

## 5.4 Eutectic Al-$Mg_2Si$ phases

The morphology of the eutectic Al-$Mg_2Si$ phases is shown in Figure 5.13. EDS analysis confirm that the lamellar microstructure of the eutectic consists of α-Al phase and $Mg_2Si$ phase. The size of the eutectic cells is about 10μm, in which the lamellar α-Al phase is 0.41μm in thickness. SEM observation on a deep-etched sample reveals that the eutectic $Mg_2Si$ phase

exhibits fine lamellae morphology and branching of the flakes is frequently observed. This suggests that the solidification follows a conventional path under a high cooling rate. There is no thick platelet $Mg_2Si$ phase observed in the samples. The amount of eutectic largely depends on the composition of the alloy. An increased level of Mg and Si in the alloy creates more eutectic Al-$Mg_2Si$ phases, which would cause an increase in strength and a decrease in ductility.

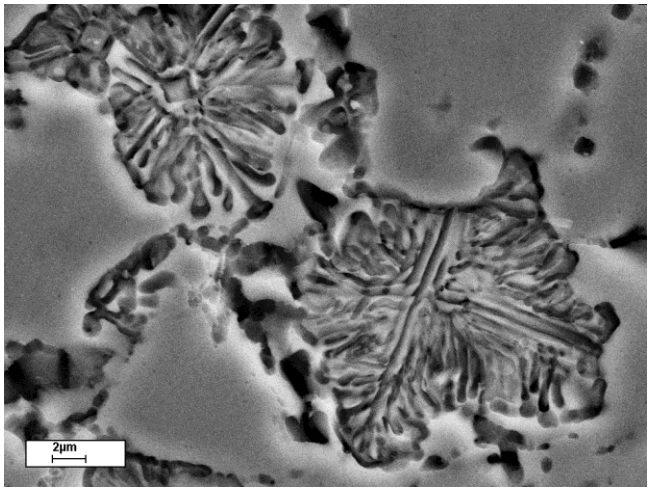


Figure 5.30 SEM micrograph, taken from a deep-etched Al-5wt.%Mg-1.5wt.%Si-0.6wt.%Mn-0.2wt.%Ti die-cast specimen, showing the morphology of the fine lamellar eutectic Al-Mg2Si phases.

## 5.5 Intermetallics

In the Al-Mg-Si-Mn alloy, Mn is kept at a level of 0.6wt.% and the Fe is controlled below 0.25wt.%. Figure 5.14a shows the intermetallic phase in the matrix (bright phase). The intermetallics exhibit a compact morphology with the size being smaller than 2μm and are located on the boundary between the primary α-Al grains or between the eutectic cells and the primary α-Al grains. This suggests that the intermetallics are formed in the die cavity, rather than in the shot sleeve. The EDS analysis shown in Figure 5.15b reveals that the compact intermetallic compounds consist of Al, Mn, Fe, Si with the composition being quantified to be 1.6at.%Si, 3.9at.%Fe and 2.3at.%Mn, most likely the α-AlFeMnSi, rather than the β-AlFeSi phase.

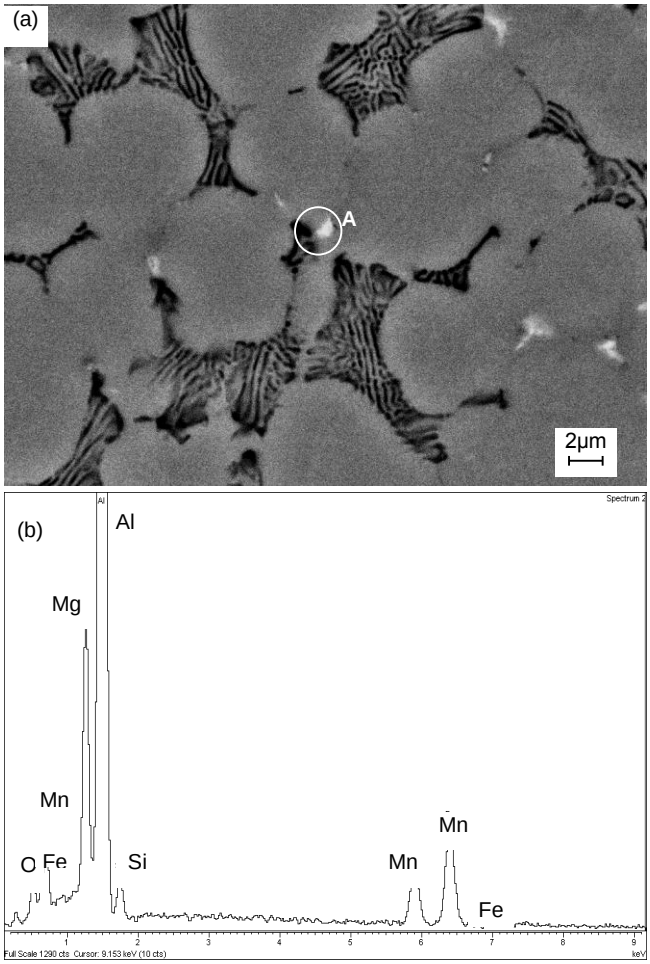


Figure 5.31 (a) Backscattered SEM micrograph showing the distribution of intermetallics along grain boundaries in Al-5wt.%Mg-1.5wt.%Si-0.6wt.%Mn-0.2wt.%Ti die-cast alloy, and (b) EDS spectrum showing the elements in particle A include Al, Mn, Si, Fe.

## 5.6 The Growth of Primary α-Al Phase

Solidification in HPDC process commences when the melt is poured into the shot sleeve. Due to the relatively low temperature of the shot sleeve, the melt in contact with the shot sleeve is immediately cooled below its liquidus temperature. Heterogeneous nucleation occurs in the melt and grows to form α-Al dendrites ($\alpha_1$). The dendrites are then partially fragmented while passing the narrow ingate with high speed and turbulent flow during the die filling process.

Because of the temperature variation and high flow rate during die filling, the Stoke's motion in the gravity field and Marangoni motion in the non-uniform temperature field promote the solidified primary phase $\alpha_1$ to segregate into the middle of casting section, which leads to the formation of non-uniform microstructure in as-cast condition [144]. Marangoni motion is proportional to the temperature gradient and therefore it is determined by the melt temperature and the die temperature. Stoke's motion is proportional to the square of particle size and reversely proportional to the viscosity of the liquid matrix. Therefore, Stoke's motion becomes significant for large particles and in a liquid with low viscosity.

On the other hand, the high turbulent flow promotes the temperature uniformity in the melt throughout the die cavity. With a high cooling rate provided by the metallic die block, nucleation inside the die cavity is expected to take place throughout the entire volume of the remaining liquid. The numerous nuclei compete growing until solidification finishes under high cooling rate inside the die cavity. The primary α-Al grains formed inside the die cavity ($\alpha_2$) have been observed to be 7.5μm in size, indicating that the fine primary α-Al grains could still be within a spherical growth morphology because the dendritic morphology that is established through unstable growth may have not yet developed. This can be explained by applying the Mullins-Sekerka growth theory [145].

The Mullins and Sekerka growth theory calculates the point where the spherical shape of crystal growing from a melt becomes morphologically unstable when its size exceeds a critical value $R_c$ (in μm)[145]:

$$R_c = \frac{2\Gamma_T(7+4k_s/k_l)}{(T_m-T_\infty)/T_m} = \frac{2(\gamma_{SL}/L_v)(7+4k_s/k_l)}{\Delta T/T_m} \quad (5.1)$$

where $T_m$ and $T_\infty$ are the melting point and melt temperature, $k_s$ and $k_l$ are thermal conductivity of liquid and solid Al at the melting point temperature, $\gamma_{SL}$ is the interfacial energy at the S/L interface, and $L_v$ the latent heat of fusion per unit volume of the solid.

It needs to be noted that the above stability equation was derived from the basic heat flow where consideration of the effect of the solute was not taken into account. However, Mullins and Sekerka [145] indicated that the stability criterion for diffusion-controlled growth of a sphere of fixed composition in a supersaturated solution is completely analogous to that of Equation (5.1) if no heat flows inside the sphere [146]. In addition, the velocity at the interface

calculated from heat flow considerations equals that calculated from mass diffusion considerations at local interface equilibrium [145, 146]. When considering the instability problem of a growing interface in an alloy melt, for instability to occur, constitutional supercooling must exceed a specified value [147,148]. Then Equation (5.1) is applicable to the spherical growth of a crystal in a supercooled multi-component alloy.

According to this stability criterion for spherical growth in a uniformly supercooled melt, one can predict that all solid spheres undergoing thermally controlled growth are morphologically stable by substituting respective values in Table 5.1 [149,150] for $k_l, k_s, \gamma_{SL}, L_v$ and $T_m$ into Equation (5.1) giving:

$$R_c = \frac{5.12}{\Delta T} \qquad (5.2)$$

Due to the unavailability of some thermal and physical properties for the particular Al-5Mg-1.5Si-0.6Mn-0.2Ti alloy in this work, the relevant data of pure Al were used in the calculation of equation (5.1). As shown in Figure 5.15, the calculation indicates that the critical radius for spherical growth of aluminium crystal, $R_c$, is quite sensitive to the undercooling for spherical growth. For example, when $\Delta$T=1K, all spherical aluminium crystals less than 10.24μm in size will be stable for spherical growth. By contrast, when $\Delta$T=0.1K, all grains smaller than 102.4μm will be spherically stable. It is obvious that a smaller undercooling will promote the formation of larger spherical crystals during solidification.

Table 5.1.Thermochemical and physical properties of solid and liquid aluminium at melting point

| Name | Symbol | Unit | Value | Refs. |
|---|---|---|---|---|
| Melting point | $T_m$ | K | 933.5 | [149] |
| Density of liquid aluminium at $T_m$ | $\rho_L$ | g/cm$^3$ | 2.385 | [149] |
| Volume change from solid to liquid at $T_m$ | $\Delta V_m$ | | 6.5% | [149] |
| Density of solid aluminium at $T_m$ | $\rho_S$ | g/cm$^3$ | 2.540* | |
| Thermal conductivity of liquid aluminium at $T_m$ | $k_L$ | W/m/K | 94.03 | [149] |
| Thermal conductivity of solid aluminium at $T_m$ | $k_S$ | W/m/K | 238** | |
| Latent heat of fusion per mole of aluminium | $L_m$ | J/mol | $1.047\times10^4$ | [149] |
| Latent heat of fusion per unit volume of aluminium | $L_v$ | J/m$^3$ | $9.857\times10^{8}$*** | [149] |
| Solid–liquid interfacial free energy of aluminium at $T_m$ | $\gamma_{SL}$ | J/m$^2$ | $158\times10^{-3}$ | [150] |

* Calculated according to $\Delta V_m$ and $\rho_L$ at melting point $T_m$.

** The value of $k_S$ is not available. The value given here is for 673 K.

*** Calculated from $L_m/k_S$.

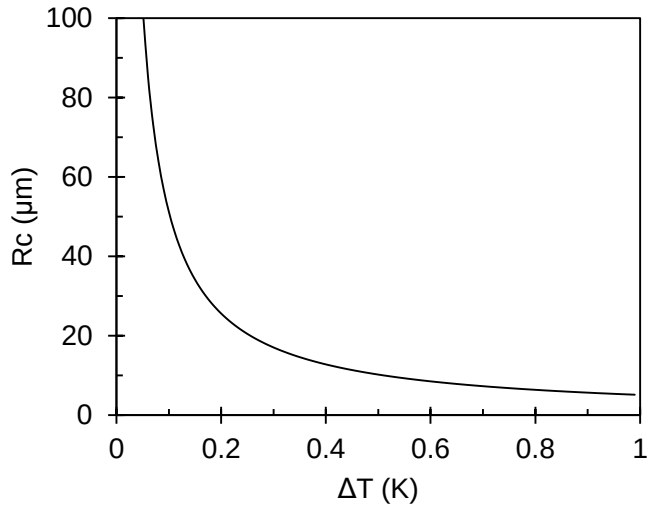


Figure 5.32 The critical radius $R_c$ for the spherical growth of aluminium crystals as a function of undercooling according to the Mullins-Sekerka growth theory.

For Al-based alloy, Burden and Hunt [151,152] measured the undercooling of an Al-Cu alloy. They found that the undercooling was 1-2K in the growth velocity range of 1-300 μm/s and the temperature gradient <10 K/cm during solidification of Al-2wt.% Cu alloy. As it is understandably difficult to directly measure the undercooling in the die casting process, we need to postulate the undercooling in the die cavity on the basis of the similarity of the physical properties during solidification of Al-Cu and Al-Mg alloys [153]. If we assume undercooling is at a similar level of 1-2 K during solidification in the die cavity, the stable spherical growth of α-Al crystals will between 5.12 to 10.24 μm in diameter according to Mullins-Sekerka stability theory. In fact, the measured α-Al grain size is 7.5 μm formed in the die cavity, indicating that the α-Al grain is close to its spherical growth limit. The microstructures also show large grains with a perturbed periphery. These might be over the critical size and have just lost their spherical morphology.

This can be further examined according to similar experimental results. Bower et al. [154] have shown that the secondary dendrite arm spacing DAS varies approximately as the cube root of the local solidification time over a wide range of solidification conditions for Al-4.5 wt.% Cu alloy. We can, therefore, approximately estimate the local solidification time for the α-Al in the Al-Mg-Si-Mn alloy. As the average grain size has been measured to be 7.5 μm, it gives a local solidification time of about 1s according to the measurement results in ref. [154]. This gives a growth rate of 3.9μm/s. According to Burden and Hunt [154, 155], an undercooling is expected to be 1.3K at this growth rate. The Mullins-Sekerka critical value can then be calculated at 7.9 μm, which is close to but larger than the average size measured in this study. As a result, grain growth during solidification within the die cavity can be within the stable growth regime and form a globular microstructure.

It needs to be noted that the growth of primary α-Al grains may be altered when the processing conditions change during solidification. For example, when the cooling rate decreases and the wall thickness of the casting increases, the undercooling becomes smaller and thus promotes the formation of larger spherical grains and vice versa. It needs to emphasise that the growth velocities of the primary aluminium grains described above is speculative on the basis of previous experimental results. Therefore, the calculated results may not be very accurate. The grains could have stopped growing as primary phase because of the occurrence of eutectic solidification at the given time. However, the results provide good indication to understand the solidification process in high pressure die casting.

The results from Mullins-Sekerka growth theory can also be used to explain the formation of the dendritic α-Al phase formed in the shot sleeve ($\alpha_1$). The melt usually stays in the shot sleeve for 2 to 3 seconds from the time of pouring into the shot sleeve to the time of injection through the ingate of the casting. If it is assumed that a similar growth velocity of 3.9 μm/s exists for the α-Al phase, the resultant spherical growth of the primary α-Al grains is 23.4μm. In fact, the growth rate is smaller than 3.9μm/s because the solidification in the shot sleeve is similar to gravity die casting with relatively lower cooling rates. Therefore, the resultant spherical growth of the primary α-Al grains formed in the shot sleeve is less than 23.4μm. However, the measured size of the primary α-Al phase is 43μm, which is much larger than the critical size predicted by the Mullins-Sekerka theory. Therefore, the grains will lose their stability for spherical growth and form a dendritic morphology.

## 5.7 Formation of the Eutectic Al-$Mg_2Si$ phases

The formation of the intergranular eutectic $Mg_2Si$ phase between the α-Al phases marks the completion of solidification in the HPDC process. The faceted $Mg_2Si$ phase can have a diversity of morphologies such as rod-like, crossed and rooftop-like, which has the same preferred [100] growth direction [155]. In the present study, the formation of fine eutectic Al-$Mg_2Si$ lamellae is attributed to the high local cooling rate. Because the solidification inside the die cavity includes the evolution of primary α-Al grains that may divide the remnant liquid into very small pockets in between. Therefore, the eutectic reaction is confined to the small intergranular areas. The high local cooling rate is then able to contribute to the formation of the fine eutectic morphology. According to the equilibrium Al-Mg-Si phase diagram, the formation of the eutectic Al-$Mg_2Si$ phases is at a temperature close to 869K (595C) when Mg is 5wt.%. This is higher than the eutectic temperature of Al-Mg binary alloy at 725K (451C). This confirms that the addition of Si into Al-Mg alloy reduces the solidification range and is beneficial for die casting which requires a narrow solidification range.

The direct measurement of the as-cast samples shows that the average eutectic spacing $\lambda$ of the eutectic α-Al phase is 0.41μm in the Al-Mg-Si-Mn alloy. According to the Jackson-Hunt theory of eutectic growth [156], the relationship between eutectic spacing $\lambda$ and growth velocity $V$ follows

$$\lambda^2 V = constant \quad (5.3)$$

Although the Jackson-Hunt theory is generally suitable for most eutectic reactions, the determination of the constant is still a challenge and the results vary from one to another. The constant was measured to be $\lambda\sqrt{V}$ = 25.2±3.2 μm$^{3/2}$s$^{-1/2}$ by Grugel and Kurz for Al-Si alloys with 6-12wt.%Si [157]. The measurement carried out by Böyük *et al.* [158] for Al–11.1wt.%Si–4.2wt.%Ni eutectic alloy gave the dependency of $\lambda_{Si}$ and $\lambda_{Al_3Ni}$ on the values of V to be $\lambda_{Si}$=12.58V$^{-0.50}$, $\lambda_{Al_3Ni}$=7.94V$^{-0.47}$. The $\lambda^2 V$ value equals to 30.609 μm$^3$/s obtained by Kaya [159] and 19.6 μm$^3$/s by Whelan and Haworth [160] for Bi-Cd eutectics, but equals to 21.1 μm$^3$/s by Trivedi *et al.* [161], 21.8 μm$^3$/s by Moore and Elliot [162], and 23.7 μm$^3$/s by Cadirli *et al.* [163] for Pb–Cd eutectic system. Kaya *et al.* [159] obtained $\lambda^2 V$=39.059 μm$^3$/s for Al-Cu eutectic while Cadirli *et al.* [164] provided a value of 156 μm$^3$/s for a similar alloy.

Because of the lack of data for the Al-Mg-Si-Mn alloy, we could take the constant for a range of 15-30 μm$^3$/s in order to get an approximate solution. If $\lambda^2 V$ = 15 to 30 μm$^3$/s, as λ is measured at 0.41μm, we can have *V*=89 to 178 μm/s. This means that very fast solidification has occurred in the die cavity during solidification. However, the growth rate calculated for the eutectic Al-$Mg_2Si$ phases is much larger than that of the primary α-Al phase. This can be attributed to the estimation of the constant. If we calculate the constant in Eq. (5.3) by using the growth rate of 3.9 μm/s obtained from the primary α-Al phase, $\lambda^2 V$ is 0.656 μm$^3$/s. This constant is smaller than the data reported in ref. [157-164]. It has to be pointed out that the constant $\lambda^2 V$ for a specific eutectic was usually obtained under controlled and constrained conditions, e.g., by directional growth, and that for the eutectic growing into an undercooled melts the Jackson-Hunt model might not be valid, i.e., $\lambda^2 V$ might not be constant anymore. It is true that, as indicated by the TMK model [165,166], the $\lambda^2 V$ is deviated from a constant value when the undercooling is very large and growth rate is very high. In our work, however, this deviation is believed not to be very much because the growth rate and undercooling during a HPDC process are still low enough compared to the cases analysed in the TMK model. It is therefore that the approximately estimated growth velocity from the Jackson-Hunt model here is reasonable.

## 5.8 Solidification Behaviour

In the Al-Mg-Si alloy with experimental compositions, the solidification process is critical for the formation of microstructure in the castings. The solidification process can be basically divided into three stages, during which the primary α-Al phase, Fe-bearing intermetallic phase and the eutectic Al+$Mg_2Si$ phase are formed sequentially from the melt.

With the decrease of melt temperature, α-Al is the first solid phase formed. Once the melt is loaded into the shot sleeve, the low temperature of the shot sleeve will chill the melt immediately to a temperature below its liquidus and result in solidification. The situation is somehow similar to gravity casting. Therefore, the solidification follows conventional approach to create dendritic microstructure. However, the solidification in the shot sleeve is terminated when the piston moves forward to push the alloy into the die cavity. At that moment, the mixture of solid and liquid is pushed forward slowly at the initial stage and quickly at the end stage. Before filling into the die cavity, the melt needs to pass the ingate (Figure. 5.1) where the melt will experience a high shear and high velocity. During this process, the solid dendrites in the melt can be fragmented partially or completely. When the melt fills the die cavity under a high velocity, the temperature within the melt is uniformed and no superheat exists in the remnant liquid. The heat transfer between the melt and the die block is also enhanced under pressure. The solidification inside the die cavity is under a high cooling rate, during which the heterogeneous nucleation is enhanced and therefore the primary α-Al phase cannot grow up to a full dendritic morphology before the completion of solidification. Consequently, the primary α-Al phase formed in the die cavity is much smaller than that formed in the shot sleeve (Figure 5.10). Two types of primary α-Al phase are easily identified by the morphology and size. In the die casting process, the pouring temperature, the resting time in the shot sleeve, and the temperature of shot sleeve and die block are important factors to affect the formation of the primary α-Al phase.

With the progress of solidification, the precipitation of α-Al phase consumes a large amount of Al in the melt and thus the solute is enriched in the remnant liquid. The enrichment of Fe, Mn and Si is easily accumulated in the interdendritic area as diffusion limitation. Consequently, the reaction for the formation of Fe-bearing phase occurs in the interdendritic region (Figure 5.11). There are several types of Fe-bearing intermetallic phases that can be formed in the

solidification of aluminium alloy. The important intermetallics in cast alloys are the hexagonal α-AlFeMnSi and the monoclinic β-AlFeSi [167]. The α-AlFeMnSi is usually in a compact morphology with high symmetry crystal structure and the β-AlFeSi is characterised by a long needle shape with low symmetry crystal structure. Obviously, the α-AlFeMnSi phase is preferable due to its less detrimental effect on the mechanical properties. The conventional metallurgical solutions to eliminate the formation of primary β-AlFeSi compounds include to limit the Fe content in the alloy, or to modify the crystal structures of β-AlFeSi compounds into α-AlFeMnSi compounds by increasing Mn/Fe ratio. However, higher amounts of Mn in aluminium melt lead to the formation of sludge in castings and increase the deleterious effect on their machinability [168, 169]. Therefore, the amount of Mn content should be controlled appropriately. Several formats have been reported for the α-AlFeMnSi compounds. Zakharov *et al.* [170] found a stoichiometry of $Al_{16}(Fe,Mn)Si_3$ for the α-AlFeMnSi phase in an alloy with 10 to 14wt.%Si, 0 to 4wt.% Fe and Mn. Devignon *et al.* [171] reported that the equilibrium compositions of the quaternary α-AlFeMnSi phase can contain 72.7 to 74.7at-% Al, 9.1 to 13.7at-%Fe, 2.8 to 5.7at-%Mn, and 9.5 to 11.5at-%Si, which exhibits the $Al_{15}(Fe,Mn)_3Si_2$ stoichiometry. This is based on Fe substitution of the Mn sublattice sites of the $Al_{15}Mn_3Si_2$ lattice, leading to idealised Al and Si contents of 75at-% and 10at-% respectively. According to the discussion by Fang *et al.* [98], the stoichiometry of the quaternary α-AlFeMnSi phase for Al-Si based alloys is best described by $Al_{15}(Fe,Mn)_3Si_2$, with the crystal structure of the ternary α-AlMnSi ($Al_{15}Mn_3Si_2$). In current study, the EDS analysis and morphology examination for the alloy confirms that the intermetallic phase is α-AlFeMnSi. As there is limited literature on the detail of the intermetallic phase in Al alloys with high Mg content, it needs more investigations to reveal its origins. With regards to the measured Mg in the EDS results, it is doubtful that a measure error may exist because the size of α-AlFeMnSi is too small in the sample which causes the reflection of back materials in the EDS measurement. It needs to be clarified that one may think the Fe-bearing phase is formed in the shot sleeve or even before the formation of primary α-Al phase. If this is true, the intermetallic phase should form a large grain size and/or dendritic morphology because of the relatively low cooling rate in the shot sleeve. The size, morphology and the distribution of intermetallics suggest that it is formed in the die cavity prior to the eutectic solidification.

The eutectic solidification forms fine eutectic cells with lamellar morphology of $Mg_2Si$ phase and α-Al phase. The high cooling rate results in the formation of fine eutectic cells that are

distributed uniformly in the matrix (Figure 5.11). The separated eutectic cells are beneficial for the mechanical properties of die-cast alloy, especially for ductility.

## 5.9 Summary

(1) In the high pressure die casting of ductile aluminium alloys, solidification commences with the formation of primary α-Al phase in the shot sleeve and is completed in the die cavity. The primary α-Al phase formed in the shot sleeve is characterized by the dendrites and fragmented dendrites with the size range from 15 to 100μm and an average of 43μm. The primary α-Al phase formed in the die cavity is characterized by fine globular grains with an average of 7.5μm in size. Solidification inside the die cavity is also responsible for the formation of the lamellar Eutectic and the Fe-rich intermetallic. The size of the eutectic cells is about 10μm, in which the lamellar α-Al phase is 0.41μm in thickness.

(2) The intermetallic compounds exhibit a compact morphology with a size smaller than 2μm and are located at the boundaries between the primary α-Al grains or between eutectic cells and the primary α-Al grains. The intermetallic contains 1.62at.%Si, 3.94at.%Fe and 2.31at.%Mn, suggesting that it is most likely the α-AlFeMnSi phase.

(3) A solute enriched circular band is always observed parallel to the surface of the casting. The band zone separates the outer skin from the central region of the casting. The solute concentration is consistent in the skin region and a general drop toward to the centre inside the band for Mg and Si. The peak of solute enrichment in the band zone is much higher than the nominal composition of the alloy. However, the die casting exhibits a combination of brittle and ductile fracture. There is no significant difference on the fracture morphology in the three regions. Therefore, the band zone is not significantly detrimental in terms of the fracture mechanism in the die casting.

(4) The stability criterion developed by Mullins and Sekerka for spherical growth can be used to provide a reasonable explanation for the difference in morphology of the primary α-Al phase solidified in the shot sleeve and in the die cavity. The solidification of the α-Al phase inside the die cavity has completed before the spherical grains begin to lose their stability, but the grains in the shot sleeve exceed the limit of spherical growth and, therefore, exhibit a dendritic morphology.

(5) The Jackson-Hunt theory can be used to estimate the growth rate of eutectic Al-$Mg_2Si$ phases in high pressure die casting process, and the results indicate that a fast solidification rate occurs in the die cavity. However, the growth rate of the aluminium phase in eutectic solidification calculated using the Jackson-Hunt theory is much larger than the growth rate of the primary α-Al phase calculated using the Mullins and Sekerka theory.

# Chapter 6
# Effect of Iron on the Microstructure and Mechanical Properties of the Alloy

## 6.1 Introduction

In this Chapter, the effect of iron on the microstructure and mechanical properties of the Al-Mg-Si die-cast alloys with different Mn concentrations is investigated. The study focuses on the effect of Mn and Fe on the morphology, size and distribution of various Fe-rich compounds in the Al-Mg-Si alloy produced by HPDC process. The mechanical properties of yield strength, ultimate tensile strength and elongation are assessed with different Fe and Mn contents. The role of alloy chemistry on the effect of Fe and Mn is investigated by CALPHAD modelling of multi-component Al-Mg-Si-Mn-Fe and Al-Mg-Si-Fe systems. The thermodynamic modelling and the experimental findings of the Fe-rich intermetallic compounds were studied with respect to the role of Mn on combating the detrimental effect of Fe in the Al-Mg-Si alloy. The discussions are focused on the phase formation of different Fe-rich intermetallic phases and the relationship between Fe-rich compounds and mechanical properties of the die-cast Al-Mg-Si alloys.

Table 6.2 Compositions of die-cast Al-Mg-Si alloys used in experiments (wt.%).

| Alloy | Si | Fe | Mn | Mg | Ti | Zn | Others | Al |
|---|---|---|---|---|---|---|---|---|
| A | 2.2±0.08 | varied* | 0.541±0.05 | 6.2±0.08 | 0.17±0.04 | 0.012±0.004 | <0.03 | bal. |
| B | 1.9±0.07 | varied† | 0.023±0.04 | 5.6±0.09 | 0.15±0.04 | 0.013±0.004 | <0.03 | bal. |

* Fe contents were measured to be 0.214, 0.389, 0.623, 0.841, 1.243, 1.490, 1.861, and 2.482.

† Fe contents were measured to be 0.086, 0.414, 0.634, 0.911, 1.188, 1.420, 1.542, and 1.821, 2.453.

Two alloys were made according to the experimental method described in Chapter 3. The composition of each alloy was obtained from an optical mass spectroscopy, in which at least five spark analyses were performed and the average value was taken as the chemical composition of alloy. The composition was further confirmed by area energy dispersive X-ray (EDX) quantification in SEM. The actual compositions of the alloys containing 0.02wt.% and 0.54wt.% Mn are shown in Table 6.1.

## 6.2 As-cast Microstructure

In the as-cast state, there was no significant change in the morphologies of the primary α-Al phase and eutectic Al-$Mg_2Si$ phases presented in the Al-Mg-Si alloys containing different levels of Fe and Mn. As mentioned in previous Chapters, the primary α-Al are labelled as '$\alpha_1$' and '$\alpha_2$' in Figure 6.1, respectively. Fe-rich intermetallic compounds were observed in the eutectic areas. In contrast to the primary α-Al phase, it is seen that the effect of Fe and Mn on the morphologies of primary Fe-rich compounds was significant. Different types and amounts of the Fe-rich intermetallics were related to the Fe and Mn contents, as shown in Figs. 6.1 and 6.2. From the experimental observations, only a small amount of fine intermetallic compounds were present in the alloys that contain up to 0.21wt.%Fe (Figure 6.1a&b and Figure 6.2a&b). The fine Fe-rich intermetallics were formed in the secondary solidification inside the die cavity (labelled as '$Fe_2$' in Figure 6.2). Most of the fine intermetallics were located between the primary α-Al phase ($\alpha_1$-Al and $\alpha_2$-Al), although some intermetallics were found inside them. No primary Fe-rich intermetallic compounds were observed in the primary α-Al phase precipitated in the first solidification. The EDX quantitive analysis by SEM identified the Fe-rich phase with the typical composition of the α-$Al_{12}(Fe,Mn)_3Si$ phase in the Al-Mg-Si alloy with Mn addition and the α-$Al_8Fe_2Si$ phase in the Al-Mg-Si alloy without Mn addition. No β-AlFe and β-AlFeSi intermetallics were observed in the samples at this composition.

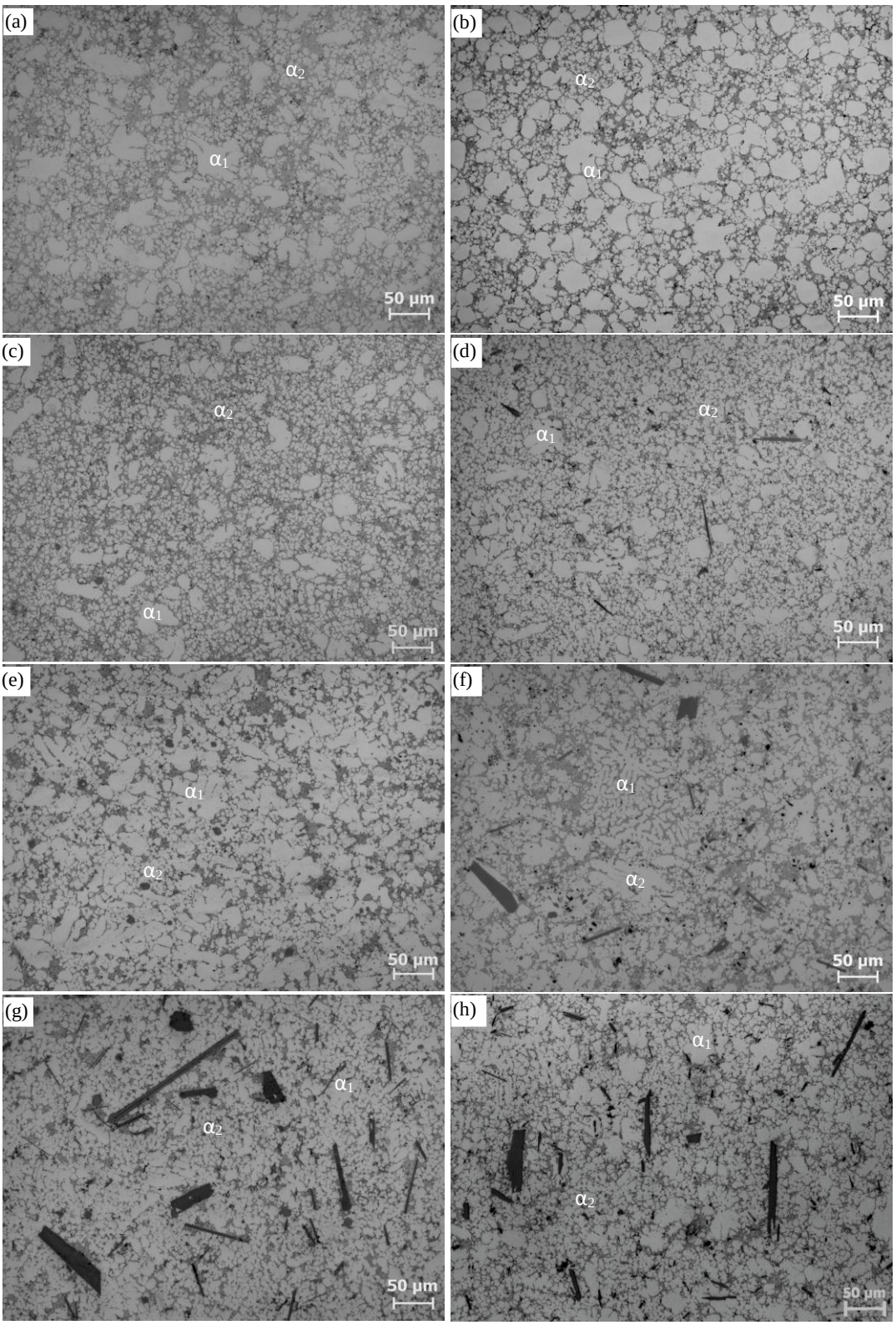


Figure 6.1 Optical micrographs showing the microstructure of die-cast alloy with different amounts of Fe and Mn, (a) 0.54Mn, 0.21Fe, (b)0.02Mn, 0.09Fe, (c) 0.54Mn,0.62Fe, (d) 0.02Mn, 0.63Fe, (e) 0.54Mn, 1.24Fe, (f) 0.02Mn, 1.19Fe, (g) 0.54Mn, 1.86Fe, (h) 0.02Mn, 1.82Fe.

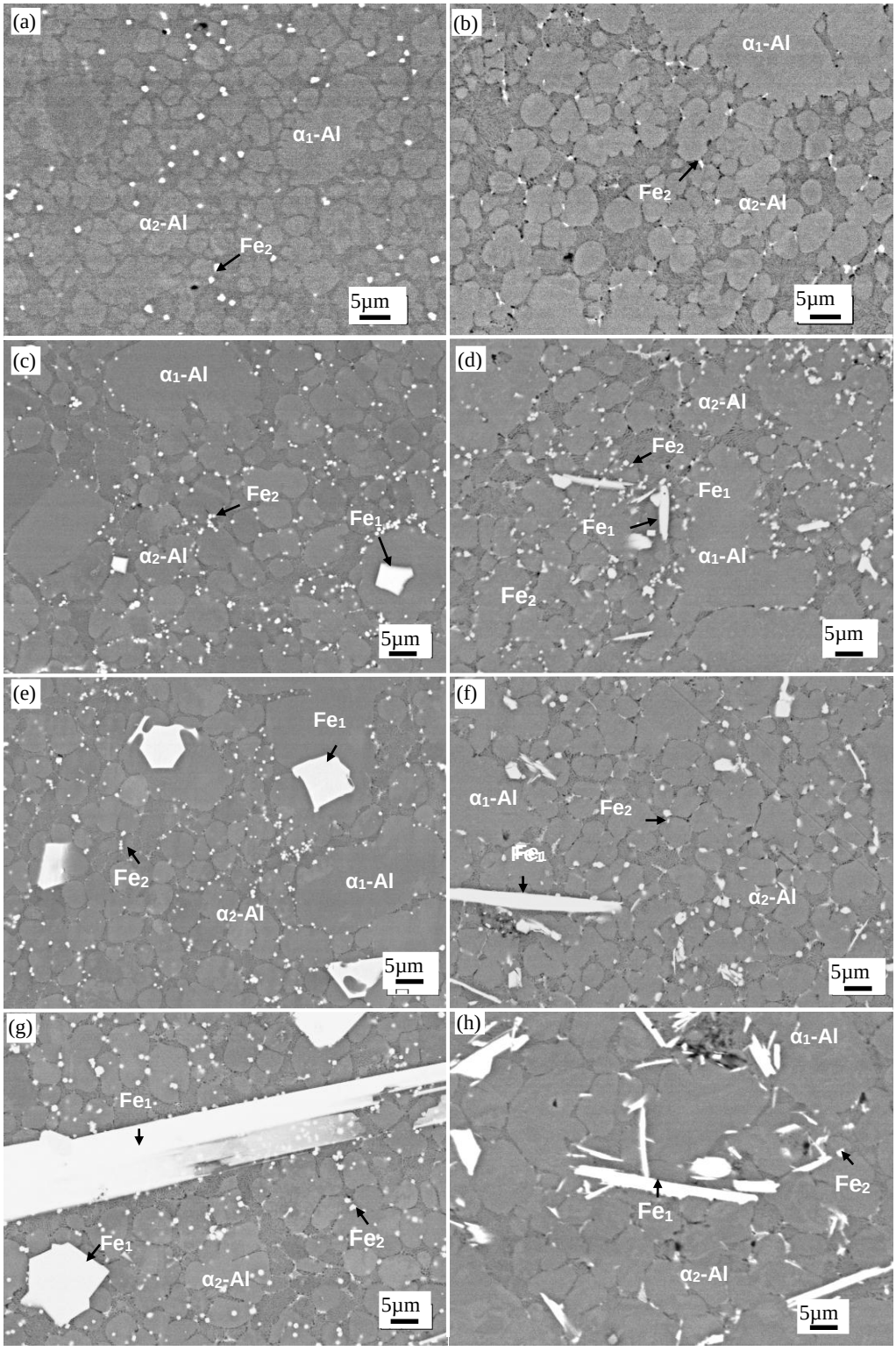


Figure 6.2 Backscattered SEM micrographs showing the morphology of Fe-rich intermetallics in the die-cast alloy with different amounts of Fe and Mn, (a) 0.54Mn, 0.21Fe, (b)0.02Mn, 0.09Fe, (c) 0.54Mn,0.62Fe, (d) 0.02Mn, 0.63Fe, (e) 0.54Mn, 1.24Fe, (f) 0.02Mn, 1.19Fe, (g) 0.54Mn, 1.86Fe, (h) 0.02Mn, 1.82Fe.

When the Fe contents in the alloys were increased to a level of 1.2wt.%Fe, there were two types of Fe-rich intermetallics observed. In the Al-Mg-Si alloy with Mn addition (Figure 6.2c&d, e&f), the Fe-rich intermetallics were formed in both the first solidification and the secondary solidification, which were labelled as '$Fe_1$' and '$Fe_2$' respectively. The $Fe_1$-rich intermetallics were usually associated with the primary $\alpha_1$-Al phase and exhibited coarse compact morphology, which were found in tetragonal, pentagonal, hexagonal shapes. EDX quantification has identified the Fe-rich intermetallics to be the α-AlFeMnSi phase with the typical composition of α-$Al_{12}(Fe,Mn)_3Si$. Meanwhile, the fine intermetallics (labelled as $Fe_2$) were associated with $\alpha_2$-Al phase and segregated in the primary α-Al grain boundaries, which were identified by EDX quantification to be the same α-AlFeMnSi phase with the typical composition of α- $Al_{12}(Fe,Mn)_3Si$. In the Al-Mg-Si alloy without Mn addition (Figs 6.2d&f), the fine Fe-rich phase was also found at the primary α-Al grain boundaries, which exhibited similar morphology and size to that in the alloy with Mn addition. The fine Fe-rich intermetallic phase was identified as the α-AlFeSi phase with the typical composition of α-$Al_8Fe_2Si$. However, the primary Fe-rich phase formed in the first solidification showed very different morphology in comparison with that formed in the alloy with Mn addition. As seen in Fig 6.2d&f, the $Fe_1$-rich phase exhibited needle-shaped morphology, which crossed through both the primary α-Al phases formed in the first solidification and the secondary solidification. The EDX quantification confirmed that the needle-shaped Fe-rich phase was β-AlFe phase with the typical composition of β-$Al_{13}Fe_4$. It is clearly seen that the additions of Mn can extend the range of Fe contents to form α-AlFeMnSi phase in the alloys. In other words, the Fe content to initialize the β-AlFe phase is increased by adding Mn in the alloys.

When the Fe contents in the alloys was further increased to a level of 1.8wt.% in Al-Mg-Si-Mn-Fe and Al-Mg-Si-Fe systems. In the Al-Mg-Si alloy with Mn addition, as shown in Figure 6.2g, a large fraction of long needle-shaped Fe-rich intermetallics were found in the microstructure (bright strip in Figure 6.2g), in addition to the compact Fe-rich phase. The coarse and the fine compact primary Fe-rich intermetallics were identified by EDX quantification as the α-AlFeMnSi phase with the typical formula of α- $Al_{12}(Fe,Mn)_3Si$. The long needle-shaped Fe-rich compounds were quantitatively confirmed as β-AlFe phase with the typical composition of β-$Al_{13}(Fe,Mn)_4Si_{0.25}$. In the alloy without Mn addition, as shown in Figure 6.2h, a large fraction of the long needle-shaped primary Fe-rich intermetallics were found in the microstructure, which were confirmed by EDX as β-AlFe phase with the typical composition of β-$Al_{13}Fe_4$. Only a small fraction of Fe-rich intermetallic compounds were in

the form of compact format, which was confirmed by EDX as α-AlFeSi phase with the typical composition of α-$Al_8Fe_2Si$.

In the as-cast microstructure, some coarse Fe-rich intermetallics developed into more complex morphologies such as star-like shapes in associated with primary α-Al phase, as shown in Figure 6.3. These Fe-rich intermetallics have been found in the castings with experimental composition of Fe>0.6wt. % and identified as α-AlFeMnSi phase with the typical composition of α- $Al_{12}(Fe,Mn)_3Si$. It was also found that the star-like α-AlFeMnSi phase were usually associated with $\alpha_1$-Al phase formed in the shot sleeve. The results indicate that the solidification environments, especially the cooling rate in the shot sleeve is capable of producing different morphologies of primary α-AlFeMnSi phase.

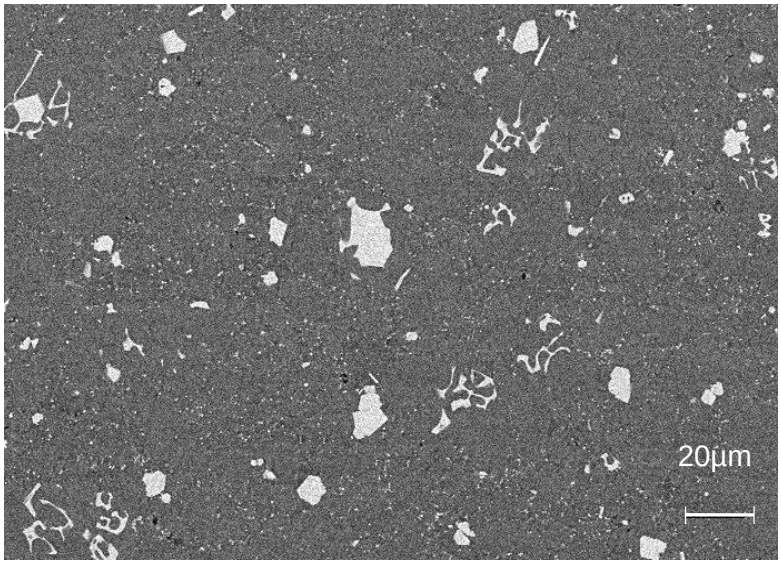


Figure 6.3 Backscattered SEM micrograph showing the morphology of Fe-rich intermetallics in the die-cast Al-5Mg-2Si alloy with 0.54Mn and 0.84Fe.

From these observations, the Fe-rich compounds of the compact and needle-shaped morphologies were identified as the α-AlFeMnSi (α-AlFeSi) and β-AlFe phase respectively. The intermetallic compounds in the Al-Mg-Si alloys with and without Mn addition are summarised in Table 6.2. It is seen that the primary α- $Al_{12}(Fe,Mn)_3Si$ intermetallics formed in the die cavity were observed in all die-cast alloys in the experimental range. However, the

primary Fe-rich intermetallics formed in the shot sleeve were significantly affected by the Fe contents. It is noticeable that the intermetallic β-$Al_{13}(Fe,Mn)_4Si_{0.25}$ and β-$Al_{13}Fe_4$ phases formed in the experimental alloys were different to the intermetallic β-$Al_5FeSi$ and β-AlFeSi phases observed in Al-Si, Al-Si-Cu and Al-Si-Mg alloys. However, the cubic α-AlFeMnSi phase of α- $Al_{12}(Fe,Mn)_3Si$ intermetallics formed in the experimental alloys was found to be very similar to α-$Al_{15}(FeMn)_3Si_2$ intermetallics formed in Al-Si, Al-Si-Cu and Al-Si-Mg alloys.

Table 6.2 Average compositions of Fe-rich intermetallic phases measured by quantitive SEM/EDX analysis.

| Mn (wt.%) | Phase morphology | Identified compounds | Al at.% | Fe | Mn | Si | Fe/Mn |
|---|---|---|---|---|---|---|---|
| 0.54 | coarse compact | Al12(Fe,Mn)3Si | 76.64 | 11.83 | 5.95 | 6.27 | 1.99 |
| | fine compact | Al12(Fe,Mn)3Si † | 75.47 | 12.16 | 6.28 | 6.09 | 1.94 |
| | large needle | $Al_{13}(Fe,Mn)_4Si_{0.25}$ | 75.62 | 19.20 | 3.81 | 1.37 | 5.04 |
| 0.02 | fine compact | $Al_8Fe_2Si$ † | 35.01 | 9.59 | - | 4.13 | - |
| | large needle | $Al_{13}Fe_4$ | 75.50 | 24.51 | - | - | - |

† The composition was further confirmed by TEM/EDX analysis

In order to characterize the Fe-rich intermetallics in the alloys, their sizes and solid fractions were measured in the microstructure. The results for the fine α-AlFeMnSi and fine α-AlFeSi particles that are formed in the die cavity are shown in Figure 6.4. Both particles followed a level correspondence to the Fe contents, which were consistently at 0.76 μm in diameter and no significant variation within the experimental ranges (Figure 6.4a). The distribution of the fine Fe-rich particles was well matched by the normal distribution curve with an average of 0.76 (Figure 6.4b). However, the volume fraction of the fine Fe-rich particles increased with the increase of Fe contents in the alloys (Figure 6.4c). As the fine Fe-rich particles were formed during the solidification in the die cavity under high cooling rate, the results indicate that the sizes of the Fe-rich intermetallics were mainly determined by the increased undercooling, enhanced heterogeneous nucleation and the shortened solidification time for the particle to grow.

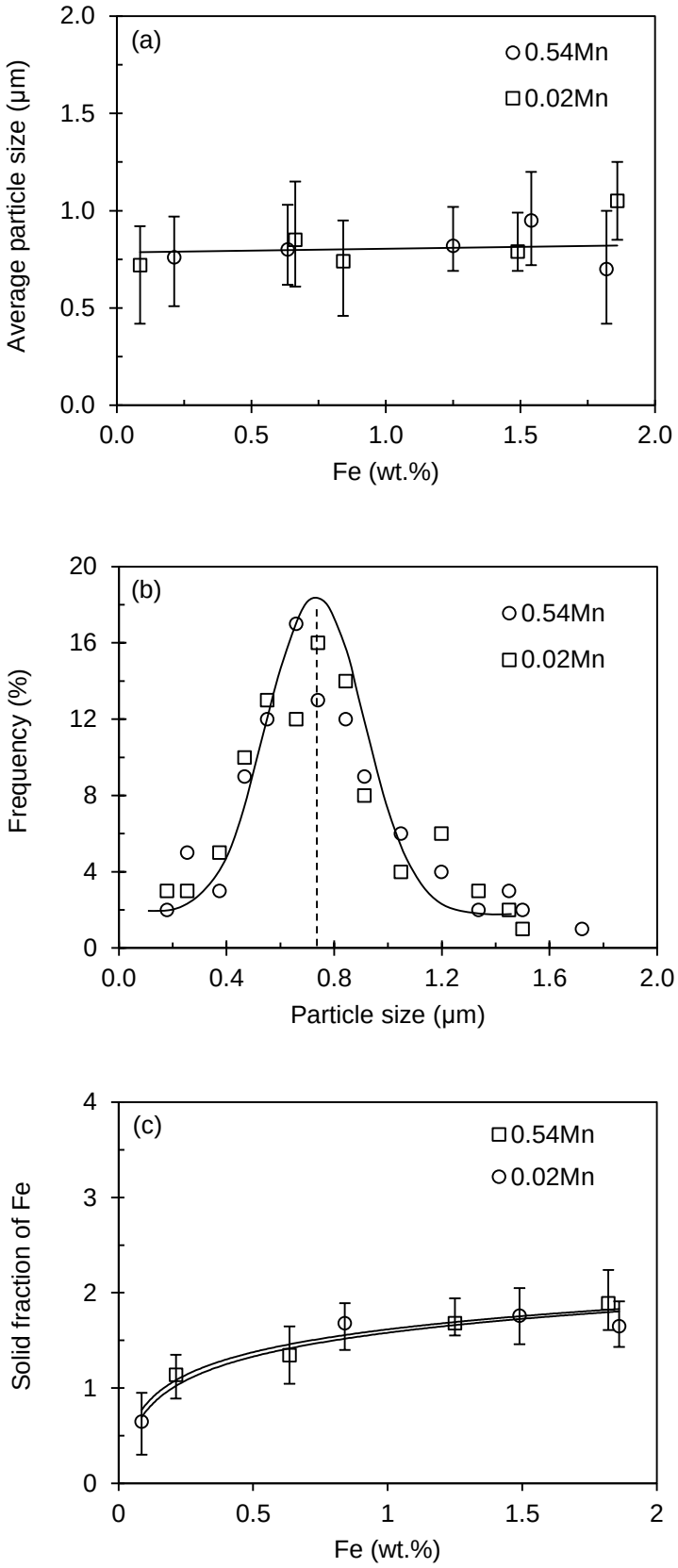


Figure 6.4 Effect Fe contents in the die-cast alloy on (a) the average size, (b) the frequency and (c) the volume fraction of Fe-rich intermetallic phase solidified in the die cavity.

In the Al-Mg-Si alloys with and without Mn addition, it is seen that the average sizes and volume fractions of the Fe-rich intermetallics solidified in the shot sleeve were obviously different to that formed in the die cavity, as shown in Figure 6.5. The volume fraction and the size of the primary Fe-rich intermetallics increased significantly with the increase of Fe contents in the alloys. However, the size of the Fe-rich intermetallics increased in different ways. A linear increase of the size in the Fe-rich intermetallics was found in the alloys without Mn addition, but the size of Fe-rich intermetallics followed two separate linear correspondences to the Fe contents at a vertex of 1.24 in the alloy with Mn addition. A gradual increase was found at Fe < 1.24wt.% and a significant increase was found at Fe>1.24wt.%. The vertex in Figure7b confirmed that the critical Mn/Fe ratio is at level of 0.5 to suppress the formation of β-$Al_{13}(Fe,Mn)_4Si_{0.25}$ in the alloys.

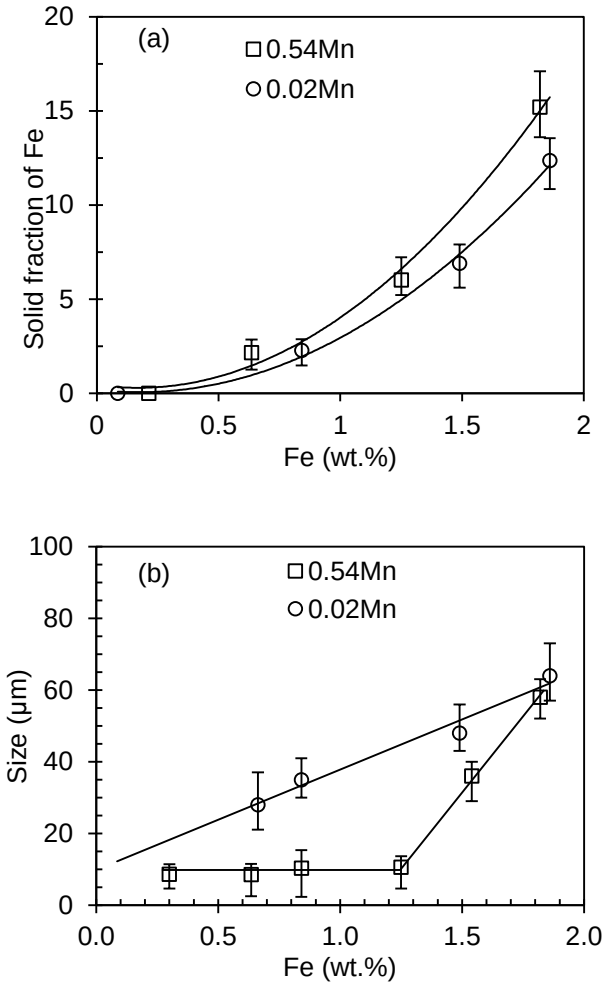


Figure 6.5 Effect of Fe contents in the die-cast alloy on (a) the volume fraction and (b) the average size of Fe-rich intermetallic phase solidified in the shot sleeve.

## 6.3 Mechanical Properties

Mechanical properties of the die-cast Al-Mg-Si alloys with different Fe and Mn contents are presented in Figure 6.7. It is seen that a slight enhancement in the yield strength and a significant detrimental to the elongation with the increase of Fe contents in the alloys. However, no obvious variation in the ultimate tensile strength was observed until Fe was higher than 0.6wt.% where it decreased. Overall, the strength and the elongation of the die-cast alloys with different Fe levels were all effectively higher in the alloys with 0.54wt.%Mn than these of their die-cast counterparts with 0.02wt.%Mn. In addition to the slightly variation of Mg and Si concentrations in the alloys, as shown in Table 1, the difference in Mn content was one of the major factors to affect the strength and elongation of the die-cast alloys. It is worth for a further emphasis that the enhancement of the yield strength for the die-cast samples is less effective than the detrimental to the elongation of the same alloy in the experimental ranges. The overall increase of the yield strength of the die-cast sample was 8% while the ultimate tensile strength decreased by 9% and the elongation decreased by 295%.

## 6.4 CALPHAD of Al-Mg-Si-Mn-Fe and Al-Mg-Si-Fe Systems

The calculated equilibrium phase diagrams on the cross sections of Al-5Mg-2Si-0.5Mn-xFe and Al-5Mg-2Si-xFe are shown in Figures 6.7 and 6.8, respectively. In Figure 6.7, it can be divided into several regions with different Fe contents. The phase formation follows: (1) $L\rightarrow$ $\alpha$-Al+$\alpha$-AlFeMnSi+$Mg_2Si$ with prior $\alpha$-Al phase at Fe<(0.25wt.%), and (2) $L\rightarrow$ $\alpha$-AlFeMnSi+$\alpha$-Al+$Mg_2Si$ with prior $\alpha$-AlFeMnSi phase at 0.21wt.%<Fe<1.4wt.%, and (3) $L\rightarrow\beta$-AlFe +$\alpha$-AlFeMnSi+$\alpha$-Al+$Mg_2Si$ with prior $\beta$-AlFe phase at Fe>1.4wt.%. It needs to emphasise that the $\beta$-AlFe phase can be formed with a very low Fe content according the equilibrium phase diagram. However, the formation of $\beta$-AlFe phase in the as-cast microstructure of the experimental alloys with 0.54wt.%Mn is from 1.2wt.%Fe. The difference may be attributed to several factors including the noon-equilibrium solidification in HPDC process, the complex of precipitation process of intermetallics during solidification, and the database used in phase diagram calculation.

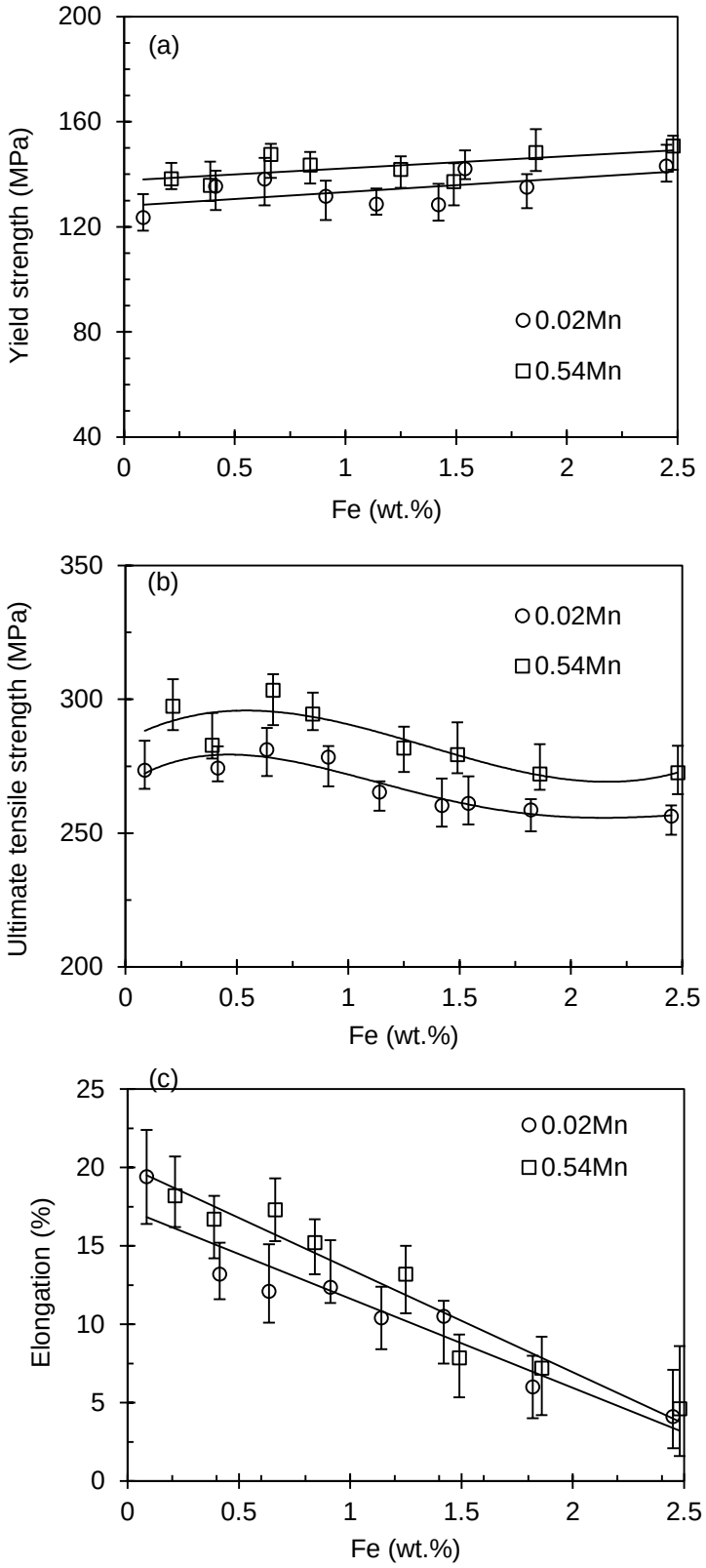


Figure 6.6 Effect of Fe content on the mechanical properties of die cast Al-Mg-Si alloys with different amounts of Mn, (a) yield strength, (b) ultimate tensile strength, and (c) elongation.

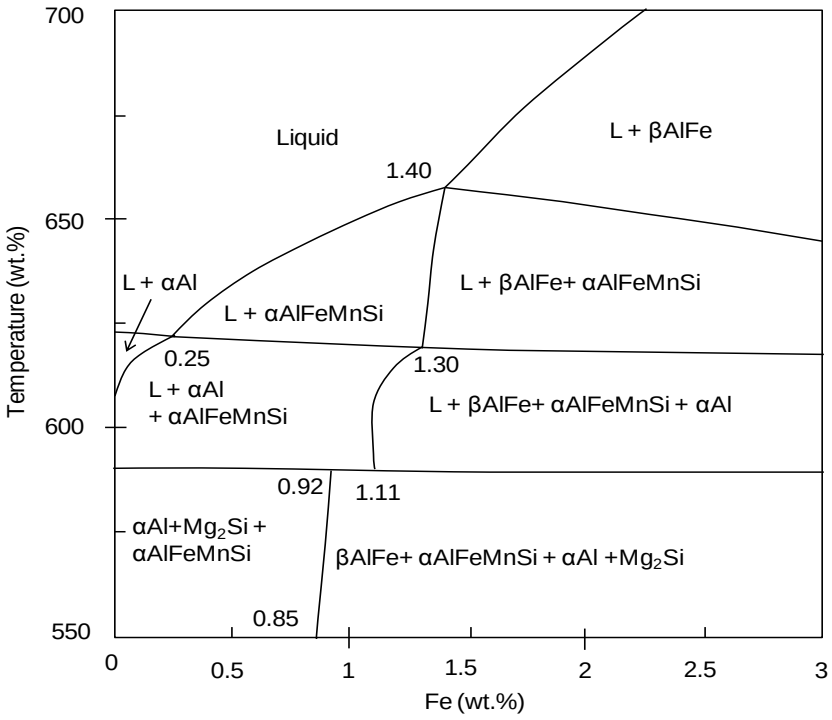


Figure 6.7 Cross section of equilibrium phase diagram of Al-5Mg-2Si-0.6Mn-xFe calculated by Pandat software.

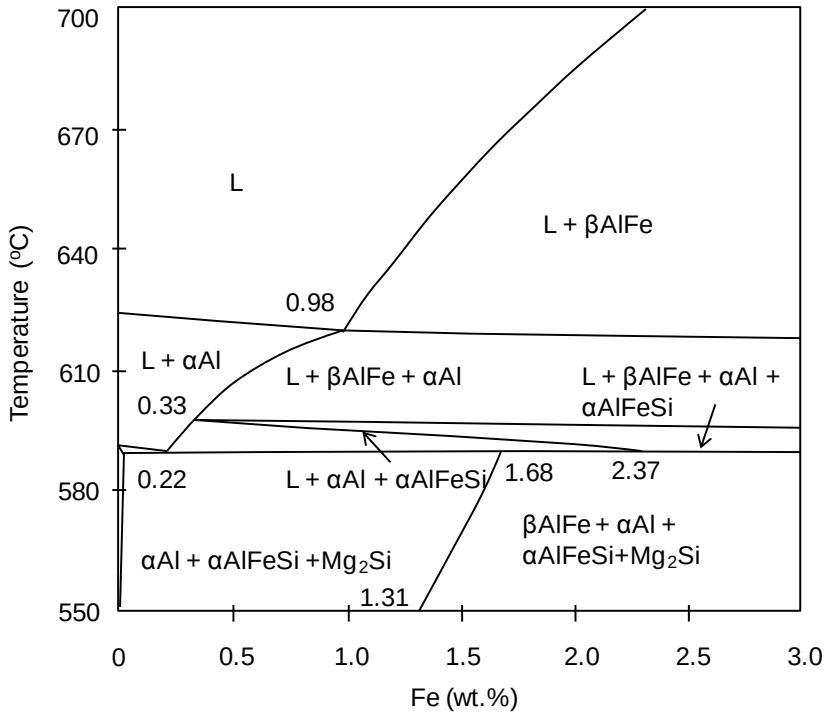


Figure 6.8 Cross section of equilibrium phase diagram of Al-5Mg-2Si-xFe calculated by Pandat software.

Similarly, for the Al-Mg-Si-Fe system shown in Figure 6.8, the solidification procedure roughly follows: (1) L→ α-Al+α-AlFeSi+$Mg_2Si$ with prior α-Al phase at Fe<(0.98wt.%), in which β-AlFe phase may exist at 0.22wt.%<Fe<0.98wt.%, and (2) L→β-AlFe + α-AlFeSi+α-Al+$Mg_2Si$ with prior β-AlFe phase at Fe>0.98wt.%. The experimental results should that the β-AlFe phase was observed in the alloy with Fe content higher than 0.62wt.%.

The effect of Mn and Fe contents on the formation of Fe-rich intermetallic compounds are further demonstrated in Figure 6.9 for the Al-Mg-Si alloys with three different levels of Mn contents at 0.2, 0.4 and 0.6wt.% respectively. It is seen that the Fe content was lowered to form prior α-Al phase with the increases of Mn contents in the alloy. In other words, with the increase of Mn in the alloy, the α-AlFeMnSi was formed as prior phase at a lower level of Fe content in the alloy. Meanwhile, the addition of Mn also increased the Fe levels to form β-AlFe phase. Therefore, the area to form α-AlFeMnSi was significantly enlarged with the increase of Mn contents. This implies that the addition of Mn in the alloy can suppress the formation of β-AlFe intermetallic compounds in the alloy with practically possible high Fe content. On the other side, as seen in Figure 6.9, the results confirmed that the increase of Mn in the alloy resulted in a significant increase of liquidus temperature of the alloy.

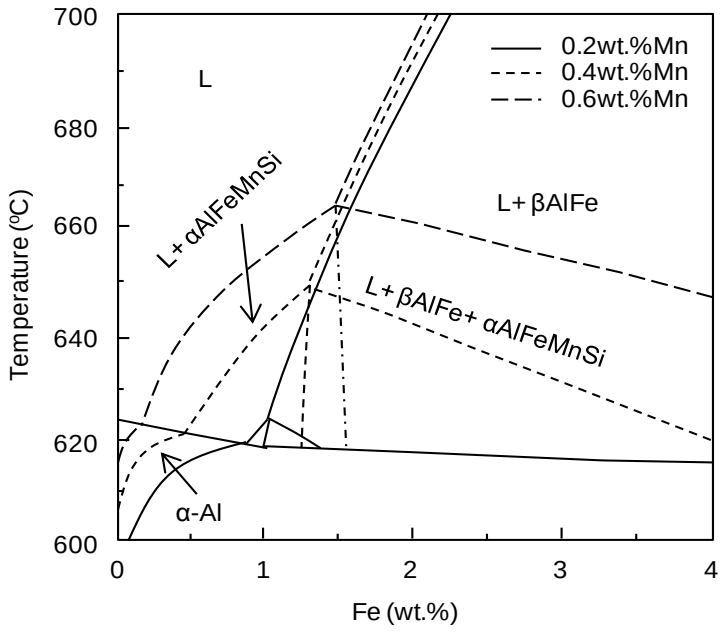


Figure 6.9 Effect of Mn on the cross section of equilibrium phase diagram of Al-5Mg-2Si-xFe calculated by Pandat software.

## 6.5 Formation of Fe-rich Intermetallics in Al-Mg-Si-Mn Alloy

The experimental observations have confirmed that (1) α-AlFeMnSi intermetallics can be formed in two solidification stages during HPDC, one is in the shot sleeve and the other is in the die cavity, which show the compact morphology with different sizes; (2) manganese increases the Fe content range over which α-AlFeMnSi phase forms; (3) the Mn/Fe ratio at 0.5 is applicable to form β-AlFe intermetallics in the Al-Mg-Si-Mn alloy during HPDC; (4) no β-$Al_5FeSi$ and β-AlFeSi intermetallics are observed in the Al-Mg-Si die-cast alloys with varied Mn and Fe contents.

Generally, the phase formation of Fe-rich intermetallics in the experimental alloys is broadly consistent with the equilibrium phase diagram calculated from CALPHAD. Therefore the solidification path can be used to explain the major features of the microstructure. The solidification process and the associated changes of liquid compositions determine the formation of different phases. From the phase diagram, it is seen that the prior phase is α-Al phase when Fe content is less than 0.25wt.%. The solidification starts to precipitate the α-Al phase in the shot sleeve, which is interrupted during die filling. The precipitation of α-Al phase continues in the die cavity, during which Si, Fe and Mn elements are enriched in the remaining liquid and the Fe-rich intermetallics are consequently formed in the melt. The high cooling rate in the die cavity and the absence of superheat in the melt enhance the heterogeneous nucleation, and therefore promote the formation of fine compact α-AlFeMnSi intermetallics. When Fe content is increased to a higher level, the prior phase becomes α-AlFeMnSi. The precipitation of α-AlFeMnSi compounds increases the undercooling in front of the interface of the crystal, resulting in the nucleation and growth of α-Al phase in associated with α-AlFeMnSi compounds. The solidification continues in the die cavity, where the compact α-AlFeMnSi compounds and α-Al phase precipitate under high cooling rate. When Fe content is further increased, the prior phase is β-AlFe phase. The precipitation of β-AlFe compounds consumes Fe element in the melt and thus alters the local melt composition with enriched Si and Mn, resulting in an increase of Mn/Fe ratio. When Mn/Fe ratio reaches the limitation, α-AlFeMnSi compound precipitates from the melt. The following solidification precipitate the α-AlFeMnSi and β-AlFe compounds. Overall, the formation of α-AlFeMnSi and β-AlFe phases consumes Fe, Mn, Si prior to the eutectic solidification. The final stage of solidification of the alloys is

the multi-eutectic transformation to generate the eutectic structure mainly of Al-$Mg_2Si$ eutectic Al-$Mg_2Si$ phases.

The absence of β-$Al_5FeSi$ intermetallics in the die-cast Al-Mg-Si alloy is one important feature. In the equilibrium state, the β-$Al_5FeSi$ intermetallics has a monoclinic crystal structure with the lattice parameters a = b=0.612 nm, c = 4.15 nm, and β = 91° or a = b=0.618 nm, c = 4.15 nm, and β = 91°. Similarly, the crystal structure of β-$Al_3Fe$ and β-$Al_{13}Fe_4$ phase is also monoclinic with a = 1.549 nm, b = 0.808 nm, c = 1.248 nm, β = 107.8° . Currently, it is still not clear for the conditions to form β-$Al_5FeSi$ or β-$Al_3Fe$ (β-$Al_{13}Fe_4$) in Al alloys. The effect factors are suspected in associated with the content of Fe and Si, in which low Fe contents and high Si/Fe ratio favour the formation of β -$Al_5FeSi$ phase, but high Fe contents and low Si/Fe ratio tend to form β-$Al_3Fe$ ($Al_{13}Fe_4$) phase [172]. Obviously, the more systematic work needs to address the mechanism in future.

## 6.6 Effect of Fe on Mechanical Properties

The experimental results have confirmed that the Fe-rich intermetallics significantly affect the mechanical properties of the Al-Mg-Si alloys. The higher the iron concentrations in the alloy, the significantly more the elongation decreases. This is accompanied by a slight enhancement of the yield strength at increased iron level in the alloys. The ultimate tensile strength maintains at similar level when Fe is less than 0.6wt. %, but it decreases significantly when the Fe contents further increases. Meanwhile, a slight enhancement of the yield strength is also observed in the alloy with Mn addition compare to that in the alloy without Mn addition.

Referring to the solidification microstructure, the enhanced yield strength is believed to correspond to the increased amounts of Fe-rich intermetallic compounds, especially the fine intermetallics present at the α-Al grain boundaries. The increase in yield strength is accompanied with decreasing elongation as the added reinforcement due to the Fe-rich compounds is at the cost of the alloy ductility. Therefore the detrimental effect of iron content on the mechanical properties in the die-cast Al-Mg-Si alloys should be determined mainly by the loss in ductility.

## 6.7 Summary

In high pressure die casting of Al-Mg-Si-Mn alloys, the formation of Fe-rich intermetallics occurs into two solidification stages. One is in the shot sleeve at lower cooling rates, and the other is in the die cavity at higher cooling rates. The Fe-rich intermetallics formed in the shot sleeve exhibit coarse compact, star-like or needle/plate shape morphology with varied sizes. The Fe-rich intermetallics formed in the die cavity are characterised by fine compact morphology with the size less than 3 μm.

In die-cast Al-Mg-Si alloys, two types of Fe-rich intermetallics are formed over the Fe content range up to 2.4wt. %. The fine compact α-AlFeSi phase has the composition of α-$Al_8Fe_2Si$ and the long needle β-AlFe phase has the composition of β-$Al_{13}Fe_4$. With 0.54wt.%Mn being added into the alloy, the fine compact intermetallic phase is found to be Al12(Fe,Mn)3Si and the long needle β-AlFe phase is β-$Al_{13}(Fe,Mn)_4Si_{0.25}$.

In die-cast Al-Mg-Si alloys containing 0.54wt.%Mn, the prior phase is α-Al when Fe is less than 0.21wt.%, but the prior phase is β-$Al_{13}(Fe,Mn)_4Si_{0.25}$ when Fe is higher than 1.24wt.%. Over the Fe contents range from 0.21 to 1.24wt%, α-$Al_{12}(Fe,Mn)_3Si$ precipitates as prior phase to form either coarse compact compounds in the shot sleeve or fine compact particles in the die cavity.

The morphology and size of α-$Al1_{24}(Fe,Mn)_6Si_2$ intermetallics are dependent on the cooling rate. The higher cooling rate in the die cavity enables the α-$Al1_{24}(Fe,Mn)_6Si_2$ phase to solidify in a fine compact morphology. However, the lower cooling rate in the shot sleeve results in the formation of compact and star-like Chinese script α-$Al1_{24}(Fe,Mn)_6Si_2$ phase in the as-cast microstructure.

Fe-rich intermetallics significantly affect the mechanical properties of the alloy castings. The higher the iron concentrations in the alloy, the more significantly the ductility reduces. This is accompanied by a slight enhancement of the yield strength. The ultimate tensile strength maintains the similar level when Fe contents is less than 0.6wt.%, but decreases significantly with the further increase of Fe contents in the die-cast alloys.

The yield strength and the ultimate tensile strength are slightly enhanced in the die-cast Al-Mg-Si alloy when Mn is added in comparison with that without Mn addition.

Manganese promotes the formation of the cubic α-AlFeMnSi phase and suppresses the formation of β-AlFe phase in die-cast Al-Mg-Si alloys. The β-AlFe compounds are formed when Mn/Fe ratio is less than 0.5.

# Chapter 7
# Effect of Nickel on the Microstructure and Mechanical Properties

## 7.1. Introduction

In the recycled aluminium alloys, the accumulation of impurity elements is a growing problem as the solute concentrations are over the limitation of registered specification, which restricts the application of recycled aluminium alloys in a closed loop cycle [173,174]. The list of problematic impurities varies from one alloy to the other. Generally, the impurity elements include but do not limit to Si, Mg, Ni, Zn, Pb, Cr, Fe, Cu, V and Mn in different aluminium alloys [16, 175 ]. Therefore, the effect of impurity elements on the microstructure and mechanical properties has been one of the major topics of many publications for the application of recycled aluminium alloys [3,176]. However, there is still a lack of understanding of the roles of some impurity elements such as Ni in aluminium alloys.

Nickel is defined as impurity in many commercial aluminium alloys with a limitation of 0.2wt.%, although it was used as alloying element up to a level of 2.5 wt.% in some commercial aluminium alloys, which can be found in both wrought and casting alloys [99]. Nickel has been recognised as a strongly partitioning and slow-diffusing element [100]. Nickel is almost insoluble in aluminium; with solubility being about 0.05 wt.% at 640 $^{o}$C and less than 0.005 wt. % at 450 $^{o}$C. In the Al-Ni binary alloy, the addition of nickel up to 2 wt.% give an increase in the strength of aluminium, but decreases in ductility [100]. Similar results were found in multicomponent aluminium systems and the aluminium matrix is unlikely to contain Ni levels above the equilibrium solubility. It was reported that Ni was mainly associated with iron to form AlFeSi intermetallics at low levels and to form $Al_3Ni$ intermetallics at higher concentration, such as in an Al-Mg-Si wrought alloy containing 1.4wt.% Ni [101]. A recent investigation [101 has also shown that Ni additions up to 0.05 wt.% did not have an obvious

influence on the phase constituents of AA6063 alloy, but this level was only at 0.015wt.%Ni for AA3102 alloy. A significant influence on the microstructure were observed in the as-cast condition of AA3102 alloy when Ni content was 0.05wt.%. For A356 alloy, Ni additions up to 0.02 wt.% did not have significant influences on the as-cast microstructure, but a new phase was formed when the Ni addition was increased to 0.05wt.%. A variety of intermetallics have been found to be AlFeMgSi and AlFeSi phases in the as-cast and heat-treated A356 alloy. Therefore, it is important to verify whether Ni is an impurity element or a useful alloying element in aluminium alloys.

In this Chapter, it is attempted to investigate the effect of Ni on the morphology, size and distribution of Ni-rich compounds in the Al-Mg-Si-Mn alloy produced by high pressure die casting process. The mechanical properties, such as yield strength, ultimate tensile strength (UTS) and elongation were assessed for the die-cast samples with different Ni contents. To enhance the understanding, the role of alloy chemistry on the effect of Ni was investigated by CALPHAD modelling of the multi-component Al-Mg-Si-Mn system. The discussions were focused on the phase formation of different Ni-rich intermetallic phases and the relationship between the Ni-rich compounds and the mechanical properties of the die-cast Al-Mg-Si-Mn alloy.

## 7.2 Effect of Ni on the As-cast Microstructure of the Die-cast Al-Mg-Si-Mn Alloy

The effect of Ni on the as-cast microstructure of the die-cast Al-Mg-Si-Mn alloy is shown in Figures 7.1 to 7.3. Generally, the increase of Ni resulted in the formation of more intermetallics in the as-cast microstructure (Figure 7.1). Most of the intermetallics exhibited dendritic morphology, although some compact intermetallics were also observed when Ni content was up to 1.11 wt.% (Figure. 4a,b&c). Two types of intermetallics were observed as shown in Figure 7.2d. One was in typical dendritic morphology and the other was not clear at low magnification. The high magnification micrographs shown in Figure 7.3 are taken from the alloy containing 2.06 wt.% Ni, where the typical laminar and dendritic intermetallic phases were seen in the grain boundaries and in the Eutectic areas. The co-existence of the Al-$Mg_2Si$ eutectics and Al with Ni-rich intermetallic eutectics indicated that two eutectic solidifications occurred during casting. Figure 7.4 shows that the solid fraction and the average size of the Ni-

rich intermetallics in the as-cast microstructure were increased with increasing Ni contents in the alloy.

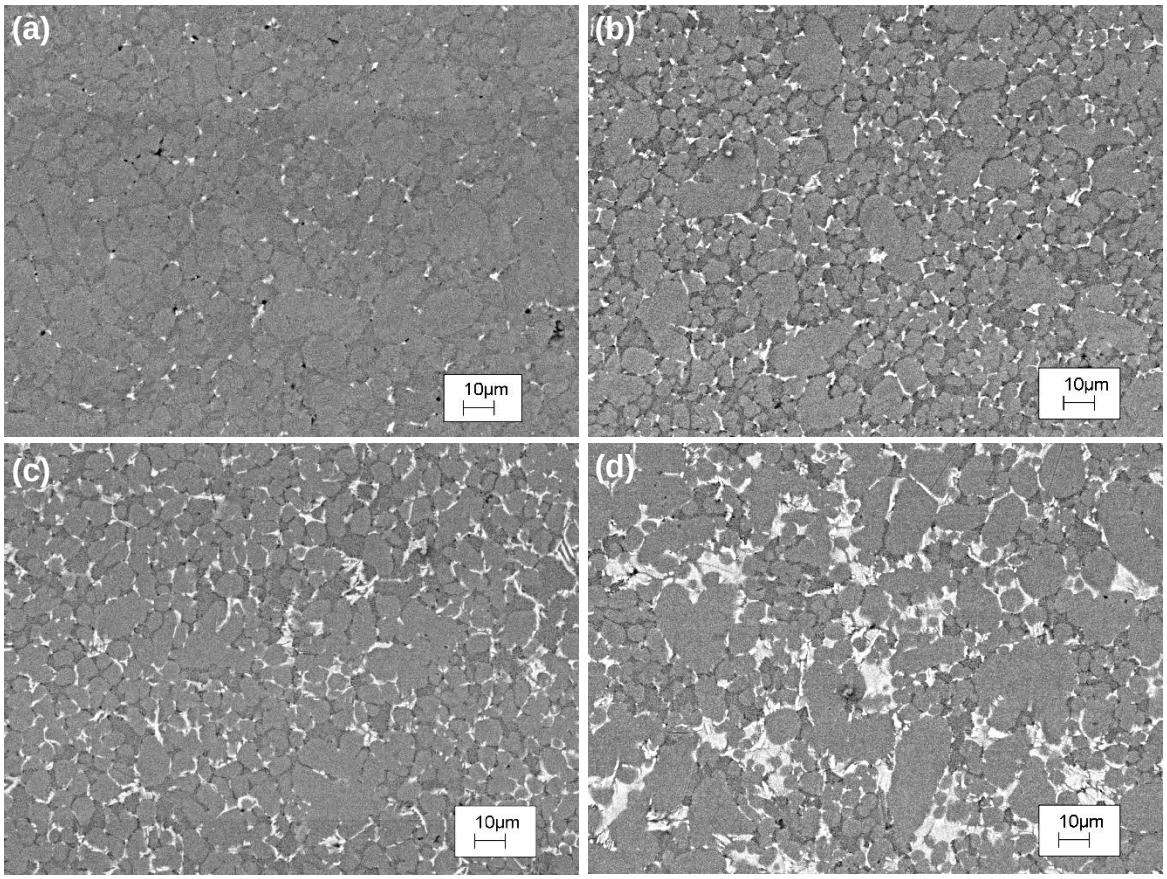


Figure 7.33 Backscattered SEM micrographs showing the morphology of Ni-rich intermetallics in the die-cast Al-Mg-Si-Mn alloys with different levels of Ni, (a) 0.16 wt.% Ni, (b) 0.57 wt.% Ni, (c) 1.11 wt.% Ni, (d) 2.06 wt.% Ni.

In comparison with the micrographs in Figure 7.2, it is seen that the eutectic spacing increased in the microstructure obtained in the alloys with a higher Ni content, as shown in Figure 7.3. The measured eutectic spacing of the eutectic Al-$Mg_2Si$ phases is summarised in Table 7.1. The average eutectic spacing of the eutectic Al phase was 0.41μm for the alloy without Ni, but it increased to 0.58 μm when Ni was raised to 2.06 wt.%. According to the data summarised in ref. [103-106] for the Eutectic reaction in similar alloys, the $\lambda^2V$=15 $\mu m^3/s$ can be used to estimate the relevant growth velocity. The calculated results are also given in Table 7.1. A significant reduction in the growth velocity of the eutectic can be seen with increasing Ni contents. This indicated that the eutectic solidification between Al and AlFeMnSiNi intermetallics might have occurred prior to or at the same temperature of the eutectic solidification of Al-$Mg_2Si$, during which the release of latent heat during Al and intermetallics

eutectic solidification could offer the resources to influence the solidification between Al and $Mg_2Si$.

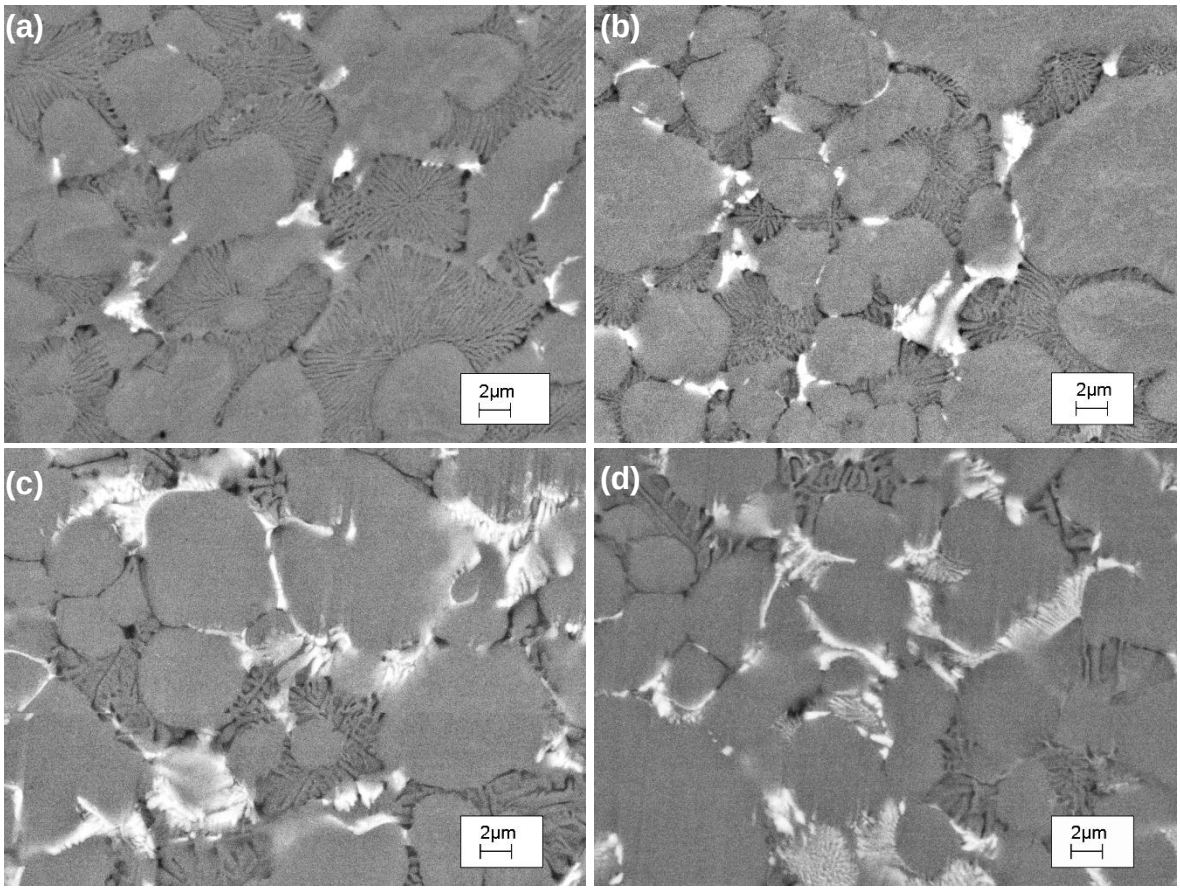


Figure 7.34 Backscattered SEM micrographs showing the morphology of Ni-rich intermetallics in the die-cast Al-Mg-Si-Mn alloys with different levels of Ni, (a) 0.16 wt.% Ni, (b) 0.57 wt.% Ni, (c) 1.11 wt.% Ni, (d) 2.06 wt.% Ni.

Table 7.1 The average eutectic spacing of the eutectic Al phase in the Al-Mg-Si-Mn alloys with different levels of Ni.

| Ni (wt.%) | Eutectic spacing between Al lamellae (μm) | Calculated growth velocity according to $\lambda^2 V = 15\ \mu m^3/s$, (μm/s) [21] |
|---|---|---|
| 0.005 | 0.41 | 89.23 |
| 0.16 | 0.43 | 81.12 |
| 0.57 | 0.47 | 67.90 |
| 1.11 | 0.52 | 55.47 |
| 2.06 | 0.58 | 44.59 |

Table 7.2 Average compositions of Fe-rich intermetallic phases measured by quantitative SEM/EDX analysis in the die-cast Al-Mg-Si-Mn alloys used in experiments.

| Ni (wt.%) | Phase morphology | Identified compounds | Al (at.%) | Si (at.%) | Mn (at.%) | Fe (at.%) | Ni (at.%) |
|---|---|---|---|---|---|---|---|
| 0.005 | irregular compact | $Al_{12}(Fe,Mn)_3Si$ | 75.47 | 6.09 | 6.28 | 12.16 | 0 |
| 0.16 | fine dendrites | $Al_{106}(Fe,Mn)_7SiNi_4$ | 91.22 | 0.71 | 2.69 | 2.36 | 3.02 |
| 0.57 | fine dendrites | $Al_{132}(Fe,Mn)_5SiNi_7$ | 92.8 | 0.57 | 1.33 | 1.52 | 3.78 |
| 1.11 | fine dendrites | $Al_{154}(Fe,Mn)_3SiNi_8$ | 94.32 | 0.49 | 0.79 | 0.71 | 3.69 |
| 2.06 | fine dendrites | $Al_{147}(Fe,Mn)_2SiNi_9$ | 94.14 | 0.51 | 0.61 | 0.37 | 4.37 |
| | Eutectic needles | $Al_{135}(Fe,Mn)_2SiNi_9$ | 93.26 | 0.56 | 0.62 | 0.45 | 5.11 |

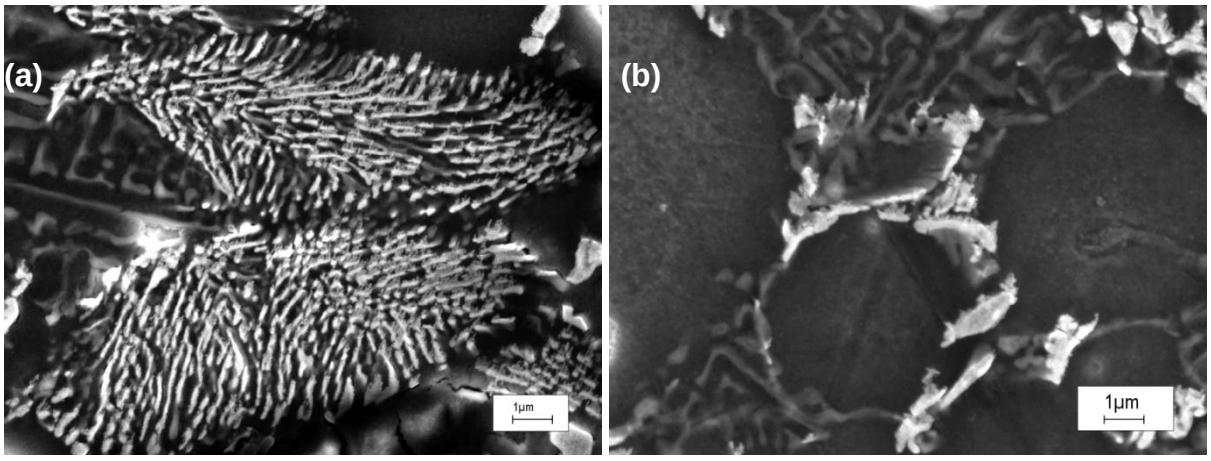


Figure 7.35 Inlens SEM images showing the morphology of (a) ternary eutectic structure and (b) dendritic Ni-rich primary phase in the Al-Mg-Si-Mn alloy with 2.06 wt.% Ni.

As shown in Figures 7.1 to 7.3, the dendritic Ni-rich intermetallics were usually associated with the primary α-Al phase. SEM/EDX quantification identified that the dendritic Ni-rich intermetallics were of the typical composition of $Al_{[100-140]}(Fe,Mn)_{[2-7]}SiNi_{[4-9]}$, as shown in Table 7.2. Meanwhile, the eutectic Ni-rich intermetallics were usually associated with eutectic Al-$Mg_2Si$ phases and also segregated at the primary α-Al grain boundaries. The eutectic Ni-rich intermetallics were identified by EDX as the same AlFeMnSiNi phase with the typical composition of $Al_{135}(Fe,Mn)_2SiNi_9$, as shown in Table 7.2. It is clearly seen that (1) the Ni-rich intermetallics essentially consisted of Fe, Mn and Si, and no $Al_3Ni$ phase was detected in

the studied alloy with Ni content up to 2.06 wt.%; and (2) two types of Ni-rich intermetallics had the same constituent composition and could be described by the same chemical formula. It is noticeable that the Ni-rich intermetallic phase formed in the alloy was different to the intermetallic phases observed in other Al-Si-Mg alloys. Song et al. found that $Al_3Ni$ were formed in the alloys with 1.4 wt.% Ni. However, this binary intermetallic was not observed in our experimental alloy with an even higher Ni content. In order to further confirm the intermediate phase, a series of experiments were performed to find out the differences in XRD spectrums and the results are shown in Figure 7.5. The peaks for α-Al and $Mg_2Si$ phases were easily identified from the experimental results. However, it was difficult to find out the corresponding peaks of the AlFeMnSiNi intermetallics. Although some peaks were identified for α-AlFeMnSi, several peaks were unable to be certainly identified with the existing database. However, the peaks were certainly not from $Al_3Ni$. The results confirmed the existence of new phases in the alloy. However, it is not able to confirm the existence of AlFeMnSiNi phase because of the insufficient information from the existing XRD database.

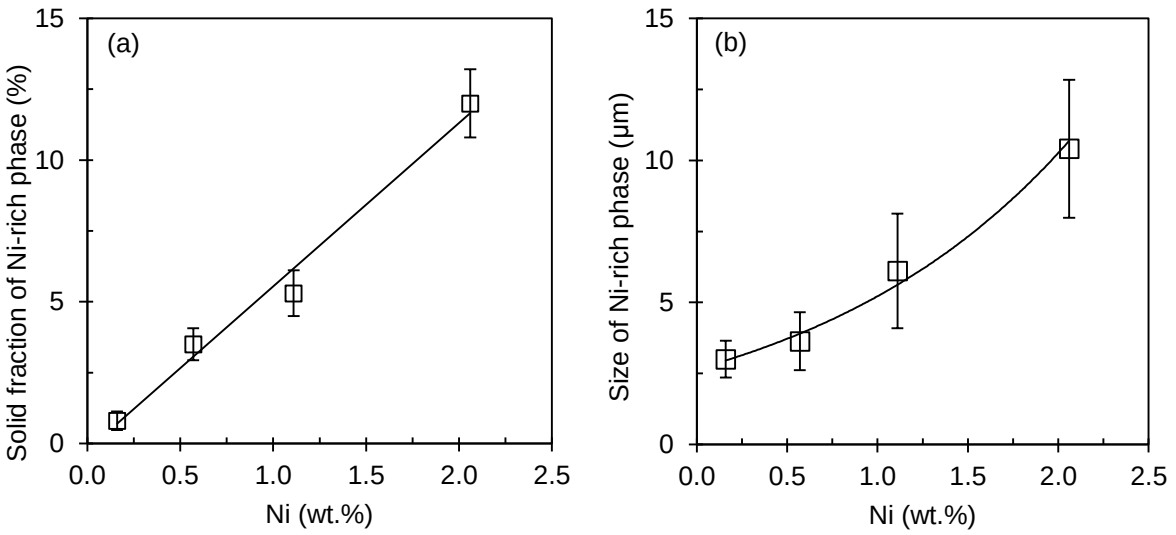


Figure 7.36 Effect of Ni content in the die-cast Al-Mg-Si-Mn alloy on (a) the volume fraction and (b) the average size of Ni-rich intermetallic phase.

On the other hand, the formation sequence of intermetallics can be indirectly confirmed by analysing the distribution of solute elements in the primary phase and the eutectic Al-$Mg_2Si$ phases. Figure 7.5 shows the elements mapping of the primary intermetallics and eutectic intermetallics in the experimental alloy. In the backscattered SEM micrograph shown in Figure 7.6a, the difference of the eutectic intermetallics in the middle and the primary intermetallics in the side was clear by their morphologies. The colour was essentially no different in the

intermetallics, indicating that the distributions of different solute elements were uniform in the whole intermetallics. This clarified that Ni was dissolved into the intermetallics, rather than the affiliation on the surface of the Fe-rich intermetallics. This indicated that the Ni was associated with Al, Fe, Mn and Si from the beginning of solidification and Ni did not form other intermetallics first and then attached to the existing AlFeMnSi phase.

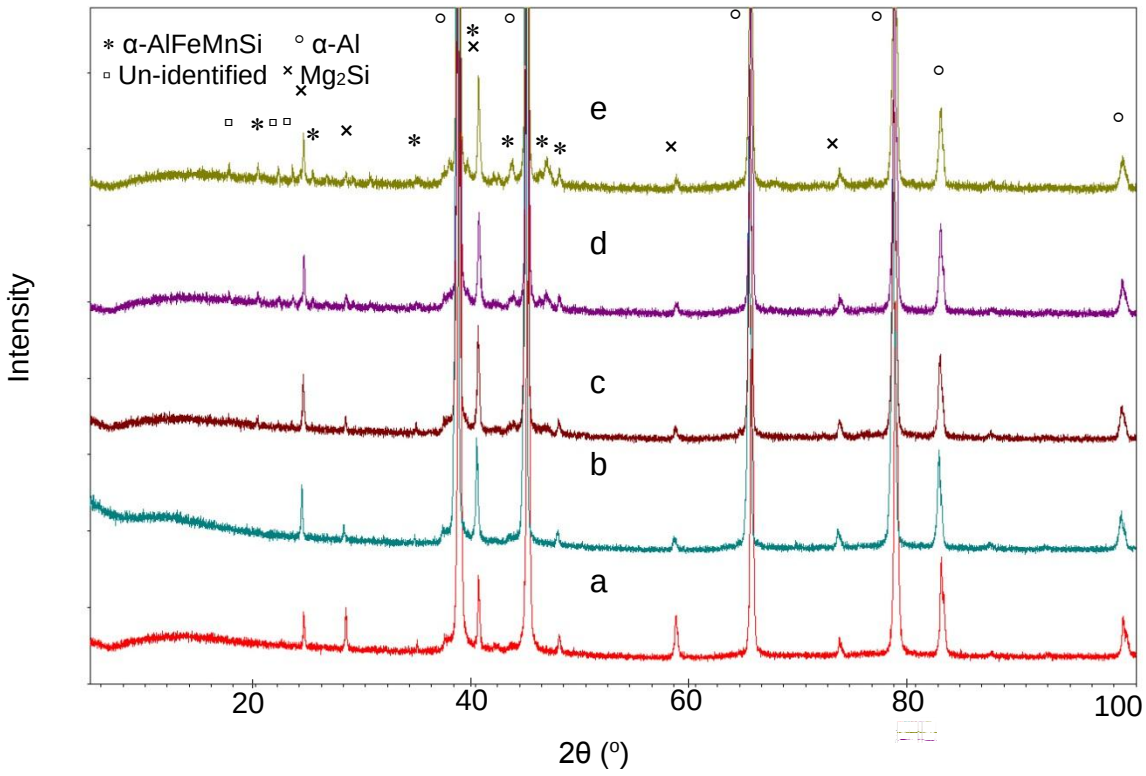


Figure 7.37 XRD spectrums of the Al-Mg-Si-Mn alloys with different levels of Ni, (a) 0.005 wt.% Ni, (b) 0.16 wt.% Ni, (c) 0.57 wt.% Ni, (d) 1.11 wt.% Ni, (e) 2.06 wt.% Ni.

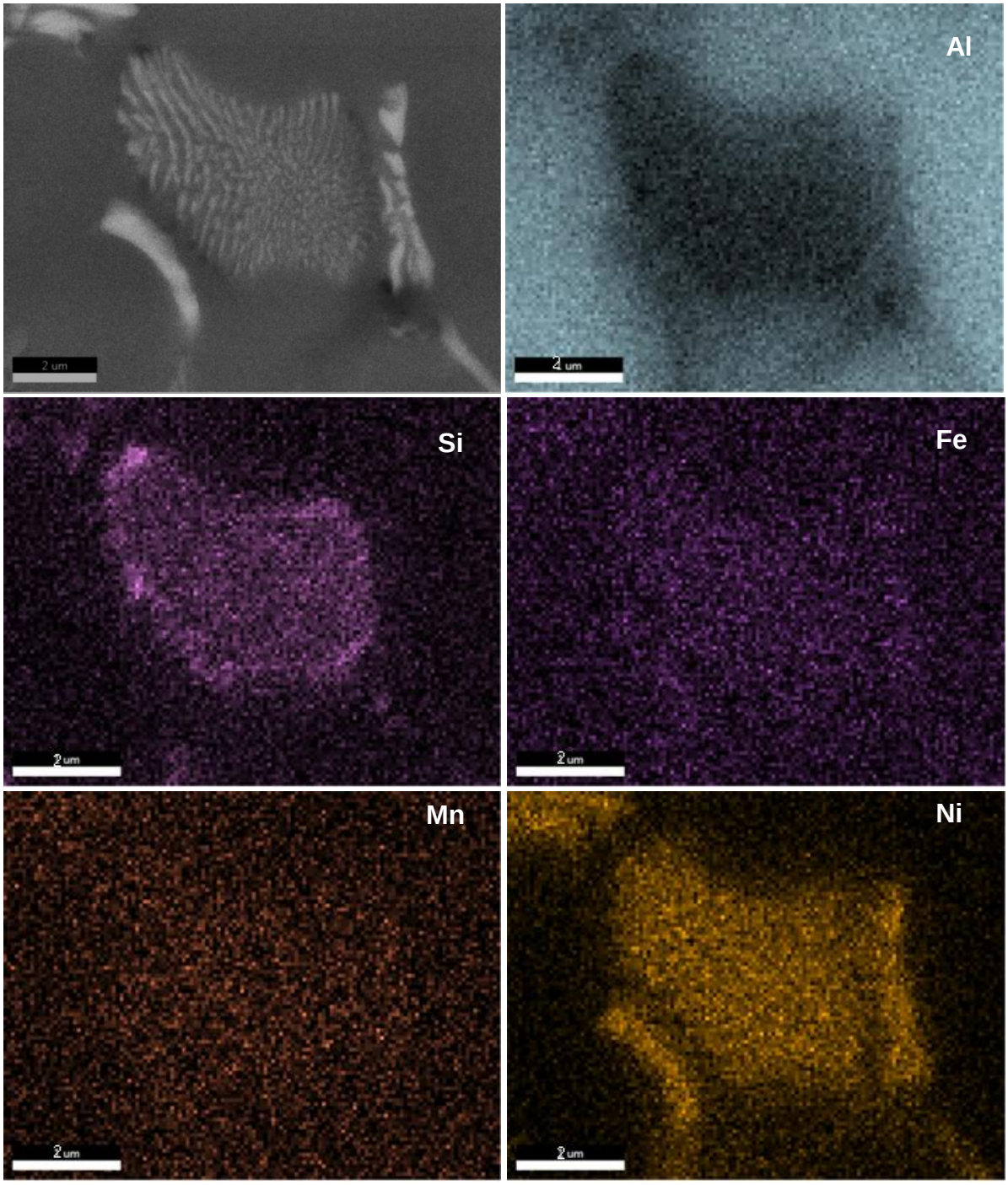


Figure 7.38 Backscattered SEM micrograph and the series of elemental maps showing the distribution of key elements in the intermetallics of the Al-Mg-Si-Mn die-cast alloy. Map conditions: 20 kV, 185nA, 5 nm step size and a counting time of 15 ms per step.

## 7.3 Mechanical Properties

Mechanical properties of the die-cast Al-Mg-Si-Mn alloy with different Ni contents are presented in Figure 7.7. It is seen a slight enhancement in the yield strength and a significant detrimental to the elongation with the increase of Ni contents in the alloys. However, no obvious variation in ultimate tensile strength (UTS) was observed, although a slight increase of UTS was found when Ni was added at a low level. It is worth for a further emphasis that the enhancement of the yield strength for the die-cast samples is less significant than the detrimental to the elongation of the same alloy in the experimental ranges. The overall increase of the yield strength of the die-cast sample was 10% while the elongation decreased by 350%.

Referring to the solidification microstructure, the enhanced yield strength is believed to correspond to the increased amounts of Ni-rich intermetallic compounds presented at the α-Al grain boundaries and eutectic Al-$Mg_2Si$ areas. The increase in the yield strength is accompanied with decreasing elongation as the added reinforcement due to the Ni-rich compounds is at the cost of the alloy ductility. Therefore the Ni content should be limited in a low level during alloy recycling in order to maintain the mechanical properties of the die-castings without significant loss in ductility.

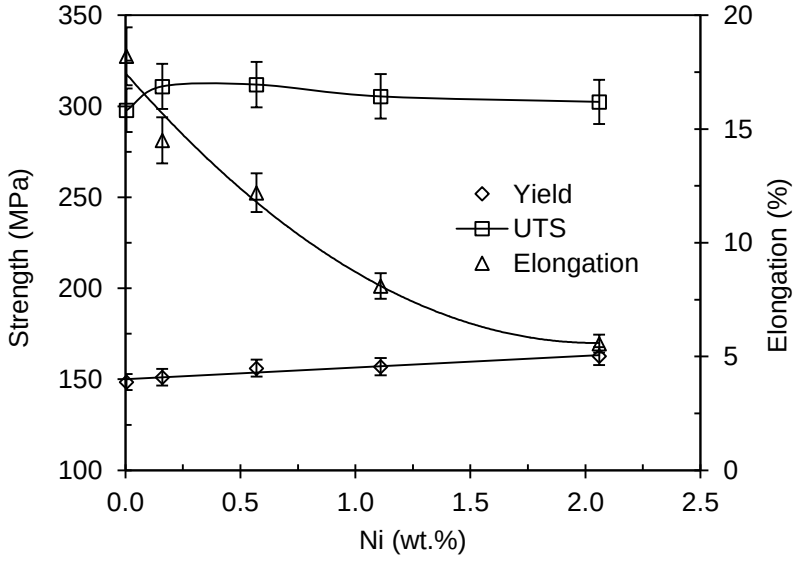


Figure 7.39 Effect of Ni content on the mechanical properties of the die-cast Al-Mg-Si-Mn alloy.

## 7.4 CALPHAD Modelling of the Multi-component Al-Mg-Si-Mn-Fe-Ni System

The calculated cross section of equilibrium phase diagram on the Al-5Mg-2Si-0.6Mn-0.2Fe-xNi alloy is shown in Figure 7.8, which could be divided into several regions with different Ni contents. The phase formation followed: (1) $L\rightarrow$ α-Al+$Mg_2Si$+$Al_{15}(Fe,Mn)_3Si_2$ with prior α-Al phase at Ni<(0.05wt.%), (2) $L\rightarrow$ α-Al+$Mg_2Si$+$Al_{15}(Fe,Mn)_3Si_2$ with prior α-$Al_{15}(Fe,Mn)_3Si_2$ phase at 0.05wt.%<Ni<0.15wt.%, and (3) $L\rightarrow$ α-Al+$Mg_2Si$+$Al_{15}(Fe,Mn)_3Si_2$ +$Al_3Ni$ with prior α-AlFeMnSi and α-Al phase at 0.15wt.%<Ni<4wt.% (4 wt.% was the calculated limits in Figure 7.8, the actual limit should be different). It needs to emphasise that the phase formation for the intermetallics according to the equilibrium phase diagram was different from the as-cast microstructure of the experimental alloys with varied contents of Ni. The difference was attributed to several factors including the non-equilibrium solidification in high pressure die-casting process, the complex of precipitation process of intermetallics during solidification, and the limitation of the database used in the phase diagram calculation. However, the equilibrium phase diagram had provided useful information for the solidification process.

The solidification process of the alloy with different contents of Ni is shown in Figure 7.9. It is seen an increase of the solid phase and a decrease of the liquid phase at a given temperature between liquidus and solidus for the alloy with increased Ni content. Figure 7.10a shows the results for the alloy containing 0.005 wt.% Ni, where no Ni-rich intermetallic phase was found in the solidification curve. This was consistent with the experimental results given in Figures 7.1 to 7.4. In Figure 7.9b, the alloy with 2.06 wt.% Ni showed different solidification features: (a) The liquidus temperature was almost the same for two alloys; (b) The primary α-Al phase emerged at 621$^o$C in Figure. 10a but 614$^o$C in Figure 7.9b; (c) The eutectic temperature was 584$^o$C in Figure. 9a and 575$^o$C in Figure 7.9b; and (d) The most interesting point was that the emergence of Ni-rich intermetallics was prior to the eutectic solidification of Al-$Mg_2Si$. In the meantime, the eutectic reactions for Al-$Mg_2Si$ and Al-AlFeMnSiNi were at the same temperature. The results confirmed that the increase of Ni in the alloy resulted in an increase of the solidification range of the alloy, therefore increasing the possibility of forming hot tearing and shrinkage porosity in the casting.

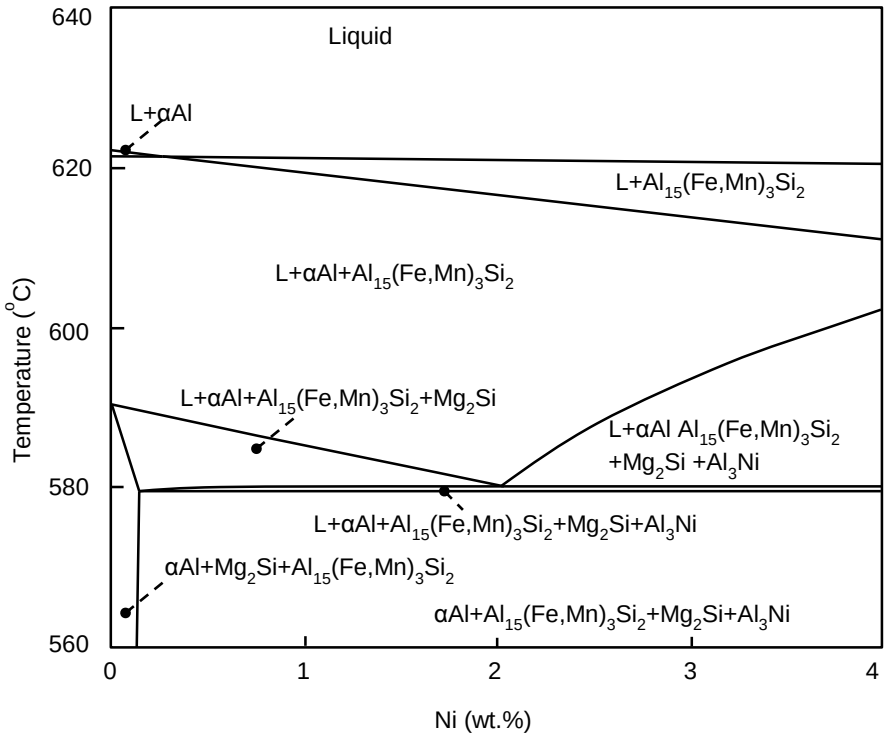


Figure 7.40 Equilibrium phase diagram of the Al-5Mg-2Si-0.6Mn-0.2Fe-xNi alloy calculated with Pandat software.

## 7.5 Formation of Ni-rich Phase in Al-Mg-Si-Mn Alloy

The experimental observations have confirmed that (1) the primary AlFeMnSiNi intermetallics were formed as prior phase during high pressure die-casting, which showed dendritic and fragmented dendritic morphology with different sizes; (2) the eutectics included Al-$Mg_2Si$ and Al-AlFeMnSiNi, but no $Al_3Ni$ intermetallics were observed in the Al-Mg-Si-Mn die-cast alloys with varied Ni contents up to 2.06 wt.%.

Generally, the phase formation of Ni-rich intermetallics in the experimental alloys is broadly consistent with the equilibrium phase diagram calculated from CALPHAD. Therefore the solidification path can be used to explain the major features of the microstructure if α-AlFeMnSi and $Al_3Ni$ are taken as the same phase from the primary solidification and eutectic

solidification. The solidification process and the associated changes of liquid compositions determine the formation of different phases. From the phase diagram in Figure. 10, the prior phase is α-Al phase when Ni content is less than 0.05wt. %. The solidification starts with the formation of the α-Al phase, followed by the formation of AlFeMnSi and eutectics of Al-$Mg_2Si$. This has been discussed in previous Chapters. When Ni content is increased to a higher level, the prior phase becomes the AlFeMnSiNi phase. The precipitation of AlFeMnSiNi compounds decreases the undercooling in front of the interface of the crystal, resulting in the nucleation and growth of α-Al phase in association with AlFeMnSiNi compounds (Figures 7.3&7.4). The solidification continues until the completion of eutectic solidification. When Ni content is further increased, the prior phase is still AlFeMnSiNi phase, but the primary solidification cannot consume all Ni in the alloy and therefore Ni takes part in the eutectic solidification to form Al- AlFeMnSiNi eutectics in association with Al-$Mg_2Si$ eutectics. Overall, Ni in the Al-Mg-Si-Mn alloy is consumed by forming primary AlFeMnSiNi phase in the primary solidification and Al- AlFeMnSiNi eutectics in the eutectic solidification, which is always associated with the consumption of Fe, Mn and Si. On the other hand, the addition of Ni in the alloy introduces new prior phase that releases latent heat during solidification. Therefore, the cooling rate for eutectic solidification is reduced, resulting in the increase of the eutectic spacing.

The absence of $Al_3Ni$ intermetallics in the die-cast Al-Mg-Si-Mn alloy is one important feature. In the equilibrium state, $Al_3Ni$ phase that contains 42wt.% Ni has an orthorhombic structure (the space group Pnma, 16 atoms in the unit cell) with the lattice parameters a = 0.6611 nm, b=0.73662 nm, and c = 0.4812 nm. The heat of forming this phase is 40 J/mol. The density of the phase in the binary system is in the range 3.95-3.96 $g/cm^3$ [177]. Currently, it is not clear yet for the association between α-AlFeMnSi and Ni in the experimental alloy. It was observed that $Al_3Ni$ were formed in a fair low Ni content in Al-Mg-Si wrought alloys, which is not consistent with the results in this work. However, the differences between previous work and this work is obvious because the Fe content is low in the wrought alloy and the Mn content is relatively high in the alloy in this work. The role of Mn in cast Al-Mg-Si-Mn alloy has been discussed in previous chapters. Although the association between Ni and AlFeMnSi intermetallics has been indirectly confirmed, the mechanism of the formation of AlFeMnSiNi intermetallics needs to be addressed as it may be important to develop materials for special application.

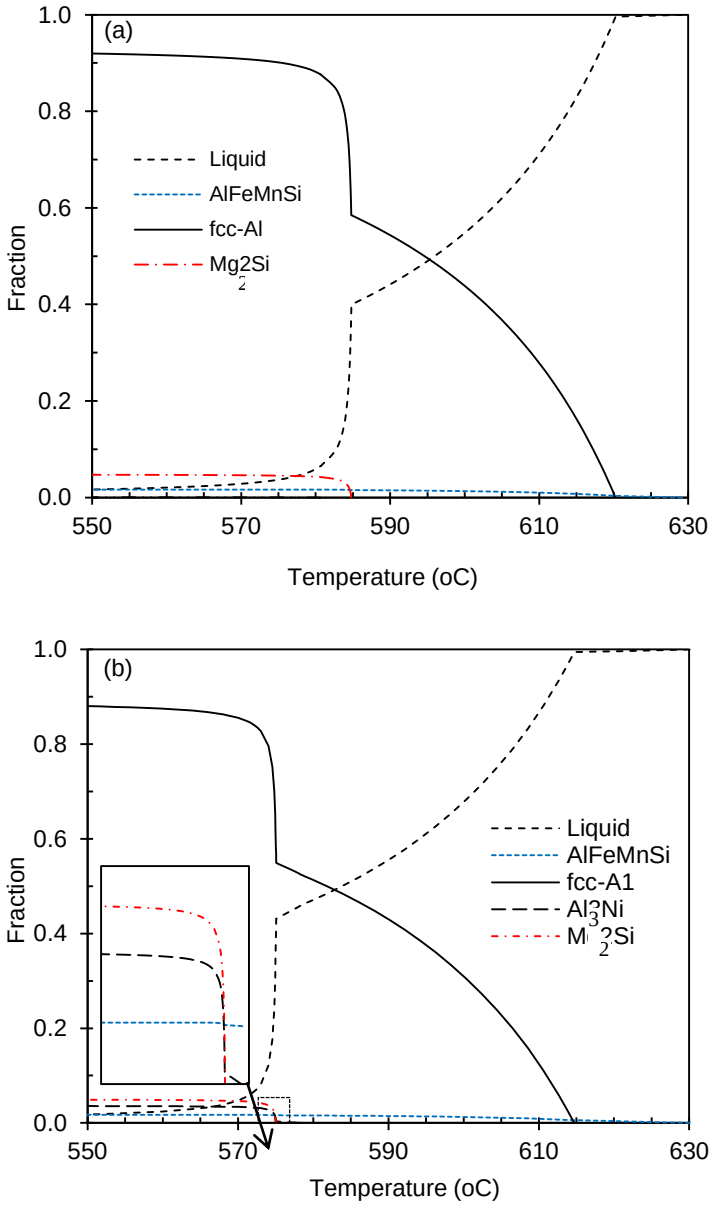


Figure 7.41 The variation of the fraction of the liquid phase and solidified phases with temperature in the solidification interval of the Al-Mg-Si-Mn alloys with (a) 0.005 wt.% Ni, (b) 2.06 wt.% Ni.

## 7.6 Summary

In the die-cast Al-Mg-Si-Mn alloy containing different Ni contents, the formation of Ni-rich intermetallics occurs consistently during solidification. The Ni-rich intermetallics exhibit dendritic and lamellar morphology during primary and eutectic solidification, respectively.

In the die-cast Al-Mg-Si-Mn alloy, Ni is always associated with Fe, Mn and Si to form AlFeMnSiNi intermetallics. No $Al_3Ni$ intermetallics is observed at Ni concentrations up to 2.06wt%, while both primary AlFeMnSiNi phase and eutectic AlFeMnSiNi phase are found in the as-cast microstructure. Both the primary and eutectic Ni-rich intermetallics are identified as the same AlFeMnSiNi phase with the typical composition of $Al_{[100\text{-}140]}(Fe,Mn)_{[2\text{-}7]}SiNi_{[4\text{-}9]}$.

The increased Ni-rich intermetallics can be found in the alloy with higher Ni contents. The increased Ni contents result in an increase in the spacing of Al-$Mg_2Si$ eutectics in the die-cast Al-Mg-Si-Mn alloy. This indicates that the increased levels of Ni contents lower the growth velocity of the eutectic Al-$Mg_2Si$ during the solidification of the die-cast Al-Mg-Si-Mn alloy.

The addition of Ni significantly affects the mechanical properties of the alloy castings. The higher the Ni concentrations in the alloy, the more significant the reduction in ductility. This is accompanied by a slight enhancement of the yield strength. The ultimate tensile strength increases slightly when adding a small amount of Ni into the die-cast alloys, but further increase of the Ni content results in the decrease of the UTS.

# Chapter 8
# Assessment of Repeatability of Castings of Al-Mg-Si-Mn Alloys

## 8.1 Introduction

The repeatability of mechanical properties in die castings is a big concern in production and now effective way to identify and describe the detail. In this Chapter, the mechanical properties were assessed for the standard samples that were directly made by high pressure die-castings and obtained from the machined high pressure die-castings at different locations in order to evaluate the repeatability of casting components made by the Al-Mg-Si-Mn alloy. The distributions of the yield strength, ultimate tensile strength (UTS) and elongation of the samples were analysed by the average value with standard deviations and by the Weibull statistical model with three parameters, during which the suitability of Weibull method for characterising the fracture behaviour was analysed and the parameters in probability function were used to compare the relative reliability of the castings at different locations. The microstructure, defects levels and fractural graphical behaviour were examined and analysed in relation to the Weibull parameters for the different types of samples.

## 8.2 Mechanical Properties of Die Casting Trials

Two sets of die were used for the present study. One was employed to cast six ASTM standard samples with three ϕ6.35 mm round samples and three flat samples with cross sections of 6.35×2mm, 6.35×3mm and 6.35×5mm, respectively. Detailed description of the casting structure with runner system and overflow can be found in Chapter 3. Another set of die was used to make a casting for automotive industry with the same machine. The casting structure with overflow and gating system is shown in Figure 8.1. The typical wall thickness is 2.8mm

for the die-casting. The injection parameters were optimised for each type of casting and the castings were made under the corresponding optimised condition. The die for trial castings was heated using the same way with the tensile sample die by circulation of mineral oil at 250°C. 20 pieces of trial castings were selected for making tensile samples. 5 standard flat samples with a cross section of 6.35×2.8mm were machined from each trial casting and the locations are marked in Figure 8.1.


Figure 8.42 The photos showing the casting structure with runner, over flow and biscuit for evaluation of the reproductivity.

The measured mechanical properties of the Al-Mg-Si-Mn alloy are shown in Figure 8.2 for 99 ϕ6.35 tensile samples with double standard deviations and the average values are also presented in Table 8.1. The average was 146.6 MPa for the yield strength, 302.7 MPa for the UTS and 16.5% for the elongation. Majority of the measured data were within the square defined by the double standard deviation. This confirms the good consistence of mechanical properties. Figure 3 shows the mechanical properties of the flat tensile samples with double standard deviations. The averages of 40 samples tested for each thickness of samples are listed in Table 8.1. As seen, the thinner samples exhibited lower elongation and lower ultimate tensile strength, but higher yield strength. The average value was 7.9% of elongation, 174.8 MPa of yield strength and 295.6MPa of UTS for 2mm thick flat sample, and the average value was 10.2% of elongation, 164.2 MPa of yield strength and 306.0MPa of UTS for 3mm thick flat samples, and the average value was 14.9% of elongation, 165.7 MPa of yield strength and 314.9MPa of UTS for 5mm thick flat samples. In the meantime, the measured data were almost within the double

standard deviations. Moreover, in comparison of the mechanical properties obtained by the round and the flat tensile samples, the yield strength, UTS and elongation were all higher for the round samples. In particular, the average elongation of the round samples was doubled over that of the 2mm thick flat samples, although the yield strength was higher and the UTS was lower for the 2mm thick flat samples. On the other hand, it is also seen an overlapping among the measured data for the different types of samples. The overlapping had different levels, but over 35% of the measured strength was seen at similar levels, which indicates that the overlapping of the data is significant.

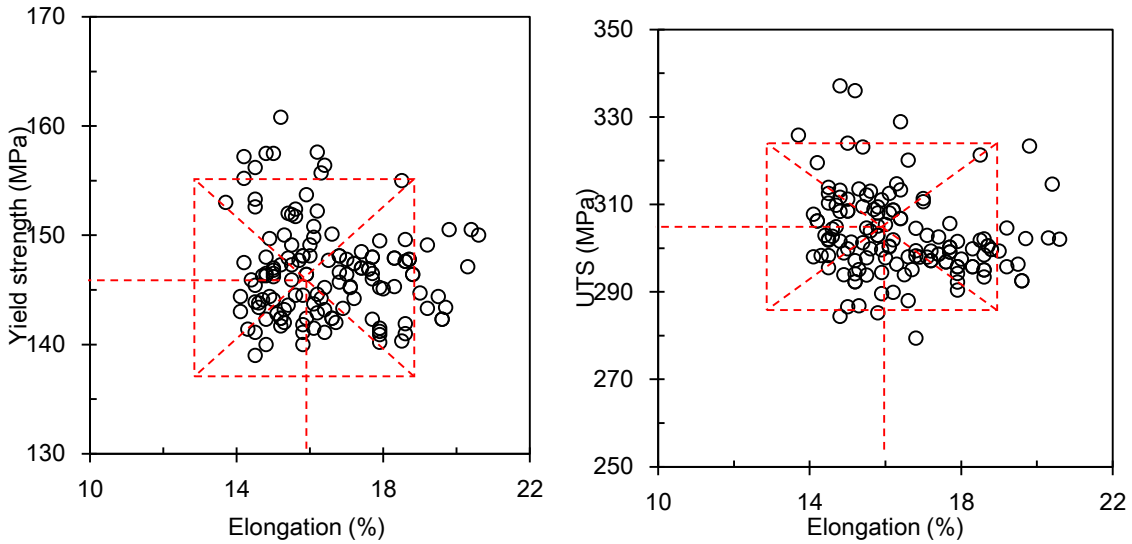


Figure 8.43 The yield strength and the ultimate tensile strength (UTS) as a function of the elongation of the standard ϕ6.35mm round samples. The squares represent the value of two times standard deviation of the tested samples and the centre of squares is the average value of tested data.

Table 8.3 The average value and standard deviation of the measured yield strength, ultimate tensile strength and elongation of the tensile samples with as-cast surface or with machined surface.

| Sample type | | Sample label and dimension | Elongation (%) | | Yield strength (MPa) | | Ultimate tensile strength (MPa) | |
|---|---|---|---|---|---|---|---|---|
| | | | Average | 2x STD | Average | 2xSTD | Average | 2x STD |
| round sample | | ϕ6.35mm | 16.47 | 3.24 | 146.63 | 8.64 | 302.70 | 19.11 |
| Cast flat sample | | 2×6.35mm | 7.98 | 2.11 | 174.79 | 20.90 | 295.61 | 15.36 |
| | | 3×6.35mm | 10.16 | 2.31 | 164.23 | 9.06 | 305.99 | 13.76 |
| | | 5×6.35mm | 14.91 | 2.52 | 165.75 | 17.25 | 314.93 | 17.91 |
| Machined flat sample | 1 | 2.8×6.35mm | 9.90 | 1.40 | 148.87 | 20.81 | 273.78 | 33.05 |
| | 2 | 2.8×6.35mm | 9.91 | 1.12 | 145.36 | 21.54 | 270.82 | 23.30 |
| | 3 | 2.8×6.35mm | 9.29 | 0.57 | 154.39 | 16.60 | 275.73 | 23.45 |
| | 4 | 2.8×6.35mm | 8.74 | 1.08 | 155.66 | 13.89 | 258.38 | 27.74 |
| | 5 | 2.8×6.35mm | 9.36 | 0.90 | 152.35 | 16.35 | 278.34 | 36.88 |
| | Total average | | 9.44 | 1.01 | 151.32 | 17.84 | 271.41 | 28.88 |

STD: standard deviation

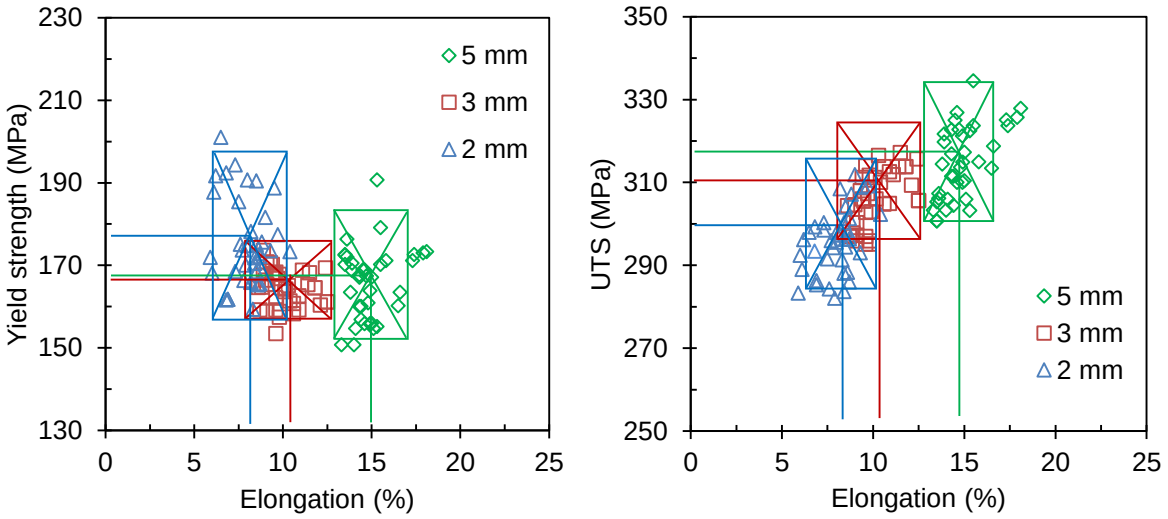


Figure 8.44 The yield strength and the ultimate tensile strength (UTS) as a function of the elongation of the standard flat tensile samples with a cross section of 6.35×2mm, 6.35×3mm, 6.35×5mm. The straight lines across to the axis represent the average value of the tested data and the squares represent the value of two times standard deviation of the tested samples.

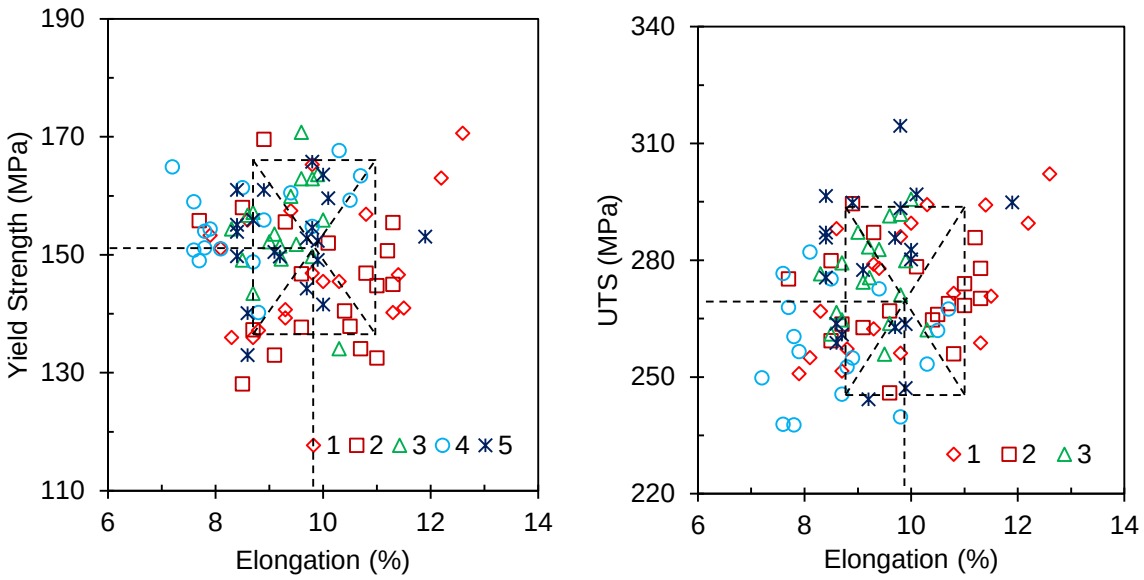


Figure 8.45 The yield strength and the ultimate tensile strength (UTS) as a function of the elongation of the flat tensile samples cut from the as-cast castings with a cross section of 6.35×2.8mm.

In order to assess the mechanical properties of the trial castings, 100 samples were machined from 20 castings, in which the different locations are shown in Figure 8.1. The machined samples were flat with two as-cast surfaces and two machined surfaces. The mechanical properties of the machined samples are shown in Figure 8.4 and the average values of measured data are also listed in Table 8.1. As seen, the measured data were almost overlapping for the different locations, although slight differences could be observed. The total average was 9.44% of elongation, 151.3 MPa of yield strength and 271.4MPa of UTS. The averages of the measured data at each location were quite close the total average because of the small standard deviations. However, the elongation and UTS at location 4 were lower than that at other locations, although the yield strength was still at similar level. This means that location 4 was the weak area in the castings. Meanwhile, the mechanical properties at location 1 showed a widest spread, and the mechanical properties at locations 2 and 3 showed a very similar distribution in comparison with the data among the 5 locations in Figure 8.4. The results in Figures 8.2 to 8.4 and Table 8.1 showed that the application of average value with standard deviations is capable of assessing the mechanical properties, but the overlapping is significant. It is thus very rough to differentiate the data scatter and error distribution in the trial castings.

## 8.3 Weibull Statistic Analysis

Weibull distribution expresses the cumulative probability of failure as a function of maximum applied tensile stress acting in an effective volume of sample. The mathematic function is expressed as [108]

$$P_f = 1 - exp\left[-\left(\frac{\sigma-\sigma_u}{\sigma_0}\right)\right]^m \quad (8.1)$$

$$ln\left(1 - P_f\right) = -\left(\frac{\sigma-\sigma_u}{\sigma_0}\right)^m \quad (8.2)$$

$$ln\left[ln\left(\frac{1}{1-P_f}\right)\right] = m[ln\,(\sigma - \sigma_u) - ln\,\sigma_0\,)] \quad (8.3)$$

where $P_f$ is the cumulative fraction of specimen failures in tensile test; $\sigma$ is the variable being measured (yield strength, UTS or elongation to fracture); $\sigma_u$ is the threshold parameter, i.e. the characteristic stress (or strain) below which no specimen is expected to fail; $\sigma_0$ is the scaling parameter, also called the characteristic stress (or strain) at which the probability of failure is 63.2%; $m$ is the shape parameter, also referred to as the Weibull modulus [178].

Equation (8.3) configures the three-parameter Weibull distribution. The double logarithm of the reciprocal ($1\text{-}P_f$) can be easily plotted with $ln(\sigma)$ because the $ln[ln(1/(1\text{-}P_f))]$ *vs.* $ln(\sigma)$ shows a straight linear relation with slope $m$ and intercept $-m \cdot ln(\sigma_0)$. If the experimental distribution is in agreement of Weibull distribution, a straight line can be produced with a simple graphical representation of the data with regression analysis. The slope $m$ physically represents the Weibull modulus.

Good structural materials should have high Weibull modulus, which means high repeatability of the strength values and high reliability of the materials. The narrow distribution of defect size and the high flaw tolerance in the materials are means of improving the Weibull modulus. Without additional information the Weibull distribution in Equation (8.3) is difficult to use because it contains many unknown variables. During calculation, the $\sigma$ values (tensile strength or elongation) are arranged in order of increasing value as follows:

$$\sigma_1 \leq \sigma_2 \leq \sigma_3 \cdots \leq \sigma_f \cdots \leq \sigma_n \quad (8.4)$$

A probability of failure is assigned to each $\sigma$ such that:

$$P_1 \leq P_2 \leq P_3 \cdots \leq P_f \cdots \leq P_n \quad (8.5)$$

where $0 \leq P_j \leq 1$. Because the sample tested is considered representative of a large population, the true value of $P_f$ for each $\sigma_f$ is not known and has to be estimated. There are a number of statistical criteria that can be used to estimate the probability of failure $P_f$ [179,180], in which the most common approach is the median rank method, alternatively referred to as the Bernard method [181], which calculates the failure probability $P_f$ as

$$P_f = (i-0.3)/(n+0.4) \quad (8.6)$$

where $i$ is the ranked position of the specimen strength (or strain) in that set of castings and $n$ is the total number of specimens.

The scaling parameter $\sigma_0$ is determined by the y-intercept at $P_f = 0.632$. The threshold parameter $\sigma_u$ is determined by calculation, during which a $\sigma_u$ is initially assumed and assigned in equation (8.3) to obtain the corresponding $\sigma$. The regression of the calculated $\sigma$ creates a linear equation and its coefficient of determination ($R^2$). Therefore, by assuming a series of $\sigma_u$ at a value less than the minimum data of measurement, a number of $R^2$ can be obtained. Then the final threshold parameter $\sigma_u$ can be found from the corresponding equation that has the maximum $R^2$.

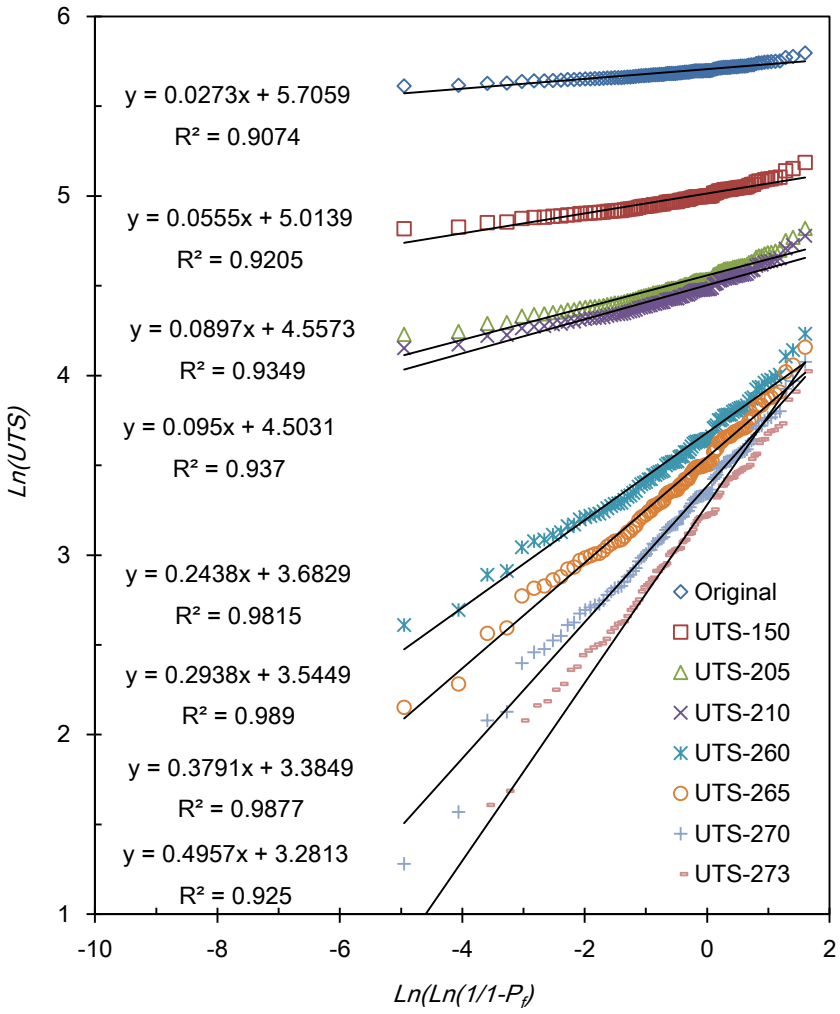


Figure 8.46 Weibull plots for the UTS of Al-Mg-Si-Mn alloy obtained from the round standard tensile test bars that were directly cast by HPDC process.

In order to assess the repeatability using Weibull analysis, the data in Figures 8.2 to 8.4 were reorganised in ascending order with calculated $P_f$ according to Eq. (8.6). Figure 8.5 shows the representative Weibull plots of the UTS obtained from the as-cast round samples. The solid lines were the corresponding linear fit with Eq. (8.3) at different levels of $\sigma_u$. Then the best-fit line was obtained by the maximum R-square value. After finding the maximum R-square value, it was immediately used to evaluate the applicability of the Weibull distribution for the measured results by using a goodness-of-fit. For assessing the goodness-of-fit, the critical values of $R^2$ with α=0.05 ( $R^2_{0.05}$) was calculated according to the formula [182]

$$R^2_{0.05} = 1.0637 - \frac{0.4174}{n^{0.3}} \qquad (8.7)$$

For the as-cast round samples, the sample number was 99, the calculated $R^2_{0.05}$ was 0.9585. The principle of assessing the measured data is that the Weibull distribution is not applicable if the $R^2$ of the linear regression from the Weibull probability plot is less than the value of $R^2$ with $\alpha$=0.05. This means that the $R^2$ from the regression equation needs to be larger than the $R^2$ at 0.05 in order to satisfy the Weibull distribution. By comparing the $R^2$= 0.9585 from the equation (8.7), the $R^2$ value was 0.9759 for the best-fit line in Figure 8.5 for the as-cast round samples. The higher $R^2$ value means that the measured data can be well described by Weibull distribution. By using the same methodology, the statistic results were obtained for different parameters with different types of samples. Table 8.2 lists the characteristic parameters in Weibull distribution of the yield strength, UTS and elongation of the tensile samples with as-cast surface and with machined surface**.**

Table 8.4 Calculated parameters in Weibull statistics analysis of the yield strength, ultimate tensile strength and elongation of the tensile samples with as-cast surface and with machined surface**.**

| Property | Sample | m | $\sigma_u$ | $\sigma_0$ | $R^2$ |
|---|---|---|---|---|---|
| Yield strength | ϕ6.35mm, as-cast surface | 4.43 | 131 | 26.78 | 0.9899 |
| | 5×6.35 mm, as-cast surface | 2.54 | 145 | 23.36 | 0.9612 |
| | 3×6.35 mm, as-cast surface | 2.78 | 145 | 18.67 | 0.9747 |
| | 2×6.35 mm, as-cast surface | 1.65 | 158 | 14.82 | 0.9755 |
| | 2.8×6.35 mm, machined surface | 3.92 | 117 | 37.71 | 0.9885 |
| Ultimate tensile strength (UTS) | ϕ6.35mm, as-cast surface | 4.17 | 260 | 43.82 | 0.9759 |
| | 5×6.35 mm, as-cast surface | 2.81 | 297 | 19.17 | 0.9728 |
| | 3×6.35 mm, as-cast surface | 2.71 | 293 | 17.67 | 0.9425 |
| | 2×6.35 mm, as-cast surface | 2.11 | 279 | 14.86 | 0.9787 |
| | 2.8×6.35 mm, machined surface | 3.34 | 223 | 54.26 | 0.9924 |
| Elongation | ϕ6.35mm, as-cast surface | 4.81 | 13.2 | 11.36 | 0.9913 |
| | 5×6.35 mm, as-cast surface | 2.40 | 4.5 | 3.88 | 0.9837 |
| | 3×6.35 mm, as-cast surface | 1.89 | 8.5 | 3.84 | 0.9904 |
| | 2×6.35 mm, as-cast surface | 1.32 | 3.7 | 2.68 | 0.9671 |
| | 2.8×6.35 mm, machined surface | 3.50 | 7.4 | 5.48 | 0.9814 |

The results in Table 8.2 confirmed that the tensile test data can be adequately modelled by three-parameter Weibull statistical analysis. For the yield strength, the as-cast round samples had a maximum Weibull modulus, which indicates that the as-cast round samples exhibited a best reliability and reducibility. Meanwhile, the machined samples exhibited the second best of Weibull modulus, which means that the machined samples have better repeatability than the as-cast flat samples. Among the flat samples, the 2mm thick samples had the lowest and the 5mm thick samples had the highest Weibull modulus, although the flat samples showed a lower value of Weibull modulus than the machined samples and the as-cast round samples. On the other hand, as described above, the parameters $\sigma_0$ and $\sigma_u$ are preferred to be higher in the castings because no sample is expected to be failed below $\sigma_u$ and the probability of failure is 63.2% at $\sigma_0$. However, it was not observed the highest $\sigma_u$ for the yield strength, UTS in the as-cast round samples and only the $\sigma_u$ for elongation is the highest value. On the other hand, although slight inconsistent in the parameters for elongation, the as-cast samples provided the higher $\sigma_u$. This means the samples with as-cast surface provided better strength than the machined samples. When reviewing the data of $\sigma_0$, the results showed that the as-cast round samples had the highest value and the machined samples had the second best results. This is consistent with the data of Weibull modulus ($m$). Overall, comparing the as-cast round samples and the as-cast flat samples, the as-cast round samples showed good repeatability and reliability. It was expected that the machined samples would show worse ductility than the as-cast samples because of the removal of casting surface. However, the machined samples showed good performance described by the Weibull parameters among the different types of samples. The repeatability and reliability of the machined samples were reasonable good, although the strength under which the samples were not failed was slightly lower in the testing samples. It is important to note that the values in the Weibull parameters in the as-cast flat samples in particular the 3mm thick flat samples were relatively close to that obtained by the machined samples. This means that the as-cast flat samples are better than the as-cast round samples and other thickness of samples for evaluating the casting performance in manufacturing.

## 8.4 Fractography and Microstructure

The fractographic observations were carried out on the fractured samples, which had the characteristic parameters close to $\sigma_0$. The fractographic micrographs of the as-cast and machined samples are shown in Figures 8.6 to 8.10. On the fractured surfaces, it is always seen a layer with smooth fracture on the casting surface and a coarse fracture area in the centre area of the samples. Multiple failure sources were observed on the fracture surfaces of each type of sample; hence the normal failure mechanism was plausibly caused by internal defects in the corresponding casting. Porosities were also observed on the fracture surfaces, which were particularly severe in the flat samples with 2 mm and 3 mm thickness. The porosities were seldom observed in the as-cast round samples but frequently seen in the 2mm flat samples.

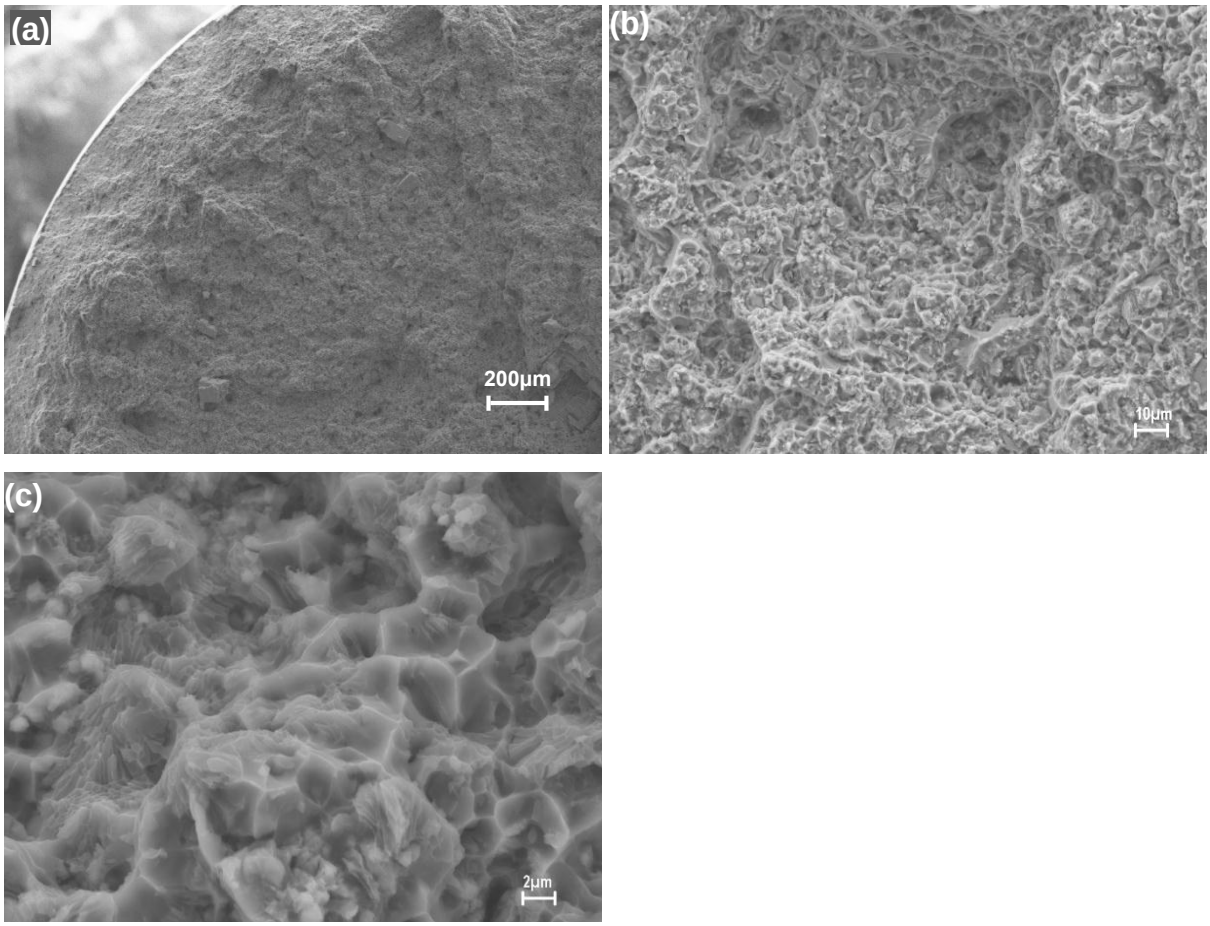


Figure 8.47 Typical fractographs on a cross section of ϕ6.35 mm die-cast tensile sample (a) overall fractural image, (b) fracture surface at high magnification, and (c) detailed fracture.

Furthermore, the porosity levels were quantitatively measured using optical microscope on the as-polished metallographic surfaces of the different type samples, which were also selected from the castings made under the same batch as the fractured samples. The results are shown in Figure 8.11. The average porosity levels were from 0.8 vol.% to 1.9 vol.%. The as-cast round samples had the least amount of porosities and the as-cast 2mm thick flat samples had the highest amount of porosities. The porosity levels in the trial castings were similar with that in the 3mm thick flat samples; both of them were higher than that in the as-cast round samples. The results of porosity levels are consistent to the parameters obtained from Weibull analysis, in which the samples with less porosity provided increased Weibull modulus, threshold parameter and scaling parameter. Therefore, the improvement of repeatability, the increase of the failed strength and the failure probability of 63.2% are achieved.

Generally, the microstructure plays key roles in determining the materials mechanical properties. Therefore, the as-cast microstructures were examined for the different types of samples. Figure 8.12 shows the microstructure on a cross section of the die-cast ϕ6.35mm tensile sample. As seen, no obvious microstructural segregation and porosities were found on the cross section. Figure 8.13 shows the detail microstructure of the die-cast ϕ6.35mm tensile sample near the surface and near the centre. The micrographs exhibited the typical die-cast microstructure. The mixture of coarse and fine primary α-Al grains was observed in Figure 8.12 and 8.13. However, the centre had more coarse primary α-Al grains and defects. The similar results could also be observed in other samples, as shown in Figures 8.14 to 8.21. However, there were several differences being found in the different samples. For the flat samples, while the 5mm thick samples showed very similar microstructure in comparison with that of ϕ6.35mm round samples, the thinner sample at 2mm and 3mm showed an apparent microstructural segregation because the fewer amounts of primary α-Al grains were seen in the surface area, which is particularly severe for the 2mm thick samples. It was also found that more porosities in the thinner samples (Figure 8.18). For the machined samples, it was found microstructural segregation near the surface area, but the coarse primary α-Al grains showed less dendritic morphology. From these results, it is clear that the samples exhibited the similar microstructure, although slight differences were observed for the coarse primary α-Al grains. The thin samples showed significant segregation in the surface area and more porosity was observed in the samples. The microstructural uniformity is also the fundamentals to result in the difference in the mechanical properties and in the Weibull parameters obtained in Weibull statistic analysis.

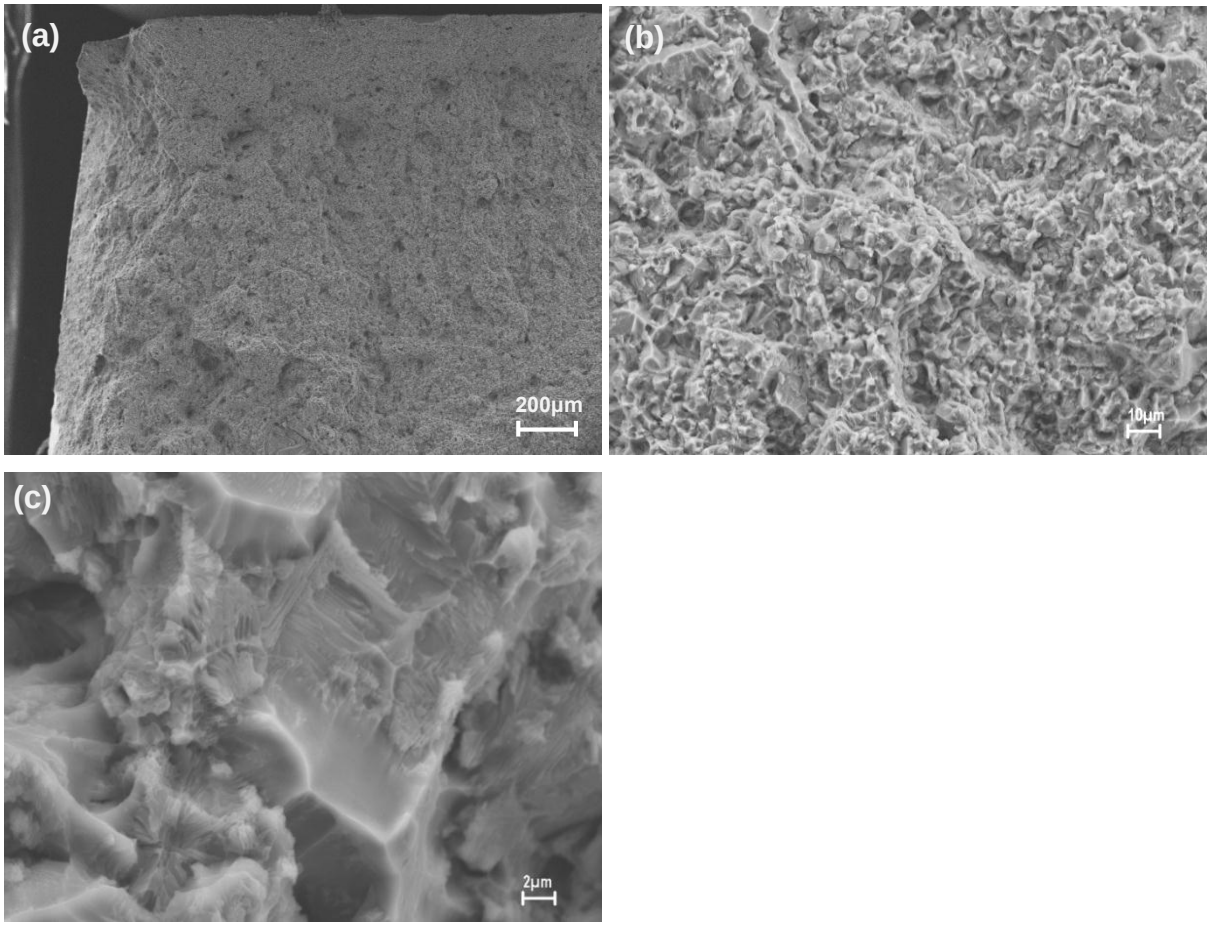


Figure 8.48 Typical fractographs on a cross section of 5×6.35 mm flat die-cast tensile sample (a) overall fractural image, (b) fracture surface at high magnification, and (c) detailed fracture.

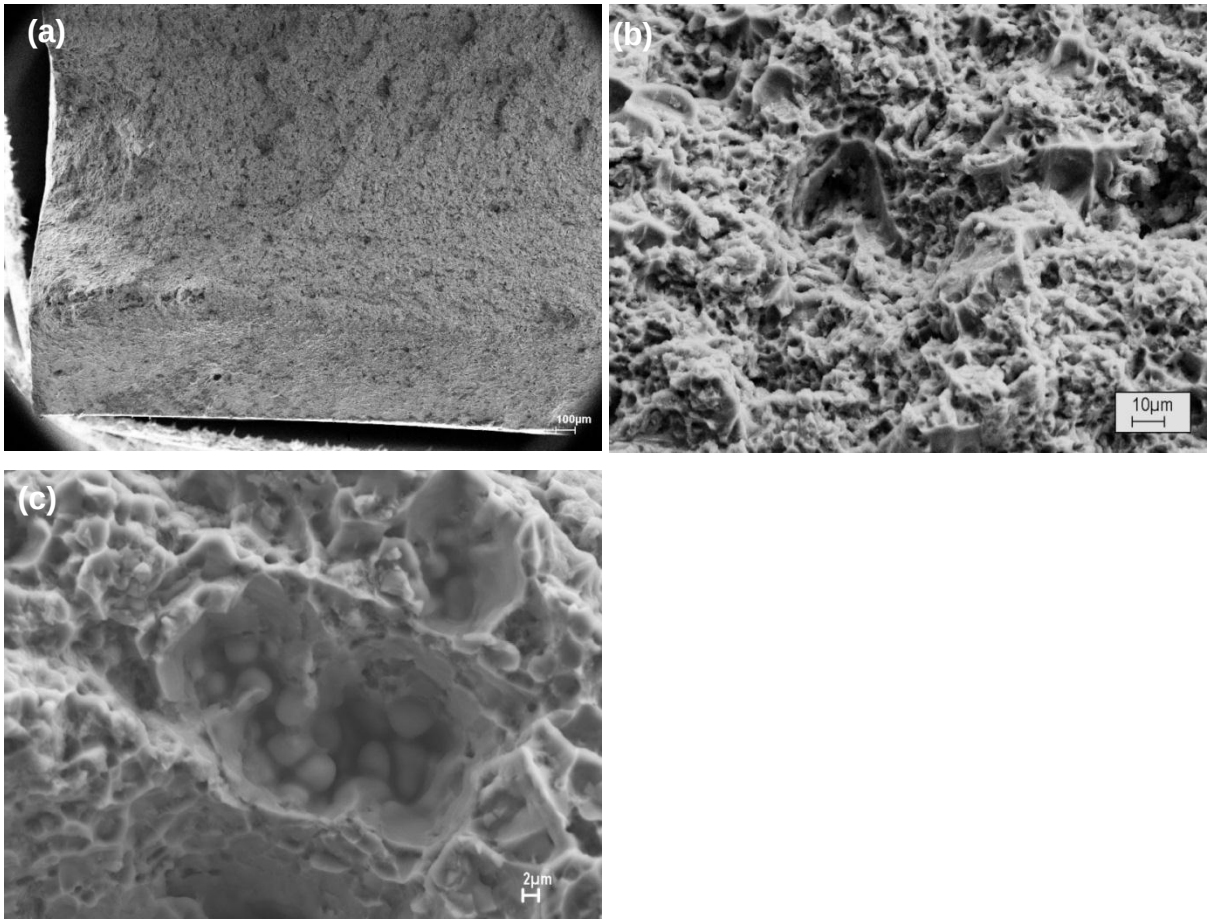


Figure 8.49 Typical fractographs on a cross section of 3×6.35 mm flat die-cast tensile sample (a) overall fracture image, (b) fracture surface at high magnification, and (c) detailed fracture.

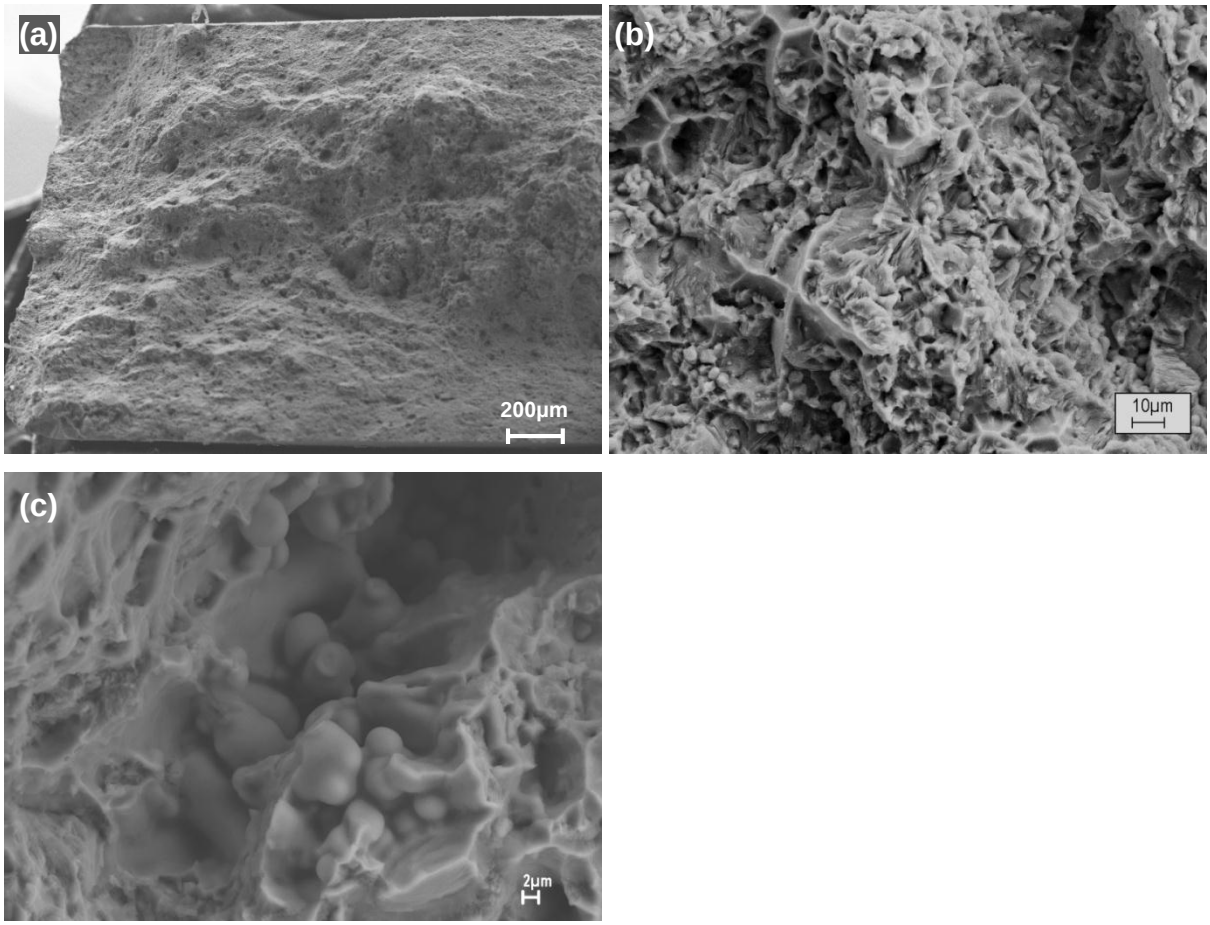


Figure 8.50 Typical fractographs on a cross section of 2×6.35 mm flat die-cast tensile sample (a) overall fractural image, (b) fracture surface at high magnification, and (c) detailed fracture.

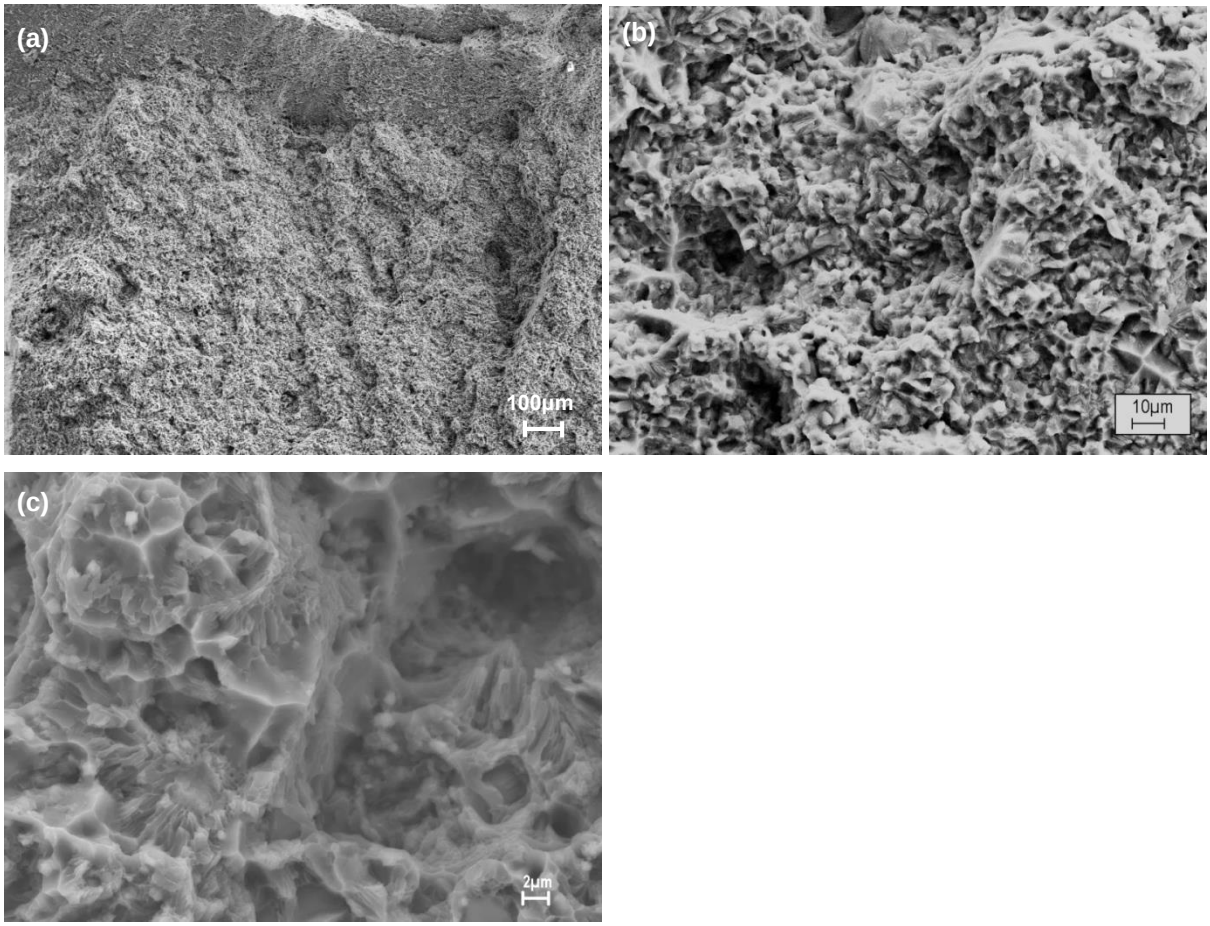


Figure 8.51 Typical fractographs on the cross section of 2.8×6.35 mm tensile sample machined from the trial castings (a) overall fractural image, (b) fracture surface at high magnification, and (c) detailed fracture.

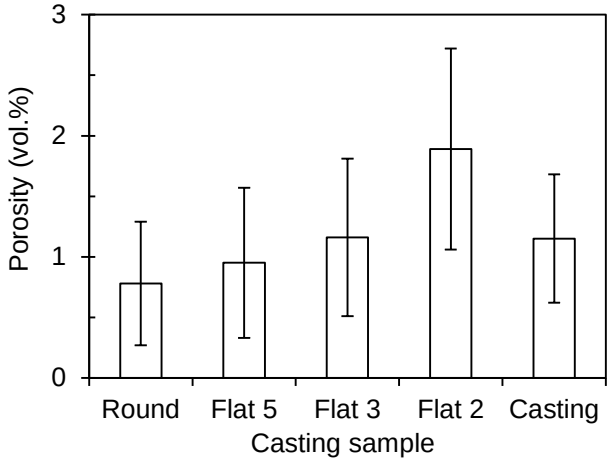


Figure 8.52 The porosity levels of the tensile samples obtained from the different shapes and surface conditions. 'Round' represents the ϕ6.35mm sample; 'Flat 5' represents the 5×6.35mm sample; 'Flat 3' represents the 3×6.35mm sample; 'Flat 2' represents the 2×6.35mm sample; 'Casting' represents the 2.8×6.35mm sample machined from the trial castings.

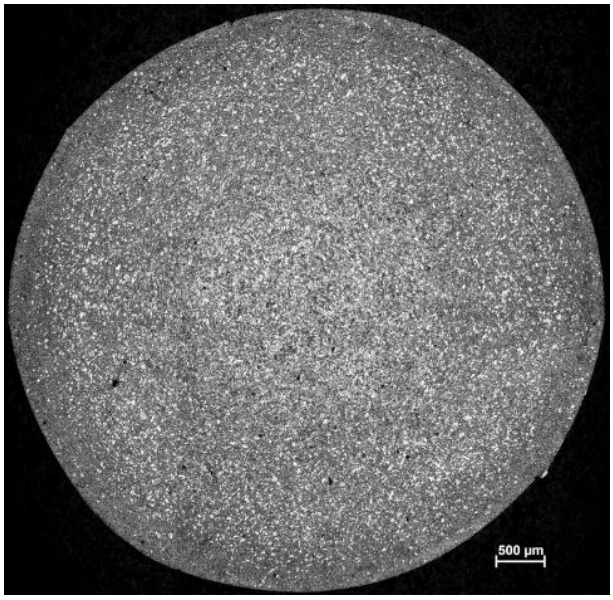


Figure 8.53 Optical micrograph showing the microstructure on a cross section of the die-cast ϕ6.35mm tensile sample.

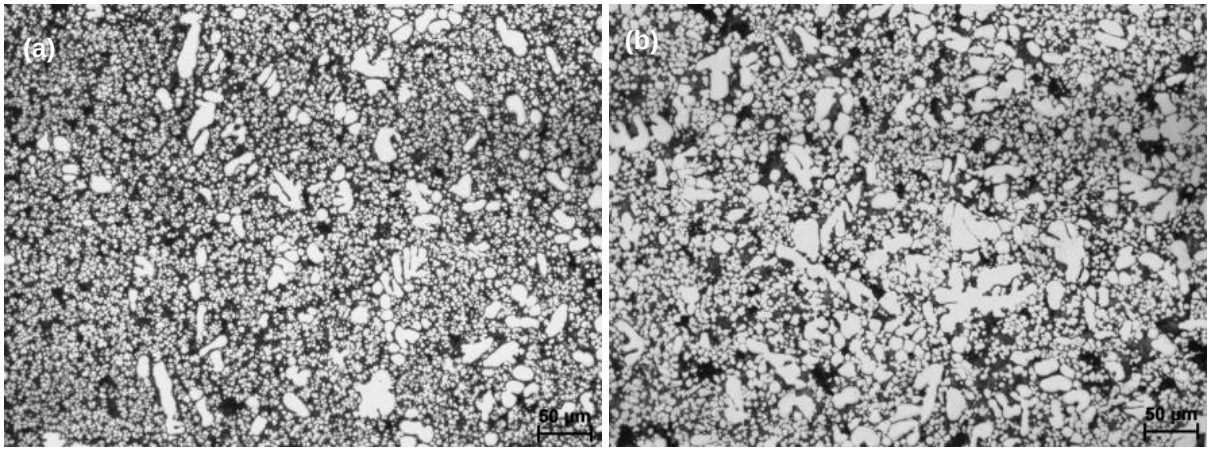


Figure 8.54 Optical micrographs showing the typical microstructure of the die-cast ϕ6.35mm round tensile sample (a) near the surface and (b) near the centre.

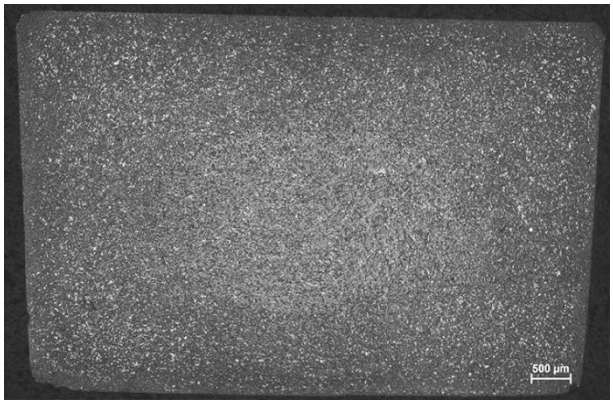


Figure 8.55 Optical micrograph showing the microstructure of the die-cast flat tensile sample with a cross section of 5×6.35 mm.

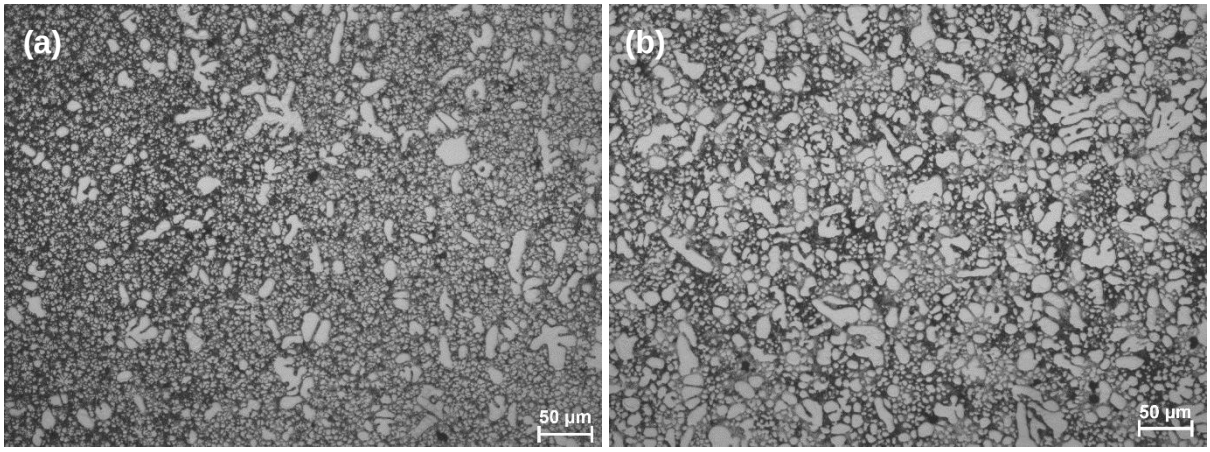


Figure 8.56 Optical micrographs showing the typical microstructure of the die-cast flat tensile sample with a cross section of 5×6.35mm (a) near the surface and (b) near the centre.

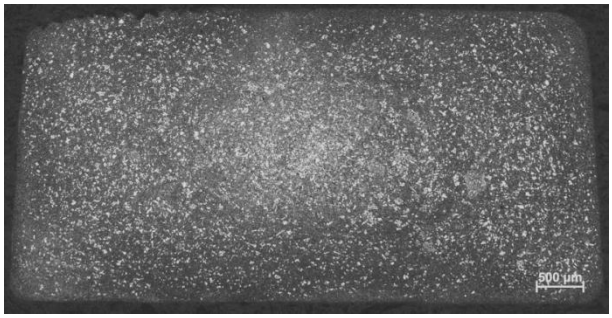


Figure 8.57 Optical micrograph showing the microstructure of the die-cast flat tensile sample with a cross section of 3×6.35 mm.

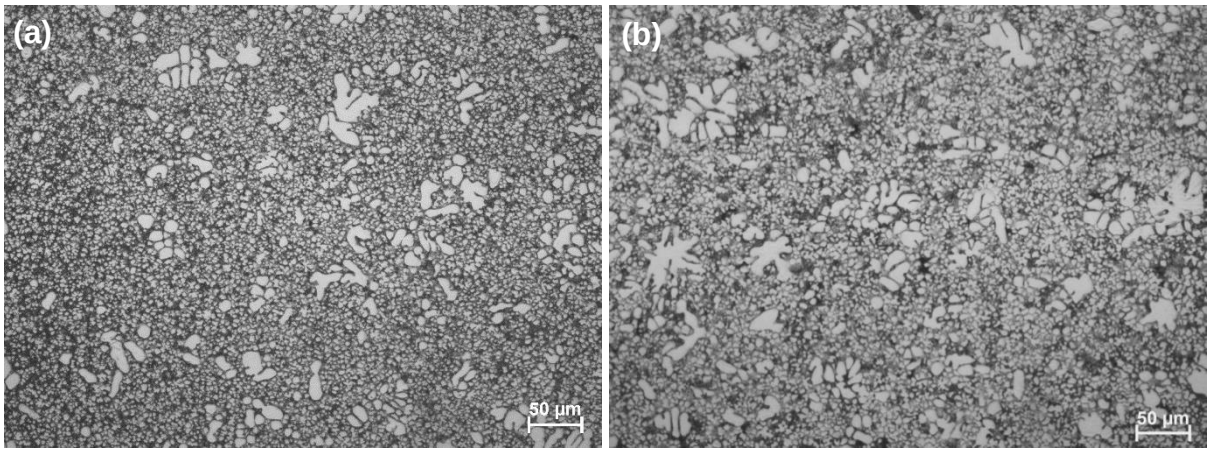


Figure 8.58 Optical micrographs showing the typical microstructure of the die-cast flat tensile sample with a cross section of 3×6.35mm (a) near the surface and (b) near the centre.

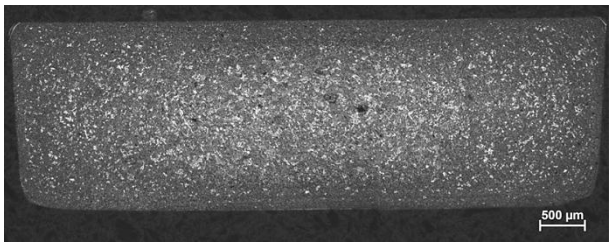


Figure 8.59 Optical micrograph showing the microstructure of the die-cast flat tensile sample with a cross section of 2×6.35 mm.

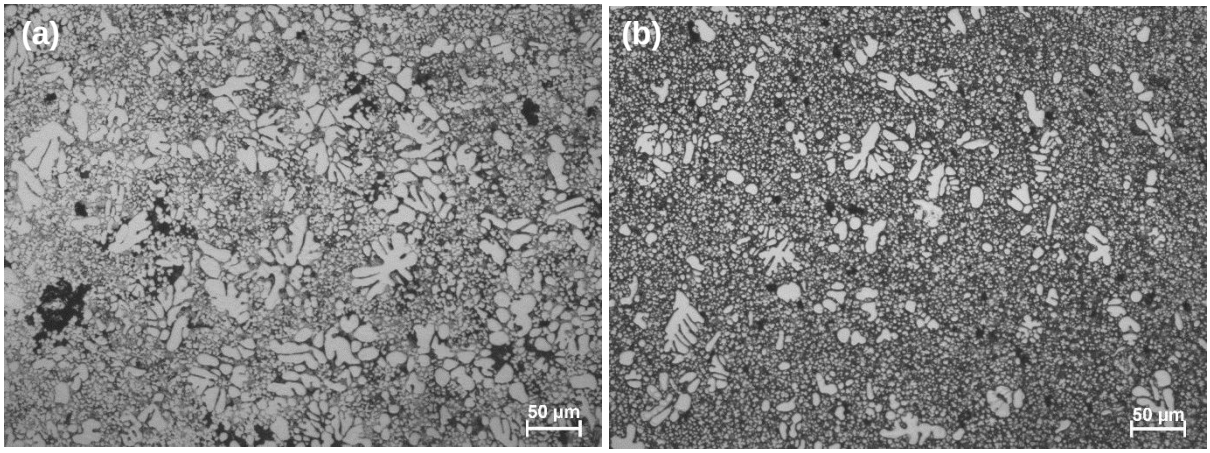


Figure 8.60 Optical micrographs showing the typical microstructure of the die-cast flat tensile sample with a cross section of 2×6.35mm (a) near the surface and (b) near the centre.

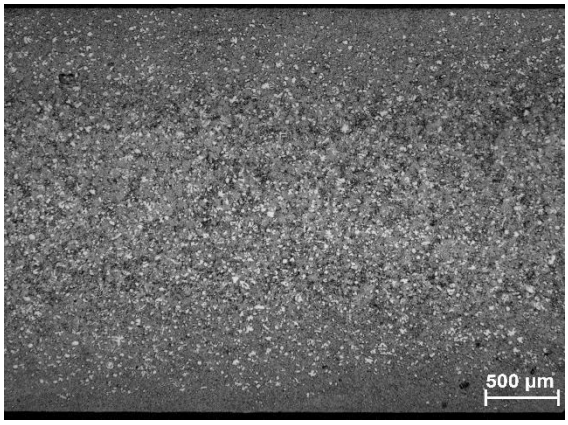


Figure 8.61 Optical micrograph showing the microstructure of the tensile sample machined from the trial casting with 2.8mm wall thickness.

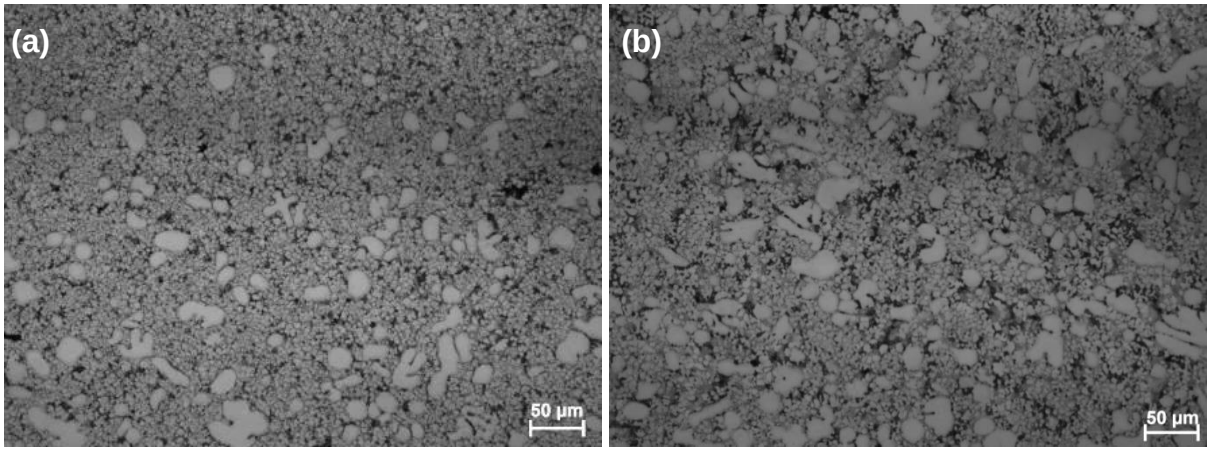


Figure 8.62 Optical micrographs showing the microstructure of the tensile sample machined from the die casting with 2.8mm wall thickness (a) near the surface and (b) near the centre.

## 8.5 Microstructure and Porosity vs. Property and Weibull Modulus

The experimental results showed the level of porosity and the uniformity of microstructure is responsible for the variation of mechanical properties and the Weibull parameters of Al-Mg-Si-Mn alloy. Therefore, the understanding the correlations between the microstructural characteristics and the mechanical properties and the Weibull parameters is important to find out the repeatability and reliability of castings. Because fracture always origins from the porosities throughout the material, the castings with less defects and more uniform microstructure are capable of providing improvement in mechanical properties and repeatability.

As described before, the microstructural formation is determined by the solidification process during HPDC manufacturing. It has been reported [183,184] that the solidification in HPDC process commences when the melt is poured into the shot sleeve. The melt in contact with the shot sleeve is immediately cooled below its liquidus temperature and α-Al phase forms in the shot sleeve with dendritic morphology. The dendrites are then partially fragmented while passing the narrow ingate with high speed and turbulent flow during the die filling. Because of the temperature variation and high flow rate during die filling, the Stoke's motion in the gravity field and Marangoni motion in the non-uniform temperature field promote the solidified primary phase $\alpha_1$ to segregate into the middle of casting section, which leads to the formation of non-uniform microstructure in as-cast condition. Marangoni motion is proportional to the temperature gradient and therefore it is determined by the melt temperature and the die temperature. Stoke's motion is proportional to the square of particle size and reversely proportional to the viscosity of the liquid matrix. Therefore, Stoke's motion becomes significant for large particles and in a liquid with low viscosity. On the other hand, the high turbulent flow promotes the temperature uniformity in the melt throughout the die cavity. With a high cooling rate provided by the metallic die block, the numerous nuclei compete growing until solidification finishes under high cooling rate inside the die cavity. However, the turbulent flow promotes the air entrapment in the casting. The porosities are formed if the entrapped air is not escaped from the melt before finishing the solidification. Therefore, the balance of different flow patterns determines the uniformity of microstructure in the die-castings.

To produce sound castings with HPDC process, the structure of gating and overflow is critical

to alter fluid flow during die filling. For example, the larger ingate size can reduce the flow rate and the degree of turbulence during die filling, thus the entrapped air porosities can be diminished. On the other hand, the optimised inject parameters can also control the melt filling into the die cavity with a proper velocity profile and temperature. The pouring temperature is also a control factor, in which an increased overheating can significantly reduce the formation of coarse primary α-phase in the microstructure and reduce the formation of internal defect such as porosities [185,186]. According to the previous results [187,188], pores present in the microstructure favour crack initiation and propagation therefore are detrimental to the mechanical performance of the material. Conversely, the reduced defects can retard the initialisation of cracks and improve the mechanical properties, in particular the ductility which is more sensitive to the levels of porosities.

The improvement of mechanical properties resulted from the reduction of defects levels can alter the parameters in Weibull statistical distribution. Because of the porosities are randomly distributed in the castings, it is uncertain to know where the porosity will be during manufacturing. The increased porosities increase of fracture possibility under load and the increase of the uncertainty of maximum stress level of castings, and therefore, the increase of scatter in the measured data. Consequently, the repeatability becomes worse and the smaller Weibull modulus in the statistical model can be obtained. Therefore, the reduction of internal defects in die-castings is an effective approach to increase the mechanical properties and obtain better repeatability and reliability in application.

## 8.6 Summary

(1) The high R-square value in the linear fitting confirms that three-parameter Weibull analysis is capable of evaluating the mechanical properties of die-cast Al-Mg-Si-Mn alloy and assessing the repeatability and reliability of castings through Weibull statistic modelling.

(2) The Weibull parameters for the yield strength, ultimate tensile strength, and elongation are different in the die-castings with different geometry including as-cast round and flat samples, and machine samples. The variations of characteristic parameters in three-parameter Weibull analysis show the importance of sampling type in determine the mechanical properties of the alloy and the repeatability and reliability of castings.

(3) The reduced porosity levels and the improved microstructural uniformity in the die-castings result in the decrement of sources for brittle fracture, and therefore improve the mechanical properties and alter the characteristic parameters in Weibull statistical distribution, in particular the repeatability and reliability of die-castings.

# Chapter 9
# Conclusions

1. The ductile die-cast aluminium alloys for automotive body structure have been developed. The optimized composition comprises of 5-5.5wt.%Mg, 1.5-2.0wt.Si%, 0.5-0.7wt.%Mn, 0.15-0.2wt.%Ti. The other impurity elements should be limited in the alloy; especially Fe should be controlled less than 0.25wt.%. The typical mechanical properties of the die-cast alloy at optimized composition are 150MPa of yield strength, 300MPa of ultimate tensile strength, and 15% of elongation under as-cast condition. The paint baking hardenability of the alloy is insignificant. The increase of the yield strength of the die-cast alloy is less than 10% after a simulated ageing under 180oC for 30min. Cu can slightly increase the yield strength under as-cast condition or under heat treated condition with significant scarifying the ductility. Therefore, Cu should be limited in the super ductile aluminium alloy.
2. In the high pressure die casting of ductile aluminium alloys, solidification commences with the formation of primary α-Al phase in the shot sleeve and is completed in the die cavity. The primary α-Al phase formed in the shot sleeve is characterized by the dendrites and fragmented dendrites with the size range from 15 to 100μm and an average of 43μm. The primary α-Al phase formed in the die cavity is characterized by fine globular grains with an average of 7.5μm in size. Solidification inside the die cavity is also responsible for the formation of the lamellar eutectics and the Fe-rich intermetallic. The size of the eutectic cells is about 10μm, in which the lamellar α-Al phase is 0.41μm in thickness. The intermetallic compounds exhibit a compact morphology with a size smaller than 2μm and are located at the boundaries between the primary α-Al grains or between eutectic cells and the primary α-Al grains. The intermetallic contains 1.62at.%Si, 3.94at.%Fe and 2.31at.%Mn, suggesting that it is most likely the α-AlFeMnSi phase.
3. A solute enriched circular band is always observed parallel to the surface of the casting. The band zone separates the outer skin from the central region of the casting. The solute

concentration is consistent in the skin region and a general drop toward to the centre inside the band for Mg and Si. The peak of solute enrichment in the band zone is much higher than the nominal composition of the alloy. However, the die casting exhibits a combination of brittle and ductile fracture. There is no significant difference on the fracture morphology in the three regions. Therefore, the band zone is not significantly detrimental in terms of the fracture mechanism in the die casting.

**4.** The stability criterion developed by Mullins and Sekerka for spherical growth can be used to provide a reasonable explanation for the difference in morphology of the primary α-Al phase solidified in the shot sleeve and in the die cavity. The solidification of the α-Al phase inside the die cavity has completed before the spherical grains begin to lose their stability, but the grains in the shot sleeve exceed the limit of spherical growth and, therefore, exhibit a dendritic morphology. The Jackson-Hunt theory can be used to estimate the growth rate of eutectic Al-$Mg_2Si$ phases in high pressure die casting process, and the results indicate that a fast solidification rate occurs in the die cavity. However, the growth rate of the aluminium phase in eutectic solidification calculated using the Jackson-Hunt theory is much larger than the growth rate of the primary α-Al phase calculated using the Mullins and Sekerka theory.

5. In the high pressure die casting of Al-Mg-Si-Mn alloys, the formation of Fe-rich intermetallics occurs into two solidification stages. One is in the shot sleeve at lower cooling rates, and the other is in the die cavity at higher cooling rates. The Fe-rich intermetallics formed in the shot sleeve exhibit coarse compact, star-like or needle/plate shape morphology with varied sizes. The Fe-rich intermetallics formed in the die cavity are characterised by fine compact morphology with the size less than 3 μm. In the alloys, two types of Fe-rich intermetallics are formed over the Fe content range up to 2.4wt. %. The fine compact α-AlFeSi phase has the composition of α-$Al_8Fe_2Si$ and the long needle β-AlFe phase has the composition of β-$Al_{13}Fe_4$. With 0.54wt.%Mn being added into the alloy, the fine compact intermetallic phase is found to be $Al_{12}(Fe,Mn)_3Si$ and the long needle β-AlFe phase is β-$Al_{13}(Fe,Mn)_4Si_{0.25}$. In the alloys containing 0.54wt.%Mn, the prior phase is α-Al when Fe is less than 0.21wt.%, but the prior phase is β-$Al_{13}(Fe,Mn)_4Si_{0.25}$ when Fe is higher than 1.24wt.%. Over the Fe contents range from 0.21 to 1.24wt%, α-$Al_{12}(Fe,Mn)_3Si$ precipitates as prior phase to form either coarse compact compounds in the shot sleeve or fine compact particles in the die cavity. The morphology and size of α-$Al1_{24}(Fe,Mn)_6Si_2$ intermetallics are dependent on the cooling rate. The higher cooling rate in the die cavity

enables the α-$Al1_{24}(Fe,Mn)_6Si_2$ phase to solidify in a fine compact morphology. However, the lower cooling rate in the shot sleeve results in the formation of compact and star-like Chinese script α-$Al1_{24}(Fe,Mn)_6Si_2$ phase in the as-cast microstructure. Fe-rich intermetallics significantly affect the mechanical properties of the alloy castings. The higher the iron concentrations in the alloy, the more significantly the ductility reduces. This is accompanied by a slight enhancement of the yield strength. The ultimate tensile strength maintains the similar level when Fe contents is less than 0.6wt.%, but decreases significantly with the further increase of Fe contents in the die-cast alloys. The yield strength and the ultimate tensile strength are slightly enhanced in the die-cast Al-Mg-Si alloy when Mn is added in comparison with that without Mn addition. Manganese promotes the formation of the cubic α-AlFeMnSi phase and suppresses the formation of β-AlFe phase in die-cast Al-Mg-Si alloys. The β-AlFe compounds are formed when Mn/Fe ratio is less than 0.5.

6. In the die-cast Al-Mg-Si-Mn alloy containing different Ni contents, the formation of Ni-rich intermetallics occurs consistently during solidification. The Ni-rich intermetallics exhibit dendritic and lamellar morphology during primary and eutectic solidification, respectively. In the alloy, Ni is always associated with Fe, Mn and Si to form AlFeMnSiNi intermetallics. No $Al_3Ni$ intermetallics is observed at Ni concentrations up to 2.06wt%, while both primary AlFeMnSiNi phase and eutectic AlFeMnSiNi phase are found in the as-cast microstructure. Both the primary and eutectic Ni-rich intermetallics are identified as the same AlFeMnSiNi phase with the typical composition of $Al_{[100-140]}(Fe,Mn)_{[2-7]}SiNi_{[4-9]}$. The increased Ni contents result in an increase in the spacing of Al-$Mg_2Si$ eutectics in the alloy. This indicates that the increased levels of Ni contents lower the growth velocity of the eutectic Al-$Mg_2Si$ during the solidification of the alloy. The addition of Ni significantly affects the mechanical properties of the alloy castings. The higher the Ni concentrations in the alloy, the more significant the reduction in ductility. This is accompanied by a slight enhancement of the yield strength. The ultimate tensile strength increases slightly when adding a small amount of Ni into the die-cast alloys, but further increase of the Ni content results in the decrease of the UTS.

7. In the experimental range, the tolerable Fe content is 0.45wt.%, at which the recycled alloys are still able to produce castings with the mechanical properties of yield strength over 140MPa, UTS over 280MPa and elongation over 15%. The Fe is steadily accumulated in

the alloy with the increased recycle times. However, after 13 cycles, the fully recycled alloys are still able to produce ductile alloy with satisfied mechanical properties.

8. The Weibull parameters for the yield strength, ultimate tensile strength, and elongation are different in the die-castings with different geometry including as-cast round and flat samples, and machine samples. The variations of characteristic parameters in three-parameter Weibull analysis show the importance of sampling type in determine the mechanical properties of the alloy and the reproducibility and reliability of castings. The reduced porosity levels and the improved microstructural uniformity in the die-castings result in the decrement of sources for brittle fracture, and therefore improve the mechanical properties and alter the characteristic parameters in Weibull statistical distribution, in particular the reproducibility and reliability of die-castings.

# Chapter 10
# Future Work

The most important work next is to try casting under vacuum condition. As seen, the castings made in conventional casting condition have lower elongation than that made for standard samples. It is expected that the fluid flow in the castings is more complex and difficult to predict. Therefore, the oxidation and porosity is increased in the casting, which result in the reduction of ductility of the alloy. Casting under vacuum assisted HPDC process can significantly reduce the contact with oxygen and less entrapment of air porosity. More importantly, a shorter filling time is possible because of the increase of pressure difference. As a result, the overall porosity level will be lower and the improved ductility is achievable.

It would be useful to study the effect of superheat on the microstructure and mechanical properties of the alloy. This will be helpful in grain refinement and help in die filling and possible very useful in casting practice. The strength and elongation of the alloy are expected to increase using a proper superheat.

The effect of minor elements such as rare earth element on the alloy can be studied in the further work. This can be useful to improve mechanical properties because of the grain refinement, reduction of oxidation.

# Publication list

**2016**

1. S Ji, HL Yang, **D Watson**, Z Fan. Weibull analysis for the repeatability of die castings made by an Al-Mg-Si-Mn alloy. TMS **2016** 145th Annual Meeting & Exhibition, February 14 – 18, 2016, Nashville, Tennessee.

**2014**

2. **D Watson**, S Ji, Z Fan. A Super-Ductile Alloy for the Die-casting of Aluminium Automotive Body Structural Components, Materials Science Forum 794(**2014**)526-531.
3. HL Yang, **D. Watson**, Y. Wang, S Ji, Effect of Ni on the microstructure and mechanical properties of Al-Mg-Si-Mn alloy, J Materials Science (**2014**) 49:8412-8422.
4. S Ji, Y Wang, **D Watson**, Z Fan, Microstructural Characteristics of Die cast AlMgSiMn Alloy, Materials Science Forum, 783-786(**2014**) 234-238.
5. HL Yang, S Ji, **D Watson**, M White, Z Fan, Microstructure and Mechanical Properties of Ductile Aluminium Alloy Manufactured by Recycled Materials, Materials Science Forum 794(**2014**) 1077-1082.

**2013**

6. S Ji, **D Watson**, Y Wang, M White, Z Fan, Effect of Ti Addition on Mechanical Properties of High Pressure Die Cast Al-Mg-Si Alloys, Materials Science Forum 765(**2013**) 23-27.
7. S Ji, Y Wang, **D Watson**, Z Fan, Microstructural evolution and solidification behavior of Al-Mg-Si alloy in high-pressure die casting, Metallurgical and Materials Transactions A, 44A(**2013**)3185-3197.
8. S Ji, W Yang, F Gao, **D Watson**, Z Fan, Effect of iron in Al-Mg-Si-Mn ductile die cast alloy, Light Metals **2013**, 317-322.
9. S Ji, W Yang, F Gao, **D Watson**, Z Fan, Effect of iron on the microstructure and mechanical property of Al-Mg-Si-Mn and Al-Mg-Si die cast alloys, Materials Science

& Engineering A 564 (2013) 130–139.

10. S. Ji, D. Watson, Z. Fan, Alloy and method of production thereof WO 2013144343

**2012**

11. S Ji, **D Watson**, Z Fan, M White, Development of a super ductile die cast Al-Mg-Si alloy, Materials Science and Engineering A 556 (**2012**) 824-833.

# Reference


[1] Transport and Magnesium, http://www.world-aluminium.org/media/filer_public/2013/01/15/fl0000172.pdf.

[2] Staley J.T., Lege D.J., 1993. Advances in aluminium alloy products for structural applications in transportation, J. Phys. IV France 03, C7-179-C7-190.

[3] Taub A.I., Krajewski P.E., Luo A.A., Owens J.N., 2007. The evolution of technology for materials processing over the last 50 years: The automotive example, JOM 2, 48-57.

[4] Codd D., 2008. Advanced Lightweight Materials Development and Technology for Increasing Vehicle Efficiency, KVA Inc., Escondido CA 92029 USA, 2008.

[5] Zeuner T., Würker L., 2003. Process Optimisation of Cast Aluminium Chassis Components WFO Technical Forum, p3.1-3.14.

[6] Tharumarajah A., 2008. Benchmarking aluminium die casting operations, Resources Conservation and Recycling 52, 1185-89.

[7] Miller W.S., Zhuang L., Bottema J., Wittebrood A.J., DeSmet P., Haszler A., Vieregge A., 2000. Recent development in aluminium alloys for the automotive industry, Mater. Sci. Eng. A 280, 37-49.

[8] European Aluminium Association. 2008. Aluminium in cars. European Aluminium Association.

[9] The Aluminium Association, Inc., 2001. Aluminium: The Corrosion Resistant Automotive Material, Publication AT7, May 2001.

[10] Ji S., 2011. Light-weighted Materials for Automotive Industry, BCAST Internal Report, Brunel University, UK, Dec. 2011.

[11] Annual Book of ASTM standards, 1993 Warrendale PA, ASTM, vol. 02.02.

[12] Stefanscu D. M., Davis J. R., Destefani J.D. (eds.), 1988. ASM metals handbook, 9th edn., vol. 15, Casting, Metals Park, OH, ASM International.

[13] Global Aluminium Recycling: - World Aluminium, http://www.world-aluminium.org/media/filer_public/2013/01/15/fl0000181.pdf.

[14] Aluminium: The Element of Sustainability, http://www.aluminum.org/sites/default/files/Aluminum_The_Element_of_Sustainability. Pdf.

[15] The Basic Metal Industry and Its Energy Use -- Prospects for the Dutch energy intensive industry, http://www.ecn.nl/docs/library/report/1997/c97019.pdf.

[16] Gaustad G., Olivetti E., Kirchain R., 2012. Improving aluminium recycling: A survey of sorting and impurity removal technologies, Resources, Conservation and Recycling 58, 79–87.

[17] Hurtalová L., Tillová, E., Chalupová M., Ďuriníková E., 2012. Effect of chemical composition of secondary Al-Si cast alloy on intermetallic phases, http://meching.com/journal/Archive/2012/9/17.pdf.

[18] Barone M.R., Caulk D.A., 2000. Analysis of liquid metal flow in die casting, Int. J. Eng. Sci. 38, 1279 -1302.

[19] Felberbaum M., 2010. Porosity in Aluminium Alloys: Visualization, Characterization, and Modelling, http://infoscience.epfl.ch/record/144087/files/EPFL_TH4639.pdf.

[20] Gariboldi E., Bonollo F., Parona P., 2010. in Handbook of defects in high pressure die castings, AIM, Milano.

[21] Butler, W. A. 2008. High-Pressure Die Casting. ASM handbook: Vol 15 Casting. United States of American: ASM International, Materials Park, OH : ASM International.

[22] Kaye, A. & Street, A., 1982. Die Casting Metallurgy, London UK, Butterworths Scientific.

[23] Apelian D., 2004. High integrity aluminium die casting (Alloys, processes, & melt preparation) Rosemount, IL: North American Die Casting Association, North American Die Casting Association.

[24] Upton B., 1982. Pressure diecasting. Pt.1, Metals, machines, furnaces, Headinton Hill Hall, Oxford OX30BW, England, Pergamon Press Ltd.

[25] Butler B., 2001. Die casting handbook Rosemont, IL : North American Die Casting Association, North American Die Casting Association.

[26] Vinarcik, E. J. 2003. High integrity die casting processes, New York, Wiley.

[27] Nadca 2009. Aluminium Cast Alloys: Enabling Tools for Improved Performance, NADCA.

[28] Thirugnanam, M. 2013. Modern High Pressure Die-Casting Processes for Aluminium Castings. Indian Foundry Journal, 59(7), 36-41.

[29] Gunasegaram D. R., Givord M. O., Donnell R. G. & Finnin B. R., 2008. Improved Quality and Reduced Cost through ATM High Pressure Die Casting. Die casting engineer, 52(1), 42-47.

[30] Wang L., Makhlouf M. & Apelian D., 1995. Aluminium die casting alloys: alloy composition, microstructure, and properties-performance relationships. International Materials Reviews, 40(6), 221-238.

[31] Twarog D. 2011. State of the Die Casting Industry Available: http://www.diecasting.org/information/soi/soi2012.pdf.

[32] Li C., Liu X. & Wu Y., 2008. Refinement and modification performance of Al–P master alloy on primary Mg2Si in Al–Mg–Si alloys. Journal of Alloys and Compounds, 465(1–2), 145-150.

[33] Fan Z. 2002. Semi-Solid Processing, Inter. Mater. Review 47, 49-85.

[34] http://www.castool.com/product/publications/vacuum-assisted-die-casting-todays-most-significant-technology.

[35] http://www.alueurope.eu/wp-content/uploads/2012/01/AAM-Manufacturing-1-Casting-methods.pdf.

[36] Atkinson H.V., 2005. Modelling the semisolid processing of metallic alloys, Progress in Materials Science 50 (3) 341–412.

[37] Flemings M. C., 1991. Behaviour of metal alloys in the semisolid state, Metall. Mater. Trans. A, 22A, 957–981.

[38] http://www.wpi.edu/Images/CMS/MPI/Jorstad.pdf.

[39] http://www.foundryinfo-india.org/images/pdf/2A2.pdf.

[40] http://www.scribd.com/doc/120254185/Aluminum-Alloy-Casting-Properties-Processes-Applications-ASM-2004.

[41] http://www.diecasting.org/docs/information/annual/20913.pdf.

[42] http://european-aluminium.eu/wp-content/uploads/2012/01/AAM-Manufacturing-1-Casting-methods.pdf.

[43] Abed E. J., 2011. The Influence of Different Casting Method on Solidification time and Mechanical Properties of Al-Sn castings, International Journal of Engineering & Technology, 11(06) 26-32.

[44] Groeneveld T.P., Winkler L.H., Goodwin F.E., 1985. Transactions - SDCE International Die Casting Exposition & Congress, Society of Die Casting Engine, Milwaukee, WI, USA, p6-11.

[45] Porter D. A. & Easterling K. E., 1992. Phase transformations in metals and alloys, London; New York, Chapman & Hall..

[46] Kaufman J. G., 2004. Aluminium alloy castings : properties, processes, and applications, United States of American, Materials Park, OH : ASM International.

[47] Hatch, J. E., 1984. Aluminium: properties and physical metallurgy, United States of American, Metals Park, Ohio: American Society for Metals.

[48] Hartman, P., 1973. Crystal growth: an introduction, Amsterdam; New York, North-Holland Pub. Co.; American Elsevier.

[49] Men H., Jiang B., Fan F., 2010. Mechanisms of grain refinement by intensive shearing of AZ91 alloy melt, Acta Mater. 58, 6526-6535.

[50] Glicksman M. E., 2010. Principles of Solidification, Springer, ISBN 978-1-4419-7344-3.

[51] Chai G., Backerud L., Rolland T., Arnberg L., 1995. Dendrite coherency during equiaxed solidification in binary aluminium alloys, Metall. Mater. Trans. 26A, p965-976.

[52] Yuan L., O'Sullivan C., Gourlay C.M., 2012, Exploring dendrite coherency with the discrete element method, Acta Materialia, 60(3), 1334-1345.

[53] Fraser D., 2000. Soldering in high pressure die casting and its prevention by lubricant and oxide coating. Ph. D., The University of Queensland.

[54] Shankar S. A. D., 2002. Die soldering: Mechanism of the interface reaction between molten aluminium alloy and tool steel. Metallurgical and Materials Transactions B, 33(3), 465-476.

[55] Riabov V. R., 1985. Aluminizing of steel, New Delhi, Oxonian Press.

[56] Tang C., 2007. Soldering in Magnesium High Pressure Die Casting and its Prevention by Surface Engineering. Swinburne University of Technology.

[57] Chen Z. W., Jahedi, M. Z., 1999. Die erosion and its effect on soldering formation in high pressure die casting of aluminium alloys. Materials & Design, 20(6), 303-309.

[58] Graff J. L., Kallien L H,1993. The effect of die lubricant spray on the thermal balance of dies, The NADCA conference in Cleveland, USA Oct. 18-21.

[59] Dahle, A. K. & StJohn, D. H., 1999. Rheological behaviour of the mushy zone and its effect on the formation of casting defects during solidification. Acta Materialia, 47(1), 31-47.

[60] Eskin D. G., Suyitno & Katgerman L., 2004. Mechanical properties in the semi-solid state and hot tearing of aluminium alloys. Progress in Materials Science, 49(5), 629-711.

[61] Laukli H., 2012. Recent Developments in Aluminium High Pressure Die Casting. Die casting engineer, 56(3), 20-23.

[62] Campbell J., 2006. Entrainment defects. Materials Science & Technology, 22(2), 127-145.

[63] Arnberg L., 2008. Castability-Fluidity and Hot Tearing. ASM handbook: Vol 15 Casting. United States of American: ASM International, Materials Park, OH : ASM International.

[64] Otarawanna S., 2009. High Pressure Die Casting of Aluminium and Magnesium Alloys:Formation of Microstructure and Defects. Dissertation/Thesis, The University of Queensland, School of Mechanical and Mining Engineering.

[65] Knott J., Beeley P. R., Griffiths J. R., Green N. R., Newton C. J. & Campbell J., 2006. Commentaries on 'Entrainment defects' by J. Campbell. Materials Science and Technology, 22(8), 999-1008.

[66] http://webhotel2.tut.fi/projects/caeds/tekstit/mould/mould_HPDC_alloys.pdf.

[67] ASM handbook, 1993. Properties and selection: nonferrous alloys and special purpose Materials: Properties of cast aluminium alloys, vol. 2.

[68] http://webhotel2.tut.fi/projects/caeds/tekstit/mould/mould_HPDC_alloys.pdf.

[69] Fruehan R. J. & Anyalebechi P. N., 2008. Gases in metals. ASM handbook: Vol 15 Casting. United States of American: ASM International, Materials Park, OH : ASM International.

[70] http://webhotel2.tut.fi/projects/caeds/tekstit/mould/mould_HPDC_alloys.pdf.

[71] Mondolfo L. F., 1976. Aluminium alloys : structure and properties, London; Boston, Butterworths.

[72] Mondolfo L. F., 1943. Metallography of aluminium alloys, New York, J. Wiley & Sons; Chapman & Hall.

[73] Polmear I. J., 2006. Light alloys from traditional alloys to nanocrystals. Amsterdam; Boston: Elsevier/Butterworth-Heinemann.

[74] Adibhatla S., Master's Thesis, IMS, University of Connecticut 2003.

[75] Meyers C.W., Hinton K.H., Chou J.S.,1992. Towards the Optimization of Heat Treatment in Aluminium Alloys. Materials Sci Forum 1992;72 102-104.

[76] Li Z., Samuel A.M., Samuel F.H., Ravindran C., Valtierra S. 2003. Effect of Alloying Elements on the Segregation and Dissolution of CuAl2 Phase in Al–Si–Cu 319 Alloys. J. Mater. Sci. 2003;38 1203–1218.

[77] Hekmat-Ardakan A., Ajersch F., 2010. Thermodynamic evaluation of hypereutectic Al–Si (A390) alloy with addition of Mg. Acta Materialia, 58(9) 3422-3428.

[78] Lin X., Liu C., Zhai Y., Wang K., 2011. Influences of Si and Mg contents on microstructures of Al–xSi–yMg functionally gradient composites reinforced with in situ

primary Si and Mg2Si particles by centrifugal casting. Journal of Materials Science, 46(4), 1058-1075.

[79] Backerud L., Chai G., Tamminen J., 1990. Solidification Characteristics of Aluminium Alloys, Foundry Alloys Vol. 2 (AFS/Skanaluminum, 1990) pp. 71- 84

[80] Shivkumar S., Wang L., Apelian D., 1990. The lost-foam casting of aluminium alloy components JOM 42(11), 38 -44.

[81] Kral M.V., McIntyre H.R., Smillie M.J., 2004. Identification of intermetallic phases in a eutectic Al–Si casting alloy using electron backscatter diffraction pattern analysis, Scripta Mater. 51, 215-219.

[82] Zheng J.G., Vincent R., Steeds J.W., 1999. Crystal structure determination of an Al-Fe-Si-Be phase by convergent-beam electron diffraction, Philos. Mag. 79 (11) 2725 -2733.

[83] Wen K.Y., Hu W., Gottstein G., 2003. Intermetallic compounds in thixoformed aluminium alloy A356, Mater. Sci. Technol. 19 (6) 762 -768.

[84] Couture A., 2003. Iron in aluminium casting alloy – A literature survey, AFS International Journal of Cast Metals, 6, 9-17.

[85] Crepeau P.N., 1995. Effect of iron in Al-Si casting alloys: A critical review, AFS Trans, 103, 361-366.

[86] Munson D., 1967. The distribution of the transition metals Fe and Mn in the Al-Si alloys, Journal of the Institute of Metals 95, 217-219.

[87] Hodgson P., Parker B. A., 1981. The composition of insoluble intermetallic phases in aluminium alloy 6010, J. Materials Science 16 (5) 1343-1348.

[88] Shabestari S.G., Gruzleski J.E., 1995. Gravity segregation of complex intermetallic compounds in liquid aluminium-silicon alloys, Metallurgical and Materials Science, 26A, 999-1006.

[89] Cao X., Campbell J.,2000. Precipitation of primary intermetallic compounds in liquid Al-11.5Si-0.4Mg alloy, Int. J. Cast Metals Res. 13 175-184.

[90] Cao X., Campbell J., 2004. Effect of Precipitation of primary intermetallic compounds on tensile properties of cast Al-11.5Si-0.4Mg alloy, AFS Transactions, 108, 391-400.

[91] Cao X., Campbell J., 2004. The solidification characteristics of Fe-rich intermetallics in Al-11.5Si-0.4Mg cast alloys, Metall. Mater. Trans. A 35A (4) 1425-1435.

[92] Sigworth G. K., Shivkumar S. and Apelian D., 1989. The influence of molten metal processing on mechanical properties of cast Al-Si-Mg alloy, AFS Trans. 97, 811-824.

[93] Samuel M., Pennors A., Villeneuve C., Samuel F., Doty H. and Valtierra S., 2000. Effect of cooling rate and Sr-modification on porosity and Fe-intermetallics formation in Al-6.5%Si-3.5%Cu-Fe alloys, Cast Metals Research, 13, 231-253

[94] Narayanan L. A., Samuel F. H., Gruzleski J. E.,1994. Crystallization behavior of iron-containing intermetallic compounds in 319 aluminium alloy, Metall. Mater. Trans. A 25A (7) 1761-1773.

[95] Seifeddine S., Svensson I. L., 2009.The influence of Fe and Mn content and cooling rate on the microstructure and mechanical properties of A380-die casting alloys, Metall. Sci. Technol., 27(1) 11-20.

[96] Niu X. P., Hu B.H., Hao S.W., 1998. Effect of iron on the microstructure and mechanical properties of Al diecasting alloys J. Mater. Sci. Letters 17, 1727-1729.

[97] Balitchev E., Jantzen T., Hurtado I., Neuschütz D.,2003. Thermodynamic assessment of the quaternary system Al–Fe–Mn–Si in the Al-rich corner, Calphad 27 (3)275-278.

[98] Fang X., Shao G., Liu Y.Q., Fan Z., 2007. Effects of intensive forced melt convection on the mechanical properties. Mater. Sci. Eng. A 445-446, 65-72..

[99] ASM Specialty Handbook (1993) Aluminium and Aluminium Alloys, Davis J. R., Davis & Associates Eds., ASM International, Materials Park, OH.

[100] Barr C.J., McDonald D.T., Xia K., 2013, Significantly enhanced tensile strength and ductility in nickel aluminium bronze by equal channel angular pressing and subsequent heat treatment, J. Mater. Sci. 48, 4749-4757.

[101] Zhu S., Yao J., Sweet L., Easton M., Taylor J., Robinson P., Parson P., 2013, Influences of Nickel and Vanadium Impurities on Microstructure of Aluminium Alloys, JOM 65:584-592.

[102] Song J.M., Lin T.Y., Chuang H.Y., 2007, Microstructural Characteristics and Vibration Fracture Properties of Al-Mg-Si Alloys with Excess Cu and Ni, Mater. Trans. 48, 854-859.

[103] Mallapur D.G., Kori S.A., Rajendra Udupa K., 2011. Influence of Ti, B and Sr on the microstructure and mechanical properties of A356 alloy, J. Mater. Sci. 46, 1622-1627.

[104] Gokhale A.M., Patel G.R., 2002. in: Subodh K.D., Michael HS (eds.) Proceedings of TMS 2002 automotive alloys and aluminium sheet symposium, TMS, Warrendale, p 65.

[105] Lee S.G., Patel G.R., Gokhale A.M., Sreeranganathan A., Horstemeyer M.F., 2005 .Variability in the tensile ductility of high-pressure die-cast AM50 Mg-alloy, Scripta Mater. 53:851.

[106] Surappa M.K., Blank E., Januet J.C., 1986. Effect of macro-porosity on the strength and ductility of cast Al-7Si-0.3Mg alloy, Scripta Metall 20 (9)1281-1286.

[107] Lee C.D., Shin K. S., 2007. Effect of microporosity on the tensile properties of AZ91 magnesium alloy, Acta Materialia 55(13) 4293–4303.

[108] Meggiolaro M.A., Castro J.T.P., 2004. Statistical evaluation of strain-life fatigue crack initiation predictions, International Journal of Fatigue 26 463–476.

[109] Ji S., Yang W., Jiang B., Patel J.B., Fan Z., 2013. Weibull statistical analysis of the effect of melt conditioning on the mechanical properties of AM60 alloy, Mat. Sci. Eng. A566, 119-125.

[110] Steen M. Fractography and fracture mechanics property assessment of advanced structural ceramics. Inter Mater Rev. 1999; 44(5):165–216.

[111] Quinn G. D., Quinn J. B., 2010. A practical and systematic review of Weibull statistics for reporting strengths of dental materials, Dent Mater. 26, 135-147.

[112] C. Reilly, N. R. Green, M. R. Jolly, 2012.Applied Mathematical Modelling The present state of modelling entrainment defects in the shape casting process, 37(3) 611-628.

[113] Campbell J.2011. Complete Casting Handbook: Metal Casting Processes, Metallurgy, Techniques and Design', UK, Elsevier Butterworth-Heinemann, pp1220.

[114] Timelli G., Bonollo F., 2010. The influence of Cr content on the microstructure and mechanical properties of AlSi9Cu3(Fe) die-casting alloys, Mat. Sci. Eng. A, 528, 273-282.

[115] Campbell J., 2003. Castings, Butterworth-Heinemann, Oxford, 2nd edn.

[116] Dai X., Yang X., Campbell J., Wood J., 2004. Influence of oxide film defects generated in filling on mechanical strength of aluminium alloy castings , Mater. Sci. Technol., 20 (4) 505-513.

[117] Dispinar D., Campbell J., 2006. Use of bifilm index as an assessment of liquid metal quality, Int. J. Cast Metals Res., 19 (1) 5-17.

[118] Tiryakioğlu M., Campbell J., 2010. Weibull Analysis of Mechanical Data for Castings: A Guide to the Interpretation of Probability Plots, Metall. Mater. Trans. A 41(12) 3121-3129.

[119] Zahedi H., Emamy M., Razaghian A., Mahta M., Campbell J., Tityakiolu M., 2007. The Effect of Fe-Rich Intermetallics on the Weibull Distribution of Tensile Properties in a Cast Al-5 Pct Si-3 Pct Cu-1 Pct Fe-0.3 Pct Mg Alloy, Metall. Mater. Trans. A, 38 (3) 659-670.

[120] ASTM B557-06, Standard Test Methods for Tension Testing Wrought and Cast Aluminium- and Magnesium-Alloy Products.

[121] Ghorbani, M. R., Emamy, M. & Nemati, N. 2011. Microstructural and mechanical characterization of Al–15%Mg2Si composite containing chromium. Materials & Design, 32(8–9), 4262-4269.

[122] Wiley V. C. H., 1988. Particle & particle systems characterization. http://onlinelibrary. wiley.com/journal/10.1002/(ISSN)1521-4117.

[123] Cao W., Chen S. L., Zhang F., Wu K., Yang Y., Chang Y. A., Schmid-Fetzer R., Oates W. A., 2009. PANDAT software with PanEngine, PanOptimizer and PanPrecipitation for multi-component phase diagram calculation and materials property simulation. Calphad, 33(2), 328-342.

[124] Chen S. L., Daniel, S., Zhang, F., Chang, Y. A., Yan, X. Y., Xie, F. Y., Schmid-Fetzer, R. & Oates, W. A. 2002. The PANDAT software package and its applications. Calphad, 26(2), 175-188.

[125] Chen, S. L., Zhang, F., Xie, F. Y., Daniel, S., Yan, X. Y., Chang, Y. A., Schmid-Fetzer, R. & Oates, W. A. 2003. Calculating phase diagrams using PANDAT and panengine. JOM, 55(12), 48-51.

[126] Rettenmayr M., 2009.Alloy development using modern tools, Int. J. Mat. Res. 100, 153-59.

[127] Zolotorevsky V.S., Belov N.A., Glazoff M.V., 2007. Casting Aluminium, ISBN 9780080453705, Elsevier, p 484.

[128] Tian R-Z., Cast Aluminium Alloys, Mid-Southern University Press, 1st ed., 2006.

[129] Koch H., Lenczowski B., Al/Mg/Si Cast Aluminium Containing Scandium, WO/2005/047554, 2005.

[130] Trenda G., Kraly A., 2006.Aluminium Alloy, WO/2006/122341.

[131] Lukas H.L., Fries S.G., Sundman B., 2007. Computational Thermodynamics: The Calphad Method, Cambridge University Press.

[132] Böyük U., Marash N., Kaya H., Çadırh E.,· Keslioglu K., 2009. Directional solidification of Al–Cu–Ag alloy, Appl. Phys A 95: 923–932.

[133] Apelian D., 2009. Aluminium Cast Alloys: Enabling Tools for Improved Performance. North American Die Casting Association, Wheeling, Illinois, USA, pp.1-68.

[134] Krug P., Koch H., Klos R.: Magsimal-25 - A new High-Ductility Die Casting Alloy for Structural Parts in Automotive Industry, www.dgm.de/download/tg/523/523_0784.pdf.

[135] Hosseinifar M., Malakhov D.V., 2011. The Sequence of Intermetallics Formation during the Solidification of an Al-Mg-Si Alloy Containing La, Metall. Mater. Trans. A, 42A, 825-33.

[136] Liu Y. L., Kang S. B., 1997. The solidification process of Al–Mg–Si alloys J. Mater. Sci., 32, 1443-1447.

[137] Kori S. A., Prabhudev M. S., Chandrashekharaiah T.M., 2009. Studies on the microstructure and mechanical properties of A356 alloy with minor additions of copper and magnesium Transactions of The Indian Institute of Metals, Trans. Indian Institute of Metals, 62, 353-356.

[138] Yu L., Liu X., Wang Z., Bian X.: Grain refinement of A356 alloy by AlTiC/AlTiB master alloys, J. Mater. Sci. 2005, vol.40, pp.3865-3871.

[139] Otarawanna S., Gourlay C.M., Laukli H.I., Dahle A.K.: Metall. Mater. Trans. A, 2009, vol. 40A, pp.1645-59.

[140] Jie J., Zou C., Wang H., Wei Z., 2010. Microstructure evolution of Al–Mg alloy during solidification under high pressure, Materials Letters, 64, 869-71.

[141] Kimura R., Hatayama H., Shinozaki K., Murashima I., Asada J., Yoshida M., 2009. Effect of grain refiner and grain size on the susceptibility of Al–Mg die casting alloy to cracking during solidification J. Mater. Processing Tech., 209 (1) 210-15.

[142] Hamasaiid A., Dargusch M.S., Davidson C.J., Tovar S., Loulou T., Rezai-Aria F., Dour G., 2007. Effect of Mold Coating Materials and Thickness on Heat Transfer in Permanent Mould Casting of Aluminium Alloys Metall. Mater. Trans. A 38, 1303-15.

[143] Raghavan V., 2007. Al-Mg-Si (Aluminium-Magnesium-Silicon), J. Phase Equilibria and Diffusion, 28,189-191.

[144] Beeley P., 2001. Foundry Technology, 2nd, Oxford: Butterworth-Heinemann.

[145] Mullins W.W., Sekerka R.F., 1963. Morphological Stability of a Particle Growing by Diffusion or Heat Flow J. Appl. Phys., 34, 323-29.

[146] Mullins W.W., Sekerka R.F., 1964. Stability of a Planar Interface During Solidification of a Dilute Binary Alloy J. Appl. Phys., 35, 444-451.

[147] Sekerka R.F., 1965. A Stability Function for Explicit Evaluation of the Mullins-Sekerka Interface Stability Criterion, J. Appl. Phys., 1965, 36, 264-68.

[148] Woodru D.P., 1973. The solid–liquid interface. Cambridge: Cambridge University Press.

[149] Brandes E.A., Brook G.B., 1992. Smithells metals reference book. 7th ed. Oxford: Butterworth.

[150] Greer A. L., Bunn A. M., Tronche A., Evans P.V., Bristow D.J., 2000. Modelling of inoculation of metallic melts: application to grain refinement of aluminium by Al–Ti–B, Acta Mater., 48(11)2823-2835.

[151] Burden M. H., Hunt J.D., 1974. Cellular and dendritic growth, J. Cryst. Growth, 22(2) 99-108.

[152] Hunt J. D., Lu S. Z., 1996. Numerical modelling of cellular/dendritic array growth: spacing and structure predictions, Metall. Mater. Trans. A, 27(3)611-623.

[153] Keslioglu K., Gunduz M., Kaya H., Cadırl E., 2004. Solid–liquid interfacial energy in the Al–Ti system, Materials Letters, 58, 3067-3071.

[154] Bower T. F., Brody H. D., Flemings M.C.: Trans. AIME., 1966, vol.236, pp.624-33.

[155] Li S-P., Zhao S-X., Pan M-X., Zhao D-Q., Chen X-C., Barabash O. M., 2001. A novel Ni-CERMET electrode based on a proton conducting electrolyte, J. Mater. Sci., 36 (3) 1569-1575.

[156] Jackson K.A., Hunt J.D.: Trans. Metall. Soc. AIME., 1966, vol.236, pp.1129-42.

[157] Grugel R., Kurz W., 1987. Growth of interdendritic eutectic in directionally solidified Al-Si alloys, Metall. Trans. A18 (6)1137-1142.

[158] Böyüka U., Enginb S., Maraşlı N., 2011. Microstructural characterization of unidirectional solidified eutectic Al–Si–Ni alloy, Materials Characterization, 62 (9), 844-51.

[159] Kaya H., Cadirli E., Gündüz M., 2007. Eutectic growth of unidirectionally solidified bismuth–cadmium alloy, J. Materials Processing Technology, 183 (2-3), 310-320.

[160] Whelan E. P., Haworth C. W., 1967. J. Aust. Inst. Met., 1.12, 77-126.

[161] Trivedi R., Mason J.T., Verhoeven J.D., Kurz W., 1991. Eutectic spacing selection in lead-based alloy systems, Metall. Mater. Trans., 22A (10)2523-2533.

[162] Moore A., Elliott R., 1967. Solidification of Metals, Proc. Conf. Iron and Steel Ins. Publ., Brighton, UK, pp.167-74.

[163] Cadirli E., Kaya H., Gunduz M., 2003. Effect of growth rates and temperature gradients on the lamellar spacing and the undercooling in the directionally solidified Pb–Cd eutectic alloy, Mater. Res. Bull., 38, 1457-1476.

[164] Cadirli E., Ulgen A., Gunduz M., 1999. Directional Solidification of the Aluminium-Copper Eutectic Alloy, Mater. Trans. JIM., 40, 989-996.

[165] Trivedi R., Magnin P, Kurz W.,1987. Theory of eutectic growth under rapid solidification conditions, Acta Metallurgica, 35, 971-980.

[166] Kurz W. and Trivedi R., 1991. Eutectic growth under rapid solidification conditions. Metall. Mater. Trans. A,22A (12)3051–3057.

[167] Villars P., Calvert L.D. (eds.), Pearson's Handbook of Crystallographic Data for Intermetallic Phases, 2nd ed., Materials Park, OH, ASM International, 1991.

[168] Gustafsson G., Thorvaldsson J., Dunlop G. L., 1986. The influence of Fe and Cr on the microstructure of cast Al-Si-Mg alloys, Metall. Mater. Trans. A, 17A(1) 45-52.

[169] Murali S., Raman K.S., Murthy K.S.S., 1995. The formation of β-FeSiAl5 and Be-Fe phases in Al-7Si-0.3Mg alloy containing Be. Mater. Sci. Eng. A, 190A, 165-72.

[170] Zakharov A.M., Guldin I.T., Aenold A.A., Yu A., 1989. Matsenko. Izv. Akad. Nauk SSSR Metall. 4, 214-23.

[171] Davignon G., Serneels A., Verlinden B., Delaey L., 1996. An isothermal section at 550 °C in the Al-Rich corner of the Al-Fe-Mn-Si system, Metall. Mater. Trans. A 27A, 3357-3361.

[172] Sweet L., Zhu S.M., Gao S.X., Taylor J.A., Easton M.A., 2011. The effect of iron content on the iron-containing intermetallic phases in a cast 6060 aluminium alloy, Metall. Mater. Trans. A, 42A (7) 1737-1749.

[173] Liu Z.K., 2003. Effect of impurities on alloys, I. T. Program. Washington, DC: Energy Efficiency and Renewable Energy, US Department of Energy.

[174] Liu L., Samuel F.H., 1997. Assessment of melt cleanliness in A356.2 aluminium casting alloy using the porous disc filtration apparatus technique: Part I Inclusion measurements, J Mater. Sci. 32, 5901-5911.

[175] Gaustad G., Olivetti E., Kirchain R., 2010. Design for recycling: evaluation and efficient alloy modification, J. Ind. Ecology 14, 286-308.

[176] Global Aluminium Recycling, 2013. A cornerstone of sustainable development, http://www.world-aluminium.org/media/filer_public/2013/01/15/fl0000181.pdf.

[177] Belov N.A., Aksenov A.A., Eskin D.G., 2002. Iron in Aluminium Alloys: Impurity and Alloying Element (Advances in Metallic Alloys), CRC Press, p23-33.

[178] Fuis V., Navrat T., 2011. Reliability of the Ceramic Head of the Total Hip Joint Endoprosthesis World Academy of Science, Engineering and Technology 58, 642-647.

[179] Kirtay S., Dispinar D., 2012. Effect of Ranking Selection on the Weibull Modulus Estimation, Gazi University Journal of Science 25,175-187.

[180] Weibull W., 1961. In Fatigue testing and analysis of results, Pergamon Press, Oxford, pp. 159-199.

[181] Rao A.R., Hamed K.H., 2000, Flood Frequency Analysis, Boca Raton, Florida: CRC Press, FL p350-355.

[182] Tiryakioglu M., Hudak D., Okten G., 2009. On evaluating Weibull fits to mechanical testing data, Mater. Sci. Eng. A 527, 397–399.

[183] Ji S., Wang Y., Fan Z., 2013. Microstructural evolution and solidification behaviour of Al-Mg-Si alloy in high-pressure die casting, Metall. Mater. Trans. A 44, 3185-3197.

[184] Ji S., Wang Y., Watson D., Fan Z., 2014. Microstructural Characteristics of Diecast AlMgSiMn Alloy, Materials Science Forum 783, 234-239.

[185] Ji S., Yang W., Gao F., Watson D., Fan Z., 2013. Effect of Iron in Al‐Mg‐Si‐Mn ductile diecast alloy, Light Metals 317-322.

[186] Yang H., Watson D., Wang Y., Ji S., 2014. Effect of nickel on the microstructure and mechanical property of die-cast Al–Mg–Si–Mn alloy, Journal of Materials Science 49 (24), 8412-8422.

[187] Mayer H., Papakyriacou M., Zettl B., Stanzl-Tschegg S.E., 2003. Influence of porosity on the fatigue limit of die cast magnesium and aluminium alloys, Int. J. Fatigue 25, 245 -256.

[188] Weiler J.P., Wood J.T., Klassen R.J., Maire E., Berkmortel R., Wang G., 2005, Relationship between internal porosity and fracture strength of die-cast Magnesium AM60B alloy, Mater. Sci. Eng. A 395 (1-2) 315-322.